



LUND UNIVERSITY

Advances in Structural Dynamics with applications to Cross-laminated Timber

Bondsman, Benjamin

2025

Document Version:

Publisher's PDF, also known as Version of record

[Link to publication](#)

Citation for published version (APA):

Bondsman, B. (2025). *Advances in Structural Dynamics with applications to Cross-laminated Timber*. [Doctoral Thesis (compilation), Department of Construction Sciences]. Department of Construction Sciences, Lund University.

Total number of authors:

1

General rights

Unless other specific re-use rights are stated the following general rights apply:

Copyright and moral rights for the publications made accessible in the public portal are retained by the authors and/or other copyright owners and it is a condition of accessing publications that users recognise and abide by the legal requirements associated with these rights.

- Users may download and print one copy of any publication from the public portal for the purpose of private study or research.
- You may not further distribute the material or use it for any profit-making activity or commercial gain
- You may freely distribute the URL identifying the publication in the public portal

Read more about Creative commons licenses: <https://creativecommons.org/licenses/>

Take down policy

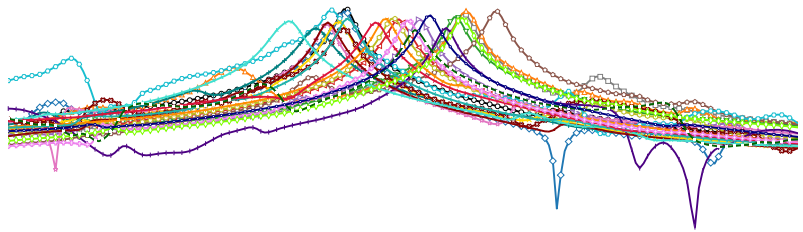
If you believe that this document breaches copyright please contact us providing details, and we will remove access to the work immediately and investigate your claim.

LUND UNIVERSITY

PO Box 117
221 00 Lund
+46 46-222 00 00



LUND
UNIVERSITY



ADVANCES IN STRUCTURAL DYNAMICS WITH APPLICATIONS TO CROSS-LAMINATED TIMBER

BENJAMIN BONDSMAN

Structural
Mechanics

Doctoral Thesis

DEPARTMENT OF CONSTRUCTION SCIENCES

DIVISION OF STRUCTURAL MECHANICS

ISRN LUTVDG/TVSM--25/1035--SE (1-162) | ISSN 0281-6679

ISBN 978-91-8104-445-4 (print) | ISBN 978-91-8104-446-1 (electronic)

DOCTORAL THESIS

**ADVANCES IN STRUCTURAL
DYNAMICS WITH APPLICATIONS
TO CROSS-LAMINATED TIMBER**

BENJAMIN BONDSMAN

Copyright © Benjamin Bondsman 2025.

Printed by V-husets tryckeri LTH, Lund, Sweden, May 2025 (PI).

For information, address:

Division of Structural Mechanics,
Faculty of Engineering LTH, Lund University, Box 118, SE-221 00 Lund, Sweden.

Homepage: www.byggmek.lth.se

Advances in Structural Dynamics with applications to Cross-laminated Timber

Benjamin Bondsman



LUND
UNIVERSITY

Organization LUND UNIVERSITY Faculty of Engineering Box 118 SE-221 00 LUND Sweden		Document name DOCTORAL THESIS	
Author(s) Benjamin Bondsman		Date of disputation 2025-06-13	
		Sponsoring organization	
Title and subtitle Advances in Structural Dynamics with applications to Cross-laminated Timber			
<p>Abstract</p> <p>Dynamic forces and vibration-induced deformations are critical considerations in engineering structures across civil, structural, nuclear, and aerospace disciplines. These forces significantly influence design strategies, operational safety, and overall system performance. For example, the oscillations of long-span bridges and buildings under wind loads and seismic activities exemplify the rate-dependent vibrations that such structures must endure. Excessive vibrations and deformation at resonance can compromise structural integrity, cause acoustical issues, and lead to fatigue and damage. With the continuous evolution of the built environment and the increasing challenges posed by global warming and climate change, there are growing initiatives to transition into a sustainable society through the integration of low-carbon-intensive materials into the construction sector. Hence, Cross-Laminated Timber (CLT) has emerged as a promising alternative to conventional building materials. However, the organic nature of wood introduces inherent variability in its mechanical properties, leading to uncertainties in the dynamic behaviour of CLT structures. Furthermore, the high strength-to-mass ratio of wood makes CLT more susceptible to vibrations than traditional alternatives. Therefore, it is essential to quantify the variability in the dynamic characteristics of CLT and develop robust computational models to predict its behaviour accurately.</p> <p>In this thesis, both computational and experimental frameworks are developed to advance the field of structural dynamics and enhance the understanding of the dynamic behaviour of CLT. This is achieved by quantifying the variability in its modal characteristics and developing robust computational methods for accurate structural assessment. Through four comprehensive studies, the thesis addresses the variability in modal characteristics of CLT using Experimental Modal Analysis (EMA) on nominally identical beam-like substructures and develops a robust derivative-free model updating framework to tune numerical models towards corresponding measurements from EMA. Furthermore, the thesis quantifies the influence of uncertainty in the mechanical properties of CLT on their associated output modal properties and proposes an uncertainty quantification procedure. Finally, the thesis introduces a coupled interface reduction technique to enhance the computational efficiency of large-scale dynamic analyses, including composite CLT structures. Although these frameworks and procedures are applied to CLT, they are presented in a general manner and can be applied to other dynamic systems.</p>			
<p>Key words</p> <p>Experimental Modal Analysis, Inverse Dynamics, Modal Updating, Uncertainty Quantification, Reduced Order Modelling, Cross-laminated Timber</p>			
Classification system and/or index terms (if any)			
Supplementary bibliographical information		Language English	
ISSN and key title ISSN 0281-6679, Report TVSM-1035		ISBN 978-91-8104-445-4 (print) 978-91-8104-446-1 (pdf)	
Recipient's notes	Number of pages 176	Price	
	Security classification		

I, the undersigned, being the copyright owner of the abstract of the above-mentioned dissertation, hereby grant to all reference sources the permission to publish and disseminate the abstract of the above-mentioned dissertation.

Signature _____

Date 2025-06-13 _____

Contents

List of publications	iv
Other publications	iv
Preface	v
Popular science summary	vi
Advances in Structural Dynamics with applications to Cross-laminated Timber	1
I Introduction and overview	3
1 Introduction	5
1.1 Aims and scope of the research	8
1.2 Limitations	10
1.3 Thesis Outline	10
2 Wood Fundamentals: From Growth to Engineering Applications	11
2.1 Structure of wood	12
2.1.1 Macroscopic level	13
2.1.2 Microscopic level	14
2.2 Wood growth	15
2.2.1 Growth increments and annual rings	15
2.2.2 Sapwood and Heartwood	15
2.2.3 Cellular composition and wood rays	15
2.2.4 Planes of wood	16
2.3 Structural timber	16
2.4 Cross-laminated Timber	17
3 Predictive modelling and simulation	19
3.1 Mechanical Deformation	20
3.1.1 Principle of virtual work	20
3.1.2 Finite Element formulation	21
3.1.3 Constitutive law	22
3.2 Dynamic problems	23
3.2.1 Damping	24
3.2.2 Modal domain and mode superposition	26

3.2.3	Time domain	28
3.2.4	Frequency domain	29
4	Experimental Modal Analysis	31
4.1	Experimental design	32
4.2	Boundary conditions	33
4.3	Data acquisition and processing	33
4.4	Estimation of transfer functions	34
4.5	Estimation of modal parameters	37
5	Inverse parameter identification and model updating	39
5.1	Residual formulation	40
5.2	Model parametrisation	41
5.3	Parameter estimation	42
5.4	Model validation	44
6	Uncertainty quantification	47
6.1	Probabilistic modelling and sampling	48
6.2	Uncertainty propagation	49
6.3	Uncertainty quantification	49
6.4	Lower and upper bounds sensitivity	50
7	Component-Mode Synthesis	53
7.1	Substructure coupling in the physical domain	54
7.2	Interior dynamics reduction	56
7.3	Interface dynamics reduction	58
7.3.1	Classical interface reduction	59
7.3.2	Coupled interface reduction	60
8	Conclusions and recommendations	63
8.1	Conclusions and contributions	63
8.2	Recommendations	64
	References	65
II	Appended publications	79
	Scientific publications	81
	Contribution statement – B. Bondsman	81
	Paper I: Experimental Modal Analysis and variability assessment of Cross-laminated Timber	83
	Paper II: Inverse parameter identification and model updating for Cross-laminated Timber substructures	103
	Paper III: Uncertainty quantification of mechanical properties and modal characteristics in Cross-laminated Timber	123

List of publications

This thesis is based on the following publications, referred to by their Roman numerals:

- I **Experimental Modal Analysis and variability assessment of Cross-laminated Timber**
B. Bondsman, A. Peplow
Mechanical Systems and Signal Processing, Vol. 228, 112466, 22.02.2025
- II **Inverse parameter identification and model updating for Cross-laminated Timber substructures**
B. Bondsman, A. Peplow
Journal of Building Engineering, Vol. 95, 110209, 15.06.2024
- III **Uncertainty quantification of mechanical properties and modal characteristics in Cross-laminated Timber**
B. Bondsman
To be published
- IV **Interface reduction technique for Enhanced Craig-Bampton method**
B. Bondsman, C-u. Ahn, & J-g. Kim
Mechanical Systems and Signal Processing, Vol. 208, 111074, 29.12.2023

Other publications

Abstract I

B. Bondsman, A. Peplow. Exploring Cross-laminated Timber Transfer Functions Using Deep Learning. *In the XIVth International Conference on Recent Advances in Structural Dynamics (RASD) – 1-3 July 2024, Southampton, UK.*

Preface

This thesis represents the culmination of a rigorous and introspective journey undertaken over three and a half years. Driven by deep-seated curiosity and a commitment to advancing the field of structural dynamics, this period has been characterised by intensive learning and sustained reflection, both of which have shaped my conviction in the significance and potential of this discipline. The research was predominantly self-funded and conducted in conjunction with my professional responsibilities as an engineer. Although balancing full-time employment with academic research presented challenges, it also fostered resilience, independence, and a steadfast determination to advance the work through to completion.

Throughout this time, I independently navigated the complexities inherent in the research process, from conceptualisation through execution. This autonomy cultivated a profound sense of responsibility and self-reliance, which led me to deeply engage with the subject matter and pursue understanding through diligent study and practical application. I am sincerely grateful for the intellectual challenges encountered along the way, as they have honed my analytical capabilities and reinforced my dedication to scholarly inquiry.

During the course of this research, I have had the honour of receiving the guidance of my esteemed supervisor, Dr Andrew Peplow, to whom I extend my deepest gratitude for his unwavering support and encouragement. His thoughtful advice and scholarly presence, generously offered, have been deeply appreciated throughout this journey. I am likewise thankful to my supervisor, Professor Kent Persson, for his attentive oversight of the broader aspects of my studies; his careful review of the comprehensive summary and the insightful feedback provided have been instrumental in refining this work. I further wish to thank Dr Jessica Dahlström for her assistance with several of the measurements employed in this study, as well as Technician Bo Zadig for his graphical contributions to the thesis cover page and related materials.

Uppsala, Sweden, May 2025

Benjamin Bondsman

Popular science summary

Dynamic forces shape the mechanical world around us. The vibrations of structures due to wind loads, seismic events, and operational conditions play a crucial role in their safety and performance. Examples include the sway of tall buildings under wind-induced motion, the vibration of nuclear facilities during operation, the response of bridges to traffic loads, and the dynamic deformation of aircraft wings during flight. Although often invisible, these forces are ever present and, if not properly understood and controlled, can lead to discomfort, structural fatigue, and even catastrophic failure. Engineers use computer simulations to analyse and control these forces, ensuring the stability and reliability of structures across various engineering fields.

Meanwhile, the construction industry faces a pressing environmental challenge. The European Union's building sector contributes around 40% of total final energy consumption and 36% of greenhouse gas emissions. In response, Cross-laminated Timber (CLT) has emerged as a sustainable, climate-friendly alternative, gaining momentum in modern construction. Unlike conventional materials, wood is a living organic material whose mechanical properties depend on the conditions under which the tree grows. This natural variability, combined with inherent defects such as knots, splits, and moisture-related distortions, introduces uncertainty in the mechanical characteristics of CLT structures. To address these challenges, the CLT industry removes visible defects and redistributes imperfections across larger volumes, improving consistency, albeit at the cost of additional material loss. In addition, the high strength-to-mass ratio of wood makes CLT more susceptible to vibrations compared to traditional alternatives.

This thesis focuses on four key research areas that aim to advance the field of structural dynamics, improve the understanding of dynamic variability in CLT, and develop robust computational frameworks. The first area, experimental dynamics, involves the investigation of the variability in the dynamic characteristics of CLT, including transfer functions, natural frequencies, modal damping, and mode shapes. This is achieved through Experimental Modal Analysis (EMA) of nominally identical CLT substructures. The second area, inverse dynamics, involves the development of a mathematical model updating framework to refine discretised models of CLT. This framework tunes computer models towards their corresponding measurement data and identifies sensitive model parameters. The third area, uncertainty quantification, explores the influence of uncertainty in the mechanical properties of CLT and their impact on the predicted results in terms of natural frequencies and vibration modes. The fourth area, substructuring, involves the introduction of an interface reduction technique to truncate the interface dynamics of discretised system matrices, thereby enhancing computational efficiency for the dynamic analysis of large-scale systems.

Advances in Structural Dynamics with applications to Cross-laminated Timber

Part I

Introduction and overview

Chapter 1

Introduction

Dynamic forces shape the mechanical world around us, influencing the stability and performance of structures, from skyscrapers to spacecraft. The oscillations of long-span bridges under traffic and wind loads [1, 2], and the sway of tall buildings induced by vortex shedding and turbulent wind [3, 4], are just a few examples of rate-dependent motion in structures. In aerospace engineering, aircraft experience flutters and buffeting during flight in adverse weather conditions [5], while space structures can undergo thermally-induced vibrations in the harsh environment of orbit [6]. In the energy sector, wind turbine blades flex and vibrate under aerodynamic loads [7], and offshore platforms oscillate due to ocean waves and heavy wind loads [8]. In nuclear engineering, pipe systems, tall chimneys and nuclear reactor components vibrate during operation due to thermal and mechanical load [9–12]. Civil engineering structures, such as building floor systems, can experience vibrations and resonances due to human-induced footfalls. In addition, other structural components are susceptible to vibrations resulting from earthquake-induced base motion [13]. In manufacturing, production robots are susceptible to vibrations, which can compromise their precision [14]. In the automotive industry, vehicle suspensions vibrate under motion induced by bumpy roads [15]. In geotechnical engineering, the interaction of soil and structure during earthquakes can dramatically alter the dynamic response of buildings [16].

Motion-induced vibrations and the resonance behaviour of vibrating structures can compromise structural integrity, lead to fatigue and damage, and cause acoustical problems in terms of noise propagation, which can cause discomfort and health-related issues. Understanding and accurately predicting these diverse dynamic phenomena is crucial for the design, analysis, and safe operation of a wide range of engineered systems across various industries [17, 18]. Accurate predictive methods enable

engineers to avoid vibration resonances, ensuring the sustainability and safety of structures.

As the built environment continues to evolve amid the growing challenges of global warming and climate change, there is an increasing need to develop advanced techniques to characterise the structural dynamics of emerging alternative sustainable systems. Previous research has indicated that the European Union (EU) building sector accounts for approximately 40% of the total final energy consumption and 36% of the greenhouse gas emissions released [19]. Therefore, there is an urgent need for transformative change within the construction sector. Consequently, sustainable alternatives to conventional construction materials have emerged, notably Engineered Wood Products (EWPs). These EWPs are considered less carbon-intensive than their traditional counterparts, such as reinforced concrete and steel [20–22]. The tradition of building with wood spans millennia, underscoring its vital role throughout human history. Archaeological evidence shows that timber was used as structural components and load-bearing elements in Neolithic longhouses in Europe as early as 5500 BC [23]. These early wooden structures, found in regions such as central Europe and Scandinavia, demonstrate sophisticated construction techniques, including post-beam framing and wattle and daub wall filling [23]. The longevity and widespread use of timber construction in diverse cultures and time periods highlight the enduring importance of wood as a building material. The use of wood as a construction material has been shown to result in lower primary energy use and carbon emissions compared to concrete throughout the building life cycle. Further research has shown that wooden frame buildings result in lower primary energy production use, greater bioenergy recovery benefits from biomass residues, and substantially lower carbon emissions throughout construction life than the concrete frame alternative, even when accounting for post-use concrete carbonation [24]. Furthermore, carbon sequestered in wood materials and more efficient post-use energy recovery from wood waste provide additional climate benefits for wood frame buildings compared to concrete structures [24].

In the context of ongoing modernisation within the construction industry and global efforts to mitigate the adverse impacts of climate change, Cross-laminated Timber (CLT) has attracted significant academic and industrial attention. CLT is an EWP composed of layers of wood boards stacked perpendicularly to each other and bonded with adhesive [25, 26], as shown in Fig. 1.1. This configuration results in a structural element with an enhanced load-bearing capacity and dimensional stability. Consequently, CLT is predominantly used in multi-story buildings, both as load-bearing slabs and as shear walls. CLT also stabilises tall timber buildings, as the cross-wise arrangement of timber boards can counteract mechanical tension and compression in multiple directions [26–29]. In recent years, CLT has gained significant momentum

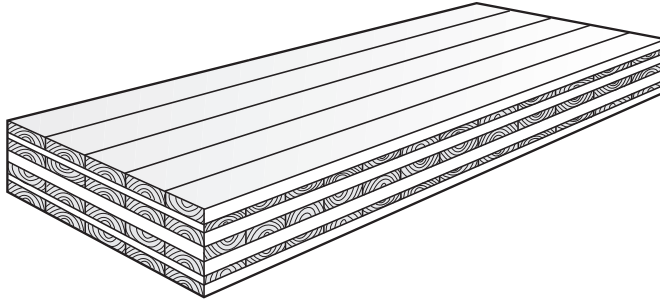


Figure 1.1: Depiction of a Cross-laminated Timber (CLT) slab comprising seven layers of juxtaposed lumber boards, glued to one another in a perpendicular pattern.

as a sustainable alternative to traditional construction materials, including reinforced concrete and steel. As a result, researchers worldwide have developed various adaptations of CLT, such as CLT with different wood species, thicknesses, lamina combinations, and orientation angles of the layers [30, 31], adhesive-free laminated timber beams and CLT panels [32–34], the incorporation of densified timber boards in CLT, and CLT with a viscoelastic mid-layer, [35].

CLT, as a lightweight floor system, is susceptible to vertical vibrations induced by human footfalls and rotating machinery. This sensitivity arises from its low mass and limited inherent damping capacity. To mitigate such vibrations, the dead weight of the CLT system is commonly increased by adding a concrete topping layer [36]. This hybrid configuration aims to improve the overall mass and stiffness of the floor system, thus shifting its natural frequency away from the critical excitation range of approximately 1 to 5 Hz, often induced by human footfalls. Although this solution may mitigate the dynamic effects on CLT floors, it involves the use of concrete, which is associated with high embodied energy and carbon emissions during production. Consequently, this approach may undermine the overall sustainability objectives of timber-based construction.

Wood, as a natural material, exhibits variability in its density and mechanical properties due to growing conditions, resulting from diverse patterns of fibre orientation. In addition, the mechanical properties of wood are influenced by its moisture content [37–40], as well as moisture-induced distortions [41]. Natural defects, such as knots [42], and cracks [43], further contribute to variability in performance. The variability in the macro- and microstructural properties of wood, especially within the individual lumber boards that constitute CLT, leads to differences in the overall behaviour of the structure. Specifically, the dynamic response is notably affected, as wood is inherently sensitive to vibration and resonance phenomena because of its low mass-to-strength ratio. These characteristics can pose challenges in structural performance, particularly in floor systems and other components where dynamic loading or human

comfort is a concern. Thus, characterisation of variability in the vibration response of CLT and its associated mechanical properties is a critical area of investigation. Additionally, the modelling of dynamic systems, particularly those involving CLT, using the Finite Element (FE) method can result in significant computational costs. As dynamic systems are often analysed in both the time and frequency domains, developing efficient model reduction techniques is essential. These techniques can improve the accuracy of dynamic analyses while significantly accelerating the design process for CLT structures.

1.1 Aims and scope of the research

Predictive modelling and analyses of structures to withstand dynamic loading require a comprehensive understanding of the structure's dynamic performance. In particular, in the case of natural materials such as wood, which exhibits diverse variability in its mechanical characteristics influenced by various factors, including fibre orientation, growth conditions, and inherent defects like splits and knots. These factors contribute to the heterogeneity in the dynamic behaviour of wood and present challenges in predictive analyses. Therefore, a thorough understanding of wood, particularly CLT's dynamic performance and associated variability, is essential for a sustainable transition to a low-carbon built environment.

In engineering practice, predictive models have become an established tool for simulating and analysing the behaviour of systems under a variety of loading conditions, thereby reducing the reliance on direct physical experimentation. These models play a crucial role in the design process by informing decision-making through the prediction of structural performance, reliability, and safety. Typical applications include assessing responses to time-varying loads, such as wind excitation or human-induced vibrations from footfall. Moreover, predictive modelling substantially reduces the need for costly and time-consuming field testing by enabling virtual experimentation. It also facilitates the study of systems under hypothetical or extreme conditions, such as ultimate limit states, dynamic instability, or fracture mechanics, where physical testing may be impractical or unsafe. However, the precision and reliability of these models depend on the validity of the modelling assumptions. These include the representation of real-world structures using idealised engineering elements and the accurate use of modelling parameters such as material properties, boundary conditions, and loading scenarios.

Modelling parameters are often identified through experimental investigations, such as Experimental Modal Analysis (EMA), the results of which are commonly employed to formulate an inverse dynamic problem. In this context, the aim is to determine

model parameters that tune the simulated results towards the measured counterparts, typically by minimising a residual function. The identification of modelling parameters in engineering dynamics frequently demands substantial computational resources, particularly due to the need for iterative evaluation of the residual function and its derivatives. In addition, the use of gradient-based model updating methods often results in ill-conditioned problems where regularisation terms are often needed [44]. As the mechanical properties of CLT exhibit variability, the resulting modal characteristics are also affected. Therefore, it is essential to quantify the extent to which variations in input mechanical properties contribute to uncertainties in these modal characteristics, as CLT structures are inherently susceptible to vibration. In engineering dynamics, the equation systems representing the mechanics of structures are often solved in time or frequency domains, which requires solving the system equations numerous times. Consequently, the adoption of substructure coupling and reduced-order modelling was explored in the 1960s [45–49]. Interface reduction of reduced system matrices was introduced in the year 2000, considering decoupled characteristics of the reduced stiffness matrix [50]. In cases where the reduced stiffness is coupled, the use of the former interface reduction results in an inaccurate reduction of the interface.

Consequently, this thesis addresses these challenges with the overarching objective of advancing the field of engineering dynamics. The research comprises both numerical and experimental approaches, related to CLT, to tackle key issues associated with predictive modelling. The overall aim of the thesis is to contribute towards the development of robust, efficient, and reliable predictive models for the vibration analysis of CLT panels. The specific objectives of the thesis include, but are not limited to:

- Analysing and determining the dynamic behaviour and associated variability in the modal characteristics of CLT through EMA, encompassing natural frequencies, modal damping across distinct modes, and vibration transfer functions across the three principal directions: out-of-plane, in-plane, and axial directions (Paper I).
- Developing and implementing a gradient-free model updating framework for the identification of mechanical properties of CLT and their associated variability using EMA as reference (Paper II).
- Quantifying the uncertainty in natural frequencies and mode shapes arising from variability in sensitive mechanical properties of CLT by employing probabilistic and stochastic modelling coupled with FE propagation (Paper III)
- Developing a coupled interface reduction technique using modified characteristic constraint modes for reduced systems with coupled stiffness (Paper IV).

The EMA approach outlined in Paper I is described in a general manner. Although applied to CLT, the approach can be directly applied to other structures and materials. The model updating approach in Paper II is derived within a general framework, rendering it applicable to the identification of model parameters in other structures. In the same manner, the uncertainty quantification approach in Paper III is formulated using general terms and can be flexibly applied to structures beyond CLT. The interface reduction technique in Paper IV is likewise derived generally, having been applied not only to CLT but also to steel. While the present applications consider linear elastic materials, the model updating procedure accommodates non-linear relationships between the model parameters.

1.2 Limitations

The scientific methods and theories used in this work assume linear elastic material behaviour under the condition of small amplitude vibrations. Accordingly, methods from linear dynamic theory are applicable. This simplification restricts the applicability of the theories and methods to materials and structures that remain within the elastic regime. Furthermore, mechanical vibration and dynamic stiffness can be influenced by environmental factors such as moisture and temperature variation, which are treated as constants in this work. Hence, the results and findings should be interpreted with these constraints in mind.

1.3 Thesis Outline

This thesis is organised into a series of introductory chapters that provide the theoretical background and essential information for the scientific articles included in the Appendix. The appendix comprises four journal articles that represent the core contributions of this work; therefore, the introductory chapters function as a comprehensive summary of these articles. The remaining chapters are structured as follows. Chapter 2 briefly discusses the fundamentals of wood and its engineering applications. Chapter 3 outlines the essential theories of predictive modelling and simulation within the linear elastic regime under vibration. Chapter 4 introduces the theory and application of EMA. Chapter 5 discusses the FE model updating using experimental data from EMA as a reference. Chapter 6 presents the concept of uncertainty quantification in mechanical and modal parameters, while Chapter 8 explores Component Mode Synthesis (CMS) and the concept of interface reduction. Finally, Chapter 8 draws conclusions from the work and provides recommendations for future research.

Chapter 2

Wood Fundamentals: From Growth to Engineering Applications

Wood is a natural organic material that is extracted from the stem of a grown tree. It has been an integral part of human civilisation for millennia, serving as a versatile and flexible structural component for construction, protection, combustion, and various other applications [51]. The distinctive attributes of wood, including its strength-to-weight ratio, renewability, and carbon sequestration capabilities, have made it an increasingly attractive material in the face of increasing environmental concerns and transitions related to sustainability [24, 52].

The complex hierarchical composition of wood, characterised by cellulose, hemicellulose, and lignin, is the source of its exceptional mechanical properties [53]. The inherent variability and anisotropic nature of wood introduce both challenges and opportunities in engineering applications [54]. Recent developments in wood science and technology have opened new possibilities for its application in high-performance structures, advanced materials, and sustainable energy systems [55]. For example, researchers have developed "super wood" with enhanced strength and toughness [56], created transparent wood composites for energy-efficient buildings [57], and used wood-derived nanomaterials in energy storage applications [58]. In addition, functionalised wood materials have shown promise in environmental remediation [59].

As a building material, wood offers numerous advantages, including excellent thermal insulation [60], aesthetic appeal, structural efficiency, and superior stiffness and strength to its mass. Its application in construction spans from traditional timber framing to modern engineered wood products such as CLT and Glued-laminated Timber (GLT) [61]. The dynamic behaviour of wooden structures is of particular in-

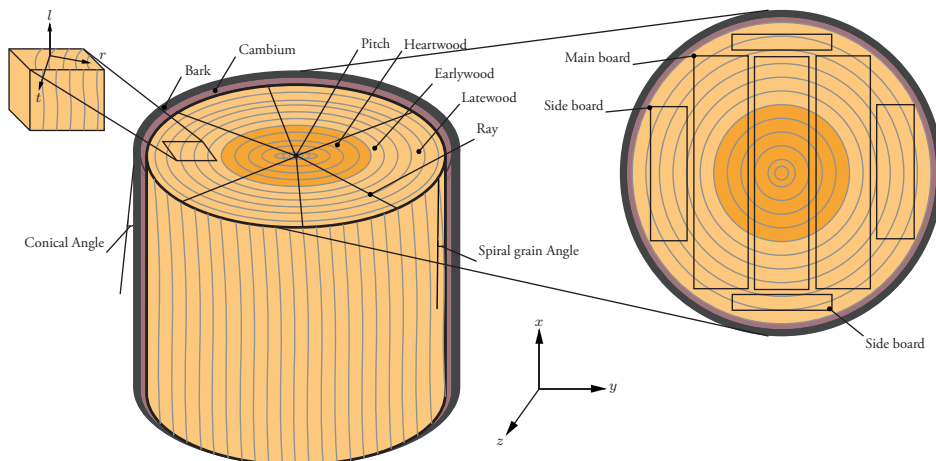


Figure 2.1: Illustration of the wood macrostructure, sawing pattern strategy, and corresponding cylindrical (longitudinal l , tangential t , and radial r) and Cartesian coordinate systems.

terest in engineering, especially in regions susceptible to seismic activity, high winds, or vibrations induced by human footfall. The natural damping properties of wood, coupled with its relatively low mass, make it an appealing option for controlling vibrations in buildings [62]. However, its low mass and moderate damping can also make it sensitive to excessive vibrations, particularly under dynamic excitations such as impact loading. The orthotropic nature of wood, its sensitivity to moisture content, and the presence of natural defects and structural variability present unique challenges in predicting its dynamic response. This requires the use of appropriate modelling techniques and careful design considerations [63], which will be explored in subsequent chapters.

2.1 Structure of wood

The structure of wood is a product of natural engineering, developed over millions of years of evolution. At its basic level, wood is composed of cellulose fibres held together by a matrix of lignin, forming a composite material with unique properties [64]. The chemical composition of wood comprises 50% carbon, 6% hydrogen and 44% oxygen (in the form of cellulose, hemicellulose, and lignin). Nordic softwoods, which are explored in this thesis, comprise approximately the following proportions: 40- 45% cellulose, 25- 30% hemicellulose and 25- 30% lignin [65].

These molecular chains or chemical substances that constitute wood, such as cellulose, are formed through a combination of photosynthesis, water, and other nutrient processes. In this process, a tree absorbs carbon dioxide (CO_2) from the atmosphere and

water from the soil to produce glucose. This glucose is then used as a building block for more complex compounds, while other nutrients absorbed from the soil support the general growth of the plant, [66].

Cellulose is a polysaccharide composed of long chains of glucose units linked by β -1,4-glycosidic bonds. The molecules of cellulose exhibit a high degree of crystallinity and are organised into strong microfibrils. This polysaccharide is characterised by its significant tensile strength, stiffness, and resistance to deformation, serving as the primary component that imparts mechanical strength and rigidity to the wood cell wall, [66].

Hemicelluloses are polysaccharides composed of various sugar monomers, such as xylose, mannose, galactose, and arabinose. Unlike cellulose, hemicelluloses have shorter chains and a higher degree of branching, resulting in a structure that is less crystalline and more amorphous. These polymers function as matrix materials, occupying the interstitial spaces between cellulose microfibrils and lignin, thereby contributing flexibility and structural cohesion to the plant cell wall. Hemicelluloses are more susceptible to hydrolysis than cellulose and have relatively lower molecular weights, [66].

Lignin is a complex, three-dimensional polymer made up of phenylpropane units linked in various configurations. Unlike cellulose or hemicellulose, lignin lacks a regular repeating structure. It is characterised by its rigidity and hardness, which provide the wood cell wall with compressive strength and stiffness. Furthermore, lignin acts as a binding agent, bonding cellulose and hemicellulose fibres, thus increasing the resistance of the cell wall to decay and environmental stresses [66].

The chemical components addressed above, specifically cellulose, hemicellulose, and lignin, constitute the fundamental components that form the wood structure. This structure of wood can be examined on multiple scales, namely macroscopic and microscopic levels, as further addressed in the following subsections.

2.1.1 Macroscopic level

The macrostructure of wood can be observed with the naked eye or by simple magnification tools. At this level, key features include the gross structure, wood rays, sapwood and heartwood, as well as growth increments, Fig. 2.1. The gross structure encompasses the cellular composition, wood rays, and cylindrical planes of wood (longitudinal, tangential, and radial), along with sapwood, heartwood, and the annual rings of growth increments.

Wood rays are horizontal or radial structures that transport nutrients and water across the grain of wood. Sapwood is the outer non-living portion of the tree trunk, whereas

heartwood is the inner, non-living part that provides structural support. Annual rings, visible in many types of wood, indicate the growth patterns of the tree over time. The cross-section of a tree trunk is also characterised by earlywood and latewood, which exhibit distinct properties. Earlywood consists of thinner-walled cells formed primarily during the spring, denoting the growth season. In contrast, latewood comprises thicker-walled cells that develop during the autumn season and are characterised by increased strength, [66]. The thickness of the cell walls can vary between different woods depending on the climate, temperature, and other growth conditions. This variability introduces in turn diverse variability in the global density of wood as well as mechanical properties. Additional structural elements of wood are described in the schematic representation provided in Fig. 2.1.

This thesis focusses primarily on the macroscopic examination of wood, with a concise discussion of the microscopic level of analysis presented for educational purposes.

2.1.2 Microscopic level

At the microscopic level, the structural characteristics of wood can be examined in greater detail than at the macroscopic level. Key features include the organisation of the cell wall, which consists of primary and secondary layers, specifically denoted as S_1 , S_2 , and S_3 . Here, S_3 represents the innermost layer of the cell wall. The microfibrils that make up these layers are primarily composed of cellulose, a polysaccharide that is essential to provide strength and stiffness to the wood structure.

Furthermore, the orientation angles of the microfibrils within these layers significantly influence the mechanical properties of the wood. For example, the orientation angles can vary as follows: $S_1 = 50^\circ - 70^\circ$, $S_2 = 5^\circ - 15^\circ$, and $S_3 = 60^\circ - 90^\circ$ [65, 66]. Variation in these angles affects the directional strength and mechanical behaviour of the wood. Furthermore, the arrangement of cellulose microfibrils within the cell wall contributes to the anisotropic behaviour of wood, leading to a diverse variability in mechanical properties along different directions (longitudinal, radial, and tangential). This variability mainly arises from the distribution and orientation of fibres within the growth rings. Furthermore, information on the micromechanical properties of wood can be found in [67].

2.2 Wood growth

2.2.1 Growth increments and annual rings

A visible factor that indicates wood growth is the formation of new annual rings, that is, the expansion of the diameter of the stem. The growth rings are circular patterns surrounding the pitch of the wood and indicate the growth of a tree over the years. Each of these annual rings is composed of earlywood and latewood. The early wood is formed during the growth season (spring), consisting of thin-walled cells, whereas the latewood comprises thick-walled cells and is formed during late summer and fall. The width and density of annual rings are significantly influenced by environmental conditions, soil quality, and available moisture.

Environmental exposure and conditions also play an important role in wood growth. Favourable conditions result in wider annual rings, whereas adverse weather conditions lead to narrower growth rings. The variability in growth increments (wide and narrow growth rings) provides information regarding growth history and diversity in mechanical characteristics (density, stiffness) across the section.

In addition to the aspects of the growth process addressed above, wood is characterised by natural defects, such as knots, splits, decay, and resin pockets. In addition, natural defects in wood can be explored in [68] and references therein.

2.2.2 Sapwood and Heartwood

The growth of a tree trunk cross-section involves the differentiation between its living and non-living tissues. The sapwood is responsible for transporting water and nutrients from the soil using the roots to the leaves through the xylem. As the tree ages, the older, innermost layers of sapwood gradually transition into heartwood, the inner portion of the trunk. Unlike sapwood, heartwood no longer participates in water transport, but serves as a structural component, providing strength and stability to the tree. Heartwood is therefore characterised by strength and a darker colour.

2.2.3 Cellular composition and wood rays

The gross structure of wood is also characterised by its cellular composition and the presence of wood rays. Wood rays are horizontal radial structures that extend from the centre of the tree trunk (pith) outward toward the bark. These rays are made up of parenchyma cells and play a crucial role in the lateral transport of water, nutrients,

and the storage of carbohydrates across the fibre direction.

2.2.4 Planes of wood

Wood is an orthotropic material with unique properties along three perpendicular axes: longitudinal (l), tangential (t), and radial (r). These planes correspond to the cylindrical growth pattern of the wood stem and define the mechanical properties and orientation of the wood cells. The longitudinal plane extends along the fibre direction of the tree trunk, while the tangential plane is tangent to and parallel to the circumference of the annual rings. The radial plane runs perpendicular to the growth rings and to the other two planes, Fig. 2.1.

2.3 Structural timber

Structural timber, particularly sawn lumber boards, refers to timber elements cut from tree logs with the purpose of further processing them into structural components for construction. Typically, a tree log is cut into multiple wood boards, which are then dried, graded, and planed to achieve the desired structural properties and dimensions, Fig. 2.1. These boards may vary in thickness, width and length and are categorised according to their strength and stiffness properties, to ensure their suitability in different structural applications (see, for example, SS-EN 338:2016 [69]). The quality and mechanical performance of structural wood depend on several factors, including the species of wood, the method of sawing, and subsequent treatments. These treatments commonly include kiln drying to reduce moisture content, improve durability, and minimise the risk of distortion. In some cases, additional chemical treatments are also applied to improve resistance to insects, fungi, and fire, further extending the life and stability of the wood. At this structural level, the presence of natural defects such as knots, grain deviations, and other imperfections introduces variability in mechanical properties, which must be accounted for in design and grading.

In construction, structural timber is widely used in load-bearing applications, including beams, columns, and framing, where it provides mechanical strength to withstand structural loads. In recent decades, there has been significant advancement in the development of engineering wood products, including GLT or Glulam and CLT. These products are created through the combination of structural wood, resulting in wooden structures with superior load-bearing capabilities. The advent of such products has enabled the construction industry to carry out the construction of large and complex sustainable structures using wood.

2.4 Cross-laminated Timber

CLT is an engineered wood product created by stacking layers of lumber boards in alternating orientations. This cross-lamination results in a structure with enhanced load-bearing capacity and dimensional stability (see Fig. 1.1). The CLT manufacturing process begins with sawing lumber boards, which are then visually inspected to remove growth defects that do not meet the strength classification requirements specified in SS-EN 14081-1:2016 [70]. At this stage, a finger joint is cut to prepare the boards for a subsequent finger joint that extends their length [71]. Subsequently, the lumber boards undergo a drying process to stabilise their internal moisture content at approximately $12 \pm 2\%$ in accordance with SS-EN 16351:2021 [72]. Due to variability in the diameter of the wood stem from which the boards are extracted (see Fig. 2.1), the dimensions of the lumber boards can vary significantly, with widths ranging between 80 and 300 mm and thicknesses between 10 and 40 mm [73]. According to SS-EN 16351:2021 [72], the recommended width-to-thickness ratio is 4; if this is not met, a reduced rolling shear modulus must be considered [71, 74]. The boards commonly used in CLT assembly are Norway Spruce with the strength class C24 [69], although different strength classes may be combined. Although softwoods are used predominantly in CLT production, the potential use of hardwoods has recently been explored [75]. The lumber boards are arranged in layers to which a suitable adhesive is applied. The layers are then assembled, with each layer orientated perpendicular to the adjacent ones. Finally, the assembled panel is pressed to ensure a strong bond between the layers, and the edges of the CLT are trimmed as a final refinement. For further information on CLT production and development, the reader is referred to the state-of-the-art review by Brandner [25] and the general description in [26].

CLT is commonly used in high-rise timber buildings as load-bearing components such as slabs and shear walls, and it is also employed in various other constructions, including residential (houses and apartments), commercial (offices and schools) and infrastructure projects (bridges and other public structures).

The CLT structures studied in Papers I, II, and III consist of softwood lumber boards, whereas the CLT structures in the application examples in Paper IV are also assumed to be composed of softwood.

Chapter 3

Predictive modelling and simulation

Predictive modelling and simulation are among the engineering tools used in the numerical modelling of solids and structures. Simulation models in modern engineering often employ the FE method to approximate differential equations describing a particular phenomenon into a set of algebraic equations. These FEs, for which the system matrices are formulated using mechanical properties, are assembled into global system matrices. These algebraic system matrices are further processed and solved directly using matrix inversion for static problems. In dynamic problems, due to the coupling between acceleration and displacement fields, the system equations are commonly solved in time, frequency, or modal domains; see Fig. 3.1. Dynamic problems are characterised by considerable influence from inertial forces and their rapid variation over time, with these forces being directly proportional to the acceleration of mass within the structure. This proportionality relation is recognised as Newton's second law of motion. However, a distinction shall be made to large inertia forces that vary slowly with time, for example, centrifugal loading and gravity in the form of dead load. The time domain solution is often divided into a transient and steady state solution, where the former has a short duration and the latter has a longer duration effect. Another type of vibration often represented in the time domain is random vibration, often generated by earthquake events. Random vibration is beyond the scope of this work and hence not covered. In cases where the excitation and response vary harmonically with time, the equations of motion can be solved in the frequency domain, for example, harmonic loading from footfalls over a slab.

This chapter briefly introduces predictive modelling and simulation of dynamic problems using a linear elastic material model, often referred to as Hooke's law for orthotropic materials. A brief derivation of fundamental theories is outlined, and, where deemed necessary, references are given to the literature.

3.1 Mechanical Deformation

3.1.1 Principle of virtual work

The deformation of solids and structures within an elastic continuum regime can be modelled using Newton's second law of motion:

$$\sigma_{ij,j} + b_i = \rho \ddot{a}_i, \quad (3.1)$$

where $\sigma_{ij,j}$ denotes the divergence of the mechanical stress tensor σ_{ij} , b_i is the component of body force per unit volume, ρ is the density of the continuum, and \ddot{a}_i represents the acceleration component in the i -direction.

To derive the weak formulation, the strong form in (3.1) is multiplied by a kinematically admissible weight function¹ δa_i , that is, a function that vanishes on the parts of the boundary where essential boundary conditions (Dirichlet) are imposed. Integration is then carried out over the volume Ω of the body in the reference configuration:

$$\int_{\Omega} \delta a_i \sigma_{ij,j} dV + \int_{\Omega} \delta a_i b_i dV = \int_{\Omega} \rho \delta a_i \ddot{a}_i dV, \quad (3.2)$$

where Ω refers to the reference configuration, and the analysis is performed under the assumption of infinitesimal deformations.²

Applying the chain rule to the term $\delta a_i \sigma_{ij,j}$ gives

$$\delta a_i \sigma_{ij,j} = (\delta a_i \sigma_{ij})_{,j} - \delta a_{i,j} \sigma_{ij},$$

which, when substituted into (3.2), results in

$$\int_{\Omega} \delta a_i \sigma_{ij,j} dV = \int_{\Omega} (\delta a_i \sigma_{ij})_{,j} dV - \int_{\Omega} \delta a_{i,j} \sigma_{ij} dV. \quad (3.3)$$

Application of Gauss' theorem to the first integral term on the left-hand side permits

$$\int_{\Omega} \delta a_i \sigma_{ij,j} dV = \int_{\partial\Omega_t} \delta a_i \bar{t}_i dS - \int_{\Omega} \delta a_{i,j} \sigma_{ij} dV, \quad (3.4)$$

¹A weight function is considered kinematically admissible if it satisfies the essential boundary conditions (i.e., $\delta a_i = 0$ where displacements are prescribed) and maintains the necessary continuity requirements across the domain. This ensures mathematical consistency with the physical constraints of the system while allowing arbitrary variations where displacement is not prescribed.

²In small strain analysis, variation in the spatial volume through deformation is considered negligible. The extension of the principle of virtual work to the analysis of large strains and deformations can be found in the work of Johannesson [76] and in the master's thesis by the author [77].

where $\bar{t}_i = \sigma_{ij}n_j$ is the prescribed traction on the Neumann boundary $\partial\Omega_t$, and n_j denotes the outward unit normal on the boundary surface.

Thus, the weak form of the equation of motion is expressed as

$$\int_{\partial\Omega_t} \delta a_i \bar{t}_i dS - \int_{\Omega} \delta a_{i,j} \sigma_{ij} dV + \int_{\Omega} \delta a_i b_i dV = \int_{\Omega} \rho \delta a_i \ddot{a}_i dV, \quad (3.5)$$

which must hold for all kinematically admissible weight functions δa_i , i.e., functions satisfying $\delta a_i = 0$ on the portion of the boundary $\partial\Omega$ where displacement is prescribed, and arbitrary elsewhere. Note that kinematic admissibility implies compatibility with the prescribed constraints.

3.1.2 Finite Element formulation

Using standard FE discretisation, the displacement field a_i can be approximated as $\mathbf{a} = \mathbf{N}(\mathbf{x})\mathbf{u}(t)$, where $\mathbf{N}(\mathbf{x})$ represents the shape functions depending on the spatial coordinates \mathbf{x} , and $\mathbf{u}(t)$ is the vector of nodal displacements. In this approximation, the time dependence of the displacement field is captured solely by the nodal displacements \mathbf{u} . The acceleration field can be discretised similarly to $\ddot{\mathbf{a}} = \mathbf{N}(\mathbf{x})\ddot{\mathbf{u}}$.

In the Galerkin approach, the weight functions are interpolated as $\delta \mathbf{a} = \mathbf{N}(\mathbf{x})\mathbf{c}$, where \mathbf{c} is a vector of test parameters. Substituting these interpolations into the weak form yields the discretised equations:

$$\underbrace{\rho \int_{\Omega} \mathbf{N}^T \mathbf{N} dV}_{\mathbf{M}} \ddot{\mathbf{u}} + \underbrace{\int_{\Omega} \mathbf{B}^T \mathbf{D} \mathbf{B} dV}_{\mathbf{K}} \mathbf{u} = \underbrace{\int_{\Omega} \mathbf{N}^T \mathbf{b} dV + \int_{\partial\Omega_t} \mathbf{N}^T \bar{\mathbf{t}} dS}_{\mathbf{p}(t)}. \quad (3.6)$$

Here, \mathbf{M} denotes the mass matrix, which represents the distribution of mass within the continuum, and \mathbf{K} is the stiffness matrix, representing the resistance of the material to deformation. The matrix \mathbf{B} is the strain-displacement matrix³, which links the strain in the material to the nodal displacements, while \mathbf{D} is the matrix of material properties, which defines the stress-strain relationship according to the constitutive law of the material. Finally, $\mathbf{p}(t)$ is the time-dependent force vector, which incorporates both body forces and surface tractions applied to the continuum. Thus, the final system of equations in matrix form is:

$$\mathbf{M}\ddot{\mathbf{u}} + \mathbf{K}\mathbf{u} = \mathbf{p}(t), \quad (3.7)$$

³The strain-displacement matrix $\mathbf{B} = \nabla \mathbf{N}$ contains spatial derivatives of the shape functions \mathbf{N} and maps nodal displacements to strains in the element, and implements the kinematic relationship between displacements and strains in a discretised form, [78–80].

where it is assumed that the excitation energy is entirely converted into vibrational motion, with no energy dissipated through damping mechanisms. Because dynamic forces vary over time, the accelerations and displacements of the nodes also depend inherently on time. To derive the system matrices employing the aforementioned theories, the reader may consult the foundational literature on the FE method, such as [78–80].

3.1.3 Constitutive law

Wood can be characterised by its orthotropic properties within a cylindrical coordinate system, where the longitudinal direction of the fibre (l), the tangential direction of its annual rings (t) and the radial direction, which is perpendicular to its annual rings (r), align with the three cylindrical axes, Fig. 2.1. The corresponding orthotropic constitutive law, defined within an elastic regime, can be expressed by Hooke's law as

$$\sigma_{ij} = D_{ijkl}\varepsilon_{kl}, \quad (3.8)$$

where σ_{ij} represents the components of the stress tensor, D_{ijkl} denotes the orthotropic stiffness tensor of the material, and ε_{kl} contains the components of the elastic strain tensor.

In the FE framework, the constitutive law is applied at each element level by approximating the strains and stresses in terms of the nodal displacements. The stress-strain relationship is thus written in matrix form as

$$\boldsymbol{\sigma} = \mathbf{D}\boldsymbol{\varepsilon} = \mathbf{D}\mathbf{B}\mathbf{u}, \quad (3.9)$$

where $\boldsymbol{\sigma}$ is the FE stress vector, \mathbf{D} is the orthotropic stiffness matrix (derived from the tensor D_{ijkl}), $\boldsymbol{\varepsilon}$ is the FE strain vector. In Voigt notation, the constitutive law can be expressed in matrix format as:

$$\begin{bmatrix} \sigma_l \\ \sigma_t \\ \sigma_r \\ \sigma_{lt} \\ \sigma_{lr} \\ \sigma_{tr} \end{bmatrix} = \begin{bmatrix} 1/E_l & -\nu_{tl}/E_t & -\nu_{rl}/E_r & 0 & 0 & 0 \\ -\nu_{lt}/E_l & 1/E_t & -\nu_{rt}/E_r & 0 & 0 & 0 \\ -\nu_{lr}/E_l & -\nu_{tr}/E_t & 1/E_r & 0 & 0 & 0 \\ 0 & 0 & 0 & G_{lt} & 0 & 0 \\ 0 & 0 & 0 & 0 & G_{lr} & 0 \\ 0 & 0 & 0 & 0 & 0 & G_{tr} \end{bmatrix}^{-1} \begin{bmatrix} \varepsilon_l \\ \varepsilon_t \\ \varepsilon_r \\ \gamma_{lt} \\ \gamma_{lr} \\ \gamma_{tr} \end{bmatrix}, \quad (3.10)$$

where the orthotropic stiffness matrix is defined as the inverse of stiffness compliance, that is, $\mathbf{D} = \mathbf{C}^{-1}$, and contains the following independent parameters: three Young

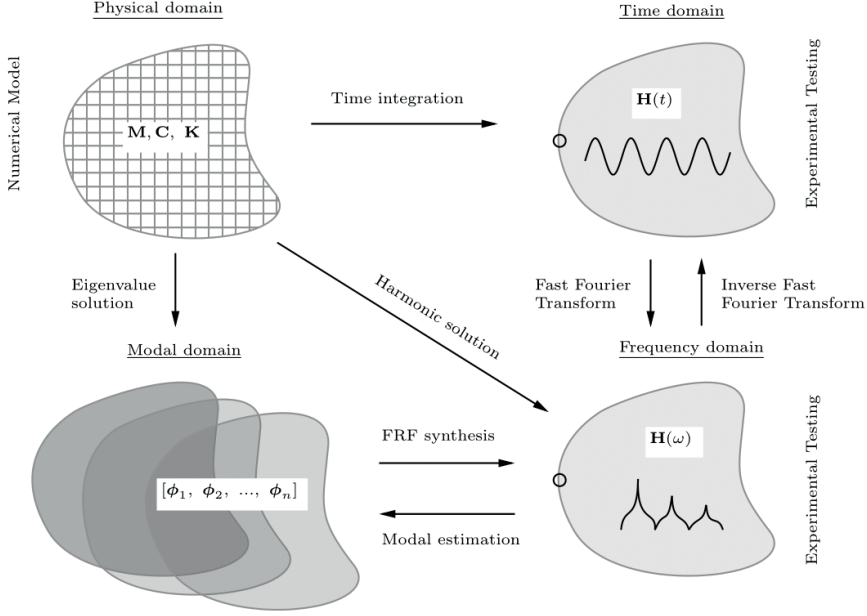


Figure 3.1: Schematic illustration of solving the Finite Element (FE) equations of motion in the modal, time and frequency domains. The time and frequency domain solutions can also be determined experimentally to estimate the natural modes.

moduli $E_i \in \{l, t, r\}$, three shear moduli $G_{ij} \in \{l, t, r\}$, and three Poisson's ratios $\nu_{ij} \in \{l, t, r\}$. The Poisson's ratios represent the variation in strain in direction i resulting from stress applied in direction j and obey the following relationship:

$$\frac{\nu_{ij}}{E_i} = \frac{\nu_{ji}}{E_j}, \quad (3.11)$$

where ν_{ij} is defined as

$$\nu_{ij} = -\frac{\varepsilon_j}{\varepsilon_i}. \quad (3.12)$$

The static mechanical properties can be directly identified using static testing. Dynamic mechanical properties can be identified through model updating with modal data as a reference as further explored in Paper II and Chapter 5.

3.2 Dynamic problems

Dynamic problems are characterised by an imbalance between the external forces and corresponding internal forces, resulting in the acceleration of the structural mass fol-

lowing

$$\mathbf{p} - \mathbf{p}_i = \mathbf{M}\ddot{\mathbf{u}}, \quad (3.13)$$

where \mathbf{p} and \mathbf{p}_i contain respectively external and internal (D'Alembert) forces. The equation above is often referred to as dynamic equilibrium or equations of motion (as the matrix contains several equations) and relates the internal and external forces to the inertia forces. The internal forces, in linear dynamics, are linearly dependent on the nodal displacement and velocity fields as

$$\mathbf{p}_i = \mathbf{C}\dot{\mathbf{u}} + \mathbf{K}\mathbf{u}, \quad (3.14)$$

where \mathbf{C} is the damping matrix and the nodal velocities are collected in $\dot{\mathbf{u}}$. Hence, the complete linear dynamics equations of motion are

$$\mathbf{M}\ddot{\mathbf{u}} + \mathbf{C}\dot{\mathbf{u}} + \mathbf{K}\mathbf{u} = \mathbf{p}(t). \quad (3.15)$$

The equation shows that small acceleration leads to small inertia forces but can cause large motions over time. This system is a coupled ordinary differential equation (ODE) that can be decoupled in the modal domain or solved in the time or frequency domains; see Fig. 3.1. The damping matrix can be derived analogously to the stiffness and mass matrices, as in (3.6). However, this approach is rarely used due to the inherent uncertainty associated with the damping characteristics of structures, often resulting from joints and non-structural components such as partitions. Hence, damping is typically formulated at the system level rather than the element level, with further details provided in the subsequent section.

3.2.1 Damping

Energy leakage, or damping, refers to the mechanisms through which energy is dissipated from a system. This energy dissipation arises from the conversion of mechanical energy to thermal energy as a result of phenomena such as friction or resistance to motion. Damping plays an essential role in reducing vibration amplitudes and preventing damage or failure of structures, Fig. 3.2. The damping properties can be determined experimentally for each vibration mode, as further elaborated in Chapter 4, or can be modelled on the system level using the Caughey series:

$$\mathbf{C} = \mathbf{M} \sum_{j=0}^{N-1} a_j (\mathbf{M}^{-1}\mathbf{K})^j \quad (3.16)$$

where N denotes the total number of modes, corresponding to the degrees of freedom of the system, [81, 82]. A simplified form of the Caughey series, considering only two

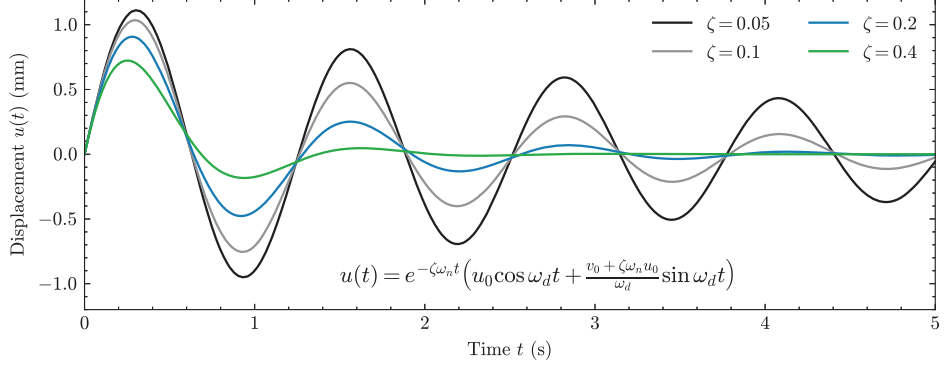


Figure 3.2: Free vibration of an underdamped Single-degree-of-freedom (SDOF) system with different damping values. The parameters are selected as $u_0 = 0$ mm, $v_0 = 6$ mm/s, $\omega_n = 5.0$ rad/s, and the damped natural frequency is defined as $\omega_d = \omega_n \sqrt{1 - \zeta^2}$.

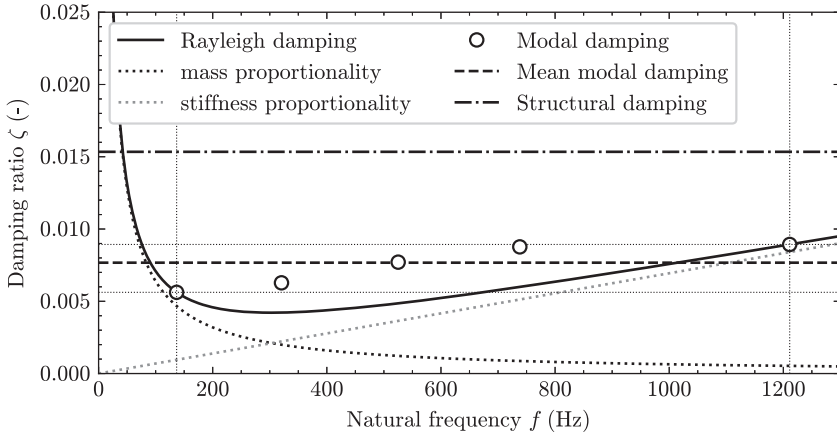


Figure 3.3: Modal damping ratios determined through Experimental Modal Analysis (EMA) using a fitted Rayleigh damping model. The structural damping proportionality constant is estimated as $\gamma = 2 \cdot \text{mean}(\zeta)$, where ζ represents the modal damping ratios. The damping values are associated with the CLT beam substructures in [37] and Paper I.

modes ($j = 0, 1$), is known as Rayleigh damping, and is often employed in numerical analyses due to its computational efficiency. The Rayleigh damping is formulated as:

$$\mathbf{C} = a_0 \mathbf{M} + a_1 \mathbf{K}, \quad (3.17)$$

where a_0 and a_1 are the proportionality constants of mass and stiffness, respectively. These constants are determined by solving the following equations:

$$\zeta_j = \frac{1}{2} \left(\frac{a_0}{\omega_j} + a_1 \omega_j \right), \quad j = 1, 2, \quad (3.18)$$

where ζ_j are the experimentally determined modal damping ratios and ω_j are the natural frequencies for the two selected modes, Fig. 3.3.

Another type of damping often used in vibration analyses is complex structural damping, which is proportional to displacement (unlike Rayleigh damping, which is proportional to velocity) and is 180° out of phase with the velocity. Complex structural damping can be represented as:

$$\mathbf{C} = i\gamma\mathbf{K} \quad (3.19)$$

where i is the imaginary unit, γ is the proportionality constant, and \mathbf{K} is the stiffness matrix. This form of damping is particularly useful in modelling systems in which energy is dissipated through mechanisms that are inherently out of phase with the applied forces, such as in the analysis of forced vibrations [83, 84]. The proportionality factor is defined as

$$\gamma = 2\zeta, \quad (3.20)$$

where ζ is the viscous damping ratio.

The damping matrix can also be constructed using individual modes and their associated information as

$$\mathbf{C} = \text{diag}(2\zeta_j\omega_j M_j), \quad j = 1, 2, \dots, N, \quad (3.21)$$

where M_j represents the modal mass.

In the attached papers, numerical damping is not considered; however, modal damping has been determined experimentally and is presented in Paper I to provide insight into variability in the modal damping ratio in CLT. The theoretical background discussed in this section is briefly outlined for educational purposes to provide context and enhance understanding.

3.2.2 Modal domain and mode superposition

The equations of motion can be solved in the modal domain to determine the structure's free harmonic oscillation characteristics, in the absence of internal damping and external forces, to extract the natural frequencies and normal modes. The undamped homogeneous equations of motion can be formulated by disregarding the external forces and internal damping in (3.15) as

$$\mathbf{M}\ddot{\mathbf{u}} + \mathbf{K}\mathbf{u} = \mathbf{0}, \quad (3.22)$$

and can be used to formulate a generalised eigenvalue problem as

$$(\mathbf{K} - \omega_j^2\mathbf{M})\boldsymbol{\phi}_j = \mathbf{0}, \quad j = 1, 2, \dots, N. \quad (3.23)$$

Here, ω_j represents the j -th angular natural frequency, and ϕ_j is the associated conjugate mode. The total number of modes a system has is defined as N . However, in dynamic analysis, only a subset of $r \ll N$ modes is often extracted, generally in the lower frequency range. The eigenvalue problem in (3.23) can be efficiently solved using numerical methods, such as the Lanczos method [85] or subspace iteration methods [86, 87]. The modes determined from (3.23) are collected in $\Phi = [\phi_1, \phi_2, \phi_3, \dots, \phi_r]$ and are mass-normalised using:

$$\Psi = \Phi \operatorname{diag} \left(\frac{1}{\sqrt{(\Phi^\top \mathbf{M} \Phi)}} \right). \quad (3.24)$$

The normal modes obtained from solving the eigenvalue problem in (3.23) serve as a basis for approximating the system's displacement field by employing the principle of mode superposition. According to this principle, the overall response of a linear system subjected to dynamic loading can be represented as a linear combination of its normal modes. Consequently, the displacement field $\mathbf{u}(t)$ can be approximated as

$$\mathbf{u}(t) = \Psi \boldsymbol{\eta} = \sum_{j=1}^r \psi_j \eta_j(t), \quad (3.25)$$

where $\eta_j(t)$ denotes the time-dependent natural coordinate associated with the j -th mode, and r is the total number of modes considered in the approximation, with $r \ll N$. As the normal modes are the eigenvectors of the system and are mass normalised, they diagonalise the system matrices by multiplying the equations of motion from the left-hand side by the modal matrix. This results in the equations of motion in natural coordinates as

$$\mathbf{M} \ddot{\boldsymbol{\eta}} + \mathbf{C} \dot{\boldsymbol{\eta}} + \mathbf{K} \boldsymbol{\eta} = \mathbf{p}(t), \quad (3.26)$$

with

$$\mathbf{M} = \Psi^\top \mathbf{M} \Psi, \quad \mathbf{C} = \Psi^\top \mathbf{C} \Psi, \quad \mathbf{K} = \Psi^\top \mathbf{K} \Psi, \quad \mathbf{p}(t) = \Psi^\top \mathbf{p}(t). \quad (3.27)$$

Mass normalisation of the mode shapes renders them orthogonal concerning both the mass and stiffness matrices. This orthogonality leads to the following relationships in modal space:

$$\Psi^\top \mathbf{M} \Psi = \mathbf{I}, \quad \Psi^\top \mathbf{K} \Psi = \boldsymbol{\Lambda} = \operatorname{diag}(\omega_i^2), \quad (3.28)$$

where \mathbf{I} is the identity matrix, and $\boldsymbol{\Lambda}$ is a diagonal matrix that contains the squared natural frequencies (eigenvalues) ω_i^2 of the system. This property enables the decoupling of the equations of motion in the modal coordinates, significantly simplifying their solution. Once the equations are solved in the modal domain, the results can

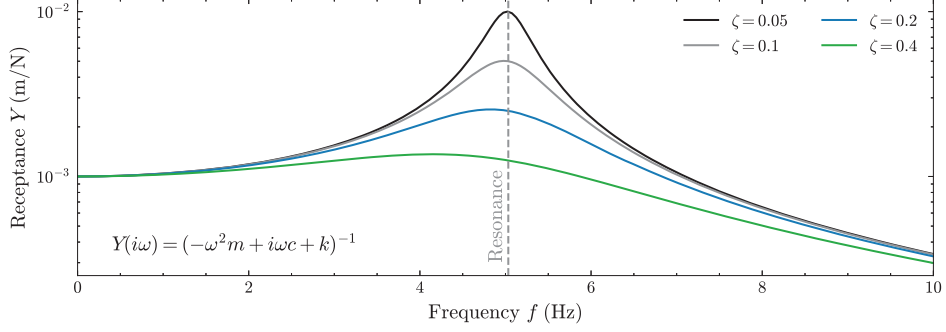


Figure 3.4: Harmonic vibration of an underdamped Single-degree-of-freedom (SDOF) system with different damping values. The parameters are selected as $m = 1$ kg, $c = 2\zeta M_n \omega_n$ N/(m/s), $\omega_n = 2\pi f$ rad/s, and $k = 10^3$ N/m.

be transformed back to the physical coordinate system using the transformation in (3.25).

Modal truncation can lead to a misrepresentation of system matrices due to the neglect of higher-order modes. To address this issue, system matrices can be effectively reduced using CMS with enhanced accuracy, as discussed in Chapter 7 and Paper IV.

3.2.3 Time domain

A spectral representation of the equations of motion, as detailed in (3.15), can be formulated in the time domain. This representation reflects the time dependence of the system's accelerations, velocities, and displacements. Within this framework, spatial variables can be represented as discrete functions of time and space. The FE method is employed to discretise the space domain, while time discretisation can be achieved through direct integration methods that are compatible with the equations of the FE system. Time integration methods are recursive methods that integrate the ordinary differential equation in (3.15) and solve for spatial unknowns stepwise. Conventional time integration methods include the central difference method [84], Newmark- β [88] and its associated extension Hilber-Hughes-Taylor (HHT) method [89], Bathe ρ_∞ [79] and its extension Noah-Bathe method [90]. For a comprehensive discussion on time integration methods, the reader may refer to Krenk's work [91] and the step-by-step derivation and experimental validation of Newmark- β in [77].

3.2.4 Frequency domain

The spatial unknowns in (3.15) are influenced by their spatial coordinates and the corresponding frequency components. Consequently, the classical Fourier decomposition can decompose the spatial response into frequency-dependent contributions [92]. This decomposition is fundamental in experimental dynamics, where vibration responses are initially measured in the time domain and then transformed into the frequency domain to extract critical characteristics of the system, such as natural frequencies, damping ratios and vibration modes, as previously discussed and elaborated in more detail in Chapter 4. The Fourier decomposition weights each time function⁴ with complex sinusoids representing counter-clockwise circular motion [95]. The displacement response can be expressed in terms of harmonic functions as:

$$\mathbf{u}(t) = \sum_{t=-N_\omega}^{N_\omega} \bar{\mathbf{U}}(\omega) e^{i\omega t}, \quad (3.29)$$

where ω denotes the natural angular frequency in rad/s, and the over-bar indicates the frequency-domain representation of the displacement amplitude. Substituting this harmonic representation into (3.15) transforms the equations of motion into the frequency domain as:

$$(-\omega^2 \mathbf{M} + i\omega \mathbf{C} + \mathbf{K}) \bar{\mathbf{U}}(\omega) = \bar{\mathbf{p}}(\omega), \quad \omega \in \mathbb{R}, \quad (3.30)$$

where the frequency-dependent dynamic stiffness⁵ matrix $\mathbf{Z}(\omega)$ is defined by:

$$\mathbf{Z}(i\omega) = -\omega^2 \mathbf{M} + i\omega \mathbf{C} + \mathbf{K}. \quad (3.31)$$

The solution for the complex frequency-dependent harmonic response in (3.30) can be expressed by inverting the dynamic stiffness matrix:

$$\bar{\mathbf{U}}(\omega) = \mathbf{Y}(i\omega) \bar{\mathbf{p}}(\omega), \quad (3.32)$$

Where $\mathbf{Y}(i\omega)$ is referred to as dynamic flexibility or admittance and defined as:

$$\mathbf{Y}(i\omega) = \mathbf{Z}(i\omega)^{-1} = (-\omega^2 \mathbf{M} + i\omega \mathbf{C} + \mathbf{K})^{-1} \quad (3.33)$$

And contains columns of the system's transfer functions. The transfer function contains resonance events that highlight the following characteristics of the system: (i)

⁴In experimental dynamics, time functions are often referred to as time signals. Unlike computational dynamics, these signals in experimental dynamics typically contain noise, which requires signal processing to reduce noise levels [93, 94].

⁵The dynamic stiffness matrix is also referred to as mechanical impedance or apparent mass in the literature [96].

before resonance, the behaviour of the system is governed by the inverse of the stiffness, $1/k$; (ii) at resonance, the system is dominated by $1/\omega c$; and (iii) after resonance, the response of the system is controlled by $1/(\omega^2 m)$, as shown in Fig. 3.4 for a single-degree-of-freedom system.

The transfer functions in (3.33) are defined as normalised displacement per unit of force under the assumption given in (3.29). However, they can be transformed to represent velocity per unit force, known as mobility, as follows:

$$\mathbf{V}(i\omega) = i\omega \mathbf{Y}(\omega), \quad (3.34)$$

and to represent acceleration per unit force, known as inertance, as:

$$\mathbf{H}(i\omega) = -\omega^2 \mathbf{Y}(\omega). \quad (3.35)$$

In addition to the spectral representations discussed above, the equations of motion can also be expressed in the Laplace domain⁶. Furthermore, alongside spatial and spectral representations, a commonly used form in system identification⁷ is the State Space representation of the equations of motion, where the second-order differential equation in (3.15) is transformed into a system of first-order differential equations. Further discussions on system identification and state space representation can be found in the comprehensive work by Ljung [98].

⁶The Laplace domain is reminiscent of the Fourier domain, which is commonly used for efficiently solving highly transient problems such as shock propagation, that cannot be represented using the mode superposition approach in section 3.2.2, Ref. [97].

⁷System identification is often used in experimental dynamics to identify noisy transfer functions, which often is further used in for example model updating and modal identification.

Chapter 4

Experimental Modal Analysis

Modal properties of solids and structures can be determined experimentally using the non-destructive testing technique EMA. These properties comprise natural frequencies, damping ratios, and mode shapes (also called natural modes or eigenmodes), which together provide a complete dynamic characterisation of the system. Understanding these modal parameters is crucial for structural design, vibration control, and health monitoring in various fields of engineering, from aerospace to civil infrastructure. In EMA a structure is excited with a known input force using a force transducer¹ and the response of the structure is measured using motion transducers, such as accelerometers². Therefore, EMA requires an integrated measurement chain comprising excitation transducers, response sensors, signal conditioning equipment, data acquisition hardware with sampling capabilities, and signal processing and modal analysis software for parameter extraction. The force and corresponding response signals are commonly measured in the time domain, which after sampling and filtering are transformed into the frequency domain using the Fourier transform³ to extract their resulting transfer functions. These transfer functions are further processed and fitted using curve fitting and modal parameter estimation techniques such as [101–103], and used to extract the modal properties.

The quality and reliability of the EMA results depend heavily on the proper selec-

¹In experimental dynamics, input force is also referred to as input signal which is generated using impulse hammer or shaker.

²Other motion transducers comprise vibrometers for measuring displacement and can be categorised as (i) Laser vibrometers, (ii) Capacitive vibrometers, and (iii) Eddy-Current vibrometers. To measure a structure's vibration velocity, electrodynamic velocity transducers can be employed. Common transducers used in EMA are piezoelectric accelerometers due to their sensitivity to dynamic changes [99].

³Modern computers use Fast Fourier Transform (FFT) which provides an efficient computation of classical Fourier Transform [92, 100].

tion of the measurement equipment, as well as careful consideration of measurement parameters such as sampling frequency, acquisition time, and anti-aliasing filters.

This chapter introduces the concept of EMA from the experimental design procedure to data extraction and outlines the strategies employed in Paper I, which uses EMA to characterise the modal properties of CLT substructures and quantify their variability. A comprehensive introduction to experimental dynamics and specifically EMA can be found in the literature, for example, [84, 104] and the references therein.

4.1 Experimental design

In EMA, the behaviour of a structure is commonly truncated to a set of critical reference points that are assumed to describe the modal characteristics of the system. These reference points, commonly referred to as nodes, are designed by performing a prestudy of the structure using FE modal analysis. The selection of these measurement points is crucial, as they must adequately capture the structure's dynamic behaviour within the frequency spectrum of interest while maintaining practical testing efficiency. Too few points may result in misidentification of the mode shapes of interest, while too many points increase testing time and complexity. The number of reference points can be selected as $n > 3$ per wavelength [105] for simple geometries or by using Fisher's information matrix, for example, the work by Kammer [106] and Linderholt and Abrahamsson [107] for complex geometries.

Once the measurement locations are selected, their associated modes can be compared using the Modal Assurance Criterion (MAC) [108] to investigate their orthogonality:

$$\text{MAC}(\psi_r, \psi_s) = \frac{|\psi_r^H \psi_s|^2}{(\psi_r^H \psi_r) (\psi_s^H \psi_s)}, \quad (4.1)$$

where ψ_r , ψ_s are two eigenvectors, that is, the components of (3.24) to be compared, and H denotes the Hermitian transpose. The MAC value lies between zero and unity, where unity represents perfect correlation between two modes, and zero indicates that they are orthogonal. For design purposes, the numerical modes can be compared with each other, and hence the MAC equation in (4.1) is sometimes called autoMAC. For a sufficient number of reference points, the off-diagonal terms of (4.1) should approach zero, while the diagonal terms are always equal to 1.

The sampling frequency range can be selected using the Nyquist-Shannon sampling theorem [109], namely $f_s \geq 2f_{\max}$. In the case of soft structures like wood, exciting higher-frequency vibrations can be challenging. Lightweight steel washers can be at-

tached to the structure at the reference points to address this. The structure can then be excited by the excitement of these washers using, for example, an impulse hammer. This strategy was used in Paper I.

4.2 Boundary conditions

The EMA aims to determine the modal properties of the structures independently of the excitation forces and boundary conditions. It is possible to hang lightweight structures with low-stiffness bungee cords to simulate rigid body modes far below the fundamental natural frequency. However, heavy structures might be positioned on air springs with rigid body modes at least 3 times below the fundamental natural frequency. The former approach has been employed in Paper I and produced the rigid body frequency far below the fundamental natural frequency. Another reason for using free-free boundary conditions is the difficulty of using proper boundary conditions, as they can be frequency-dependent in vibration analysis. For example, the structural mass can provide sufficient contact between the structure and the supports at lower frequencies, whereas frequency-dependent contact is at higher frequencies. Furthermore, natural frequencies, modal damping, and vibration modes can be influenced by boundary conditions. In addition, frequency-dependent boundary conditions are difficult to simulate numerically as modal data are often used in inverse dynamics, as further elaborated in Chapter 5 and Paper II.

4.3 Data acquisition and processing

In experimental dynamics, measurements in the time domain of the force and associated response are typically acquired using transducers. These signals are analogous and must be sampled and digitised for further processing in computational dynamics. The sampled signals are digitised using signal conditioning devices, such as analogue-to-digital converters (ADC). Once the signals are digitised, it is necessary to apply windowing before transforming them to the frequency domain. Windowing is required to reduce spectral leakage, which occurs when the signal is not periodic within the observation window. By applying a window function, such as a quadratic window for the forcing signal or an exponential window for the corresponding viscous response, spectral leakage is mitigated, leading to more accurate frequency-domain representations, as shown in Fig. 4.1.

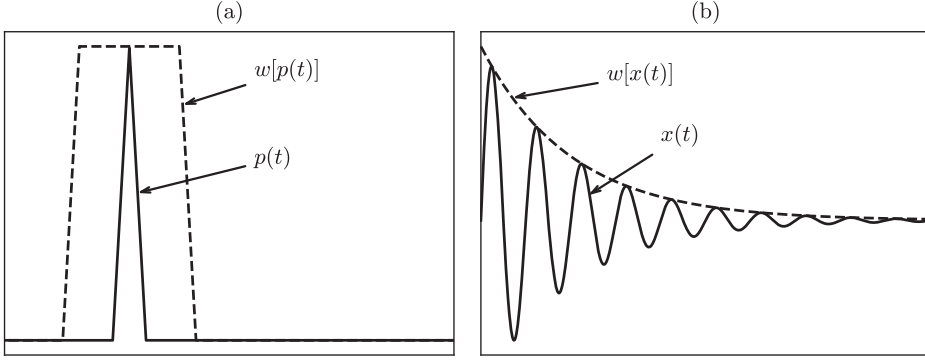


Figure 4.1: Application of windowing to constrain signals: (a) Transient input signal $p(t)$ with a quadratic window $w[p(t)]$, and (b) Viscous response $x(t)$ with an exponential window $w[x(t)]$.

4.4 Estimation of transfer functions

A transfer function represents the frequency response function of a specific position in a structure per unit of force. Therefore, time-domain signals, measured by force transducers (e.g. impulse hammers) and accelerometers, are transformed to the frequency domain using the Fourier transform:

$$P(\omega) = \mathcal{F}[p(t)] = \int_{-\infty}^{\infty} p(t) e^{-i2\pi ft} dt, \quad (4.2a)$$

$$X(\omega) = \mathcal{F}[x(t)] = \int_{-\infty}^{\infty} x(t) e^{-i2\pi ft} dt, \quad (4.2b)$$

where $P(\omega)$ and $X(\omega)$ denote the frequency-domain force and resulting response, respectively, while $p(t)$ and $x(t)$ represent their corresponding time-domain signals [110, 111], Fig. 4.2.

In practical measurements, particularly in EMA, the arrangement of excitation and response measurement locations can be constrained by accessibility. In this context, the principle of reciprocity becomes especially important. This principle asserts that, for linear, time-invariant, and passive mechanical systems, the transfer function obtained by applying a force at point i and measuring the response at point j is identical to the transfer function obtained by reversing the roles, applying the force at point j and measuring the response at point i . In other words, the transfer function between two reference points remains unchanged, regardless of which point is designated as the input or output. The principle of reciprocity offers several advantages, including enhanced measurement flexibility, validation of experimental results, and improved test coverage, particularly in large-scale structures where uniformly applying excita-

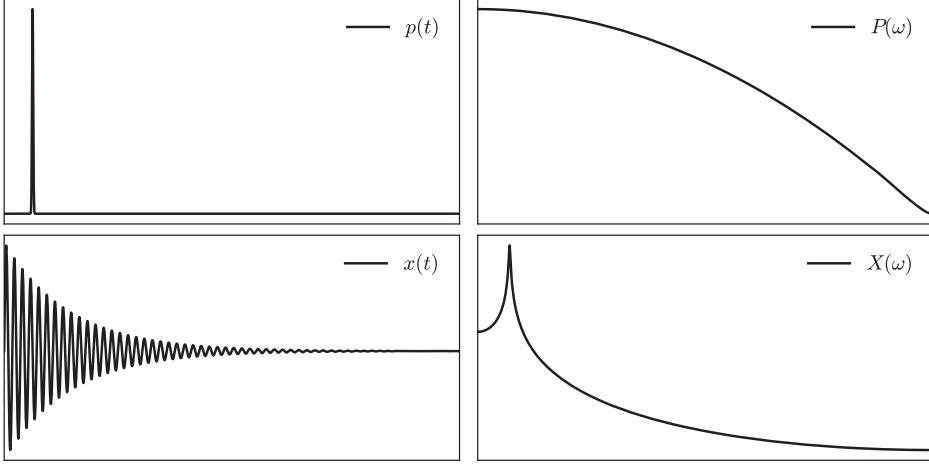


Figure 4.2: Time domain representation of measured impulse force $p(t)$ and viscous response $x(t)$ and their respective frequency domain representations, i.e., $P(\omega)$ and $X(\omega)$, as outlined in (4.2).

tion forces may be difficult.

Equation (4.2) shows that the time samples are weighted by a complex function, integrated over time, with ω representing the driving angular frequency. Using the frequency domain components in (4.2), we can determine the following transfer functions:

$$X(\omega)\overline{P(\omega)} = H(\omega)P(\omega)\overline{P(\omega)} \quad \longrightarrow \quad H_1(\omega) = \frac{X(\omega)\overline{P(\omega)}}{P(\omega)\overline{P(\omega)}} = \frac{G_{PX}(\omega)}{G_{PP}(\omega)}, \quad (4.3a)$$

$$X(\omega)\overline{X(\omega)} = H(\omega)P(\omega)\overline{X(\omega)} \quad \longrightarrow \quad H_2(\omega) = \frac{X(\omega)\overline{X(\omega)}}{X(\omega)\overline{P(\omega)}} = \frac{G_{XX}(\omega)}{G_{XP}(\omega)}, \quad (4.3b)$$

where H_1 is suitable for systems with output noise, and H_2 is accurate for systems with input noise. Here, $G_{PX}(\omega)$ and $G_{XP}(\omega)$ are cross-power spectra, while $G_{XX}(\omega)$ and $G_{PP}(\omega)$ are the autopower spectrum of the system, and an over-bar denotes the complex conjugate [105].

For a system with both input and output noise, an average of H_1 and H_2 can be derived as:

$$H_3(\omega) = \sqrt{H_1(\omega) \cdot H_2(\omega)} = \sqrt{\frac{G_{XX}(\omega)}{G_{PP}(\omega)} \frac{G_{XP}(\omega)}{|G_{XP}(\omega)|}}. \quad (4.4)$$

A comparison of the transfer functions defined in (4.3) and (4.4) for low-noise vi-

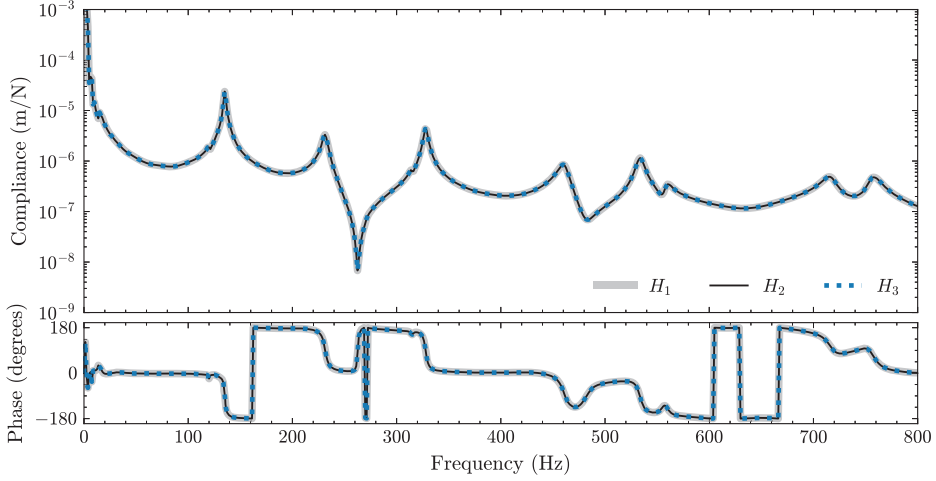


Figure 4.3: Bode plot of Frequency Response Functions (FRFs) computed using H_1 , H_2 , and H_3 procedures in (4.3) and (4.4), as detailed in Paper I.

bration measurements, as detailed in Paper I, is presented in Fig. 4.3. Estimation of the transfer function reveals that for low-noise vibration conditions, all three transfer functions, namely H_1 , H_2 , and H_3 , are nearly identical.

To evaluate the strength of the relationship between input and output signals, ordinary coherence acts as a key metric. Coherence measures the degree to which input energy is effectively transferred to output energy. In high-quality measurements, the coherence values typically approach 1, indicating a strong correlation between the input and output signals. However, deviations from this ideal behaviour can occur, particularly during antiresonance events, where oscillatory effects may reduce coherence. Using the auto- and cross-power spectra in (4.3), the coherence is defined as:

$$\gamma^2(\omega) = \frac{|G_{PX}(\omega)|^2}{|G_{PP}(\omega)| |G_{XX}(\omega)|}, \quad 0 \leq \gamma^2(\omega) \leq 1, \quad (4.5)$$

where a coherence value of unity indicates complete transmission of the input signal into output energy, while zero indicates no transmission. The coherence function is calculated from averaged auto- and cross-power spectra over repeated measurements.

Vibration is commonly measured in terms of acceleration, as accelerometers are the most widely used transducers. Consequently, transfer functions are often expressed in terms of acceleration per unit force (inertance). However, it may be more practical in analysis to examine velocity per unit force (mobility) or displacement per unit force (compliance). Therefore, the frequency response function (FRF) matrix can be

integrated as follows:

$$V_{ij}(\omega) = \int_{\omega} H_{ij}(\omega) d\omega = \frac{H_{ij}(\omega)}{2\pi f_j}, \quad (4.6a)$$

$$Y_{ij}(\omega) = \iint_{\omega} H_{ij}(\omega) d\omega = \frac{H_{ij}(\omega)}{(2\pi f_j)^2}, \quad (4.6b)$$

where $V_{ij}(\omega)$ and $Y_{ij}(\omega)$ denote the mobility and compliance components of the FRF, respectively. Here, H_{ij} represents elements of the inertance matrix and ω is the driving angular frequency.

4.5 Estimation of modal parameters

Estimating the modal parameters aims to identify the critical components of vibrating signals, which describe the performance of the structure and its vulnerabilities under vibration. Signals from all excitation points are collected and transformed into frequency-domain transfer functions using the procedure described above. Curve fitting techniques are used to locate consistent resonance peaks across the frequency spectrum in the transfer functions. Limiting the frequency range under investigation can improve the precision of these estimates. The ultimate objective is to extract stable poles with complex values, represented by $\lambda_k = -\zeta_k \omega_{n,k} \pm i\omega_{d,k}$, where (i) ζ_k denotes the modal damping ratio which governs the decay rate of the oscillation, (ii) $\omega_{n,k}$ is the corresponding natural frequency, and (iii) $i\omega_{d,k}$ signifies the damped natural frequency, which is associated with peaks in the system responses at resonance, Figs. 3.4 and 4.3. To maintain stability, the real part of the pole should be negative, ensuring that the oscillations diminish with time.

The transfer functions can be approximated by summing the contributions of multiple single-degree-of-freedom (SDOF) models and can be represented in several mathematical forms, including (i) polynomial, (ii) pole-zero, (iii) partial fraction, and (iv) exponential. An SDOF version of the dynamic flexibility in (3.33) can be expressed as:

$$Y(i\omega) = Z(i\omega)^{-1} = \frac{1}{(-\omega^2 m + i\omega c + k)}, \quad (4.7)$$

and its corresponding partial fraction form, after summation over k excitation points, as:

$$\mathbf{Y}(i\omega) = \sum_k \left(\frac{\mathbf{A}_k}{i\omega - \lambda_k} + \frac{\overline{\mathbf{A}}_k}{i\omega - \overline{\lambda}_k} \right), \quad (4.8)$$

where λ_k and its conjugate $\bar{\lambda}_k$ represent the poles of the system, given by:

$$\lambda_k, \bar{\lambda}_k = -\zeta_k \omega_{n,k} \pm i \omega_{n,k} \sqrt{1 - \zeta_k^2} = -\zeta_k \omega_{n,k} \pm i \omega_{d,k}. \quad (4.9)$$

Here, $\omega_{n,k}$ represents the undamped natural angular frequency, $\omega_{d,k}$ is the damped natural frequency, and ζ_k is the damping ratio.

In equation (4.8), the residues \mathbf{A}_k and $\bar{\mathbf{A}}_k$ contain information about the modal amplitudes and scaling factors. Consequently, the transfer function can be expanded as:

$$\mathbf{Y}(i\omega) = \sum_k \frac{Q_k \psi_k \psi_k^\top}{i\omega - \lambda_k} + \frac{\bar{Q}_k \bar{\psi}_k \bar{\psi}_k^H}{i\omega - \bar{\lambda}_k}, \quad (4.10)$$

where ψ_k and $\bar{\psi}_k$ are the mode vectors, and Q_k and \bar{Q}_k are the corresponding scaling factors, obtained by fitting this expression to the observed transfer functions [84, 110]. The angular frequency is represented by $\omega = 2\pi f$. The expression in (4.10) is applicable to compliance transfer functions⁴, however, it can be extended to transfer functions representing mobility⁵ and inertance⁶ using the expressions in (3.34) and (3.35) as:

$$\mathbf{V}(i\omega) = \sum_k i\omega \left(\frac{Q_k \psi_k \psi_k^\top}{i\omega - \lambda_k} + \frac{\bar{Q}_k \bar{\psi}_k \bar{\psi}_k^H}{i\omega - \bar{\lambda}_k} \right), \quad (4.11)$$

and

$$\mathbf{H}(i\omega) = \sum_k -\omega^2 \left(\frac{Q_k \psi_k \psi_k^\top}{i\omega - \lambda_k} + \frac{\bar{Q}_k \bar{\psi}_k \bar{\psi}_k^H}{i\omega - \bar{\lambda}_k} \right), \quad (4.12)$$

In the attached papers, the estimation of the modal parameters was carried out in the z -domain [102, 112] using the Brüel & Kjær–BK Connect software suite [113]. The transfer function amplitude experiences a phase shift at resonance, which can be determined in degrees using:

$$\phi_j(\omega) = \frac{180}{\pi} \tan^{-1} \left(\frac{\Im(H_j(\omega))}{\Re(H_j(\omega))} \right). \quad (4.13)$$

Here, the steepness of the phase shift, often characterised by the rate of change around resonance, is influenced by the damping properties of the system. Higher damping typically results in a broader and less pronounced phase shift, while lower damping leads to a steeper and more abrupt transition.

⁴Displacement per unit force is also referred to as receptance in literature.

⁵Velocity per unit force is referred to as mobility.

⁶Acceleration per unit force is referred to as accelerance or inertance.

Chapter 5

Inverse parameter identification and model updating

Accurate computational models are essential to ensure the safety, reliability of predictive models and optimal use of materials. Despite extensive research in material modelling and advanced FE modelling strategies, real-world applications often reveal discrepancies between computational and experimental dynamics [114]. These discrepancies, commonly referred to as representation errors, can be broadly categorised into (i) idealisation errors, (ii) discretisation errors, and (iii) uncertain mechanical properties. Idealisation errors arise from abstracting or simplifying real-world structures into engineering representations, such as finite elements (e.g., solids, shells, beams, bars). These idealisations often neglect geometric or physical complexities, which may lead to deviations between the computational model and the real system. Discretisation errors arise from the numerical approximation of the differential equation of physics using the FE method. The choice of element type, discretisation density, and order of interpolation functions and integration also influence the model's accuracy. Uncertainty in material properties constitutes a critical source of representation error often seen in predictive modelling. These uncertainties arise from incomplete or incorrect assumptions regarding material behaviour, including variations in mass distribution, energy dissipation characteristics (e.g., damping), and fundamental mechanical properties such as strength, stiffness, or thermal conductivity.

The uncertainty in mechanical strength and distribution of mass is often associated with complex materials with inherent variability in their fibre structure coupled with anisotropic behaviour, for example, wood as a material and CLT as an engineered composite structure. Other variations in the mechanical properties of structures are

caused by environmental and temperature fluctuations [115–117], cyclic fatigue, and damage [118–120]. Although experimental data are considered as references in the validation of computational models, they can also contain uncertainties stemming from environmental noise, excitation variability, boundary conditions, non-linearities, and sensor positioning, to mention a few.

To identify uncertain model parameters, the concept of inverse parameter identification through model updating was introduced in the 1970s [121–124] and developed further in the 1980s [125]. The approach to inverse identification of model parameters consists of updating the stiffness and mass matrix using observed data from the EMA. The discrepancy between the predicted results from computational FE models and the observed results from EMA is determined by formulating a residual, which is subsequently minimised to a satisfactory level while identifying the unknown model parameters.

This chapter introduces the concept of optimisation-based model updating technique and inverse identification of model parameters using a gradient-free approach derived in Paper II to identify unknown mechanical properties of CLT.

5.1 Residual formulation

The natural frequencies and vibration modes observed from the EMA in (4.10), (4.11), or (4.12) together with their corresponding predicted resonance frequencies and eigenmodes in (3.23) can be used to formulate a residual function that quantifies the distance between the observed and predicted results. The distance between the natural frequencies can be measured using a relative distance as:

$$\mathcal{R}_f^{(k)}(\boldsymbol{\theta}) = \mathbf{r}_f^{(k)\top} \mathbf{W}_f^{(k)} \mathbf{r}_f^{(k)} = \sum_{j=1}^{N_j} W_{f,jj}^{(k)} \left(|\tilde{f}_j - f_j^{(k)}(\boldsymbol{\theta})| / f_j^{(k)}(\boldsymbol{\theta}) \right)^2, \quad (5.1)$$

where \mathbf{r}_f is a vector containing residual distances between observed natural frequencies \tilde{f}_j and their corresponding predicted resonance frequencies $f_j(\boldsymbol{\theta})$. The predicted natural frequencies are a function of the model parameters, that is, $\theta_i \in \{1, 2, \dots, p\}$. The matrix $\mathbf{W}_f^{(k)}$ is a semidefinite positive symmetric matrix that represents the uncertainty in the residual terms related to the model parameters. The total number of natural frequencies is denoted N_j , and the minimisation state is denoted as k . Similarly, the relative difference between the observed and predicted

vibration modes can be quantified using:

$$\mathcal{R}_{\psi}^{(k)}(\boldsymbol{\theta}) = \mathbf{r}_{\psi}^{(k)\top} \mathbf{W}_{\psi}^{(k)} \mathbf{r}_{\psi}^{(k)} = \sum_{i,j=1}^{N_j} W_{\psi,jj}^{(k)} \left[1 - \text{diag} \left(\text{MAC}^{(k)} \left(\tilde{\boldsymbol{\psi}}_i, \boldsymbol{\psi}_j^{(k)}(\boldsymbol{\theta}) \right) \right) \right], \quad (5.2)$$

where \mathbf{r}_{ψ} contains residual distances between the observed and predicted vibration modes and the Modal Assurance Criterion (MAC) [108] is defined as:

$$\text{MAC}^{(k)} \left(\tilde{\boldsymbol{\psi}}_i, \boldsymbol{\psi}_j^{(k)}(\boldsymbol{\theta}) \right) = \frac{|\tilde{\boldsymbol{\psi}}_i^H \boldsymbol{\psi}_j^{(k)}(\boldsymbol{\theta})|^2}{\left(\tilde{\boldsymbol{\psi}}_i^H \tilde{\boldsymbol{\psi}}_i \right) \left(\boldsymbol{\psi}_j^{(k)H}(\boldsymbol{\theta}) \boldsymbol{\psi}_j^{(k)}(\boldsymbol{\theta}) \right)}, \quad (5.3)$$

and $\tilde{\boldsymbol{\psi}}_i$ and $\boldsymbol{\psi}_j$ respectively denote observed and predicted natural modes, and H denotes the Hermitian transpose.

A combination of (5.1) and (5.2) results in

$$\begin{aligned} \mathcal{R}^{(k)}(\boldsymbol{\theta}) &= \sum_{j=1}^{N_j} W_{f,jj}^{(k)} \left(|\tilde{f}_j - f_j^{(k)}(\boldsymbol{\theta})| / f_j^{(k)}(\boldsymbol{\theta}) \right)^2 \\ &+ \sum_{i,j=1}^{N_j} W_{\psi,jj}^{(k)} \left[1 - \text{diag} \left(\text{MAC}^{(k)} \left(\tilde{\boldsymbol{\psi}}_i, \boldsymbol{\psi}_j^{(k)}(\boldsymbol{\theta}) \right) \right) \right], \end{aligned} \quad (5.4)$$

which is often referred to as a weighted sum-of-squared residual (WSSR) and comprises all discrepancies between all-natural frequencies and vibration modes. Natural frequencies and modes are paired, if necessary, using (5.3) when computing the residual in (5.4). The values of $W_{f,jj}$ and $W_{\psi,jj}$ can be used for Tikhonov regularisation terms in the case of poorly posed problems [44, 126]. In Paper II, the regularisation values were set to unity whilst ill conditions were minimised through strategies discussed in the next section.

5.2 Model parametrisation

The computational model, which includes the system matrices, particularly the mass and stiffness matrices in the equations of motion, must be parametrised for successful model updating and inverse identification of unknown model parameters. The model parameters can include geometrical definitions, mechanical properties, or external conditions. To ensure an effective model updating procedure, the parameterisation should adhere to the following criteria:

- Restrict the unknown parameters to avoid ill-conditioning.
- Ensure that the parameters capture the model's uncertainty.
- Ensure the sensitivity of the model to variations in the selected parameters.

The sensitive model parameters can be easily determined through a sensitivity analysis using, for example, one parameter variation, if they are not already known. Once the parameters are selected, the mass and stiffness matrices can be parametrised as follows:

$$\mathbf{M}^{(k)}(\boldsymbol{\theta}) = \sum_{e=1}^{n_{el}} \mathbf{M}_e^{(k)} (1 - \delta_e^m) = \mathbf{M}_0 - \sum_{e=1}^{n_{el}} \mathbf{M}_e^{(k)} \delta_e^m, \quad (5.5a)$$

$$\mathbf{K}^{(k)}(\boldsymbol{\theta}) = \sum_{e=1}^{n_{el}} \mathbf{K}_e^{(k)} (1 - \delta_e^k) = \mathbf{K}_0 - \sum_{e=1}^{n_{el}} \mathbf{K}_e^{(k)} \delta_e^k, \quad (5.5b)$$

where $\mathbf{M}_0^{(k)}$ and $\mathbf{K}_0^{(k)}$ denote initial mass and stiffness matrices determined through initial conditions and δ_e^m , δ_e^k are respectively element mass and stiffness steps at iteration k . The expression indicates that each FE is updated before assembly in the global system matrices, in which n_{el} denotes the total number of FEs.

5.3 Parameter estimation

Using the expression in (5.4) and the unknown bounds of the model parameters, the following unconstrained problem can be formulated,

$$(\mathbb{P}) \begin{cases} \underset{\boldsymbol{\theta} \in \mathbb{R}^3}{\text{argmin}} & \mathcal{R}(\boldsymbol{\theta}), \\ \text{where} & \boldsymbol{\theta} \in \{E_1, G_{12} = G_{13}, G_{23}\}, \end{cases} \quad (5.6)$$

with the residual function $\mathcal{R}(\boldsymbol{\theta})$ defined as:

$$\begin{aligned} \mathcal{R}(\boldsymbol{\theta}) = & \sum_{j=1}^{N_j} W_{f,jj}^{(k)} \left(|\tilde{f}_j - f_j^{(k)}(\boldsymbol{\theta})| / f_j^{(k)}(\boldsymbol{\theta}) \right)^2 \\ & + \sum_{i,j=1}^{N_j} W_{\psi,jj}^{(k)} \left[1 - \text{diag} \left(\text{MAC}^{(k)} \left(\tilde{\boldsymbol{\psi}}_i, \boldsymbol{\psi}_j^{(k)}(\boldsymbol{\theta}) \right) \right) \right]. \end{aligned} \quad (5.7)$$

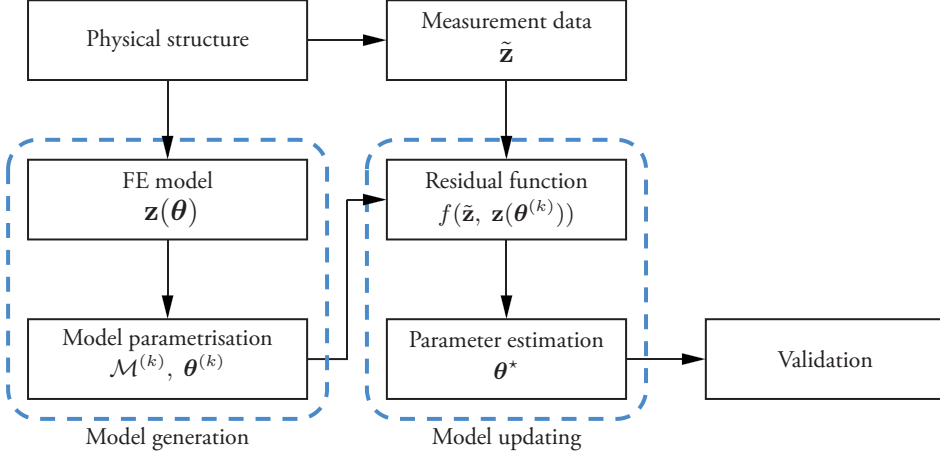


Figure 5.1: Flowchart depicting the sequential process for generating, updating, and validating finite element (FE) models in structural dynamics. The notations $\tilde{\mathbf{z}}$, $\mathbf{z}(\boldsymbol{\theta})$, $\mathcal{M}^{(k)}$, $\boldsymbol{\theta}^{(k)}$, and $\boldsymbol{\theta}^*$ denote the observed results, predicted results, FE model at iteration k , tuning parameters at iteration k , and the optimal tuning parameters, respectively.

To identify the corresponding resonances, it is preferable to first treat the second component of the expression in (5.7) and accordingly identify the paired modes, as suggested by Allemang [108]. The formulation in (5.7) comprises two nested objectives related to natural frequencies and their associated conjugate modes. Consequently, simultaneous minimisation of the objective in (5.6), subject to sensitive model parameters, results in a Single-Objective Optimisation (SOO) problem. A schematic flow chart of the model updating and parameter estimation process for validation is illustrated in Fig. 5.1.

The problem in (5.6), subject to the sensitive model parameters, can be minimised using the gradient-free simplex method by Nelder and Mead [127]. The advantage of using the simplex method stems from its independence from the gradients of the residual function, which is often non-differentiable in model updating. Furthermore, the simplex method does not require bounds on the sensitive model parameters, making it particularly suitable for model updating in cases such as CLT, where stiffness bounds might be unknown. Consequently, the SOO in (5.6) takes an unconstrained optimisation form.

The sequential procedure of simplex minimisation involves iteratively refining a geometric simplex with $p+1$ vertices in \mathbb{R}^p , where p denotes the number of model parameters. At each iteration, the simplex undergoes a series of transformations—reflection, expansion, contraction, and shrinkage—based on the residual function values at the vertices. These operations aim to converge the simplex to a region of the parameter

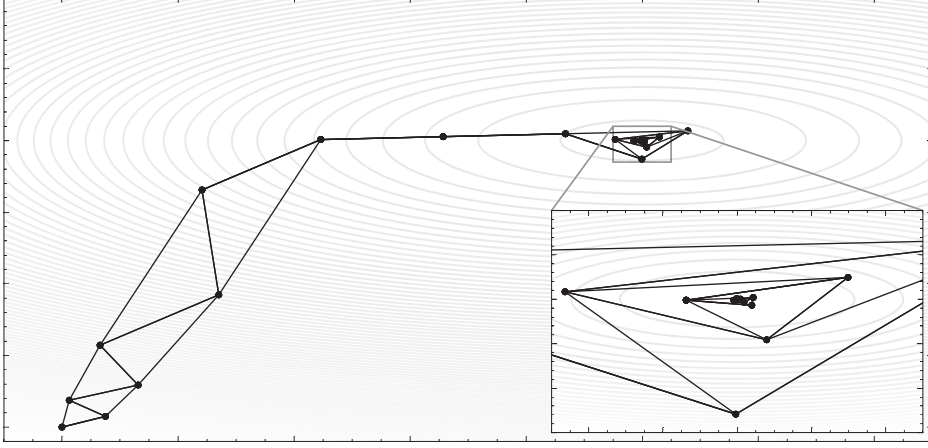


Figure 5.2: Optimisation process of an arbitrary conic section defined by $x^2 + y^2 - 4x - 6y + 5 = 0$ using Simplex minimisation in \mathbb{R}^2 . The contour plots show the residual domain, with the black lines representing the simplex triangles in each iteration of the optimisation procedure.

space that minimises the residual function. Sequential transformations continue until the convergence criterion is met, such as a predefined tolerance, a maximum number of iterations, or a distance constraint between the previous and current steps. A progression illustration of the simplex method to minimise a three-vertex simplex in \mathbb{R}^2 can be found in Fig. 5.2. The algorithm 1 provides a detailed, step-by-step implementation of the gradient-free model updating process. Further insights into the implementation of the simplex approach are available in [128].

In Paper II, the computational simplex was used to minimise the objective in (5.6) to identify key sensitive stiffness parameters of CLT, comprising the longitudinal Young's modulus E_l , the internal shear moduli $G_{lt} = G_{lr}$ and the rolling shear modulus G_{rt} that enters the constitutive law in (3.10), see Fig. 5.3.

5.4 Model validation

The optimal model parameters determined through the model updating procedure discussed in the previous section and summarised in Algorithm 1 can be used to validate the model. The equations of motion shall be updated using θ^* and the predicted results shall be compared with the corresponding observed results. The relative distance between the natural frequencies can be quantified using:

$$\text{Relative frequency difference} = \frac{|\tilde{f}_j - f_j(\theta^*)|}{f_j(\theta^*)}, \quad j = 1, 2, \dots, N_j, \quad (5.8)$$

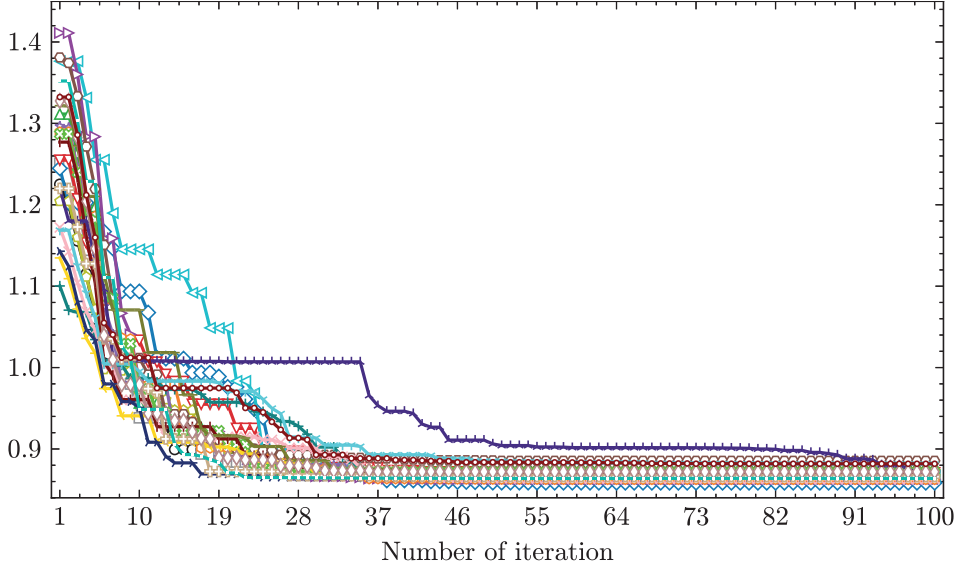


Figure 5.3: Progressive solution of the optimisation problem in (5.6) to determine stiffness components of the constitutive law in (3.10) for CLT as further elaborated in Paper II.

where \tilde{f}_j and $f_j(\theta^*)$ denote respectively natural frequency components of the observed and corresponding predicted results, and N_j is the total number of natural frequencies. In the above equation, the index j is used for both observed and predicted natural frequencies assuming that their order is determined through mode pairing [108].

The predicted eigenmodes can be compared similarly with their corresponding observed natural modes using MAC,

$$\text{MAC}(\tilde{\psi}_i, \psi_j(\theta^*)) = \frac{|\tilde{\psi}_i^H \psi_j(\theta^*)|^2}{(\tilde{\psi}_i^H \tilde{\psi}_i)(\psi_j^H(\theta^*) \psi_j(\theta^*))}, \quad j = 1, 2, \dots, N_j, \quad (5.9)$$

where $\tilde{\psi}_j$ and $\psi_j(\theta^*)$ denote, respectively, the observed and predicted mode shapes, and N_j is the total number of modes. For a perfect correlation, the diagonal terms of (5.9) approach unity. However, due to the presence of noise, modelling errors, or other sources of uncertainty, achieving unity is often impractical. In engineering applications, values $\text{MAC} > 0.8$ are commonly considered acceptable as an indicator of strong correlation.

Algorithm 1 Step-by-step model updating procedure for parameter estimation.

```

1: Initialise:  $\theta^0$ ,  $M_0$ ,  $K_0$ ,  $\tilde{f}$ ,  $\tilde{\Psi}$ ,  $\epsilon$ ,  $\gamma^s = \delta^{ic} = \delta^{oc} = 1/2$ ,  $\delta^r = 1$ ,  $\delta^e = 2$ 
2: Compute  $\mathcal{R}(\theta^0)$  in (5.4)
3: for  $i = 1$  to  $p$  do
4:   Perturb  $\theta_i = \theta_i^0 + \epsilon$  ▷ Each component of  $\theta$ 
5:   Update  $M(\theta)$  and  $K(\theta)$ , in (5.5)
6:   Compute  $\mathcal{R}(\theta)$  in (5.4)
7: end for
8: while  $\|\theta^{(k)} - \theta^{(k-1)}\| > 1 \times 10^{-2}$  do
9:   Sort  $\mathcal{R}(\theta^0) \leq \mathcal{R}(\theta^1) \leq \dots \leq \mathcal{R}(\theta^p)$ 
10:   $\theta^c = \sum_{i=0}^{p-1} \theta^i / p$  ▷ Centroid calculation
11:   $\theta^r = \theta^c + \delta^r(\theta^c - \theta^p)$  ▷ Reflection step
12:  if  $\mathcal{R}(\theta^0) \leq \mathcal{R}(\theta^r) < \mathcal{R}(\theta^{p-1})$  then
13:     $Y_{k+1} \leftarrow \{\theta^0, \theta^1, \dots, \theta^{p-1}, \theta^r\}$ 
14:    break
15:  end if
16:  if  $\mathcal{R}(\theta^r) < \mathcal{R}(\theta^0)$  then ▷ Expansion step
17:     $\theta^e = \theta^c + \delta^e(\theta^c - \theta^p)$ 
18:    if  $\mathcal{R}(\theta^e) \leq \mathcal{R}(\theta^r)$  then
19:       $Y_{k+1} \leftarrow \{\theta^0, \theta^1, \dots, \theta^{p-1}, \theta^e\}$ 
20:      break
21:    else
22:       $Y_{k+1} \leftarrow \{\theta^0, \theta^1, \dots, \theta^{p-1}, \theta^r\}$ 
23:      break
24:    end if
25:  end if
26:  if  $\mathcal{R}(\theta^r) \geq \mathcal{R}(\theta^{p-1})$  then ▷ Contraction step
27:    if  $\mathcal{R}(\theta^r) < \mathcal{R}(\theta^p)$  then ▷ Outward contraction
28:       $\theta^{oc} = \theta^c + \delta^{oc}(\theta^c - \theta^p)$ 
29:       $Y_{k+1} \leftarrow \{\theta^0, \theta^1, \dots, \theta^{p-1}, \theta^{oc}\}$ 
30:    else if  $\mathcal{R}(\theta^r) \geq \mathcal{R}(\theta^p)$  then ▷ Inward contraction
31:       $\theta^{ic} = \theta^c + \delta^{ic}(\theta^c - \theta^p)$ 
32:       $Y_{k+1} \leftarrow \{\theta^0, \theta^1, \dots, \theta^{p-1}, \theta^{ic}\}$ 
33:    end if
34:  else ▷ Shrinking step
35:     $Y_{k+1} \leftarrow \{\theta^0 + \gamma^s(\theta^i - \theta^0) \text{ for } i \in \{1, 2, \dots, p-1\}\}$ 
36:  end if
37:   $\theta^{(k)} = Y_{k+1}$  ▷ Update the simplex
38: end while
39: Output: Optimal model parameters  $\theta^* = \theta^{(k)}$ 
40: Validation: Validate  $\theta^*$  using (5.8) and (5.9)

```

Chapter 6

Uncertainty quantification

The accuracy and reliability of FE analysis depend on underlying modelling assumptions, including material properties, geometric variations, boundary conditions, and numerical approximations. To tune FE models towards their corresponding reference measurements, the concept of model updating was introduced in Chapter 5. However, this process cannot eliminate all uncertainties that are classified as aleatory or epistemic. Aleatory uncertainties arise from inherent variability, such as material inconsistencies and manufacturing tolerances, and cannot be reduced through further modelling. For example, variations in the direction of the wood grain affect stiffness and strength, leading to deviations in structural performance. In contrast, epistemic uncertainties stem from incomplete knowledge, including insufficient material characterisation and model simplifications, and can be reduced with improved data acquisition and modelling techniques, [129, 130]. For example, in FE model updating, using a truncated set of vibration modes may introduce epistemic uncertainty by omitting higher-order modes that influence structural behaviour. Furthermore, measurement noise in EMA affects the accuracy of the identified modal parameters, such as natural frequencies, damping ratio, and mode shapes. These issues can be mitigated by incorporating more modes, refining experimental techniques, improving signal processing methods, and the use of effective system identification tools. In the case of structures with inherent variability in their mechanical properties, such as wood, Uncertainty Quantification (UQ) is essential to assess how uncertainties propagate through their FE models and affect their associated predictions, thus enhancing confidence in simulation-based decisions. The following sections present strategies for UQ using probabilistic and stochastic processes, focussing on uncertainty propagation in FE models and quantifying the influence of input uncertainties on output variability.

6.1 Probabilistic modelling and sampling

The variability and randomness in the mechanical properties of CLT can be modelled using the observed mechanical properties determined through model updating. Using, for example, the procedure in Chapter 5. For probabilistic modelling, Gaussian processes (GPs) can be used to obtain a full posterior distribution over the mechanical properties using the Radial Basis Function (RBF). In GP, the observed data (denoted by \mathbf{x}_1) and the new (predicted) data points (denoted by \mathbf{x}_2) are assumed to be jointly Gaussian. Hence, their joint distribution can be formulated as follows.

$$\begin{Bmatrix} \mathbf{x}_1 \\ \mathbf{x}_2 \end{Bmatrix} \sim \mathcal{N} \left(\begin{Bmatrix} \boldsymbol{\mu}_1 \\ \boldsymbol{\mu}_2 \end{Bmatrix}, \begin{bmatrix} \boldsymbol{\Sigma}_{11} & \boldsymbol{\Sigma}_{12} \\ \boldsymbol{\Sigma}_{21} & \boldsymbol{\Sigma}_{22} \end{bmatrix} \right), \quad (6.1)$$

where $\boldsymbol{\mu}$ and $\boldsymbol{\Sigma}$ denote the mean vector and covariance matrix, respectively. The conditional probability of new random variables using observed data from (6.1) can be expressed as:

$$p(\boldsymbol{\mu}_2 \mid \boldsymbol{\mu}_1, \mathbf{x}_1, \mathbf{x}_2) \sim \mathcal{N}(\boldsymbol{\mu}_{2|1}, \boldsymbol{\Sigma}_{2|1}), \quad (6.2)$$

with

$$\boldsymbol{\mu}_{2|1} = \boldsymbol{\Sigma}_{21} \boldsymbol{\Sigma}_{11}^{-1} \mathbf{x}_1, \quad (6.3a)$$

$$\boldsymbol{\Sigma}_{2|1} = \boldsymbol{\Sigma}_{22} - \boldsymbol{\Sigma}_{21} \boldsymbol{\Sigma}_{11}^{-1} \boldsymbol{\Sigma}_{12}. \quad (6.3b)$$

The covariance matrices used to compute the conditional probability above can be simply determined from the RBF function,

$$k(x_1, x_2) = \exp \left(-\frac{1}{2l^2} \|x_1 - x_2\|^2 \right), \quad (6.4)$$

with l being the length scale which controls the smoothness of the distribution, and $\|x_1 - x_2\|$ is the Euclidean distance between two points [131–133].

Additional sampling methods comprise stochastic sampling of the mechanical properties using the observed mechanical properties determined from model updating. The stochastic sampling methods used in Paper III comprise Latin Hypercube Sampling (LHS) [134–136] and Monte Carlo (MC) sampling [137, 138]. These methods can be used with the minimum and maximum bounds of the observed mechanical properties obtained from (5.6) in Paper II to describe the stochastic variation in the mechanical properties.

6.2 Uncertainty propagation

The model parameters obtained from the statistical modelling in the previous section can be propagated into the FE model to determine the degree of uncertainty in their corresponding output. In Paper III, the outputs are selected as natural frequencies and vibration modes, which results in the following model:

$$\mathbf{y}^{(k)}(\boldsymbol{\theta}) = \left(\left[\mathbf{K}^{(k)}(\boldsymbol{\theta}) - \omega_j^{(k)^2}(\boldsymbol{\theta}) \mathbf{M}^{(k)}(\boldsymbol{\theta}) \right] \boldsymbol{\psi}_j^{(k)}(\boldsymbol{\theta}) = \mathbf{0} \right), \quad j = 1, 2, \dots, N_j, \quad (6.5)$$

where the subscript j denotes the number of eigensolutions and the superscript k denotes quantities associated with k th subset of model inputs $\theta_i \in \{1, 2, \dots, p\}$. The expression in (6.5) can be simply denoted $\mathcal{M}(\boldsymbol{\theta})$, which for a set of input model parameters produces outputs that comprise the natural frequencies and vibration modes,

$$\mathbf{y}^{(k)}(\boldsymbol{\theta}) = \{\omega_1^{(k)}(\boldsymbol{\theta}), \omega_2^{(k)}(\boldsymbol{\theta}), \dots, \omega_{N_j}^{(k)}(\boldsymbol{\theta}); \boldsymbol{\psi}_1^{(k)}(\boldsymbol{\theta}), \boldsymbol{\psi}_2^{(k)}(\boldsymbol{\theta}), \dots, \boldsymbol{\psi}_{N_j}^{(k)}(\boldsymbol{\theta})\}. \quad (6.6)$$

In Paper III, the input parameters $\boldsymbol{\theta}$ were selected to be the global density ρ , longitudinal Young's modulus E_l , interior shear moduli $G_{lt} = G_{lr}$, and the rolling shear modulus G_{rt} , which collectively represent the sensitive mechanical properties of CLT.

6.3 Uncertainty quantification

The analysis of input-output uncertainties in the model allows for quantifying the uncertainty in the mechanical properties used as input, as well as their associated natural frequencies and vibration modes. Natural frequencies can be identified using the MAC in (5.3), which compares the observed modes with their corresponding predicted counterparts. The identified natural frequencies can be categorised into bending and torsional natural frequencies, as in Paper III. Furthermore, the uncertainty in the output natural frequencies and their associated sensitive mechanical properties can be evaluated through their respective relative differences:

$$\text{Relative Difference} = \frac{\mathbf{x} - \mu(\mathbf{x})}{\mu(\mathbf{x})}, \quad (6.7)$$

where $\mu(\mathbf{x})$ denotes the mean value operator. The uncertainty in the mechanical properties generated using probabilistic and stochastic methods and their corresponding natural frequencies can be further evaluated using a univariate normal distribution, following:

$$\mathbf{x} \sim \mathcal{N}(\mu(\mathbf{x}), \sigma^2), \quad (6.8)$$

where $\mu(\mathbf{x})$ is the mean value and σ^2 is its associated variance. The probability density function (PDF) of a normalised Gaussian function is given by

$$p(\mathbf{x}|\mu(\mathbf{x}), \sigma) = \frac{1}{\sqrt{2\pi\sigma^2}} \exp\left(-\frac{(\mathbf{x} - \mu(\mathbf{x}))^2}{2\sigma^2}\right), \quad (6.9)$$

where \mathbf{x} represents the vector containing random variables. The PDF distribution can be summed to determine their Cumulative distribution function (CDF) using

$$F(\mathbf{x}) = \sum \frac{1}{\sqrt{2\pi\sigma^2}} \exp\left(-\frac{(\mathbf{x} - \mu(\mathbf{x}))^2}{2\sigma^2}\right). \quad (6.10)$$

6.4 Lower and upper bounds sensitivity

To determine the lower and upper bound sensitivity, the model $\mathcal{M}(\boldsymbol{\theta})$ in (6.5) can be fed with lower, mean, and upper bounds of the mechanical properties using:

$$\mathbf{y}^\pm(\boldsymbol{\theta}) = \mathcal{M}(\boldsymbol{\theta}^\pm), \quad (6.11a)$$

$$\mathbf{y}^\mu(\boldsymbol{\theta}) = \mathcal{M}(\boldsymbol{\theta}^\mu), \quad (6.11b)$$

where $\boldsymbol{\theta}^\mu \in \{\theta_1^\mu, \theta_2^\mu, \dots, \theta_{N_j}^\mu\}$ represents the mean values of the model parameters, while $\boldsymbol{\theta}^\pm \in \{\theta_1^-, \theta_2^-, \dots, \theta_{N_j}^-; \theta_1^+, \theta_2^+, \dots, \theta_{N_j}^+\}$ denotes the respective lower and upper parameter bounds, as summarised in Tab. 2 in Paper III. The corresponding outputs obtained from (6.11) are given by:

$$\begin{aligned} \mathbf{y}^\pm(\boldsymbol{\theta}) &= \{\omega_1^-, \omega_2^-, \dots, \omega_{N_j}^-, \psi_1^-, \psi_2^-, \dots, \psi_{N_j}^-; \\ &\quad \omega_1^+, \omega_2^+, \dots, \omega_{N_j}^+, \psi_1^+, \psi_2^+, \dots, \psi_{N_j}^+\}, \end{aligned} \quad (6.12a)$$

$$\mathbf{y}^\mu(\boldsymbol{\theta}) = \{\omega_1^\mu, \omega_2^\mu, \dots, \omega_{N_j}^\mu, \psi_1^\mu, \psi_2^\mu, \dots, \psi_{N_j}^\mu\}. \quad (6.12b)$$

To assess the sensitivity of the model outputs to parameter variations, each parameter was individually perturbed to its upper and lower limits, while all other parameters remained fixed at their mean values. The corresponding natural frequencies and mode shapes were subsequently computed. The sensitivity of the natural frequencies was quantified as follows:

$$S_{j,\omega}^\pm(\boldsymbol{\theta}) = \frac{\mathbf{y}_{j,\omega}^\pm(\boldsymbol{\theta}) - \mathbf{y}_{j,\omega}^\mu(\boldsymbol{\theta})}{\mathbf{y}_{j,\omega}^\mu(\boldsymbol{\theta})}, \quad (6.13)$$

whereas the sensitivity of the mode shapes was evaluated using the MAC in (5.3) as:

$$S_{j,\psi}^\pm(\boldsymbol{\theta}) = \frac{\text{MAC}(\boldsymbol{\psi}_j^\pm(\boldsymbol{\theta}), \boldsymbol{\psi}_j^\mu(\boldsymbol{\theta})) - \text{MAC}(\boldsymbol{\psi}_j^\mu(\boldsymbol{\theta}), \boldsymbol{\psi}_j^\mu(\boldsymbol{\theta}))}{\text{MAC}(\boldsymbol{\psi}_j^\mu(\boldsymbol{\theta}), \boldsymbol{\psi}_j^\mu(\boldsymbol{\theta}))}. \quad (6.14)$$

where $\psi_j^\mu(\boldsymbol{\theta})$, $\psi_j^-(\boldsymbol{\theta})$, and $\psi_j^+(\boldsymbol{\theta})$ correspond to the numerically computed mode shapes associated with the mean, lower, and upper bounds of the mechanical properties. In Paper III, the sensitivity analysis performed in (6.13) and (6.14) is performed for all j , encompassing six bending, torsional, and out-of-plane bending modes. However, only extremal values (minimum and maximum) were used to quantify the uncertainty in the results.

Chapter 7

Component-Mode Synthesis

Component Mode Synthesis (CMS) or Substructure Coupling for Dynamic Analyses represents a distinct category of reduced-order modelling within the field of computational dynamics. The application of FE discretisation to the differential equations governing physical laws facilitates the predictive modelling of dynamic systems, as explored in Chapter 3. This process results in a set of algebraic equations of motion that are systematically assembled into global system matrices. For complex structures with many natural components, the global system matrices can result in a large number of equations. In predictive computational dynamics, the response of a system is often solved in the time or frequency domains. Consequently, system equations must be solved across a domain spectrum, which introduces a significant computational burden and increases the demand for computational resources. In the development of industrial products, subcomponents of a structure are often designed and developed in different divisions. Therefore, before analysing the global system, it is essential to enable the independent development and analysis of individual components. Once a component is fully developed, it can be coupled with others, allowing the system to be analysed at a global level. Driven by computational challenges in structural dynamics, Guyan [47] and Irons [48] developed the static condensation method to simplify equations of motion by neglecting inertia terms. Hurty published several reports on the use of CMS with fixed interface modes for substructure coupling [45, 46]. In his approach, Hurty accounted for the neglected inertia terms in static condensation with a set of dynamic modes. A simplification of Hurty's work for substructure coupling with reduced interior dynamics was later presented in 1968 by Craig and Bampton [49], often referred to as the Craig-Bampton (CB) method. In 2001, Castanie et al. [50] introduced a system-level interface reduction technique that considered the decoupled characteristics of the CB

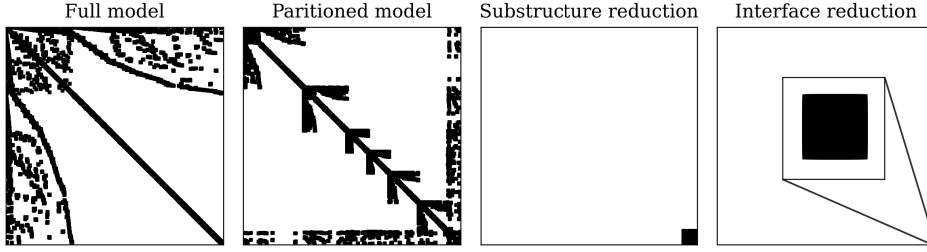


Figure 7.1: Illustration of reduction process from the full model to interface reduction in the CMS domain. The black dots denote numbers associated with DOFs in the system matrix. The presented data is associated with the Stiffened steel plate example in Paper IV.

stiffness matrix using characteristic constraint (CC) modes. A visual illustration of the reduction process can be found in Fig. 7.1.

The precision of the CMS method, specifically the CB method, was further improved in [139] by adding residual modes, resulting in the Enhanced Craig-Bampton (ECB) method. The system matrices generated by the ECB method lead to coupled stiffness, in contrast to the CB method. Therefore, when applying interface reduction to the ECB system matrices, this coupling must be accounted for to maintain the accuracy of the reduced system. Consequently, Paper IV introduces a coupled system-level interface reduction technique to further reduce the system matrices generated by the ECB method. This chapter provides an overview of substructure coupling and reduced-order modelling and presents the interface reduction technique discussed in Paper IV.

7.1 Substructure coupling in the physical domain

The system matrices derived for each subcomponent of a structure can be coupled in the physical domain using primal and dual assembly methods. Primal assembly allows for the coupling of substructures through primal unknowns, specifically the interface displacement fields, whereas dual assembly achieves coupling by enforcing interface force equilibrium. In this section, substructures are coupled using primal assembly, while for dual assembly, the reader is referred to the works of Rixen [140] and de Klerk et al. [141].

To facilitate primal coupling, the substructure system matrices and primal unknowns are decomposed into interior and boundary regions as:

$$\begin{bmatrix} \mathbf{M}_{ii}^{(s)} & \mathbf{M}_{ib}^{(s)} \\ \mathbf{M}_{bi}^{(s)} & \mathbf{M}_{bb}^{(s)} \end{bmatrix} \begin{Bmatrix} \ddot{\mathbf{u}}_i^{(s)} \\ \ddot{\mathbf{u}}_b^{(s)} \end{Bmatrix} + \begin{bmatrix} \mathbf{K}_{ii}^{(s)} & \mathbf{K}_{ib}^{(s)} \\ \mathbf{K}_{bi}^{(s)} & \mathbf{K}_{bb}^{(s)} \end{bmatrix} \begin{Bmatrix} \mathbf{u}_i^{(s)} \\ \mathbf{u}_b^{(s)} \end{Bmatrix} = \begin{Bmatrix} \mathbf{0}_i \\ \mathbf{p}_b^{(s)} \end{Bmatrix}, \quad (7.1)$$

where the indices i and b denote the interior and boundary regions, respectively, and the superscript s denotes the substructure. In the expression above, all loaded degrees of freedom (DOFs) are treated as boundary DOFs. The substructure equations of motion in (7.1) for all substructures can be expressed in a block diagonal format as:

$$\begin{aligned}\check{\mathbf{M}} &= \text{diag}(\mathbf{M}^{(1)}, \dots, \mathbf{M}^{(N_s)}) = \begin{bmatrix} \mathbf{M}^{(1)} & & \\ & \ddots & \\ & & \mathbf{M}^{(N_s)} \end{bmatrix}, \\ \check{\mathbf{K}} &= \text{diag}(\mathbf{K}^{(1)}, \dots, \mathbf{K}^{(N_s)}), \quad \check{\mathbf{p}} = \begin{Bmatrix} \mathbf{p}^{(1)} \\ \vdots \\ \mathbf{p}^{(N_s)} \end{Bmatrix},\end{aligned}\tag{7.2}$$

where N_s denotes the total number of substructures to be coupled. To ensure interface compatibility between the assembled substructures, a localisation Boolean matrix \mathbf{L} is used:

$$\mathbf{u}^{(s)} = \mathbf{L}^{(s)} \mathbf{u}_g,\tag{7.3}$$

where $\mathbf{L}^{(s)}$ is derived for each substructure to recover the substructure displacement field $\mathbf{u}^{(s)}$ from the coupled global displacement field \mathbf{u}_g . Using this Boolean operator, the substructures in (7.2) can be coupled at their interfaces as follows:

$$\mathbf{M}_g = \mathbf{L}^T \check{\mathbf{M}} \mathbf{L} = \begin{bmatrix} \mathbf{M}_{ii} & \mathbf{M}_{ib} \\ \mathbf{M}_{bi} & \mathbf{M}_{bb} \end{bmatrix},\tag{7.4a}$$

$$\mathbf{K}_g = \mathbf{L}^T \check{\mathbf{K}} \mathbf{L} = \begin{bmatrix} \mathbf{K}_{ii} & \mathbf{K}_{ib} \\ \mathbf{K}_{bi} & \mathbf{K}_{bb} \end{bmatrix},\tag{7.4b}$$

$$\mathbf{p}_g = \mathbf{L}^T \check{\mathbf{p}} = \begin{Bmatrix} \mathbf{p}_i \\ \mathbf{p}_b \end{Bmatrix},\tag{7.4c}$$

where \mathbf{M}_g , \mathbf{K}_g , and \mathbf{p}_g denote the coupled global mass matrix, stiffness matrix, and force vector, respectively. The total number of interface DOFs in the global system is fewer than the total number of interface DOFs associated with the individual substructures, due to interface compatibility. In (7.4), the substructure Boolean matrices are assembled into a global matrix. For details on constructing the Boolean matrix, the reader is referred to the work of de Klerk et al. [141]. The coupled system in (7.4) results in the following equations of motion

$$\mathbf{M}_g \ddot{\mathbf{u}}_g + \mathbf{K}_g \mathbf{u}_g = \mathbf{p}_g.\tag{7.5}$$

7.2 Interior dynamics reduction

The interior partition of the substructure system matrices in (7.1) can be reduced using the CB method before the primal assembly in (7.4). This reduction combines static condensation, as introduced by Guyan [47] and Irons [48], with the synthesis of dynamic modes constrained by fixed interfaces [45, 46, 49]. The interior vibration modes of a substructure system can be derived from an eigenvalue analysis,

$$\left(\mathbf{K}_{ii}^{(s)} - \omega_{i,j}^{(s)2} \mathbf{M}_{ii}^{(s)} \right) \boldsymbol{\psi}_{i,j}^{(s)} = \mathbf{0}, \quad j = 1, 2, \dots, N_{i,d}^{(s)}, \quad (7.6)$$

where $\omega_{i,j}^{(s)2}$ and $\boldsymbol{\psi}_{i,j}^{(s)}$ denote the j th interior eigenvalue and its associated conjugate mode, and $N_{i,d}^{(s)}$ is the total number of eigensolution. The interior modes in (7.6) are selected within the lower frequency spectrum, or selected using mode selection techniques [142]. The modes in (7.6) can be collected in a mode matrix with their interface partition set to zero as:

$$\boldsymbol{\Psi}_{i,d}^{(s)} = \begin{bmatrix} \boldsymbol{\psi}_{i,1}^{(s)} & \boldsymbol{\psi}_{i,2}^{(s)} & \boldsymbol{\psi}_{i,3}^{(s)} & \dots & \boldsymbol{\psi}_{i,d}^{(s)} \\ \mathbf{0} & \mathbf{0} & \mathbf{0} & \dots & \mathbf{0} \end{bmatrix}. \quad (7.7)$$

The static condensation part of the CB method can be derived simply by neglecting the inertia terms of the first row in (7.1). A relation between the interior displacement partition and boundary displacement part can be derived as:

$$\mathbf{u}_i = -\mathbf{K}_{ii}^{(s)-1} \mathbf{K}_{ib}^{(s)} \mathbf{u}_b. \quad (7.8)$$

The relation above can be expressed in matrix format as:

$$\begin{Bmatrix} \mathbf{u}_i \\ \mathbf{u}_b \end{Bmatrix}^{(s)} \approx \begin{bmatrix} -\mathbf{K}_{ii}^{(s)-1} \mathbf{K}_{ib}^{(s)} \\ \mathbf{I}^{(s)} \end{bmatrix} \mathbf{u}_b^{(s)}. \quad (7.9)$$

A combination of (7.7) and (7.9) results in the CB transformation matrix,

$$\mathbf{u}^{(s)} \approx \bar{\mathbf{T}}_{\text{CB}}^{(s)} \begin{Bmatrix} \boldsymbol{\eta}_{i,d} \\ \mathbf{u}_b \end{Bmatrix}, \quad \bar{\mathbf{T}}_{\text{CB}}^{(s)} = \begin{bmatrix} \boldsymbol{\Psi}_{i,d}^{(s)} & -\mathbf{K}_{ii}^{(s)-1} \mathbf{K}_{ib}^{(s)} \\ \mathbf{0} & \mathbf{I}_{bb}^{(s)} \end{bmatrix}. \quad (7.10)$$

where $\boldsymbol{\eta}_{i,d}$ contains generalised coordinates associated with the retained modes in (7.6).

Substituting the relation in (7.10) into (7.1) and pre-multiplying by $\bar{\mathbf{T}}_{\text{CB}}^{(s)\top}$ truncates the interior dynamics of the substructure equations of motion to:

$$\widehat{\mathbf{M}}^{(s)} \widehat{\ddot{\mathbf{u}}} + \widehat{\mathbf{K}}^{(s)} \widehat{\mathbf{u}} = \widehat{\mathbf{p}}^{(s)}, \quad (7.11)$$

with

$$\widehat{\mathbf{M}}^{(s)} = \bar{\mathbf{T}}_{\text{CB}}^{(s)\top} \mathbf{M}^{(s)} \bar{\mathbf{T}}_{\text{CB}}^{(s)} = \begin{bmatrix} \hat{\mathbf{I}}_{ii}^{(s)} & \hat{\mathbf{M}}_{ib}^{(s)} \\ \hat{\mathbf{M}}_{bi}^{(s)} & \hat{\mathbf{M}}_{bb}^{(s)} \end{bmatrix} \quad (7.12a)$$

$$\widehat{\mathbf{K}}^{(s)} = \bar{\mathbf{T}}_{\text{CB}}^{(s)\top} \mathbf{K}^{(s)} \bar{\mathbf{T}}_{\text{CB}}^{(s)} = \begin{bmatrix} \hat{\mathbf{K}}_{ii}^{(s)} & \mathbf{0}_{ib}^{(s)} \\ \mathbf{0}_{bi}^{(s)} & \hat{\mathbf{K}}_{bb}^{(s)} \end{bmatrix}, \quad (7.12b)$$

$$\widehat{\mathbf{p}}^{(s)} = \bar{\mathbf{T}}_{\text{CB}}^{(s)\top} \mathbf{p}^{(s)} = \begin{Bmatrix} \hat{\mathbf{0}}_i^{(s)} \\ \hat{\mathbf{p}}_b^{(s)} \end{Bmatrix}, \quad (7.12c)$$

with the decoupled characteristics of CB stiffness are achieved through the assumption that the boundary DOFs respond quasi-statically to the interior DOFs as seen in (7.8). The substructure equations with reduced interior dynamics can be coupled similarly to (7.4) and derive the reduced equations of motion

$$\widehat{\mathbf{M}}_g \widehat{\ddot{\mathbf{u}}}_g + \widehat{\mathbf{K}}_g \widehat{\mathbf{u}}_g = \widehat{\mathbf{p}}_g. \quad (7.13)$$

The CB transformation matrix in (7.10) only considers a set of dominant modes of vibration, while disregarding the residual modes. To improve the accuracy of the reduced matrices, residual modes can be added to the CB transformation matrix in (7.10), resulting in

$$\mathbf{u}^{(s)} \approx \bar{\mathbf{T}}_{\text{ECB}}^{(s)} \mathbf{u}_b^{(s)}, \quad \bar{\mathbf{T}}_{\text{ECB}}^{(s)} = \left[\bar{\mathbf{T}}_{\text{CB}}^{(s)} + \bar{\mathbf{T}}_{\text{R}}^{(s)} \right] \quad (7.14)$$

with

$$\bar{\mathbf{T}}_{\text{R}}^{(s)} = \begin{bmatrix} \mathbf{0} & \mathbf{F}_{rs}^{(s)} \left[-\mathbf{M}_{ii}^{(s)} \mathbf{K}_{ii}^{(s)-1} \mathbf{K}_{ib}^{(s)} + \mathbf{M}_{ib}^{(s)} \right] \\ \mathbf{0} & \mathbf{0} \end{bmatrix} \bar{\mathbf{M}}_{\text{CB}}^{(s)-1} \bar{\mathbf{K}}_{\text{CB}}^{(s)}, \quad (7.15a)$$

$$\mathbf{F}_{rs}^{(s)} = \mathbf{K}_{ii}^{(s)} - \boldsymbol{\Psi}_{i,d}^{(s)} \boldsymbol{\Lambda}_{i,d}^{(s)-1} \boldsymbol{\Psi}_{i,d}^{(s)\top}, \quad \boldsymbol{\Lambda}_{i,d}^{(s)} = \boldsymbol{\Psi}_{i,d}^{(s)\top} \mathbf{K}_{ii}^{(s)} \boldsymbol{\Psi}_{i,d}^{(s)}, \quad (7.15b)$$

where $\mathbf{F}_{rs}^{(s)}$ represents the residual modal effect and $\boldsymbol{\Lambda}_{i,d}^{(s)}$ contains interior eigenvalues. Further derivations concerning the residual mode compensation can be found in [139].

With substitution of (7.14) into (7.1) and premultiplication of $\bar{\mathbf{T}}_{\text{ECB}}^{(s)\top}$, the internal dynamics of the substructure equations of motion can be truncated to

$$\bar{\mathbf{M}}^{(s)} \ddot{\bar{\mathbf{u}}} + \bar{\mathbf{K}}^{(s)} \bar{\mathbf{u}} = \bar{\mathbf{p}}^{(s)}, \quad (7.16)$$

with

$$\bar{\mathbf{M}}^{(s)} = \bar{\mathbf{T}}_{\text{ECB}}^{(s)\top} \mathbf{M}^{(s)} \bar{\mathbf{T}}_{\text{ECB}}^{(s)} = \begin{bmatrix} \bar{\mathbf{I}}_{ii}^{(s)} & \bar{\mathbf{M}}_{ib}^{(s)} \\ \bar{\mathbf{M}}_{bi}^{(s)} & \bar{\mathbf{M}}_{bb}^{(s)} \end{bmatrix} \quad (7.17a)$$

$$\bar{\mathbf{K}}^{(s)} = \bar{\mathbf{T}}_{\text{ECB}}^{(s)\top} \mathbf{K}^{(s)} \bar{\mathbf{T}}_{\text{ECB}}^{(s)} = \begin{bmatrix} \bar{\mathbf{K}}_{ii}^{(s)} & \bar{\mathbf{K}}_{ib}^{(s)} \\ \bar{\mathbf{K}}_{bi}^{(s)} & \bar{\mathbf{K}}_{bb}^{(s)} \end{bmatrix}, \quad (7.17b)$$

$$\bar{\mathbf{p}}^{(s)} = \bar{\mathbf{T}}_{\text{ECB}}^{(s)\top} \mathbf{p}^{(s)} = \begin{Bmatrix} \bar{\mathbf{0}}_i^{(s)} \\ \bar{\mathbf{p}}_b^{(s)} \end{Bmatrix}. \quad (7.17c)$$

The expression in (7.17) indicates that due to the addition of the residual mode effect to the quasi-static condensation part of (7.10) in (7.14), the stiffness matrix using ECB becomes coupled.

The substructure system matrices with reduced interior dynamics can be coupled using the primal assembly approach using (7.2) through (7.5). Using ECB to truncate interior dynamics of substructures, the coupled global equations of motion results in

$$\bar{\mathbf{M}}_g \ddot{\bar{\mathbf{u}}}_g + \bar{\mathbf{K}}_g \bar{\mathbf{u}}_g = \bar{\mathbf{p}}_g. \quad (7.18)$$

7.3 Interface dynamics reduction

In the previous section, the interior dynamics of each substructure was reduced. Subsequently, the substructures were coupled at their interfaces using the displacement compatibility approach, known as primal assembly. For structures with many coupled natural components, the system-level equations of motion can still contain many equations. Therefore, further reduction of interface equations was proposed by Castanie et al. [50] using modal truncation of the interface considering the decoupled characteristics of the interior and interface stiffness equations. This assumption is accurate for the original CB method due to its decoupled stiffness resulting from the quasi-static assumption and low-frequency vibration. Since the use of ECB results in a coupled substructure stiffness matrix, the use of modal truncation of the interface results in inaccurate system matrices. Hence, Paper IV introduces a coupled system-level interface reduction technique that provides further reduction of the interface equations with enhanced accuracy.

7.3.1 Classical interface reduction

Taking into account the decoupled characteristics of the stiffness matrix (7.12) as the CB reduction produces, the interface equations can be further reduced using a simple modal truncation [50]. Hence, the global interface displacement vector can be approximated as:

$$\mathbf{u}_b \approx \Psi_{b,d} \boldsymbol{\eta}_{b,d}, \quad (7.19)$$

where $\Psi_{b,d}$ contains columns of fixed-interior interface modes and $\boldsymbol{\eta}_{b,d}$ is their associated generalised coordinates. The fixed interior modes can be computed from an eigenvalue analysis by restraining all interior equations as:

$$(\mathbf{K}_{bb} - \omega_{b,j}^2 \mathbf{M}_{bb}) \boldsymbol{\psi}_{b,j} = \mathbf{0}, \quad j = 1, 2, \dots, N_{b,d}, \quad (7.20)$$

with $N_{b,d} \ll N_b$ indicating the total number of retained interface modes (with N_b being the total number of interface modes). Since the interface reduction operation is performed on the global system for which the interior dynamics are reduced, the global displacement vector in the field is reduced to

$$\bar{\mathbf{u}}_g \approx \bar{\mathbf{T}}_{\text{IR1}} \begin{Bmatrix} \boldsymbol{\eta}_{i,d} \\ \boldsymbol{\eta}_{b,d} \end{Bmatrix}, \quad \bar{\mathbf{T}}_{\text{IR1}} = \begin{bmatrix} \mathbf{I}_{i,d} & \mathbf{0}_{i,d} \\ \mathbf{0}_{b,d} & \Psi_{b,d} \end{bmatrix}, \quad (7.21)$$

where $\boldsymbol{\eta}_{i,d}$ and $\boldsymbol{\eta}_{b,d}$, respectively, contain respectively generalised coordinates associated with retained dominant interior and interface modes, and $\Psi_{b,d}$ contains columns of the interface modes computed in (7.20).

The relation in (7.21) can be substituted into the global equation of motion with truncated interior dynamics in (7.13) and pre-multiplied with $\bar{\mathbf{T}}_{\text{IR1}}^\top$ to further reduce

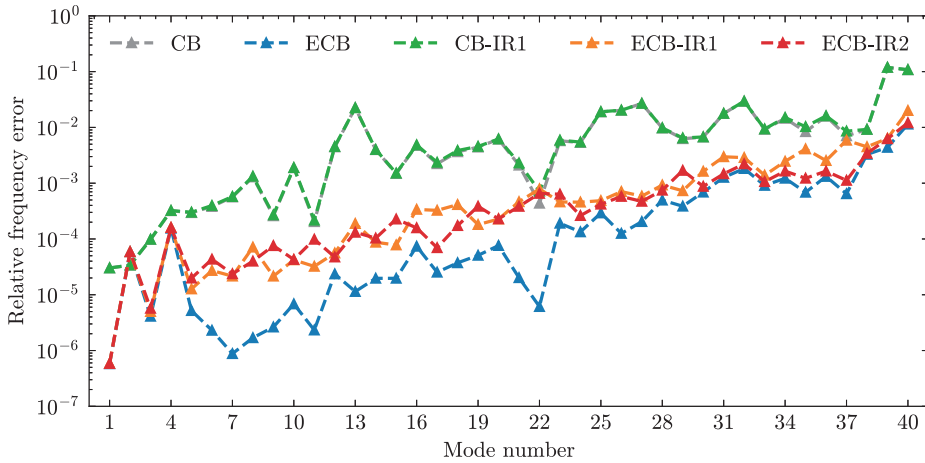


Figure 7.2: Relative frequency error with respect to the full model for the composite CLT plate in Paper IV.

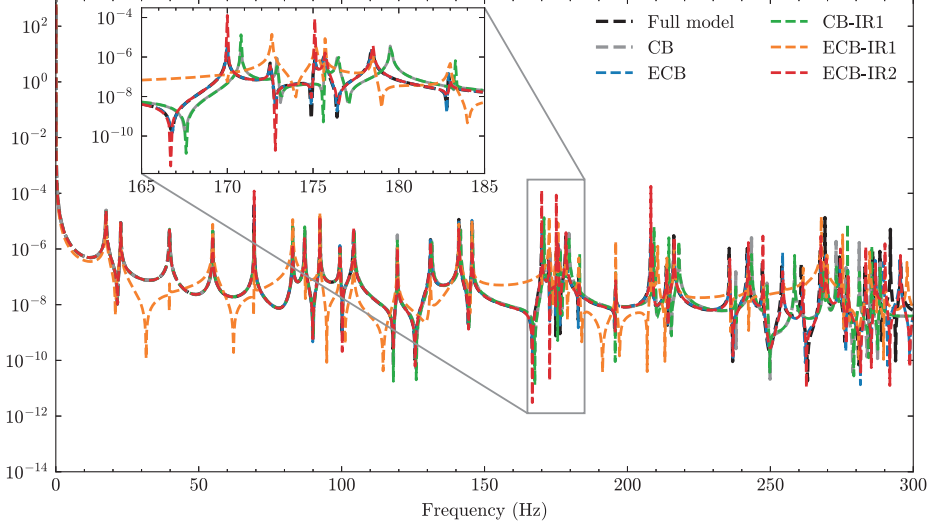


Figure 7.3: Transfer functions associated with the composite CLT plate in Paper IV.

the system matrices to

$$\widehat{\mathbf{M}}_g \widehat{\ddot{\mathbf{u}}}_g + \widehat{\mathbf{K}}_g \widehat{\mathbf{u}}_g = \widehat{\mathbf{p}}_g \quad (7.22)$$

with

$$\widehat{\mathbf{M}}_g = \widehat{\mathbf{T}}_{\text{IR1}}^\top \widehat{\mathbf{M}}_g \widehat{\mathbf{T}}_{\text{IR1}}, \quad \widehat{\mathbf{K}}_g = \widehat{\mathbf{T}}_{\text{IR1}}^\top \widehat{\mathbf{K}}_g \widehat{\mathbf{T}}_{\text{IR1}}, \quad \widehat{\mathbf{p}}_g = \widehat{\mathbf{T}}_{\text{IR1}}^\top \widehat{\mathbf{p}}_g. \quad (7.23)$$

In cases where the stiffness is coupled, this approach results in system matrices with reduced accuracy. This is particularly apparent in the transfer functions; see Fig. 7.3 (ECB-IR1).

7.3.2 Coupled interface reduction

Considering coupled characteristics of the stiffness matrix under the ECB method, the boundary portion of the global system matrices in (7.5) can be approximated using

$$\mathbf{u}_b \approx \mathbf{\Xi} \boldsymbol{\eta}_{i,d} + \boldsymbol{\Psi}_{b,d} \boldsymbol{\eta}_{b,d}, \quad (7.24)$$

where $\mathbf{\Xi}$ is a constraint mode matrix projecting interior equations onto the interface, and $\boldsymbol{\eta}_{i,d}$ and $\boldsymbol{\eta}_{b,d}$ contain respectively generalised coordinates associated with retained dominant interior and boundary modes. The mode matrix $\boldsymbol{\Psi}_{b,d}$ contains interface modes, which can be computed using (7.20).

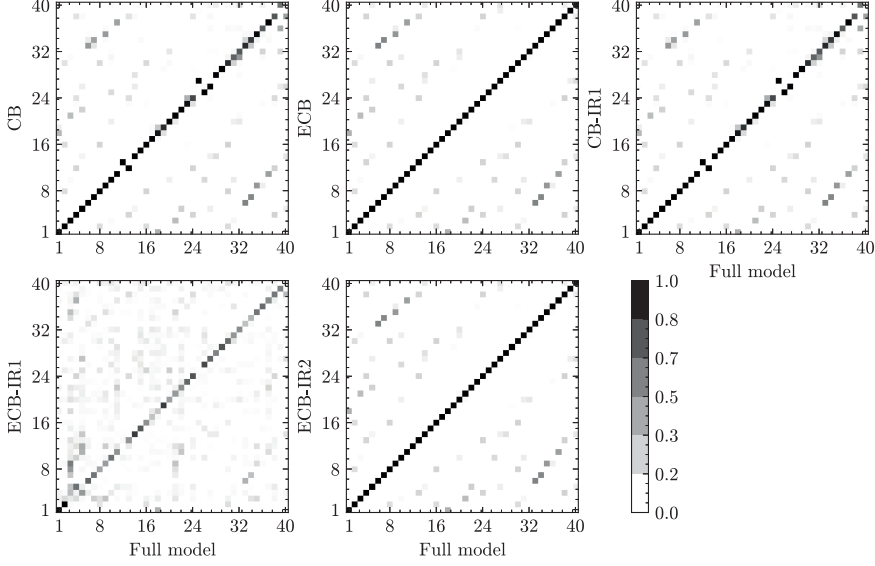


Figure 7.4: Modal Assurance Criterion comparing 40 flexible modes of the composite CLT plate example in Paper IV.

With the expressions in (7.24) and (7.20) the displacement field of the global system using ECB can be further reduced to

$$\bar{\mathbf{u}}_g \approx \bar{\mathbf{T}}_{\text{IR}2} \begin{Bmatrix} \eta_{i,d} \\ \eta_{b,d} \end{Bmatrix}, \quad \bar{\mathbf{T}}_{\text{IR}2} = \begin{bmatrix} \mathbf{I}_{i,d} & \mathbf{0}_{i,d} \\ \bar{\boldsymbol{\Xi}}_{b,d} & \bar{\boldsymbol{\Psi}}_{b,d} \end{bmatrix}, \quad \bar{\boldsymbol{\Xi}}_{b,d} = -\bar{\mathbf{K}}_{bb}^{-1} \bar{\mathbf{K}}_{bi}, \quad (7.25)$$

where $\bar{\mathbf{K}}_{bb}$ and $\bar{\mathbf{K}}_{bi}$ are components of (7.18).

The relation in (7.25) can be substituted into the global equation of motion with truncated interior dynamics in (7.18) and pre-multiplied with $\bar{\mathbf{T}}_{\text{IR}2}^\top$ to further reduce the system matrices to

$$\bar{\bar{\mathbf{M}}}_g \ddot{\bar{\mathbf{u}}}_g + \bar{\bar{\mathbf{K}}}_g \bar{\mathbf{u}}_g = \bar{\bar{\mathbf{p}}}_g \quad (7.26)$$

with

$$\bar{\bar{\mathbf{M}}}_g = \bar{\mathbf{T}}_{\text{IR}2}^\top \bar{\mathbf{M}}_g \bar{\mathbf{T}}_{\text{IR}2}, \quad \bar{\bar{\mathbf{K}}}_g = \bar{\mathbf{T}}_{\text{IR}2}^\top \bar{\mathbf{K}}_g \bar{\mathbf{T}}_{\text{IR}2}, \quad \bar{\bar{\mathbf{p}}}_g = \bar{\mathbf{T}}_{\text{IR}2}^\top \bar{\mathbf{p}}_g. \quad (7.27)$$

Comparison of resonance frequencies in Fig. 7.2, transfer functions in Fig. 7.3, and modes in Fig. 7.4 indicate that the coupled component in the interface reduction matrix enhances the accuracy of the reduced system matrices. In particular, in the prediction of the transfer functions and vibration modes. Further mathematical derivations, implementation details, and application examples can be found in Paper IV.

Chapter 8

Conclusions and recommendations

8.1 Conclusions and contributions

In this thesis, both computational and experimental strategies have been developed to analyse dynamic structures, with a particular focus on Cross-Laminated Timber (CLT). As the world faces climate challenges, the need to conserve materials has led to the design of more slender structures, which are more susceptible to vibrations compared to heavier ones. In addition, wood, as a natural material, exhibits variability in its mechanical behaviour. Quantifying this variability is crucial for developing robust computational methods. Hence, the findings of this thesis contribute to the fields of structural dynamics and sustainable building practices.

In Paper I, an experimental approach was developed to determine the variability in transfer functions and modal characteristics of CLT by testing nominally identical CLT substructures. These modal characteristics were then used as a reference to develop a derivative-free model updating framework in Paper II. This framework was designed to tune predictive results towards measurements, thereby identifying key sensitive mechanical properties of these substructures along with their variability. The identified mechanical properties were further used to generate probabilistic and stochastic samples, which were subsequently propagated back to the predictive model in Paper III. This process formulated an uncertainty quantification procedure to assess the extent to which uncertain mechanical properties influence the modal characteristics of CLT. Finally, in Paper IV, a coupled interface reduction technique was developed to enhance the computational efficiency of systems with truncated interior dynamics in the simulation of dynamic systems.

The implementation and presentation of the work presented here were carried out

primarily using Python and its associated numerical and visualisation packages. The key contributions of the work presented herein include, but are not limited to:

- Evaluation and determination of variability in the transfer functions, modal parameters, and sensitive mechanical properties of CLT using nominally identical CLT substructures (Papers I and II).
- A derivative-free computational framework for inverse parameter identification and model updating of CLT models using EMA as reference (Paper II).
- An uncertainty quantification procedure for quantification of the degree to which input uncertainty in mechanical properties results in output variability in modal parameters of CLT (Paper III).
- Development of a coupled interface reduction technique for further reduction of dynamic system matrices with truncated interior dynamics in the presence of stiffness coupling (Paper IV).

8.2 Recommendations

Based on the findings and conclusions drawn from this thesis, several recommendations are proposed for future work and practical applications. Firstly, it is recommended that further research be conducted on the variability of CLT to explore the variability in transfer functions and modal parameters across a broader range of substructures. The results of such research can be used to train neural network models, which can facilitate efficient and computationally inexpensive analysis. This work has already been initiated by the author. Secondly, the derivative-free computational framework for inverse parameter identification and model updating can be extended to encompass the model updating of coupled systems, such as vibroacoustic, thermoelastic, and electromechanical systems. Additionally, this framework can be adapted for structural health monitoring of structures subjected to dynamic loading, including vibrations and radiation. Furthermore, future research should focus on improving the uncertainty quantification procedure to account for a wider range of input uncertainties. This includes investigating various mechanical properties and their impact on the variability of modal parameters. The coupled interface reduction technique should be further extended to free-interface systems, such as the dual Craig-Bampton method. Moreover, extending interface reduction to coupled systems, including vibroacoustic, thermo-mechanical, and electromechanical models, would significantly advance the field of reduced-order modelling. These recommendations aim to build upon the current research, addressing its limitations and expanding its scope to enhance the understanding of dynamic systems and application of CLT in structural engineering.

References

- [1] JMW Brownjohn, Filipe Magalhaes, Elsa Caetano, and Alvaro Cunha. Ambient vibration re-testing and operational modal analysis of the humber bridge. *Engineering Structures*, 32(8):2003–2018, 2010.
- [2] Stana Živanović, Aleksandar Pavic, and Paul Reynolds. Finite element modelling and updating of a lively footbridge: The complete process. *Journal of Sound and Vibration*, 301(1-2):126–145, 2007.
- [3] Thai-Hoa Le and Luca Caracoglia. Modeling vortex-shedding effects for the stochastic response of tall buildings in non-synoptic winds. *Journal of Fluids and Structures*, 61:461–491, 2016.
- [4] MA Bezabeh, GT Bitsuamlak, M Popovski, and S Tesfamariam. Dynamic response of tall mass-timber buildings to wind excitation. *Journal of Structural Engineering*, 146(10):04020199, 2020.
- [5] Raymond L Bisplinghoff, Holt Ashley, and Robert L Halfman. *Aeroelasticity*. Courier Corporation, 2013.
- [6] Jing Wang, Dengge Jin, Chao Fan, Yanqiang Bi, Xinming Su, Guoqing Liu, and Zhihai Xiang. Predicting the on-orbit thermally induced vibration through the integrated numerical and experimental approach. *Acta Astronautica*, 192:341–350, 2022.
- [7] Martin Hansen. *Aerodynamics of wind turbines*. Routledge, 2015.
- [8] Subrata Chakrabarti. *Handbook of Offshore Engineering (2-volume set)*, volume 1. Elsevier, 2005.
- [9] Michel J Pettigrew and CE Taylor. Vibration analysis of shell-and-tube heat exchangers: an overview—part 1: flow, damping, fluidelastic instability. *Journal of fluids and structures*, 18(5):469–483, 2003.

- [10] MJ Pettigrew, LN Carlucci, CE Taylor, and NJ Fisher. Flow-induced vibration and related technologies in nuclear components. *Nuclear Engineering and Design*, 131(1):81–100, 1991.
- [11] MK Au-Yang and WH Connelly. A computerized method for flow-induced random vibration analysis of nuclear reactor internals. *Nuclear Engineering and Design*, 42(2):257–263, 1977.
- [12] Wensheng Zhao, Yanhui Li, Meixin Xue, Pengfei Wang, and Jin Jiang. Vibration analysis for failure detection in low pressure steam turbine blades in nuclear power plant. *Engineering Failure Analysis*, 84:11–24, 2018.
- [13] Stana Živanović, ALEKSANDAR Pavic, and Paul Reynolds. Vibration serviceability of footbridges under human-induced excitation: a literature review. *Journal of sound and vibration*, 279(1-2):1–74, 2005.
- [14] Yusuf Altintas. *Manufacturing automation: metal cutting mechanics, machine tool vibrations, and CNC design*. Cambridge university press, 2012.
- [15] Thomas Gillespie. *Fundamentals of vehicle dynamics*. SAE international, 2021.
- [16] Steven Lawrence Kramer. *Geotechnical earthquake engineering*. Pearson Education India, 1996.
- [17] David J Ewins. *Modal testing: theory, practice and application*. John Wiley & Sons, 2009.
- [18] Nuno Manuel Mendes Maia and Júlio Martins Montalvão e Silva. Theoretical and experimental modal analysis. (*No Title*), 1997.
- [19] In focus: Energy efficiency in buildings — commission.europa.eu. https://commission.europa.eu/news/focus-energy-efficiency-buildings-2020-02-17_en. [Accessed 03-09-2024].
- [20] Adel Younis and Ambrose Dodoo. Cross-laminated timber for building construction: A life-cycle-assessment overview. *Journal of Building Engineering*, 52:104482, 2022.
- [21] Angeliki Kylili and Paris A Fokaides. Policy trends for the sustainability assessment of construction materials: A review. *Sustainable Cities and Society*, 35:280–288, 2017.

- [22] Guillaume Habert, Sabbie A Miller, Vanderley M John, John L Provis, Aurélie Favier, Arpad Horvath, and Karen L Scrivener. Environmental impacts and decarbonization strategies in the cement and concrete industries. *Nature Reviews Earth & Environment*, 1(11):559–573, 2020.
- [23] Anton Steurer. *Developments in timber engineering: the Swiss contribution*. Birkhäuser, 2006.
- [24] Ambrose Dodoo. *Life cycle primary energy use and carbon emission of residential buildings*. PhD thesis, Mittuniversitetet, 2011.
- [25] Reinhard Brandner. Production and technology of cross laminated timber (CLT): A state-of-the-art report. In *Focus Solid Timber Solutions—European Conference on Cross Laminated Timber (CLT)*, pages 3–36. University of Bath, 2013. Focus Solid Timber Solutions—European Conference on Cross Laminated Timber (CLT), CLT ; Conference date: 21-05-2013 Through 22-05-2013.
- [26] Reinhard Brandner, Georg Flatscher, Andreas Ringhofer, Gerhard Schickhofer, and Alexandra Thiel. Cross laminated timber (CLT): overview and development. *European Journal of Wood and Wood Products*, 74:331–351, 2015.
- [27] Brad Douglas and Erol Karacabeyli. Clt handbook: Cross-laminated timber. *FPInnovations and Binational Softwood Lumber Council*, 2013.
- [28] Ario Ceccotti, Carmen Sandhaas, and Motoi Yasumura. Seismic behaviour of multistory cross-laminated timber buildings. In *Proceedings of the International Convention of Society of Wood Science and Technology and United Nations Economic Commission for Europe-Timber Committee*, pages 1–14, 2010.
- [29] Shiling Pei, John W van De Lindt, Marjan Popovski, Jeffrey W Berman, J Daniel Dolan, James Ricles, R Sause, H Blomgren, and Douglas R Rammer. Cross-laminated timber for seismic regions: Progress and challenges for research and implementation. *Journal of Structural Engineering*, 142(4):E2514001, 2016.
- [30] Sung-Jun Pang and Gi Young Jeong. Effects of combinations of lamina grade and thickness, and span-to-depth ratios on bending properties of cross-laminated timber (clt) floor. *Construction and Building Materials*, 222:142–151, 2019.
- [31] Dietrich Buck, Alice Wang, Olle Hagman, and Anders Gustafsson. Bending properties of cross laminated timber (clt) with a 45 alternating layer configuration. *BioResources*, 11(2):4633–4644, 2016.

- [32] TA Bui, M Oudjene, P Lardeur, M Khelifa, and Yann Rogaume. Towards experimental and numerical assessment of the vibrational serviceability comfort of adhesive free laminated timber beams and clt panels assembled using compressed wood dowels. *Engineering Structures*, 216:110586, 2020.
- [33] Zhongwei Guan, Adeayo Sotayo, Marc Oudjene, Imane El Houjeiri, Annette Harte, Sameer Mehra, Peer Haller, Siavash Namari, Ahmed Makradi, Salim Belouettar, et al. Development of adhesive free engineered wood products—towards adhesive free timber buildings. *Proc. WCTE*, pages 20–23, 2018.
- [34] Lei Han, Andreja Kutnar, Jakub Sandak, Iztok Šušteršič, and Dick Sandberg. Adhesive-and metal-free assembly techniques for prefabricated multi-layer engineered wood products: A review on wooden connectors. *Forests*, 14(2):311, 2023.
- [35] Fredrik Ljunggren. Innovative solutions to improved sound insulation of clt floors. *Developments in the Built Environment*, 13:100117, 2023.
- [36] Jakob Baader and Mario Fontana. Active vibration control of lightweight floor systems. *Procedia engineering*, 199:2772–2777, 2017.
- [37] Benjamin Bondsman and Andrew Peplow. Inverse parameter identification and model updating for cross-laminated timber substructures. *Journal of Building Engineering*, 95:110209, 2024.
- [38] Forest Products Laboratory (U.S.). *Wood Handbook: Wood as an Engineering Material*. Number 72 in Agriculture Handbook. U.S. Department of Agriculture, Forest Service, Forest Products Laboratory, Madison, WI, 1987.
- [39] David W Green, Jerrold E Winandy, and David E Kretschmann. Mechanical properties of wood. *Wood handbook: wood as an engineering material*. Madison, WI: USDA Forest Service, Forest Products Laboratory, 1999. *General technical report FPL; GTR-113: Pages 4.1-4.45*, 113, 1999.
- [40] Charles C Gerhards. Effect of moisture content and temperature on the mechanical properties of wood: an analysis of immediate effects. *Wood and Fiber Science*, pages 4–36, 1982.
- [41] Sigurdur Ormarsson. *Numerical analysis of moisture-related distortion in sawn timber*. PhD thesis, Chalmers University of Technology, Dep. of Structural Mech, 1999.
- [42] Vanessa Baño, Francisco Arriaga, and Manuel Guaita. Determination of the influence of size and position of knots on load capacity and stress distribution

- in timber beams of *pinus sylvestris* using finite element model. *Biosystems engineering*, 114(3):214–222, 2013.
- [43] Elke Mergny, Raquel Mateo, Miguel Esteban, Thierry Descamps, and Pierre Latteur. Influence of cracks on the stiffness of timber structural elements. In *Proceedings of the World conference on timber engineering, Vienna, Austria*, 2016.
 - [44] Andrey Nikolayevich Tikhonov. Solutions of ill-posed problems. *VH Winston and Sons*, 1977.
 - [45] Walter C Hurty. Dynamic analysis of structural systems using component modes. *AIAA journal*, 3(4):678–685, 1965.
 - [46] Walter C Hurty. Vibrations of structural systems by component mode synthesis. *Journal of the Engineering Mechanics Division*, 86(4):51–69, 1960.
 - [47] Robert J Guyan. Reduction of stiffness and mass matrices. *AIAA journal*, 3(2):380–380, 1965.
 - [48] Bruce Irons. Structural eigenvalue problems-elimination of unwanted variables. *AIAA journal*, 3(5):961–962, 1965.
 - [49] Roy R Craig Jr and Mervyn CC Bampton. Coupling of substructures for dynamic analyses. *AIAA journal*, 6(7):1313–1319, 1968.
 - [50] Matthew P Castanier, Yung-Chang Tan, and Christophe Pierre. Characteristic constraint modes for component mode synthesis. *AIAA journal*, 39(6):1182–1187, 2001.
 - [51] Michael H Ramage, Henry Burr ridge, Marta Busse-Wicher, George Fereday, Thomas Reynolds, Darshil U Shah, Guanglu Wu, Li Yu, Patrick Fleming, Danielle Densley-Tingley, et al. The wood from the trees: The use of timber in construction. *Renewable and sustainable energy reviews*, 68:333–359, 2017.
 - [52] Galina Churkina, Alan Organschi, Christopher PO Reyer, Andrew Ruff, Kira Vinke, Zhu Liu, Barbara K Reck, TE Graedel, and Hans Joachim Schellnhuber. Buildings as a global carbon sink. *Nature sustainability*, 3(4):269–276, 2020.
 - [53] Tobias Keplinger, Johannes Konnerth, Véronique Aguié-Béghin, Markus Rüggeberg, Notburga Gierlinger, and Ingo Burgert. A zoom into the nanoscale texture of secondary cell walls. *Plant Methods*, 10:1–7, 2014.
 - [54] John M Dinwoodie. *Timber: its nature and behaviour*. CRC Press, 2000.

- [55] Hongli Zhu, Wei Luo, Peter N Ciesielski, Zhiqiang Fang, JY Zhu, Gunnar Henriksson, Michael E Himmel, and Liangbing Hu. Wood-derived materials for green electronics, biological devices, and energy applications. *Chemical reviews*, 116(16):9305–9374, 2016.
- [56] Jianwei Song, Chaoji Chen, Shuze Zhu, Mingwei Zhu, Jiaqi Dai, Upamanyu Ray, Yiju Li, Yudi Kuang, Yongfeng Li, Nelson Quispe, et al. Processing bulk natural wood into a high-performance structural material. *Nature*, 554(7691):224–228, 2018.
- [57] Yuanyuan Li, Qiliang Fu, Shun Yu, Min Yan, and Lars Berglund. Optically transparent wood from a nanoporous cellulosic template: combining functional and structural performance. *Biomacromolecules*, 17(4):1358–1364, 2016.
- [58] Chaoji Chen, Yiju Li, Jianwei Song, Zhi Yang, Yudi Kuang, Emily Hitz, Chao Jia, Amy Gong, Feng Jiang, JY Zhu, et al. Highly flexible and efficient solar steam generation device. *Advanced materials*, 29(30):1701756, 2017.
- [59] Selin Vitas, Tobias Keplinger, Nico Reichholf, Renato Figi, and Etienne Cabbage. Functional lignocellulosic material for the remediation of copper (ii) ions from water: Towards the design of a wood filter. *Journal of hazardous materials*, 355:119–127, 2018.
- [60] Jonas Garemark, Jesus E Perea-Buceta, Daniel Rico del Cerro, Stephen Hall, Barbara Berke, Ilkka Kilpeläinen, Lars A Berglund, and Yuanyuan Li. Nanosstructurally controllable strong wood aerogel toward efficient thermal insulation. *ACS Applied Materials & Interfaces*, 14(21):24697–24707, 2022.
- [61] Rune B Abrahamsen and Kjell Arne Malo. Structural design and assembly of “treet”—a 14-storey timber residential building in norway. In *World conference on timber engineering*, volume 2014, 2014.
- [62] Ario Ceccotti, Carmen Sandhaas, Minoru Okabe, Motoi Yasumura, Chikahiro Minowa, and Naohito Kawai. Sofie project—3d shaking table test on a seven-storey full-scale cross-laminated timber building. *Earthquake engineering & structural dynamics*, 42(13):2003–2021, 2013.
- [63] Massimo Fragiocomo, Bruno Dujic, and Iztok Sustersic. Elastic and ductile design of multi-storey crosslam massive wooden buildings under seismic actions. *Engineering structures*, 33(11):3043–3053, 2011.
- [64] Lorna J Gibson. The hierarchical structure and mechanics of plant materials. *Journal of the royal society interface*, 9(76):2749–2766, 2012.

- [65] Per Bergkvist. *Design of Timber Structures: Structural Aspects of Timber Construction*. Swedish Forest Industries Federation, 2015.
- [66] A Wilfred Jr and Franz FP Kollmann. *Principles of wood science and technology*. Springer, 1968.
- [67] Kent Persson. *Micromechanical Modelling of Wood and Fibre Properties*. Doctoral thesis (monograph), Structural Mechanics, 2000.
- [68] Antti Hanhijärvi, Alpo Ranta-Maunus, and Goran Turk. Potential of strength grading of timber with combined measurement techniques: Report of the combigrade-project-phase 1. VTT Publications 568, VTT Technical Research Centre of Finland, Espoo, Finland, 2005.
- [69] SIS. Structural timber – strength classes. Standard SS-EN 338:2016, Swedish Institute for Standards, Stockholm, Sweden, 2016.
- [70] Swedish Standards Institute (SIS). Timber structures - strength graded structural timber with rectangular cross section - part 1: General requirements. Technical Report STD-80015570, Swedish Standards Institute (SIS), September 2019.
- [71] Reinhard Brandner. Production and technology of cross laminated timber (clt): A state-of-the-art report. In *Focus solid timber solutions-European conference on cross laminated timber (CLT)*, pages 3–36. University of Bath, 2013.
- [72] Swedish Standards Institute (SIS). Timber structures - cross laminated timber - requirements. Technical Report SS-EN 16351:2021, Swedish Standards Institute (SIS), March 2021. Standard No. STD-80028025.
- [73] Sylvain Gagnon and Ciprian Pirvu. Clt handbook: cross-laminated timber. (*No Title*), 2011.
- [74] Shaheda T Akter. *Experimental characterization and numerical modeling of compression perpendicular to the grain in wood and cross-laminated timber*. PhD thesis, Linnaeus University Press, 2022.
- [75] Omar Espinoza and Urs Buehlmann. Cross-laminated timber in the usa: Opportunity for hardwoods? *Current Forestry Reports*, 4:1–12, 2018.
- [76] Björn Johannesson. *Thermodynamics of Single Phase Continuous Media with Numerical Examples*. Linnaeus University, Växjö, 2019.
- [77] Benjamin Bondsman. Numerical modelling and experimental investigation of large deformation under static and dynamic loading. Master’s thesis, Linnaeus University, Faculty of Technology, Department of Building Technology, 2021.

- [78] Thomas J. R. Hughes. *The Finite Element Method: Linear Static and Dynamic Finite Element Analysis*. Courier Corporation, Cambridge, MA, 1st edition, 2003.
- [79] Klaus-Jürgen Bathe. *Finite element procedures*. Klaus-Jurgen Bathe, 2006.
- [80] Niels Ottosen and Hans Petersson. *Introduction to Finite Element Method*. Pearson Education, 1992.
- [81] T. K. Caughey. Classical normal modes in damped linear dynamic systems. *Journal of Applied Mechanics*, 27(1):1–12, 1960.
- [82] Man Liu and Dadiv G Gorman. Formulation of rayleigh damping and its extensions. *Computers & structures*, 57(2):277–285, 1995.
- [83] Theodore Theodorsen and IE Garrick. *Mechanism of flutter: a theoretical and experimental investigation of the flutter problem*, volume 685. NACA Langley Field, VA, USA, 1940.
- [84] Roy R. Craig Jr and Andrew J. Kurdila. *Fundamentals of Structural Dynamics*. John Wiley & Sons, 2006.
- [85] C. Lanczos. An iteration method for the solution of the eigenvalue problem. *Journal of Research of the National Bureau of Standards*, 45(4):255–282, 1950.
- [86] V. Krylov, D. Fadeyev, and V. Fadeyev. Method of subspace iteration for solving eigenvalue problems. *Numerical Mathematics*, 35(1):1–16, 1980.
- [87] Klaus-Jürgen Bathe. The subspace iteration method—revisited. *Computers & Structures*, 126:177–183, 2013.
- [88] Nathan M Newmark. A method of computation for structural dynamics. *Journal of the engineering mechanics division*, 85(3):67–94, 1959.
- [89] Hans M Hilber, Thomas JR Hughes, and Robert L Taylor. Improved numerical dissipation for time integration algorithms in structural dynamics. *Earthquake Engineering & Structural Dynamics*, 5(3):283–292, 1977.
- [90] Gunwoo Noh and Klaus-Jürgen Bathe. An explicit time integration scheme for the analysis of wave propagations. *Computers & structures*, 129:178–193, 2013.
- [91] Steen Krenk. *Non-linear modeling and analysis of solids and structures*. Cambridge University Press, 2009.
- [92] James W Cooley and John W Tukey. An algorithm for the machine calculation of complex fourier series. *Mathematics of computation*, 19(90):297–301, 1965.

- [93] Alan V. Oppenheim. *Discrete-time Signal Processing*. Pearson Education India, 1999.
- [94] John G Proakis. *Digital signal processing: principles, algorithms, and applications, 4/E*. Pearson Education India, 2007.
- [95] E. Oran Brigham. *The fast Fourier transform and its applications*. Prentice-Hall, Inc., USA, 1988.
- [96] Matthew S Allen, Daniel Rixen, Maarten Van der Seijs, Paolo Tiso, Thomas Abrahamsson, and Randall L Mayes. *Substructuring in engineering dynamics*. Springer, 2020.
- [97] Michel G radin and Daniel J Rixen. *Mechanical vibrations: theory and application to structural dynamics*. John Wiley & Sons, 2015.
- [98] Lennart Ljung. *System Identification: Theory for the User*. Prentice Hall, Upper Saddle River, NJ, 2nd edition, 1999.
- [99] Ramon Pallas-Areny and John G Webster. *Sensors and signal conditioning*. John Wiley & Sons, 2012.
- [100] Carl Friedrich Gauss. *Theoria Interpolationis Methodo Nova Tractata*. Reiner, Leipzig, 1866. Published posthumously. This work includes the earliest explicit formula for the Discrete Fourier Transform (DFT) containing both sine and cosine series. The original manuscript was likely written in 1805.
- [101] CY Shih, YG Tsuei, RJ Allemang, and DL Brown. Complex mode indication function and its applications to spatial domain parameter estimation. *Mechanical systems and signal processing*, 2(4):367–377, 1988.
- [102] Alessandro Fasana. Modal parameters estimation in the z-domain. *Mechanical Systems and Signal Processing*, 23(1):217–225, 2009.
- [103] Mahmoud El-Kafafy, Bart Peeters, Theo Geluk, and Patrick Guillaume. The mlmm modal parameter estimation method: A new feature to maximize modal model robustness. *Mechanical Systems and Signal Processing*, 120:465–485, 2019.
- [104] Randall Allemang and Peter Avitabile. *Handbook of experimental structural dynamics*. Springer Nature, 2022.
- [105] Anders Brandt. *Noise and vibration analysis: signal analysis and experimental procedures*. John Wiley & Sons, 2023.

- [106] Daniel C Kammer. Sensor placement for on-orbit modal identification and correlation of large space structures. *Journal of Guidance, Control, and Dynamics*, 14(2):251–259, 1991.
- [107] Andreas Linderholt and Thomas Abrahamsson. Optimising the informativeness of test data used for computational model updating. *Mechanical systems and signal processing*, 19(4):736–750, 2005.
- [108] Randall J Allemang. A correlation coefficient for modal vector analysis. In *Proc. 1st Int. Modal Analysis Conference*, pages 110–116, 1982.
- [109] Claude E Shannon. Communication in the presence of noise. *Proceedings of the IRE*, 37(1):10–21, 1949.
- [110] Randall J Allemang et al. Vibrations: Experimental modal analysis. *Structural Dynamics Research Laboratory, Department of Mechanical, Industrial and Nuclear Engineering, University of Cincinnati*, 1999.
- [111] Peter Avitabile. *Modal testing: a practitioner's guide*. John Wiley & Sons, 2017.
- [112] Mark H Richardson and David L Formenti. Parameter estimation from frequency response measurements using rational fraction polynomials. In *Proceedings of the 1st international modal analysis conference*, volume 1, pages 167–186. Citeseer, 1982.
- [113] Brüel & Kjær. Bk connect structural dynamics: Modal analysis type 8420, modal analysis (advanced) type 8420-a and geometry type 8410. Product Data BP 1523 – 16, Brüel & Kjær Sound & Vibration Measurement, Nærum, Denmark, 2021.
- [114] Michael Friswell and John E Mottershead. *Finite element model updating in structural dynamics*, volume 38. Springer Science & Business Media, 1995.
- [115] Babak Moaveni and Iman Behmanesh. Effects of changing ambient temperature on finite element model updating of the dowling hall footbridge. *Engineering Structures*, 43:58–68, 2012.
- [116] Kaipeng Sun, Yonghui Zhao, and Haiyan Hu. Identification of temperature-dependent thermal–structural properties via finite element model updating and selection. *Mechanical Systems and Signal Processing*, 52:147–161, 2015.
- [117] José Humberto S Almeida Jr, Tales V Lisbôa, Axel Spickenheuer, and Luc St-Pierre. A sequential finite element model updating routine to identify creep parameters for filament wound composite cylinders in aggressive environments. *Computers & Structures*, 276:106939, 2023.

- [118] Xuefei Guan, Ratneshwar Jha, and Yongming Liu. Model selection, updating, and averaging for probabilistic fatigue damage prognosis. *Structural Safety*, 33(3):242–249, 2011.
- [119] Boris A Zárate, Juan M Caicedo, Jianguo Yu, and Paul Ziehl. Bayesian model updating and prognosis of fatigue crack growth. *Engineering Structures*, 45:53–61, 2012.
- [120] Ruoxue Zhang and Sankaran Mahadevan. Model uncertainty and bayesian updating in reliability-based inspection. *Structural Safety*, 22(2):145–160, 2000.
- [121] Menahem Baruch and Itzhack Y. Bar Itzhack. Optimal weighted orthogonalization of measured modes. *AIAA journal*, 16(4):346–351, 1978.
- [122] Menahem Baruch. Optimization procedure to correct stiffness and flexibility matrices using vibration tests. *AIAA journal*, 16(11):1208–1210, 1978.
- [123] Alex Berman. Mass matrix correction using an incomplete set of measured modes. *AIAA journal*, 17(10):1147–1148, 1979.
- [124] J-C Chen, C-P Kuo, and J Garba. Direct structural parameter identification by modal test results. In *24th Structures, Structural Dynamics and Materials Conference*, page 812, 1983.
- [125] A Berman and EJ Nagy. Improvement of a large analytical model using test data. *AIAA journal*, 21(8):1168–1173, 1983.
- [126] Daniel T Bartilson, Jinwoo Jang, and Andrew W Smyth. Finite element model updating using objective-consistent sensitivity-based parameter clustering and bayesian regularization. *Mechanical Systems and Signal Processing*, 114:328–345, 2019.
- [127] John A Nelder and Roger Mead. A simplex method for function minimization. *The computer journal*, 7(4):308–313, 1965.
- [128] Fuchang Gao and Lixing Han. Implementing the nelder-mead simplex algorithm with adaptive parameters. *Computational Optimization and Applications*, 51(1):259–277, 2012.
- [129] Armen Der Kiureghian and Ove Ditlevsen. Aleatory or epistemic? does it matter? *Structural safety*, 31(2):105–112, 2009.
- [130] Michael Havbro Faber. On the treatment of uncertainties and probabilities in engineering decision analysis. *Journal of Offshore Mechanics and Arctic Engineering*, 2005.

- [131] David Duvenaud. The kernel cookbook: Advice on covariance functions. *URL* <https://www.cs.toronto.edu/duvenaud/cookbook>, 2014.
- [132] Christopher KI Williams and Carl Edward Rasmussen. *Gaussian processes for machine learning*, volume 2. MIT press Cambridge, MA, 2006.
- [133] F. Pedregosa, G. Varoquaux, A. Gramfort, V. Michel, B. Thirion, O. Grisel, M. Blondel, P. Prettenhofer, R. Weiss, V. Dubourg, J. Vanderplas, A. Passos, D. Cournapeau, M. Brucher, M. Perrot, and E. Duchesnay. Scikit-learn: Machine learning in Python. *Journal of Machine Learning Research*, 12:2825–2830, 2011.
- [134] Michael D McKay, Richard J Beckman, and William J Conover. A comparison of three methods for selecting values of input variables in the analysis of output from a computer code. *Technometrics*, 42(1):55–61, 2000.
- [135] Jon C Helton and Freddie Joe Davis. Latin hypercube sampling and the propagation of uncertainty in analyses of complex systems. *Reliability Engineering & System Safety*, 81(1):23–69, 2003.
- [136] Rickard Sjögren and Daniel Svensson. pydoe2: An experimental design package for python, 2018.
- [137] Christiane Lemieux. *Monte carlo and quasi-monte carlo sampling*, volume 20. Springer, 2009.
- [138] Charles R. Harris, K. Jarrod Millman, Stéfan J. van der Walt, Ralf Gommers, Pauli Virtanen, David Cournapeau, Eric Wieser, Julian Taylor, Sebastian Berg, Nathaniel J. Smith, Robert Kern, Matti Picus, Stephan Hoyer, Marten H. van Kerkwijk, Matthew Brett, Allan Haldane, Jaime Fernández del Río, Mark Wiebe, Pearu Peterson, Pierre Gérard-Marchant, Kevin Sheppard, Tyler Reddy, Warren Weckesser, Hameer Abbasi, Christoph Gohlke, and Travis E. Oliphant. Array programming with NumPy. *Nature*, 585(7825):357–362, September 2020.
- [139] Jin-Gyun Kim and Phill-Seung Lee. An enhanced craig–bampton method. *International Journal for Numerical Methods in Engineering*, 103(2):79–93, 2015.
- [140] Daniel J. Rixen. A dual craig–bampton method for dynamic substructuring. *Journal of Computational and Applied Mathematics*, 168(1):383–391, 2004. Selected Papers from the Second International Conference on Advanced Computational Methods in Engineering (ACOMEN 2002).
- [141] Dennis de Klerk, Daniel J Rixen, and SN Voormeeren. General framework for dynamic substructuring: history, review and classification of techniques. *AIAA journal*, 46(5):1169–1181, 2008.

- [142] Lars AL Janssen, Rob HB Fey, Bart Besselink, and Nathan van de Wouw. Mode selection for component mode synthesis with guaranteed assembly accuracy. *Journal of Sound and Vibration*, page 118596, 2024.

Part II

Appended publications

Scientific publications

Contribution statement – B. Bondsman

Paper I: Conceptualisation, Data curation, Formal analysis, Investigation, Methodology, Resources, Software, Validation, Visualisation, Writing – original draft, Writing – review & editing.

Paper II: Conceptualisation, Data curation, Formal analysis, Investigation, Methodology, Resources, Software, Validation, Visualisation, Writing – original draft, Writing – review & editing.

Paper III: Conceptualisation, Data curation, Formal analysis, Investigation, Methodology, Resources, Software, Validation, Visualisation, Writing – original draft, Writing – review & editing.

Paper IV: Conceptualisation, Data curation, Formal analysis, Investigation, Methodology, Resources, Software, Validation, Visualisation, Writing – original draft, Writing – review & editing.

Paper I

B. Bondsman, A. Peplow

Experimental Modal Analysis and variability assessment of Cross-laminated Timber
Mechanical Systems and Signal Processing, Vol. 228, 112466, 22.02.2025.



Experimental Modal Analysis and variability assessment in Cross-laminated Timber

Benjamin Bondsman^a, Andrew Peplow^b

^a Lund University, John Ericssons väg 1, SE-223 63, Lund, Kingdom of Sweden

^b Hawkins & Associates, 9 High Street, Histon, CB24 9JD, Cambridge, United Kingdom

ARTICLE INFO

Communicated by E. Chatzi

Keywords:

Experimental Modal Analysis
Cross-laminated Timber (CLT)
Vibration performance
Structural dynamics
Dynamic variability

ABSTRACT

Experimental Modal Analysis (EMA) plays a crucial role in understanding the dynamic responses of structures to vibration by extracting their modal parameters such as natural frequencies and modal damping and vibration modes. These parameters are essential for assessing structural performance and identifying potential vulnerabilities. As the construction industry embraces sustainable materials, Cross-laminated Timber (CLT) has become a sustainable alternative to traditional materials like reinforced concrete and steel. However, the inherent variability of wood, resulting from factors such as growth conditions, fibre structure, and moisture content, introduces significant fluctuations in the dynamic response of CLT. This variability presents challenges in the broader application of CLT in construction. Despite its increasing use in multistory buildings, a comprehensive assessment of its vibrational characteristics remains incomplete. This study addresses this gap by identifying the dispersion in CLT's transfer functions and modal parameters through EMA. A CLT slab was divided into 24 nominally identical beam-like substructures, composed of outer layers of Norway spruce and a middle layer of Scots pine. EMA was performed in a broad frequency spectrum along three principal directions, revealing notable variability in resonance frequencies, modal damping, and vibration transfer functions. The study also examines the distinct characteristics of the bending, torsional, and axial vibration modes, providing deeper insights into the variability between the different modes. The findings of this article contribute to a more refined understanding of the dynamic properties of CLT and their associated variability.

1. Introduction

Over recent decades, Experimental Modal Analysis (EMA) has become a crucial methodology for understanding and characterising the dynamic behaviour of vibrating structures. The methodology gained prominence with the advent of the computer-based Fourier transform, known as the Fast Fourier Transform (FFT) [1]. EMA has since evolved into a fundamental technique in experimental dynamics, enabling the decomposition of vibration signals into a set of modal parameters that highlight the frequency-dependent performance and vulnerabilities of structures. In EMA, vibration signals are generated by rate-dependent input forces — mechanical, acoustic, thermal, or electrical — that excite structures and the corresponding output responses. The performance of a structure is described using frequency-dependent characteristics, such as inertance, mobility, and compliance. Vulnerabilities arise during resonance events, where the vibration amplitude increases significantly. The vibration amplitude during a resonance event is primarily controlled by the structure's energy dissipation characteristics, which often arise due to friction or the conversion of

* Corresponding author.

E-mail address: benjamin.bondsman@construction.lth.se (B. Bondsman).

<https://doi.org/10.1016/j.ymssp.2025.112466>

Received 21 October 2024; Received in revised form 8 January 2025; Accepted 10 February 2025

Available online 22 February 2025

0888-3270/© 2025 The Authors. Published by Elsevier Ltd. This is an open access article under the CC BY license (<http://creativecommons.org/licenses/by/4.0/>).

vibration energy into thermal energy, and is quantified as modal damping. At each resonance event, the structure exhibits a specific mode shape or a natural mode. Hence, for each resonance event, there is a natural frequency, modal damping, and mode shape. These parameters are determined through the analysis of input–output signals, transformed into the frequency domain, and estimated using modal estimation techniques, for example, [2–4]. Understanding the modal characteristics of structures has become important as the global focus shifts toward sustainable and innovative structural design solutions. This understanding is particularly important in the optimisation of structural performance by improving damping mechanisms, minimising vibration amplitudes, and preventing the occurrence of resonances.

In the field of structural engineering, Engineered Wood Products (EWPs) have emerged in recent decades as sustainable and low carbon emissions alternatives to traditional construction materials, such as reinforced concrete and steel, which are considered carbon-emission-intensive materials [5–7]. Among these, Cross-Laminated Timber (CLT) has gained significant popularity as a structural element in the construction industry. CLT is produced by stacking layers of lumber boards in a crosswise pattern, with adjacent layers orientated at a 90-degree angle. These layers are bonded using polyurethane adhesive, creating a composite that combines the strength and dimensional stability of wood with improved load-bearing capabilities [8–11]. Hence, large constructions use CLTs as load-bearing slabs and shear panels. However, wooden structures have a low mass-to-stiffness ratio compared to their traditional counterparts, making them more susceptible to vibrations and sound transmission. Wood as a material also exhibits variability in its mechanical characteristics, mainly due to differences in growing conditions, fibre structure, and moisture content [12–15]. In addition, the mechanical characteristics of wood are influenced by natural defects such as knots [16], splits [17], and moisture-induced distortions, as further elaborated by Ormarsson [18]. The variability in macro- and microstructure characteristics of wood, particularly in the assembled lumber boards constituting the CLT, introduces diverse variations in the structure's behaviour. To reduce this variability and due to insufficient comprehensive knowledge, the CLT manufacturing sector produces laminated components using lumber boards where significant visible defects are removed and the remaining minor imperfections are spread over a larger volume. This process aims to achieve a more uniform material distribution on a larger scale, thus mitigating the inherent heterogeneity of wood, as noted by Steiger et al. [19]. However, this process may result in significant material loss, as natural defects are an inherent part of wood. The extent of this material loss, while variable, remains a potential drawback of current CLT manufacturing practices.

In recent years, several efforts have been made to gain in-depth knowledge concerning the dynamic behaviour of CLT slabs and buildings. Kawrza et al. [20] conducted transverse EMA on a large-scale CLT slab with point-supported boundary conditions and a dense measurement grid comprising 651 points. Data collection spanned 10 h, with actual measurements being performed over 2 days. The modal parameters of the CLT were found to exhibit variability due to environmental influences. This variability contributes to the dispersion observed in the modal parameters of CLT. Faircloth et al. [21] performed transverse EMA on CLT panels to investigate the influence of boundary conditions. Their study examined six different boundary conditions and concluded that a freely supported system provided higher resolution results, with an error of less than 10% compared to a corresponding Finite Element (FE) model, in addition to offering advantages in terms of simplicity of setup. Kawrza et al. [22] also identified the modal parameters of a CLT floor during three construction stages, observing variability, which was subsequently used to update a corresponding FE model. Furthermore, EMA has been used to determine the modal properties of multi-story buildings with different wood frame configurations [23]. Additional research has addressed model updating for CLT buildings [24,25], hybrid wood–concrete building models [26], and hybrid CLT–concrete composite floors [27] using EMA as reference. Further studies have focused on the numerical validation of the EMA results for CLT slabs under various boundary conditions, as demonstrated in [28]. Ljunggren [29] performed transverse EMA on different CLT specimens, including standard spruce CLT panels, densified spruce and birch CLT panels, and CLT panels with intermediate elastic layers. Modal parameters related to five out-of-plane vibration modes were extracted in the lower frequency range, which exhibited variability. However, the study did not explore vibration characteristics in the in-plane and axial directions. These directions are particularly relevant given CLT's frequent use as shear walls and stabilisation elements in multi-story buildings. Recently, results from thirteen months of operational monitoring of an eight-story building were published in [30], indicating dispersion in natural frequencies and damping ratios throughout the measurement period, resulting from factors such as moisture content and temperature fluctuations. Although these studies provide valuable information, they are often limited by the number of samples tested, the influence of specific boundary conditions used, and a narrow focus on the lower-frequency spectrum. Therefore, despite the availability of the research articles discussed above, a comprehensive understanding of the vibration characteristics of CLT and its associated variability remains incomplete. To address this gap, a thorough investigation into the variability of the modal characteristics of CLT is essential, particularly in the in-plane and axial directions across a broad frequency spectrum, to comprehensively evaluate the variability in its modal parameters, using comparable specimens. The lack of knowledge regarding this variability can present challenges in the design of CLT structures, especially in light of the discrepancies identified in recent studies. For example, research by the authors [12] found that the dynamic orthotropic properties of CLT (including the substructures explored here), determined through model updating with EMA as a reference, differ from the values provided by the SS-EN 338:2016 code [31], commonly used in structural design. These discrepancies suggest that design practices based on current standards may not fully capture the dynamic behaviour of CLT, potentially leading to either over- or underestimation of its vibrational performance. Given the growing use of CLT in mid- and high-rise buildings, such discrepancies could result in less-than-optimal designs, particularly under dynamic loading conditions such as wind or seismic events.

In response to the lack of a comprehensive understanding of the variability in the modal characteristics of CLT, this study provides a detailed investigation of the dynamic properties of 24 nominally identical CLT beam-like substructures, extracted from a slab, using EMA in the three main directions, covering a wide frequency range up to 2 kHz. To acquire high-resolution data, a measurement grid consisting of $n > 3$ points per wavelength was selected, and the measurements were performed under free-free conditions to

Table 1

Orthotropic material properties of lumber boards of strength class C35 from [31,32]. The subscripts x, y, and z are respectively consistent with the orthotropic orientations of wood in longitudinal, radial and tangential directions. The density ρ corresponds to the mean density value of the beams.

ρ (kg/m ³)	E_x (MPa)	E_y (MPa)	E_z (MPa)	G_{xy} (MPa)	G_{xz} (MPa)	G_{yz} (MPa)	ν_{xy} (–)	ν_{xz} (–)	ν_{yz} (–)
473	13,000	262	430	810	810	57	0.48	0.42	0.28

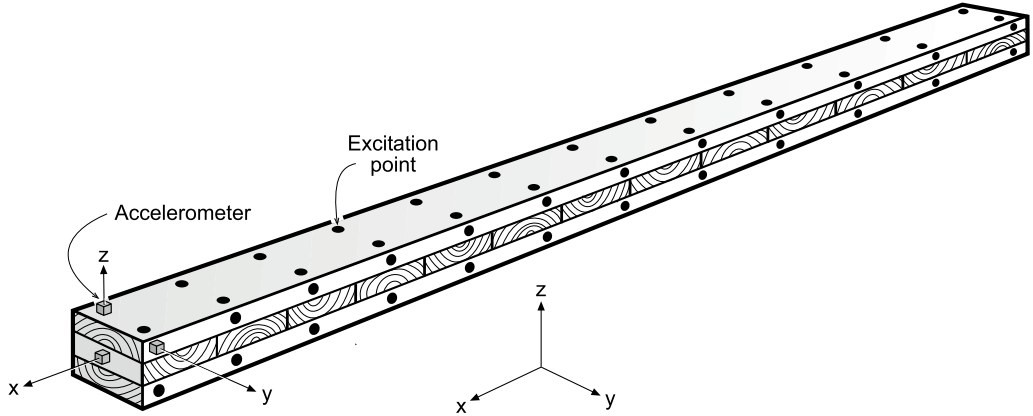


Fig. 1. Schematic illustration of the Experimental Modal Analysis (EMA) setup for the CLT beams, featuring 11×2 transversal, 11×2 lateral, and one axial excitation point. The axial excitation point is located in the centre of the cross section on the hidden side of the beam. The dimensions are as follows: length (l) \times width (w) \times height (h) = $2 \text{ m} \times 0.12 \text{ m} \times 0.12 \text{ m}$. Each layer has a thickness of 40 mm.

eliminate uncertainties arising from boundary conditions. The tests were carried out in a laboratory with a stable climate, leading to variability of the moisture content in the substructures ranging from 9.1% to 10.5%. Although the geometric dimensions of the tested specimens are not typical for standard CLT applications, they were intentionally selected to ensure consistency across all tests and comparability of the results. The study's findings include a detailed analysis of the variability in vibration transfer functions, natural frequencies, and damping associated with the three main directions. A distinction is also made regarding the variability in the modal parameters associated with different types of modes, i.e., bending, torsional, and axial modes. Furthermore, the article provides the necessary mathematical derivations, a detailed experimental procedure, and a rigorous evaluation of variability through confidence intervals, the Frequency Response Assurance Criterion (FRAC), and relative differences in natural frequencies and damping between vibration modes. These findings offer valuable information to advance the understanding of the dynamic characteristics of CLT, providing a detailed understanding of the dispersion in the inherent modal characteristics of nominally identical CLT substructures.

The remainder of this paper is organised as follows: Section 2 presents a detailed experimental framework and the corresponding mathematical derivations. Section 3 discusses the experimental results along with their statistical variations. Finally, Section 4 provides the concluding remarks.

2. Experimental modal analysis

This section details the experimental framework used in this study, beginning with the experimental design, addressing practical considerations, and concluding with the post-experimental data processing along with evaluation metrics. The objects tested here comprise 24 CLT beam-like substructures cut from a large CLT slab, where each beam is one lamella wide, Fig. 1. The substructures comprise two covering layers of Norway Spruce and an intermediate layer of Scots Pine.

2.1. Experimental design

The beams were modelled and numerically discretised using FE brick elements with quadratic interpolation to determine the experimental excitation locations. The orthotropic mechanical properties corresponding to the mean density value of the beams, as detailed in Table 1, were assigned to the FE model. A conventional tie coupling between the top-mid-bottom layers (along the z-axis) was considered, whereas no coupling between the individual intermediate boards (along the x-axis) was considered. This reflects the presence of adhesive glue between the upper intermediate and lower layers, whereas the individual intermediate layers are not glued, Fig. 1. Accordingly, the undamped homogeneous equations of motion were derived as follows:

$$\mathbf{M}\ddot{\mathbf{x}}(t) + \mathbf{K}\mathbf{x}(t) = \mathbf{0}, \quad (1)$$

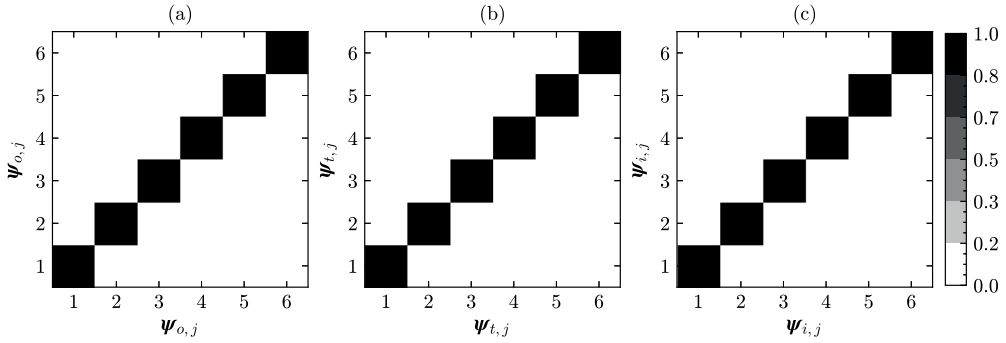


Fig. 2. Illustration of autoMAC matrices comparing (a) six out-of-plane bending, (b) six torsional, and (c) six in-plane bending modes. The modes are compared with themselves for orthogonality check and validation of the experimental excitation grid.

where $\mathbf{M} \in \mathbb{R}^{N \times N}$ is the lumped mass matrix and $\mathbf{K} \in \mathbb{R}^{N \times N}$ is the positive semi-definite stiffness matrix. The rate-dependent nodal accelerations and displacements are collected in $\ddot{\mathbf{x}} \in \mathbb{R}^{N \times 1}$ and $\mathbf{x} \in \mathbb{R}^{N \times 1}$, respectively. As the experiments were intended to be carried out in the absence of boundary conditions, Dirichlet conditions were not imposed on the system matrices. The numerical natural frequencies and modes were determined by solving the following eigenvalue problem:

$$(\mathbf{K} - \lambda_j \mathbf{M}) \boldsymbol{\psi}_j = \mathbf{0}, \quad j = 1, 2, \dots, N, \quad (2)$$

where λ_j is the j th eigenvalue and $\boldsymbol{\psi}_j$ is the corresponding conjugate eigenmode. The corresponding natural frequencies, in Hz, can be computed using the simple relation $f_n = \sqrt{\lambda}/2\pi$, in which $\sqrt{\lambda} = \omega_n$ is the angular frequency in rad/s. The natural frequencies are used to design the excitation frequency spectrum whilst the modes were used to design the excitation grid. The beams, due to their slenderness resonate frequently in the transversal (out-of-plane) and lateral (in-plane) directions. Therefore the modal coordinates were categorised into three modal matrices, with $\boldsymbol{\Psi}_o$ containing out-of-plane bending modes, $\boldsymbol{\Psi}_t$ containing torsional modes, and $\boldsymbol{\Psi}_i$ containing in-plane bending modes. The modal coordinates of $\boldsymbol{\Psi}_o$ and $\boldsymbol{\Psi}_t$ were extracted from the top-surface (xy plane) nodes of the beams whereas the modal coordinates in $\boldsymbol{\Psi}_i$ were extracted from the lateral surface (xz plane) nodes of the beams, Fig. 1. The structure of the modal matrices follows:

$$\boldsymbol{\Psi}_o = \begin{bmatrix} \psi_{o,11} & \psi_{o,12} & \dots & \psi_{o,16} \\ \psi_{o,21} & \psi_{o,22} & \dots & \psi_{o,26} \\ \vdots & \vdots & \dots & \vdots \\ \psi_{o,n} & \psi_{o,n} & \dots & \psi_{o,n} \end{bmatrix}, \quad \boldsymbol{\Psi}_t = \begin{bmatrix} \psi_{t,11} & \psi_{t,12} & \dots & \psi_{t,16} \\ \psi_{t,21} & \psi_{t,22} & \dots & \psi_{t,26} \\ \vdots & \vdots & \dots & \vdots \\ \psi_{t,n} & \psi_{t,n} & \dots & \psi_{t,n} \end{bmatrix}, \quad \boldsymbol{\Psi}_i = \begin{bmatrix} \psi_{i,11} & \psi_{i,12} & \dots & \psi_{i,16} \\ \psi_{i,21} & \psi_{i,22} & \dots & \psi_{i,26} \\ \vdots & \vdots & \dots & \vdots \\ \psi_{i,n} & \psi_{i,n} & \dots & \psi_{i,n} \end{bmatrix}, \quad (3)$$

where the subscript n denotes the total number of reference coordinates. Reference coordinates were selected so that $n > 3$ points per wavelength [33]. Other researchers have also proposed methods for the selection of optimal reference coordinates using Fisher's information matrix, e.g., the work by Kammer [34] and Linderholt and Abrahamsson [35]. To validate the excitation grid, which contains 22 transverse and 22 lateral excitation points, as shown in Fig. 1, a similarity check between the modes of interest was calculated using the Modal Assurance Criterion (MAC), [36]. MAC is a quantitative tool for comparing orthogonality between two modes, returning zero for absolute orthogonality and one for identical modes. The MAC value is calculated using the following equation:

$$\text{MAC}(\boldsymbol{\psi}_r, \boldsymbol{\psi}_s) = \frac{|\boldsymbol{\psi}_r^H \boldsymbol{\psi}_s|^2}{(\boldsymbol{\psi}_r^H \boldsymbol{\psi}_r) (\boldsymbol{\psi}_s^H \boldsymbol{\psi}_s)}, \quad (4)$$

where $\boldsymbol{\psi}_r$ and $\boldsymbol{\psi}_s$ are the mode shape vectors of the r th and s th modes, respectively, and H denotes the Hermitian (complex conjugate transpose) of the vector. The MAC was computed for all three modal matrices in (3) resulting in excellent orthogonality with $\text{MAC}_{rs} < 0.2$ for $r \neq s$, Fig. 2. In addition to the excitation points in the xy plane and the xz plane, an additional axial point on the yz plane was included in the measurement design. Since the axial point comprises one coordinate, it was not included in the MAC evaluation.

The sampling frequency range was designed to follow the Nyquist-Shannon sampling theorem [37], namely $f_s \geq 2f_{\max}$ with 3200 samples in the time domain. Hence, a maximum frequency of 2 kHz was reached.

2.2. Experimental setup

The beams were discretised with an excitation grid comprising 22 points in the xy plane, 22 points in the xz plane, and one point in the yz plane, as designed in the previous section, Fig. 1. Steel washers (weighing about 3 grammes each) were glued to the beams

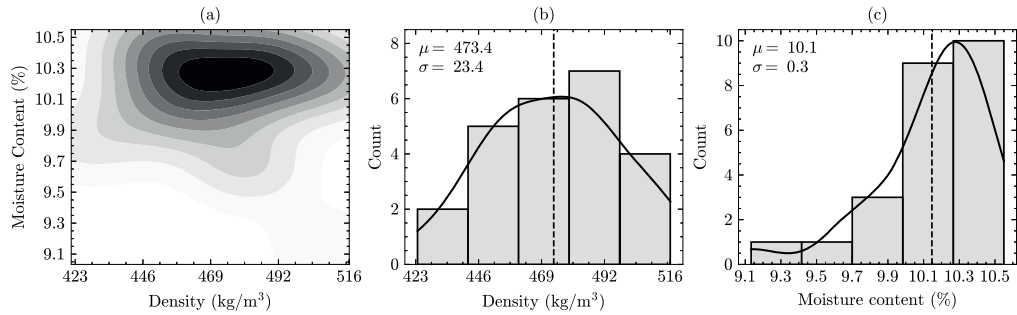


Fig. 3. Visualisation of (a) joint distribution between density and moisture content, (b) histogram with kernel density function of density values, and (c) histogram with kernel density function of moisture content values of the beams. The density values are nearly normally distributed, whereas the moisture content demonstrates a skewness of -1.57 .

at the excitation points to reach a higher frequency range. The beams were suspended from the laboratory ceiling using bungee cords to achieve free-free boundary conditions. This setup ensures that the vibration energy imparted to the structure via excitation force remains until it naturally decays due to energy leakage (damping) [33]. Previous research by Carne et al. [38] has indicated damping sensitivity due to support conditions. Hence, as a rule of thumb, the suspending bungees were chosen to be soft enough to produce rigid body modes far below a tenth of the fundamental natural frequency. The laboratory environment offered during the measurement campaign a variation in relative humidity ranging between 40 and 45% and a temperature variation ranging between 18 and 20 centigrade.

Before measurements were performed, the geometric dimensions and weights of the beams were documented. The density of each beam was calculated by dividing its weight by the measured volume of the midsection. In addition, the moisture content of each beam was measured at both ends and in the middle, between two layers. These values were averaged to determine the moisture content of each beam. The joint distributions of density and moisture content, along with their individual distributions and their respective mean and standard deviation, are presented in Fig. 3.

A single-input-single-output (SISO) approach was chosen, using an impact hammer with a sensitivity of 22.7 mV/N and an aluminium tip [39]. The acceleration response at each excitation point was measured using a corresponding uniaxial cubic charge piezoelectric accelerometer with a sensitivity of 0.316 pC/ms⁻² (picocoulombs per unit of acceleration) [40]. The cubic-charge accelerometers were chosen due to their low sensitivity to extraneous environmental effects. Consequently, three uniaxial accelerometers were used to measure acceleration along the x, y, and z axes, and were placed as shown in Fig. 1.

Accelerometers are piezoelectric sensors that detect base motion and convert it into an electrical signal proportional to the detected motion. The signal conditioners within these transducers convert the electrical signal into an analogue voltage that is a continuous function of time. To facilitate further processing, analogue signals from the transducers must be filtered and sampled to avoid aliasing before digitisation. Consequently, a data acquisition system was used to perform these tasks [41]. Detailed information on practical data acquisition can be found in a recent work by Allemang and Avitabile [42].

A square and an exponential window were applied to the input and response signals to minimise spectral leakage in the FFT when transforming the time domain into the frequency domain to compute FRFs, [1,43]. These windows enforce zero boundaries to the signals since the FFT assumes the periodicity of the signals outside the windows. However, the true nature of transient signals is non-periodic, but rather short-duration events with high energy content.

A three-excitation averaging approach was used to minimise signal leakage and mitigate uncertainties associated with environmental noise. Concurrently, the coherence of the input-output signals was monitored to ensure that the input energy corresponded closely to the output response, with exceptions noted for antiresonances characterised by very low response. The estimation of the FRFs and their associated coherence will be elaborated in the next section.

2.3. Estimation of frequency-response functions

Each measurement point is energised and its associated response is measured individually considering a SISO approach. Therefore, each point measurement can be considered as a single degree of freedom (SDOF) system, for which the numerical equation of motion can be formulated as:

$$f(t) = m\ddot{x} + c\dot{x} + kx, \quad (5)$$

where the input force $f(t)$ is balanced by internal forces comprising mass m and its associated acceleration \ddot{x} , energy leakage forces comprising damping constant c and its associated velocity \dot{x} , and potential energy comprising stiffness k and displacement x . The equilibrium in (5) can be expressed in the frequency domain considering the harmonic energising of the system,

$$F(\omega) = Z(\omega)X(\omega), \quad Z(\omega) = (k + j\omega c - \omega^2 m), \quad (6)$$

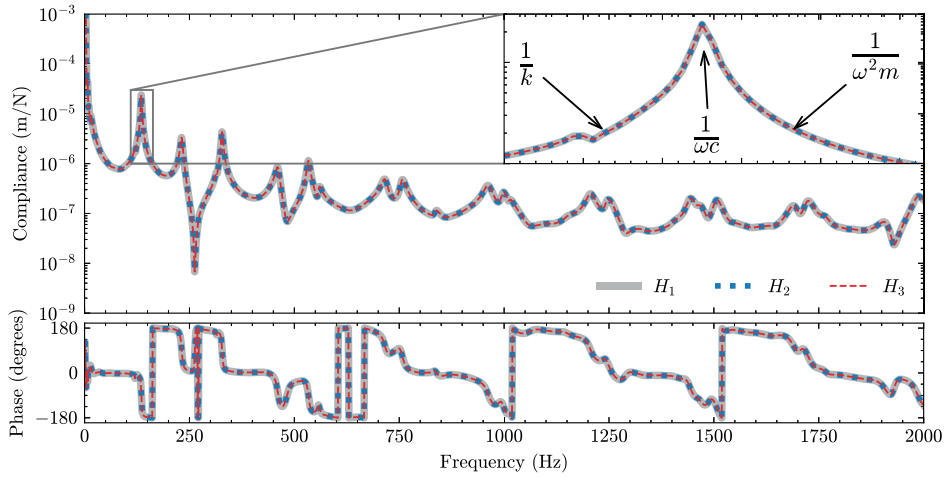


Fig. 4. Bode plot of Frequency Response Functions (FRFs) computed using H_1 , H_2 , and H_3 procedures in (16) and (17).

where $Z(\omega)$ is the dynamic stiffness of the system and its inverse is dynamic compliance, $F(\omega)$ is the energising force, and $X(\omega)$ is its' response conjugate. The frequency response function of the system, that is, the frequency response per unit force, can be determined as a ratio between output and input:

$$H(\omega) = Z(\omega)^{-1} = \frac{X(\omega)}{F(\omega)} = \frac{1}{k + j\omega c - \omega^2 m}. \quad (7)$$

In the frequency domain, vibration control is often characterised by three distinct stages corresponding to different frequency regimes where stiffness, damping, and inertia dominate the system's response. In the low-frequency range, the stiffness control is dominant, where the system behaves like a spring and the stiffness k primarily governs the impedance $Z(\omega)$, resulting in low displacement. As frequency increases, the system enters a critical middle-frequency frequency range where damping c plays a key role in controlling vibration. Here, energy dissipation due to damping $j\omega c$ is the most effective, reducing the amplitude of oscillations by absorbing vibrational energy. In the high-frequency regime, the inertial effects $-\omega^2 m$ dominate the response, where the mass m of the system resists acceleration, leading to a decrease in the effectiveness of vibration control. This phase is characterised by a decrease in displacement as the system becomes mass-controlled. Together, these three stages reflect the balance between stiffness, damping, and inertia in a dynamic system, influencing the approach to vibration mitigation.

Considering the measurements, the energising impulse force $f(t)$ is a transient high-energy signal with a short duration measured in the time domain. Similarly, its associated response $x(t)$ is measured in the time domain. As described in the previous section, both $f(t)$ and $x(t)$ are signals observed within specific time windows. In the time domain, the response can be related to the input force via Duhamel's convolution as:

$$x(t) = \int_{-\infty}^{\infty} h(t - \tau) f(\tau) d\tau, \quad (8)$$

where $h(t - \tau)$ is the impulse response function of the system, describing the response at time t due to an impulse energising at time τ , independent of the excitation [44]. The integral in (8) concerns all incremental impulses at times τ before the final time t , [44]. The expression in (8) after integration results in:

$$\begin{Bmatrix} x_1(\Delta t) \\ x_2(\Delta t) \\ x_3(\Delta t) \\ \vdots \\ x_N(\Delta t) \end{Bmatrix} = \begin{bmatrix} h_{11}(\Delta t) & 0 & \dots & 0 & 0 \\ h_{21}(\Delta t) & h_{22}(\Delta t) & \dots & 0 & 0 \\ h_{31}(\Delta t) & h_{32}(\Delta t) & h_{33}(\Delta t) & 0 & 0 \\ \vdots & \vdots & \vdots & \ddots & 0 \\ h_{N1}(\Delta t) & \dots & \dots & 0 & h_{NN}(\Delta t) \end{bmatrix} \begin{Bmatrix} f_1(\Delta t) \\ f_2(\Delta t) \\ f_3(\Delta t) \\ \vdots \\ f_N(\Delta t) \end{Bmatrix}, \quad (9)$$

where Δt denotes the time interval for the discretisation as the analogue signals are digitised, and N denotes the total number of time points. The discretised convolution in (9) can be simply expressed as:

$$\mathbf{x}(t) = \mathbf{H}(t) \mathbf{f}(t). \quad (10)$$

The expression in (10) introduces an important concept, namely relating the response of the system $\mathbf{x}(t)$ to the energising force $\mathbf{f}(t)$ using the impulse response function $\mathbf{H}(t)$. The impulse response function represents the system's time-dependent resistance to

excitation; analogous, for example, to the resistance of a multistorey building under severe motion-induced wind loads or the thermal conductivity of nuclear reactor components exposed to high-temperature loads.

The auto-correlation of the input and output signals in the time domain can be computed using:

$$R_{ff}(\tau) = \mathbb{E}[f(t), f(t + \tau)] = \lim_{T \rightarrow \infty} \frac{1}{T} \int_T f(t)f(t + \tau) dt, \quad (11a)$$

$$R_{xx}(\tau) = \mathbb{E}[x(t), x(t + \tau)] = \lim_{T \rightarrow \infty} \frac{1}{T} \int_T x(t)x(t + \tau) dt, \quad (11b)$$

where \mathbb{E} denotes expected value, τ is the time delay (or lag) which shifts the signal in time, and T denotes observation time. The limit as T approaches infinity indicates that the calculation is performed over an infinitely long time interval to ensure that all relevant variations and patterns in the signal are captured. Similarly, the cross-correlations of the input and output signals can be computed,

$$R_{fx}(\tau) = \mathbb{E}[f(t), x(t + \tau)] = \lim_{T \rightarrow \infty} \frac{1}{T} \int_T f(t)x(t + \tau) dt, \quad (12a)$$

$$R_{xf}(\tau) = \mathbb{E}[x(t), f(t + \tau)] = \lim_{T \rightarrow \infty} \frac{1}{T} \int_T x(t)f(t + \tau) dt. \quad (12b)$$

The frequency domain components of the input energising and output response signals can be simply extracted using the Fourier transform \mathcal{F} :

$$F(\omega) = \mathcal{F}[f(t)] = \int_{-\infty}^{\infty} f(t) e^{-j2\pi ft} dt, \quad (13a)$$

$$X(\omega) = \mathcal{F}[x(t)] = \int_{-\infty}^{\infty} x(t) e^{-j2\pi ft} dt, \quad (13b)$$

where $f(t)$ and $x(t)$ are discrete-time samples of the input and output signals, respectively, at time t . The complex exponential term $e^{-j2\pi ft}$ corresponds to the frequency component of f in the Fourier transform. The measurements presented in this article were carried out with a frequency resolution $\Delta f = 1/T_0 = 1.25$ Hz, where $T_0 = 0.8$ s denotes the total duration of the sample, resulting in an FFT frame size of 1600 bins. The Fourier function \mathcal{F} transforms the time domain signals $f(t)$ and $x(t)$ into their frequency domain representations $F(\omega)$ and $X(\omega)$, respectively. The signals in the time domain are functions of t in seconds, while their corresponding signals in the frequency domain are functions of the driving frequency ω in rad/s. The Fourier components are often computed using FFT. Further insights into the application of FFT analysers and their characteristics can be explored in the technical report authored by Thrane [45].

The auto-power spectrum of the input and output signals can be computed by:

$$G_{FF}(\omega) = \int_{-\infty}^{\infty} R_{ff}(\tau) e^{-j2\pi f\tau} d\tau = F(\omega)\overline{F(\omega)}, \quad (14a)$$

$$G_{XX}(\omega) = \int_{-\infty}^{\infty} R_{xx}(\tau) e^{-j2\pi f\tau} d\tau = X(\omega)\overline{X(\omega)}, \quad (14b)$$

where an over-line denotes a complex conjugate. The auto-power spectrum is a real function of frequency, in which the phase information is lost. Similarly, the cross-power spectrum of the signals can be determined using the following:

$$G_{FX}(\omega) = \int_{-\infty}^{\infty} R_{fx}(\tau) e^{-j2\pi f\tau} d\tau = F(\omega)\overline{X(\omega)}, \quad (15a)$$

$$G_{XF}(\omega) = \int_{-\infty}^{\infty} R_{xf}(\tau) e^{-j2\pi f\tau} d\tau = X(\omega)\overline{F(\omega)}, \quad (15b)$$

where it is noted that the cross-power spectrum is a complex function that carries both magnitude and phase. Recalling the convolution in (8) and the concept of relating input signal to output signal via $h(t)$ in the time domain, a similar function can be formulated in the frequency domain,

$$X(\omega)\overline{F(\omega)} = H(\omega)F(\omega)\overline{F(\omega)} \rightarrow H_1(\omega) = \frac{X(\omega)\overline{F(\omega)}}{F(\omega)\overline{F(\omega)}} = \frac{G_{XF}(\omega)}{G_{FF}(\omega)}, \quad (16a)$$

$$X(\omega)\overline{X(\omega)} = H(\omega)F(\omega)\overline{X(\omega)} \rightarrow H_2(\omega) = \frac{X(\omega)\overline{X(\omega)}}{F(\omega)\overline{X(\omega)}} = \frac{G_{XX}(\omega)}{G_{FX}(\omega)}, \quad (16b)$$

where H_1 is accurate for systems with output noise, whereas H_2 is accurate in the presence of input noise. Hence, an average of H_1 and H_2 must be accurate in handling both input and output noise,

$$H_3(\omega) = \sqrt{H_1(\omega) \cdot H_2(\omega)} = \sqrt{\frac{G_{XX}(\omega)}{G_{FF}(\omega)} \frac{G_{XF}(\omega)}{G_{XF}(\omega)}}. \quad (17)$$

Due to the sensitivity of the FRFs to noise, the three FRFs in (16) and (17) were calculated and compared. As shown in Fig. 4, all three FRFs produce similar results, indicating that the noise levels present in the FRFs are minimal. Finally, the complete system can be presented in a manner similar to (10), however, in the frequency domain as:

$$\mathbf{X}(\omega) = \mathbf{H}(\omega) \mathbf{F}(\omega), \quad (18)$$

where $\mathbf{H}(\omega)$ represents the FRF matrix for the system consisting FRFs associated with all measurement coordinates n ,

$$\begin{Bmatrix} X_1(\omega) \\ X_2(\omega) \\ X_3(\omega) \\ \vdots \\ X_n(\omega) \end{Bmatrix} = \begin{bmatrix} H_{11}(\omega) & H_{12}(\omega) & H_{13}(\omega) & \dots & H_{1n}(\omega) \\ H_{21}(\omega) & H_{22}(\omega) & H_{23}(\omega) & \dots & H_{2n}(\omega) \\ H_{31}(\omega) & H_{32}(\omega) & H_{33}(\omega) & \dots & \vdots \\ \vdots & \vdots & \vdots & \ddots & \vdots \\ H_{n1}(\omega) & H_{n2}(\omega) & \dots & \dots & H_{nn}(\omega) \end{bmatrix} \begin{Bmatrix} F_1(\omega) \\ F_2(\omega) \\ F_3(\omega) \\ \vdots \\ F_n(\omega) \end{Bmatrix}. \quad (19)$$

To assess the fidelity of the relationship between the input and output signals, ordinary coherence serves as a crucial metric. Coherence quantifies the extent to which the input energy translates into the corresponding output energy. Therefore, in high-quality measurements, coherence values typically approach 1, indicating a strong correlation between the signals. Exceptions to this are observed during antiresonance events, where oscillatory patterns can lead to deviations from this ideal behaviour. With the auto- and cross-power spectrum in (14) and (15), the coherence can be defined as:

$$|G_{XF}(\omega)|^2 \leq |G_{FF}(\omega)| |G_{XX}(\omega)| \rightarrow \gamma^2(\omega) = \frac{|G_{XF}(\omega)|^2}{|G_{FF}(\omega)| |G_{XX}(\omega)|}, \quad 0 \leq \gamma^2(\omega) \leq 1, \quad (20)$$

where unity denotes the full translation of the input signal into output energy and zero denotes otherwise. The coherence function shall be computed from averaged auto- and cross-powers for repeated measurements.

Vibration is often measured in terms of acceleration, as accelerometers are the most common transducers. Therefore, the transfer functions typically represent acceleration per unit force (inertance). However, in analysis, it is often more intuitive to examine velocity per unit of force (mobility) or displacement per unit of force (compliance). Accordingly, the FRF matrix can be simply integrated using:

$$H_{v,ij}(\omega) = \int_{\omega} H_{ij}(\omega) d\omega = \frac{H_{ij}(\omega)}{2\pi f_j}, \quad (21a)$$

$$H_{c,ij}(\omega) = \iint_{\omega} H_{ij}(\omega) d\omega = \frac{H_{ij}(\omega)}{(2\pi f_j)^2}, \quad (21b)$$

where $H_{v,ij}(\omega)$ and $H_{c,ij}(\omega)$ are the mobility and compliance FRF components, respectively, H_{ij} are components of the inertance matrix in (19), and ω is the driving angular frequency.

The equations described above outline a concise derivation of the FRF estimation, acknowledging the minimal noise in the measurements presented later in this article. However, signal processing and FRF estimation from noisy signals involve complexities beyond this brief overview. Interested readers are encouraged to explore the extensive work of Oppenheim et al. [46] and the referenced literature therein, as well as Proakis and Manolakis [47], for further information.

2.4. Modal parameter estimation

With a subset of low-noise transfer functions, the modal characteristics of the beams can be extracted. Modal parameter estimation focusses on determining the resonance frequencies, modal damping, and their corresponding natural modes. This process requires a curve fitting procedure to identify consistent peaks within the transfer functions across the frequency spectrum. If necessary, the frequency spectrum can be constrained to a specific range to improve accuracy. From the peaks, our objective is to find consistent poles with complex values ($p_k = \zeta_k + j\omega_{d,k}$), where (i) ζ_k is the real part representing the rate at which oscillations decay (modal damping), and (ii) $j\omega_{d,k}$ is the imaginary part representing the oscillatory rate. The term $j\omega_{d,k}$ corresponds to the damped natural frequency, which describes how a small excitation causes a large response. A negative value of ζ_k indicates that the oscillations decrease over time, whereas a positive value indicates that the oscillations grow over time. Hence, for a stable system, ζ_k must be negative.

The transfer functions are the sum of several SDOF systems. They can be expressed in various forms: (i) polynomial form, (ii) pole-zero form, (iii) partial fraction form, and (iv) exponential form. In this work, we express the transfer functions in partial fraction form:

$$H(j\omega) = \sum_k \left(\frac{A_{ij,k}}{j\omega - p_k} + \frac{\bar{A}_{ij,k}}{j\omega - \bar{p}_k} \right), \quad (22)$$

where the poles p_k , \bar{p}_k (real and complex conjugate, respectively) represent

$$p_k, \bar{p}_k = -\zeta_k \omega_{n,k} \pm j\omega_{n,k} \sqrt{1 - \zeta_k^2} = -\zeta_k \omega_{n,k} \pm j\omega_{d,k}. \quad (23)$$

where $\omega_{n,k}$ is the undamped natural angular frequency, $\omega_{d,k}$ is its damped correspondence, and ζ_k is the modal damping factor.

The residues $A_{ij,k}$ and $\bar{A}_{ij,k}$ in expression (22) contain information on the modes and their associated scaling factors. The transfer function can thus be expressed as

$$H(j\omega) = \sum_k \frac{Q_k \Psi_k \Psi_k^T}{j\omega - p_k} + \frac{\bar{Q}_k \bar{\Psi}_k \bar{\Psi}_k^H}{j\omega - \bar{p}_k}, \quad (24)$$

where ψ_k and $\bar{\psi}_k$ are the mode shapes and Q_k and \bar{Q}_k are the corresponding scaling factors determined through fitting the above expression to the measured transfer functions, [44,48]. In the above equations, $\omega = 2\pi f$ denotes the angular frequency. In the present work, estimation of the modal parameters has been carried out in the z-domain [3,49,50].

2.5. Evaluation metrics

To evaluate the degree of similarity between the transfer functions across different CLT beams, a Frequency Response Assurance Criterion (FRAC) can be used:

$$\text{FRAC}(H_{rs}, \hat{H}_{rs}) = \frac{\left| \sum_{\omega} H_{rs}(\omega) \hat{\bar{H}}_{rs}(\omega) \right|^2}{\sum_{\omega} H_{rs}(\omega) \bar{H}_{rs}(\omega) \sum_{\omega} \hat{H}_{rs}(\omega) \hat{\bar{H}}_{rs}(\omega)}, \quad (25)$$

where $H_{rs}(\omega)$ and $\hat{H}_{rs}(\omega)$ are the two transfer functions at each discrete driving angular frequency ω to be evaluated [51], and the overline denotes the complex conjugate. Since all transfer functions chosen for the evaluation regarding their variability are extracted from the same location across different beams, they are expected to exhibit a low degree of orthogonality.

The degree of complexity in the vibration modes of a structure can be examined using the Modal Complexity Factor (MCF). In an ideal, undamped structure, the modes are purely imaginary, corresponding to simple harmonic motion with no energy loss. However, in real-world structures, damping and local nonlinearities introduce complexities, making the modes inherently complex with both real and imaginary components. Normalised to real values, the MCF yields a value between zero and one, where zero denotes a purely real mode shape (indicating simple harmonic motion with no phase difference between structural components), while a value of one indicates an entirely complex mode shape (reflecting significant phase differences and damping effects). The MCF can be computed using

$$\text{MCF}(\Re[\psi_j], \Im[\psi_j]) = 1 - \frac{(\Re[\psi_j]^T \Re[\psi_j]) - (\Im[\psi_j]^T \Im[\psi_j])^2 + 4(\Re[\psi_j]^T \Im[\psi_j])^2}{(\Re[\psi_j]^T \Re[\psi_j]) + (\Im[\psi_j]^T \Im[\psi_j])^2}, \quad (26)$$

where \Re and \Im denote respectively real and imaginary components of mode ψ_j .

Additional evaluations, such as the classical relative difference between the natural frequencies and modal damping relative to their mean values, as well as Kernel Density Estimation (KDE) and Confidence Interval [52], have been used. These methods are straightforward and well documented in the literature and therefore the equations are not presented here.

3. Experimental results

This section presents the experimental results and evaluates their associated variability. Data were collected from the test of 24 nominally identical CLT beams, each beam representing one lamella. Each beam was discretised using 45 reference points (Fig. 1): 22 points in the xy plane, 22 points in the xz plane, and 1 point in the yz plane. Consequently, the total number of transfer functions is 24×45 . Presenting all transfer functions is impractical as not all of them excite every resonance. Therefore, the focus is on the driving transfer functions along the y and z axes, together with the axial transfer function along the x axis. These transfer functions excite all the resonances that are presented later in this section.

3.1. Transfer functions

The transversal transfer functions (along the z -axis) exhibit minimal variability in the lower frequency range (except for the outliers), as depicted in Fig. 5. However, variability increases significantly at higher frequencies. Specifically, in the frequency range of 600–790 Hz (the zoomed region in Fig. 5), the variability in the resonance peaks makes it challenging to differentiate between them, whereas the peaks in the 0–400 Hz range are more distinct. Despite this increased variability, the magnitude of the transfer functions shows minimal variation (except for the outliers), indicating a consistent dynamic response per unit force across the beams. Furthermore, the magnitude and sharpness of the resonance peaks decrease with higher frequencies, suggesting increased overall damping, in particular, associated with resonances at higher frequencies, Fig. 5. The overall quality of the measurements, assessed using excitation coherence in (20), demonstrates that nearly all excitation energy is effectively translated into vibration energy, with the exception of antiresonances, Fig. 5.

Consistent with observations from the transversal transfer functions, the lateral transfer functions (along the y -axis) also display variability across the excitation spectrum. This variability becomes more pronounced with increasing frequency, which complicates the differentiation between resonance peaks due to the distinct characteristics of the beams, as shown in the zoomed region of Fig. 6. Unlike transverse FRFs, lateral FRFs exhibit increased variability in magnitude as the frequency range increases. This behaviour indicates that lateral FRFs exhibit greater variability at higher frequencies compared to their transverse counterparts. Furthermore, the magnitude of the transfer functions generally decreases with increasing frequency, indicating higher damping in the structure at these frequencies.

The excitation coherence analysis confirms that a substantial portion of the excitation energy is effectively translated into vibration energy, except for anti-resonance events, where the structure generates minimal vibration, further validating the quality of the measurements, Fig. 6.

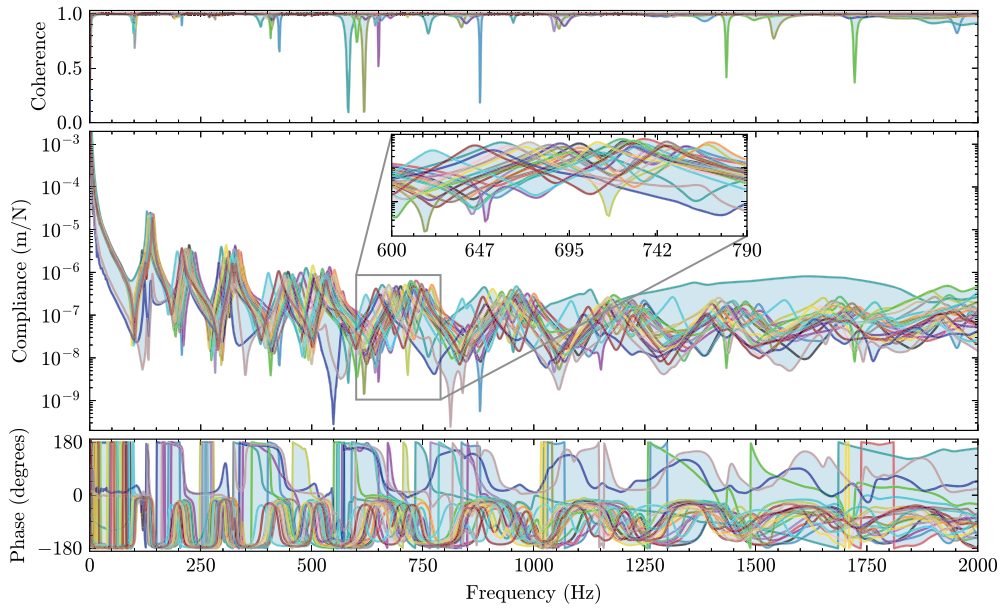


Fig. 5. Bode plot of the driving transfer functions across 24 beams due to excitation against the z-axis (Fig. 1), including their associated excitation coherence and envelope (in blue shade).

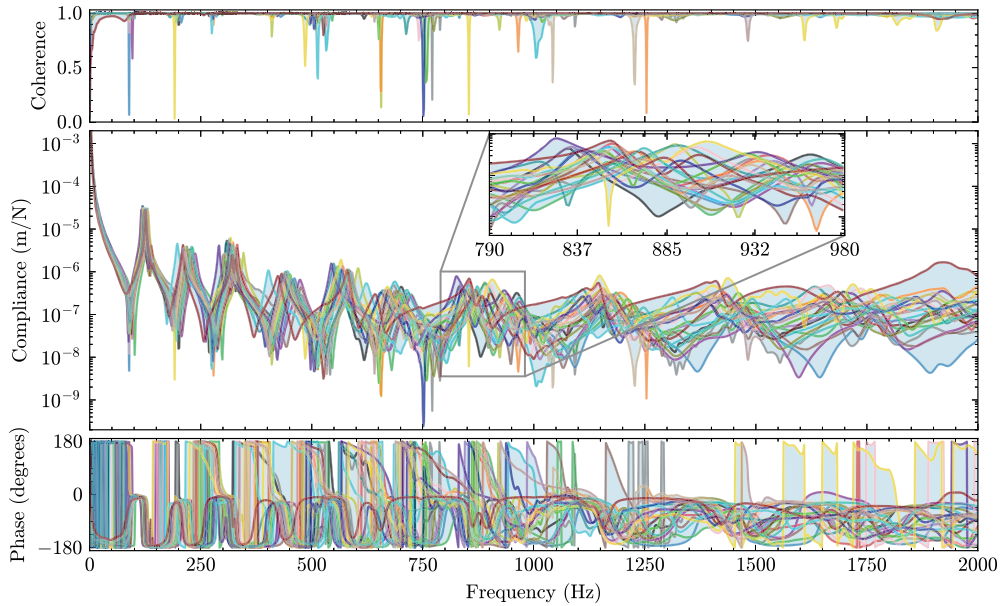


Fig. 6. Bode plot of the driving transfer functions across 24 beams due to excitation against the y-axis, and their associated excitation coherence and envelope (in blue shade). The line colours are consistent with Fig. 5.

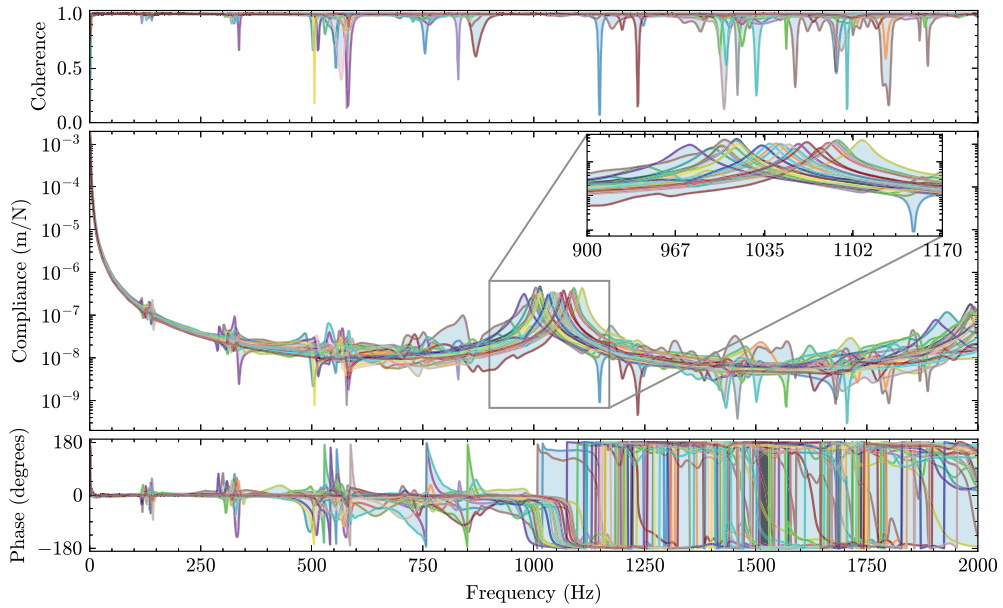


Fig. 7. Bode plot of transfer functions across 24 beams due to excitation against the x-axis (Fig. 1), along with their associated excitation coherence and envelope (in blue shade). The line colours are consistent with Figs. 5, and 6.

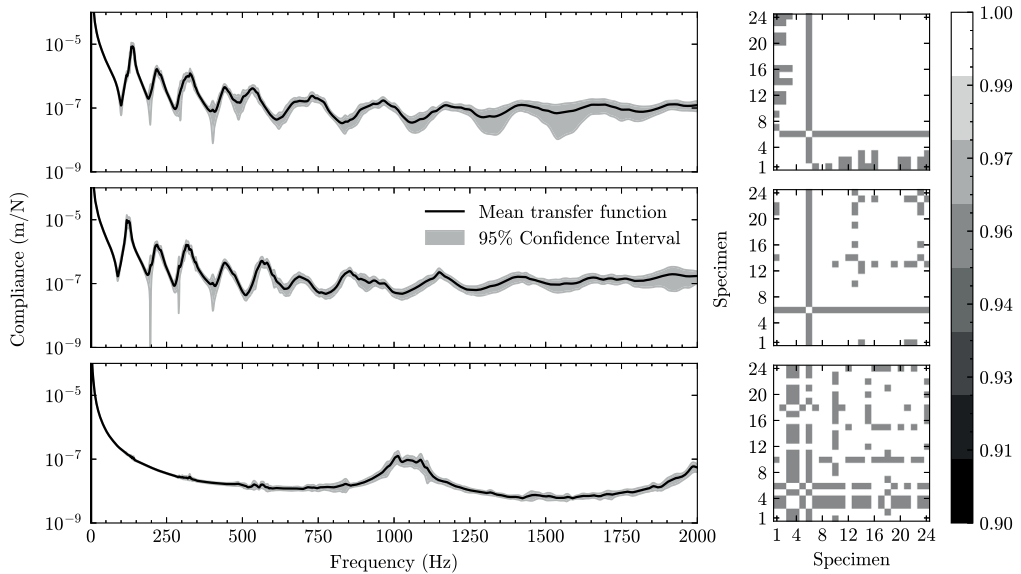


Fig. 8. From top to bottom: Mean transfer functions with their associated 95% confidence intervals and the Frequency Response Assurance Criterion (FRAC), which encompasses the driving FRFs in the transverse (z-axis), lateral (y-axis), and transfer FRF axial (x-axis) directions. The minimum correlations are approximately 0.94, 0.92, and 0.91, respectively.

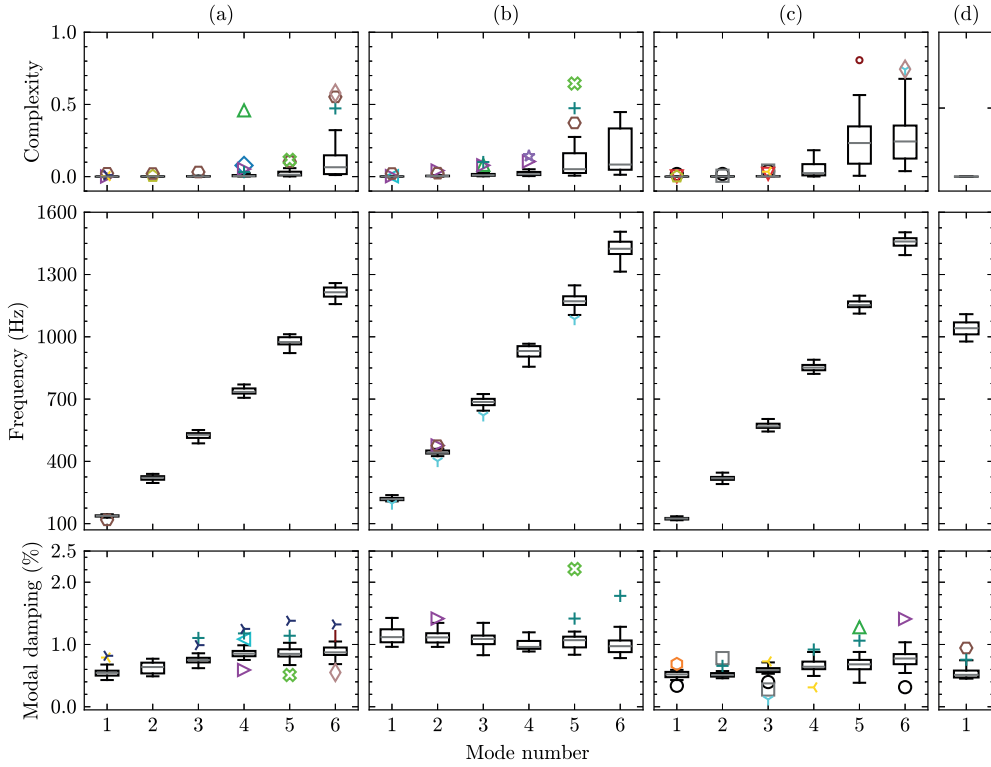


Fig. 9. Resonance frequencies and their associated modal complexities and modal damping: (a) Out-of-plane bending, (b) Torsional, (c) In-plane bending, and (d) Axial modes. The outlier marker colours are consistent with Figs. 5, 6, and 7.

Consistent with the transversal transfer functions, the axial transfer functions resulting from excitation along the x -axis exhibit shifting variability across the excitation spectrum, while maintaining minimal variability in their magnitude (see Fig. 7). Unlike the transversal and lateral transfer functions, the axial transfer functions feature more antiresonances and local resonance peaks, particularly noticeable in the regions flanking the resonance events. The overall coherence function demonstrates the effective translation of excitation energy into vibration energy, with this effect being particularly evident at resonance events.

Since the transfer functions illustrated in Figs. 5, 6, and 7 exhibit variability throughout the excitation spectrum, quantifying this variability is essential. Consequently, the mean values of the transfer functions, along with their associated confidence intervals of 95%, were calculated. Furthermore, the FRAC was also calculated for these transfer functions in various directions, as defined in (25). The results, shown in Fig. 8, reveal smaller confidence regions in the lower frequency spectrum, whereas these regions grow as the frequency range increases consistent with the previously observed behaviour of the transfer functions. This behaviour is particularly evident for the transverse and lateral FRFs. In contrast, the FRAC values range from 0.9 to 1, with the majority close to 1. This suggests minimal variability in the transfer functions across different beams.

3.2. Resonance frequencies and modal damping

The transfer functions discussed in the previous section exhibit a shift across the excitation spectrum, which affects the resonance events. Therefore, it is crucial to quantify to what extent this shift influences the resonance characteristics. A distinction is made among out-of-plane bending, torsional, in-plane bending, and axial modes. Visualisation of these modes can be found in Fig. A.1, see Appendix. Specifically, out-of-plane bending and torsional resonances and their associated data were obtained from transverse excitation against the z axis. In-plane bending resonances were derived from lateral excitation against the y -axis, while axial resonances were extracted from excitation along the x -axis, Fig. 1. In the modal estimation, the frequency spectrum was constrained between 0–1600 to extract all the modes of interest. A similar classification is applied to the modal damping of these resonances. Furthermore, the complexity of the resonance modes was assessed for all modes using the MCF defined in (26).

The results in the upper subplots of Fig. 9 indicate minimal overall modal complexity for lower-order modes (Modes 1–4). For higher-order modes (Modes 5–6), the modal complexities exhibit significant variability, particularly among the fifth torsional

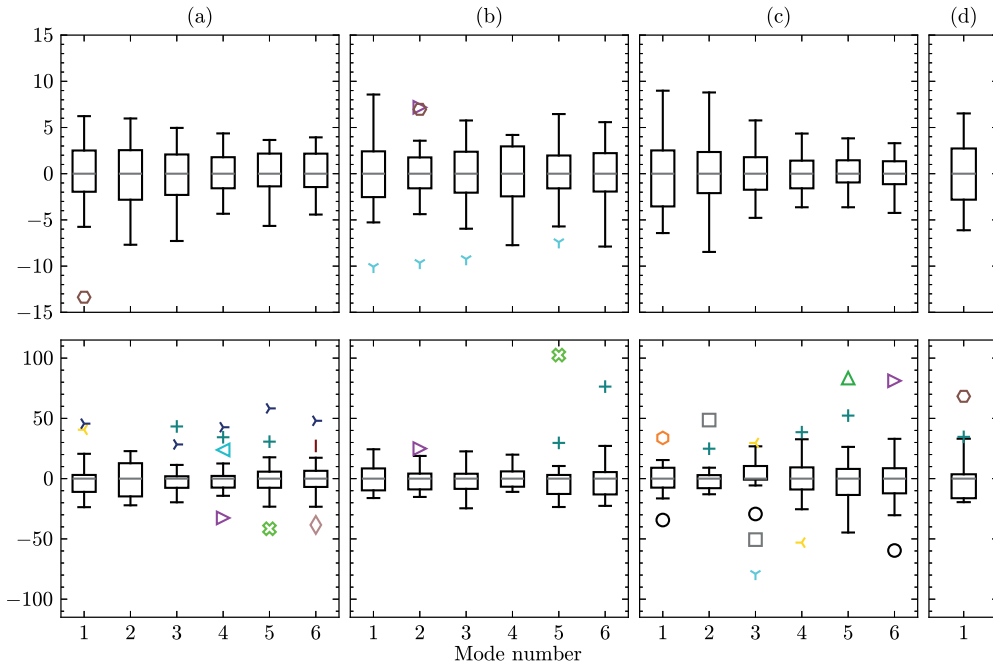


Fig. 10. Percentage relative variation in resonance frequencies (top subplots) [32] and corresponding modal damping (bottom subplots) for different modes: (a) Out-of-plane bending, (b) Torsional, (c) In-plane bending, and (d) Axial modes. The outlier marker colours are consistent with Figs. 5, 6, 7, and 9.

and in-plane bending modes. The sixth mode, in particular, shows high variability across all out-of-plane bending, torsional, and in-plane bending modes. The axial mode, on the other hand, displays a consistent modal complexity of nearly zero. Resonances exhibit increasing variability with higher-order modes, with torsional modes showing the highest overall variability, as illustrated in the mid-subplots of Fig. 9. Additionally, out-of-plane bending modes resonate at frequencies lower than those of torsional and in-plane bending modes. Despite these differences, the frequency spacing between modes appears relatively uniform. The percentage modal damping values reveal different characteristics and varying variability between the modes, as shown in the lower subplots of Fig. 9. On average, the mean modal damping value of the torsional modes is approximately 1%, while the out-of-plane and in-plane bending modes exhibit mean modal damping values of 0.76% and 0.62%, respectively. The torsional modal damping also shows a minimal number of outliers (indicated by markers). The variability in modal damping increases among higher-order modes compared to lower-order modes.

Insights into the relative variability in the resonances and their associated modal damping, with respect to their mean values, reveal different trends in different modes. For resonances, a consistent pattern of decreased variability is observed with an increase in the number of modes for the out-of-plane and in-plane bending modes. However, no such trend was observed among the torsional modes. In general, the variability in the resonances ranges mostly between ± 5 – 10% with respect to their mean values, except for a few outliers (see the top subplots in Fig. 10). The axial mode, on the other hand, displays a variability consistent with the first modes of vibration, that is, approximately $\pm 7\%$. In contrast, modal damping values exhibit significantly higher variability in all modes. The most substantial variability is observed in the higher-order torsional and in-plane bending modes, with values reaching up to ± 10 – 45% , except for outliers. Unlike the resonances, no consistent pattern of decreasing variability is identified for higher-order modes. On average, the variability in the modal damping is significantly higher than the relative variability in the natural frequencies. In addition, a higher number of outliers was identified for the modal damping values compared to the resonances, as shown at the bottom of Fig. 10.

Fitting a KDE function across the beams provides further insight into the variability in the resonances and their associated modal damping. The KDE estimation in Fig. 11 depicts the frequency and damping regions where resonance events and their related damping are likely to occur. The KDE estimation indicates the highest probability density among the bending modes compared to the torsional and axial modes, as shown in Fig. 11. The probability density decreases with an increasing frequency range. The KDE modal damping indicates a decrease in modal damping and their associated probability density with an increasing frequency range. The highest modal damping is observed among the torsional modes, whereas the lowest modal damping is observed among the in-plane bending and axial modes. The KDE estimation in Fig. 11 further highlights the more frequent occurrence coincidence of the out-of-plane and in-plane bending resonances within the lower frequency range. Variability across the frequency range also reveals wider variability ranges associated with torsional and axial modes compared to bending modes.

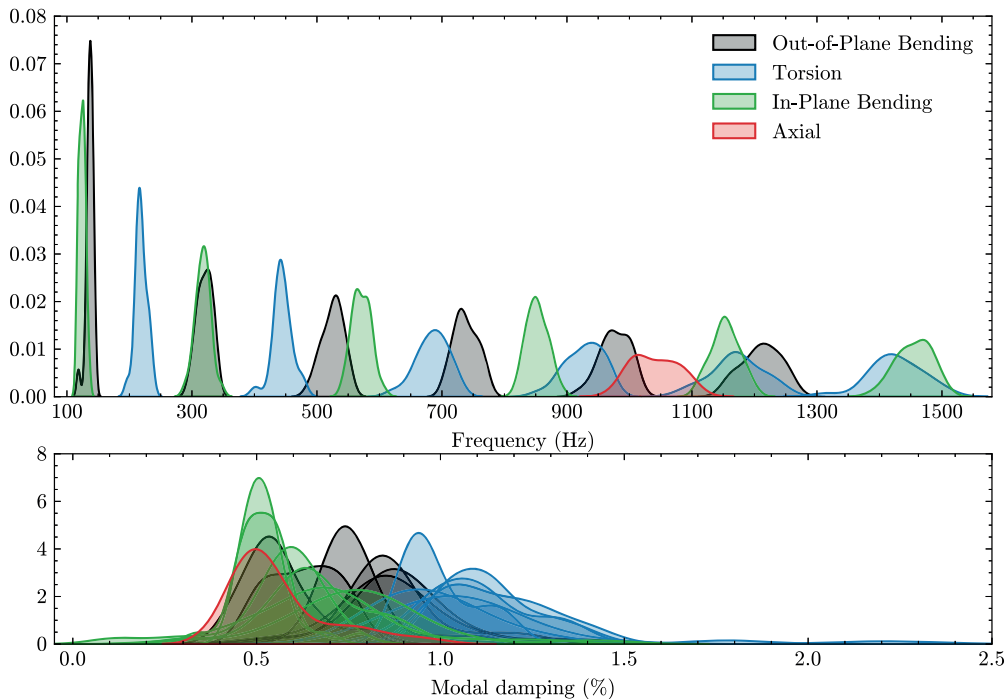


Fig. 11. Kernel Density Estimate (KDE) of the resonance distributions and their associated modal damping. The data includes six out-of-plane bending modes, six in-plane bending modes, six torsional modes, and one axial mode.

4. Conclusions

In this study, a detailed analysis of the variability in the modal characteristics of Cross-Laminated Timber (CLT) was performed. Experimental Modal Analysis (EMA) was performed on 24 beam-like CLT substructures, which were sawn from a larger CLT slab, under free-free boundary conditions to capture their vibration characteristics. The substructures were excited in the transverse, lateral, and axial directions to comprehensively assess their modal behaviour. The study focused on distinguishing the dynamic characteristics associated with out-of-plane bending, torsional, in-plane bending, and axial modes, as well as their respective modal parameters.

Analysis of driving transverse and axial transfer functions revealed a variation shift across the frequency spectrum while maintaining relatively small variability in resonance magnitudes. In contrast, lateral transfer functions exhibited not only a variability shift across the higher frequency spectrum but also an increased variability in magnitude with increasing frequency.

To quantify the variability in the amplitude of the transfer functions across the principal axes, the 95% confidence intervals were calculated, indicating that the variability in magnitude increases with increasing frequency among the transverse and lateral transfer functions. The Frequency Response Assurance Criterion (FRAC) showed variability in the transfer functions ranging between 0.9 and 1, with higher frequencies generally associated with increased variability.

The resonances and their associated modal damping indicate that the torsional modes exhibit higher variability and modal damping values compared to the other modes. A slight increase in the modal damping values was observed for the out-of-plane and in-plane bending modes. In contrast, a slight decrease in modal damping values was observed for torsional modes. Relative variability in the resonances with respect to their mean values indicated a variability between plus or minus 5–10% (except for outliers), with the torsional modes showing a higher overall variability. The analysis also showed a decrease in the variability with an increase in the number of modes among the out-of-plane bending and in-plane bending modes. In contrast, the relative variability of the modal damping values relative to their mean values showed significant variability between the modes, ranging between plus or minus 10–45% (except for outliers).

The Kernel Density Estimate (KDE) of the resonances confirmed a trend of increased variability with higher frequency ranges, with the highest variability observed in the torsional modes. Similarly, KDE analysis of modal damping confirmed that the torsional modes exhibit higher modal damping.

In conclusion, torsional modes were identified as having the highest variability in both resonance frequencies and modal damping, underscoring their sensitivity to changes in the structural characteristics of CLT. This finding highlights the importance

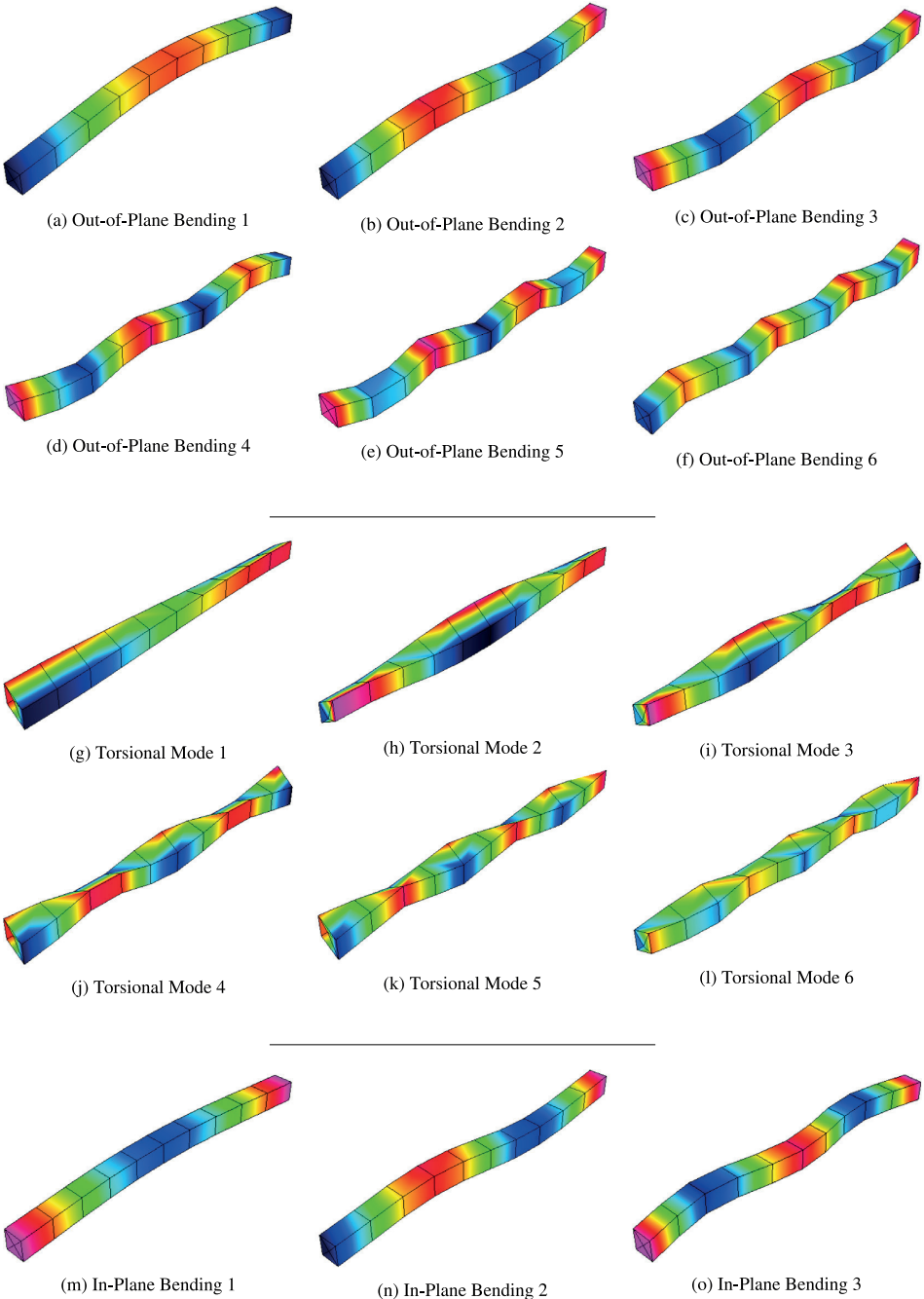


Fig. A.1. Illustration of six Out-of-plane bending modes, six torsional modes, six in-plane modes, and one axial mode. The colour map represents the modal displacement.

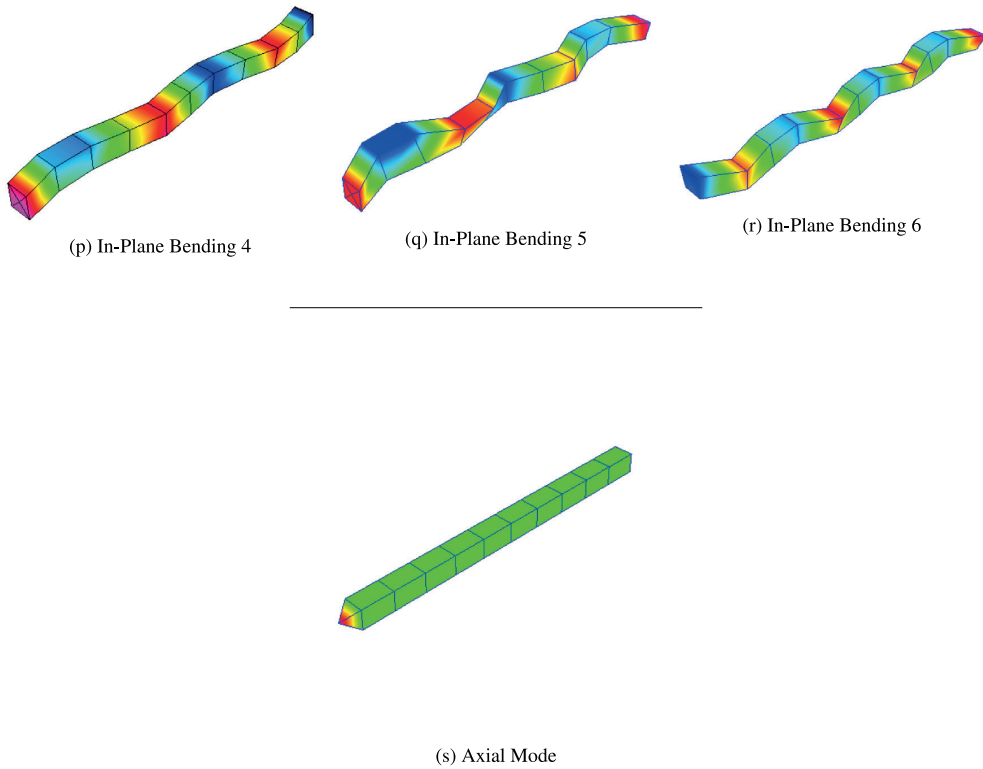


Fig. A.1. (continued).

of carefully considering torsional modes in the design and application of CLT structures, particularly where dynamic performance is critical.

Future research should explore the analysis of time-domain signals and investigate the effects of various types of excitation and averaging methods on the modal characteristics of CLT. Furthermore, examining the variability in the modal characteristics of tall CLT buildings subjected to stochastic excitations would provide further insights into the dynamic behaviour of CLT structures. This research will contribute to a deeper understanding of the dynamic performance of CLT and support advances in the design, safety, and optimisation of CLT structures.

CRediT authorship contribution statement

Benjamin Bondsman: Writing – review & editing, Writing – original draft, Visualization, Validation, Software, Resources, Methodology, Investigation, Formal analysis, Data curation, Conceptualization. **Andrew Peplow:** Writing – review & editing, Validation, Conceptualization.

Declaration of competing interest

The authors declare that they have no known competing financial interests or personal relationships that could have appeared to influence the work reported in this paper.

Acknowledgements

Tested materials were provided by Södra. The production of this article received no financial support.

Appendix

See Fig. A.1.

Data availability

Data will be made available on request.

References

- [1] James W. Cooley, John W. Tukey, An algorithm for the machine calculation of complex Fourier series, *Math. Comp.* 19 (90) (1965) 297–301.
- [2] C.Y. Shih, Y.G. Tsuei, R.J. Allemang, D.L. Brown, Complex mode indication function and its applications to spatial domain parameter estimation, *Mech. Syst. Signal Process.* 2 (4) (1988) 367–377.
- [3] Alessandro Fasana, Modal parameters estimation in the Z-domain, *Mech. Syst. Signal Process.* 23 (1) (2009) 217–225.
- [4] Mahmoud El-Kafafy, Bart Peeters, Theo Geluk, Patrick Guillaume, The MLM modal parameter estimation method: A new feature to maximize modal model robustness, *Mech. Syst. Signal Process.* 120 (2019) 465–485.
- [5] Adel Younis, Ambrose Dodoo, Cross-laminated timber for building construction: A life-cycle-assessment overview, *J. Build. Eng.* 52 (2022) 104482.
- [6] Angeliki Kylii, Paris A. Fokaides, Policy trends for the sustainability assessment of construction materials: A review, *Sustain. Cities Soc.* 35 (2017) 280–288.
- [7] Guillaume Habert, Sabbie A Miller, Vanderley M John, John L Provis, Aurélie Favier, Arpad Horvath, Karen L Scrivener, Environmental impacts and decarbonization strategies in the cement and concrete industries, *Nat. Rev. Earth Environ.* 1 (11) (2020) 559–573.
- [8] Reinhard Brandner, Georg Flatscher, Andreas Ringhofer, Gerhard Schickhofer, Alexandra Thiel, Cross laminated timber (CLT): Overview and development, *Eur. J. Wood Wood Prod.* 74 (2016) 331–351.
- [9] Reinhard Brandner, Production and technology of cross laminated timber (CLT): A state-of-the-art report, in: *Focus Solid Timber Solutions-European Conference on Cross Laminated Timber, CLT, University of Bath*, 2013, pp. 3–36.
- [10] Xiaofeng Sun, Minjuan He, Zheng Li, Novel engineered wood and bamboo composites for structural applications: State-of-art of manufacturing technology and mechanical performance evaluation, *Constr. Build. Mater.* 249 (2020) 118751.
- [11] Erol Karacabeyli, B. Douglas, CLT Handbook, US ed., FPInnovations and Binational Softwood Lumber Council, Point-Claire, Quebec, 2013.
- [12] Benjamin Bondsman, Andrew Peplow, Inverse parameter identification and model updating for cross-laminated timber substructures, *J. Build. Eng.* 95 (2024) 110209.
- [13] Forest Products Laboratory (US), *Wood Handbook: Wood as an Engineering Material*, vol. Number 72, The Laboratory, 1987.
- [14] David W. Green, Jerrold E. Winandy, David E. Kretschmann, Mechanical properties of wood, in: *Wood Handbook: Wood As an Engineering Material, General technical report FPL; GTR-113*, vol. 113, USDA Forest Service, Forest Products Laboratory, 1999, Madison, WI, 1999, pp. 4.1–4.45.
- [15] Charles C. Gerhards, Effect of moisture content and temperature on the mechanical properties of wood: An analysis of immediate effects, *Wood Fiber Sci.* (1982) 4–36.
- [16] Vanessa Baño, Francisco Arriaga, Manuel Guaita, Determination of the influence of size and position of knots on load capacity and stress distribution in timber beams of *pinus sylvestris* using finite element model, *Biosyst. Eng.* 114 (3) (2013) 214–222.
- [17] Elke Mergny, Raquel Mateo, Miguel Esteban, Pierre Latteur, Influence of cracks on the stiffness of timber structural elements, in: *Proceedings of the World Conference on Timber Engineering, Vienna, Austria*, 2016.
- [18] Sigurdur Ormarsson, Numerical Analysis of Moisture-Related Distortion in Sawn Timber (Ph.D. thesis), Chalmers University of Technology, Dep. of Structural Mech, 1999.
- [19] René Steiger, Arne Gülzow, Daniel Gsell, Non destructive evaluation of elastic material properties of crosslaminated timber (CLT), in: *Conference COST E*, vol. 53, Citeseer, 2008, pp. 29–30.
- [20] M. Kawrza, T. Furtmüller, C. Adam, R. Maderebner, Experimental modal analysis of a cross-laminated timber slab, *Mater. Today: Proc.* 62 (2022) 2611–2616.
- [21] Adam Faircloth, Loic Brancheriau, Hassan Karampour, Stephen So, Henri Bailleres, Chandan Kumar, Experimental modal analysis of appropriate boundary conditions for the evaluation of cross-laminated timber panels for an in-line approach, *For. Prod. J.* 71 (2) (2021) 161–170.
- [22] Michael Kawrza, Thomas Furtmüller, Christoph Adam, Experimental and numerical modal analysis of a cross laminated timber floor system in different construction states, *Constr. Build. Mater.* 344 (2022) 128032.
- [23] Thomas Reynolds, Daniele Casagrande, Roberto Tomasi, Comparison of multi-storey cross-laminated timber and timber frame buildings by in situ modal analysis, *Constr. Build. Mater.* 102 (2016) 1009–1017.
- [24] Blaž Kurent, Boštjan Brank, Wai Kei Ao, Model updating of seven-storey cross-laminated timber building designed on frequency-response-functions-based modal testing, *Struct. Infrastruct. Eng.* 19 (2) (2023) 178–196.
- [25] Angelo Aloisio, Dag Pasca, Roberto Tomasi, Massimo Fragiaco, Dynamic identification and model updating of an eight-storey CLT building, *Eng. Struct.* 213 (2020) 110593.
- [26] Blaž Kurent, Wai Kei Ao, Aleksandar Pavic, Fernando Pérez, Boštjan Brank, Modal testing and finite element model updating of full-scale hybrid timber-concrete building, *Eng. Struct.* 289 (2023) 116250.
- [27] Khai Quang Mai, Aron Park, Khoa Tan Nguyen, Kihak Lee, Full-scale static and dynamic experiments of hybrid CLT–concrete composite floor, *Constr. Build. Mater.* 170 (2018) 55–65.
- [28] Ebenezer Ussher, Kaveh Arjomandi, Jan Weckendorf, Ian Smith, Predicting effects of design variables on modal responses of CLT floors, in: *Structures*, vol. 11, Elsevier, 2017, pp. 40–48.
- [29] Fredrik Ljunggren, Innovative solutions to improved sound insulation of CLT floors, *Dev. Built Environ.* 13 (2023) 100117.
- [30] Angelo Aloisio, Dag Pasquale Pasca, Blaž Kurent, Roberto Tomasi, Long-term continuous dynamic monitoring of an eight-story CLT building, *Mech. Syst. Signal Process.* 224 (2025) 112094.
- [31] SIS, Structural Timber – Strength Classes, Standard SS-EN 338:2016, Swedish Institute for Standards, Stockholm, Sweden, 2016.
- [32] Benjamin Bondsman, Ola Flodén, Henrik Danielsson, Peter Persson, Erik Serrano, Modal analysis of CLT beams: Measurements and predictive simulations, in: *Alphose Zingoni (Ed.), Current Perspectives and New Directions in Mechanics, Modelling and Design of Structural Systems*, 2022, pp. 56–62.
- [33] Anders Brandt, Noise and Vibration Analysis: Signal Analysis and Experimental Procedures, John Wiley & Sons, 2023.
- [34] Daniel C. Kammer, Sensor placement for on-orbit modal identification and correlation of large space structures, *J. Guid. Control Dyn.* 14 (2) (1991) 251–259.
- [35] Andreas Linderholt, Thomas Abrahamsson, Optimising the informativeness of test data used for computational model updating, *Mech. Syst. Signal Process.* 19 (4) (2005) 736–750.
- [36] Randall J. Allemang, A correlation coefficient for modal vector analysis, in: *Proc. of the 1st IMAC*, 1982, pp. 110–116.
- [37] Claude E. Shannon, Communication in the presence of noise, *Proc. IRE* 37 (1) (1949) 10–21.
- [38] Thomas G. Carne, D. Todd Griffith, Miguel E. Casias, Support conditions for experimental modal analysis, *Sound Vib.* 41 (6) (2007) 10–16.
- [39] Brüel, Kjær, Impact Hammers — Types 8206, 8206-001, 8206-002 and 8206-003, Product Data BP 2078 – 12, Brüel & Kjær Sound & Vibration Measurement, Nærum, Denmark, 2005.
- [40] Brüel, Kjær, Piezoelectric Charge Accelerometer Types 4500-A, 4501-A, and 4501-A-001, Product Data BP1427 – 15, Brüel & Kjær Sound & Vibration Measurement, Nærum, Denmark, 2018.

- [41] Brüel, Kjær, LAN-XI Data Acquisition Hardware: Frames, Modules and Front Panels, Product Data BP 2215 – 38, Brüel & Kjær Sound & Vibration Measurement, Nærum, Denmark, 2022.
- [42] Randall Allemang, Peter Avitabile, Handbook of Experimental Structural Dynamics, Springer Nature, 2022.
- [43] James W. Cooley, John W. Tukey, On the origin and publication of the FFT paper—A citation-classic commentary on an algorithm for the machine calculation of complex Fourier-series by cooley, JW, and tukey, JW, *Curr. Contents/ Phys. Chem. Earth Sci.* 51–52 (1993) 8–9.
- [44] Roy R. Craig Jr., Andrew J. Kurdila, Fundamentals of Structural Dynamics, John Wiley & Sons, 2006.
- [45] N. Thrane, The Discrete Fourier Transform and Fft Analyzers, Technical Review No. 1, Bruel & Kjaer, 1979.
- [46] Alan V. Oppenheim, Discrete-time Signal Processing, Pearson Education India, 1999.
- [47] John G. Proakis, Digital Signal Processing: Principles, Algorithms, and Applications, 4/E, Pearson Education India, 2007.
- [48] Randall J. Allemang, et al., Vibrations: Experimental Modal Analysis, Structural Dynamics Research Laboratory, Department of Mechanical, Industrial and Nuclear Engineering, University of Cincinnati, 1999.
- [49] Brüel, Kjær, BK Connect Structural Dynamics: Modal Analysis Type 8420, Modal Analysis (advanced) Type 8420-A and Geometry Type 8410, Product Data BP 1523 – 16, Brüel & Kjær Sound & Vibration Measurement, Nærum, Denmark, 2021.
- [50] Mark H. Richardson, David L. Formenti, Parameter estimation from frequency response measurements using rational fraction polynomials, in: *Proceedings of the 1st International Modal Analysis Conference*, vol. 1, Citeseer, 1982, pp. 167–186.
- [51] Ward Heylen, Stefan Lammens, FRAC: A consistent way of comparing frequency response functions, in: *Proceedings of the Conference on Identification in Engineering Systems*, 1996, pp. 48–57.
- [52] Pauli Virtanen, Ralf Gommers, Travis E. Oliphant, Matt Haberland, Tyler Reddy, David Cournapeau, Evgeni Burovski, Pearu Peterson, Warren Weckesser, Jonathan Bright, Stéfan J. van der Walt, Matthew Brett, Joshua Wilson, K. Jarrod Millman, Nikolay Mayorov, Andrew R.J. Nelson, Eric Jones, Robert Kern, Eric Larson, C J Carey, İlhan Polat, Yu Feng, Eric W. Moore, Jake VanderPlas, Denis Laxalde, Josef Perktold, Robert Cimrman, Ian Henriksen, E.A. Quintero, Charles R. Harris, Anne M. Archibald, António H. Ribeiro, Fabian Pedregosa, Paul van Mulbregt, SciPy 1.0 Contributors, SciPy 1.0: Fundamental algorithms for scientific computing in python, *Nature Methods* 17 (2020) 261–272.

Paper II

B. Bondsman, A. Peplow

Inverse parameter identification and model updating for Cross-laminated Timber substructures

Journal of Building Engineering, Vol. 95, 110209, 15.06.2024



Contents lists available at ScienceDirect

Journal of Building Engineering

journal homepage: www.elsevier.com/locate/job

Full length article

Inverse parameter identification and model updating for Cross-laminated Timber substructures

Benjamin Bondsman^{a,*}, Andrew Peplow^b^a Lund University, John Ericssons väg 1, SE-223 63, Lund, Kingdom of Sweden^b Sweco, Malmö Acoustics, Drottningstorg 14, SE-211 25, Malmö, Kingdom of Sweden

ARTICLE INFO

Keywords:

Model updating
Single-Objective Optimisation
Experimental Modal Analysis
Cross-laminated Timber
Mechanical properties

ABSTRACT

Finite Element (FE) model updating is crucial for identifying key parameters in structural design and improving predictive accuracy. Despite extensive research on advanced FE procedures approved for user applications, persistent disparities remain in real-world scenarios, especially for complex materials like wood. Capturing accurate mechanical characteristics with traditional models poses challenges in sustainability projects. This study introduces a derivative-free model updating procedure using a Single-Objective Optimisation (SOO) incorporating observed and predicted natural frequencies and vibration modes. The objective function optimises tuning parameters to minimise discrepancies between predicted and observed outcomes. The focus is on Cross-laminated Timber (CLT), a composite wooden structure gaining traction as a sustainable alternative to materials like reinforced concrete and steel. However, the mechanical properties of CLT can vary due to inherent variability in wood's mechanical characteristics. This research identifies sensitive mechanical properties — longitudinal Young's modulus, internal shear moduli, and rolling shear modulus of CLT — using a model updating procedure based on a comprehensive set of data from Experimental Modal Analysis (EMA). The study provides mathematical algebraic derivations of the updating procedure and a step-by-step implementation algorithm to facilitate practical application in structural engineering.

1. Introduction

In the field of structural engineering and analysis, accurate modelling and representation of structures are essential to ensure the safety, reliability, and optimal use of materials. A precise computer representation of structures allows for the simulation of scenarios that can be challenging to measure in reality. For example, simulation of multistorey buildings under motion-induced wind loads with different excitation patterns, investigation of long-span bridges under varying traffic load patterns, analysis of the dynamic response of an aircraft during landings in adverse weather conditions, or simulation of the dynamic behaviour of radioactive components within nuclear reactors. These computer simulations help engineers uncover potential weaknesses and vulnerabilities in the design of structures subjected to dynamic loading throughout their useful life. Despite the availability of advanced Finite Element (FE) modelling procedures [1], real-world applications frequently expose disparities between predicted and observed results, primarily attributable to inherent modelling assumptions [2]. FE representation errors can be divided into the following categories: (i) idealisation errors, (ii) discretisation errors, and (iii) incorrect material properties. Idealisation errors comprise the representation of physical structures using engineering structural elements (e.g., beams, plates, or shells). In contrast, the discretisation errors include using FEs and their associated order of approximation. And errors stemming from incorrect material

* Corresponding author.

E-mail address: Benjamin.bondsman@construction.lth.se (B. Bondsman).<https://doi.org/10.1016/j.job.2024.110209>

Received 1 February 2024; Received in revised form 19 June 2024; Accepted 12 July 2024

Available online 15 July 2024

2352-7102/© 2024 The Author(s). Published by Elsevier Ltd. This is an open access article under the CC BY license (<http://creativecommons.org/licenses/by/4.0/>).

properties that encompass incorrect assumptions regarding material strength or distribution of mass. Although measurements are often considered as references in model updating procedures, they can also contain uncertainties due to environmental noise, boundary conditions, excitation variability, etc. [3,4]. A detailed description of these errors can be found in the work of Mottershead, Link, and Friswell, [2].

In the case of complex materials such as wood, whose mechanical behaviour and properties are strongly linked to growing conditions, the approximation of its mechanical properties often fails to yield accurate assumptions. The complexity of wood behaviour underlines the challenges faced in accurately representing its mechanical characteristics within the confines of traditional modelling approaches. Therefore, updating an FE representation model based on observed experimental data becomes imperative to attain an accurate representation model. Mitigating the discord between the predicted and observed results can be accomplished by formulating a residual term that encapsulates the discrepancy between the predicted and observed results. Subsequently, adjusting the modelling assumptions (or tuning parameters) to mitigate the residual term to a satisfactory level, [5]. Consequently, computational procedures have been developed to update the tuning parameters on the basis of observed data. In particular, the observed data from Experimental Modal Analysis (EMA) have found broad applications as a target to identify optimal tuning parameters, [5,6]. The model updating procedure has become important in the identification of unknown model parameters, primarily due to a lack of existing knowledge or a variation in the mechanical properties of structures over time. The unknown model parameters are often associated with new or complex materials such as wood. The variation in material properties over time includes changes caused by environmental and temperature fluctuations [7–9], cyclic fatigue, and damage [10–12].

Several procedures have been proposed to identify the mechanical properties of materials. In 1978, Baruch and Bar-Itzhack introduced a direct model updating approach by minimising the weighted norm of the difference between observed and predicted modes, subject to orthogonality to the mass matrix, [13]. In their method, they focused on updating the stiffness matrix while assuming the correctness of the mass matrix. Baruch extended this approach by proposing a similar model updating procedure that specifically targeted the stiffness matrix. This was achieved by minimising the weighted norm of the difference between observed and predicted stiffness, using Lagrange multipliers, [14]. The latter approach of Baruch was further developed by Berman, who introduced a direct method to update the mass matrix using Lagrange multipliers, [15]. Chen et al. suggested the simultaneous updating of the mass and stiffness matrices, [16]. In 1983, Berman and Nagy combined the sequential updating of the stiffness and mass matrices with mode orthogonality constraints to introduce a complete model-updating procedure [17]. The model updating techniques described in [13–15] constitute a comprehensive set of model updating techniques, encompassing both stiffness and mass updating while adhering to orthogonality constraints of the modes. Model updating methods can be categorised into Sensitivity-based model updating [2,18,19], Bayesian model updating [20], Optimisation-based model updating [21–23], FE model correlation [24,25], Statistical model updating [26,27], and Sequential model updating [28,29]. Other researchers have also proposed the optimisation of the informativeness of test data for model updating, e.g. the work by Linderholt and Abrahamsson [30]. For further reading on the development of model update methods, the reader is referred to [5,31–34] and the state-of-the-art review by Sehgal and Kumar, [35].

In this work, the main focus is on the optimisation-based model updating of Cross-laminated Timber (CLT) substructures to identify unknown sensitive mechanical properties. CLT, as a sustainable and versatile alternative to conventional building materials such as reinforced concrete and steel, has gained prominence in modern construction over recent decades. The composition of CLT involves a unique arrangement of juxtaposed layers of lumber boards, positioned crosswise at an angle of 90° between one layer and the adjacent ones. More information on the development of CLT can be found in [36]. Previous studies on updating the CLT model have focused primarily on multi-storey CLT buildings, using lower frequency modes of vibration, as seen in [22,37–39]. However, because of inherent disparities in the nature of wood, individual wooden structures exhibit different properties. Consequently, obtaining statistical data, particularly from numerous nominally identical CLT substructures, is imperative for a comprehensive understanding of the mechanical properties of CLT. Hence, this paper introduces a numerical computational framework for model updating, employing an optimisation-based approach, which utilises EMA results obtained from multiple nominally identical CLT substructures. The optimisation problem is mathematically formulated as a Single-Objective Optimisation (SOO) comprising two nested objectives related to natural frequencies and vibration modes. The SOO is subsequently minimised using the derivative-free simplex method by Nelder and Mead [40]. The key reason for using the derivative-free simplex method lies in its independence from the gradient of the objective function, which is often approximated using numerical differentiation (e.g., Finite Difference Method (FDM)) [41]. Thus, the derivative-based optimisation algorithms require computation of the Jacobian or Hessian, which can be computationally intensive. A study by Ozaki et al. [42], comparing different optimisation methods, indicates that the simplex method outperforms several popular existing optimisation methods such as Random Search, Bayesian Optimisation, Coordinate-search method and Covariance Matrix adaptation evolution strategy. Furthermore, the simplex method has been successfully applied to a wide range of problems; for example, see [43] and references therein. Moreover, the simplex method does not necessitate any bounds for tuning parameters, making it particularly suitable for updating the CLT model where such bounds may be unknown. By employing the simplex method, we avoid the approximations inherent in computing gradients, Jacobians, Hessians, and associated regularisation terms, and tuning parameter boundaries.

This work focuses primarily on updating the FE model to determine the mechanical properties of CLT and quantify their variability. The presented model updating procedure effectively reduces discrepancies between predicted and observed results while identifying pertinent tuning parameters. The findings of this study provide crucial insight for design engineers and researchers in the field of timber engineering.

The structure of the rest of this article is structured as follows. Section 2 presents a comprehensive derivation of the model generation and updating framework. Section 3 details the model updating of CLT substructures using an extensive collection of observed data from the EMA as a reference, and conclusions are drawn in Section 4.

2. Model generation and updating framework

This section offers the necessary definitions and mathematical algebraic derivations. A residual function is introduced to construct an objective function which is subsequently minimised to quantify and address the disparity between the observed (measurements) and predicted (FE) outcomes. The analogy behind model updating comprises the following key steps: (i) selecting several observed outputs and their corresponding predicted counterparts, (ii) comparing these outputs and determining the distance (in some cases relative distance) between them, and (iii) updating the sensitive tuning parameters to minimise the distance between the observed and predicted outcomes. The model outputs often comprise natural frequencies and modes in structural dynamics, whilst the tuning parameters often comprise stiffness, mass, and geometrical parameters to be updated. Therefore, the tuning parameters are updated until the distance between the output quantities is minimised to a satisfied criterion, [2].

2.1. Residual formulation

To compute the predicted outputs, it is necessary to discretise the physical structure within the FE framework. The undamped equations of motion for the corresponding FE model denoted as $\mathcal{M}^{(k)}$ at iteration k , can be expressed as:

$$\mathbf{M}^{(k)}\ddot{\mathbf{U}}^{(k)} + \mathbf{K}^{(k)}\mathbf{U}^{(k)} = \mathbf{f}^{(k)}, \quad (1)$$

where $\mathbf{M}^{(k)}$ and $\mathbf{K}^{(k)}$ are respectively lumped mass matrix and positive semi-definite stiffness matrix. The time-dependent nodal accelerations, displacements, and external forces are denoted $\ddot{\mathbf{U}}^{(k)}$, $\mathbf{U}^{(k)}$, and $\mathbf{f}^{(k)}$, respectively. The superscript k signifies the quantities at k th iteration as the model gets updated. The predicted outputs employed in the model updating procedure can be obtained from an eigenvalue analysis as:

$$\left(\mathbf{K}^{(k)} - \omega_j^{2(k)} \mathbf{M}^{(k)} \right) \boldsymbol{\psi}_j^{(k)} = \mathbf{0}^{(k)}, \quad j = 1, 2, \dots, N_j, \quad (2)$$

where $\omega_j^{(k)}$ is j th angular eigensolution in [rad/s] and $\boldsymbol{\psi}_j^{(k)}$ is the associated conjugate mode. The angular eigensolution's equivalent natural frequency in [Hz] can be determined as $f_j^{(k)} = \omega_j^{(k)} / 2\pi$. The eigenmodes are all mass-normalised such that $\boldsymbol{\psi}_j^{(k)\top} \mathbf{M}^{(k)} \boldsymbol{\psi}_j^{(k)} = \mathbf{I}$, in which \mathbf{I} denotes unity. The total number of eigensolutions to be determined is denoted N_j , which also denotes the total number of outputs.

The predicted outputs are denoted $\mathbf{z}(\theta)$, which is a function of p model parameters θ , i.e., $\theta_i \in \{1, 2, \dots, p\}$, whilst their corresponding observed counterparts are denoted $\bar{\mathbf{z}}$. The discrepancy between the observed and predicted outputs can be determined by formulating a residual term,

$$\mathbf{r}(\theta)^{(k)} = \bar{\mathbf{z}} - \mathbf{z}^{(k)}(\theta). \quad (3)$$

The relationship between the residual $\mathbf{r}^{(k)}(\theta)$ and the model parameters $\theta^{(k)}$ is often non-linear. Studies employing classical gradient-based optimisation have suggested linearising the residual using a truncated Taylor series, as indicated by Bartilson et al. in their work [44]. However, it is important to note that, in the present case, such linearisation is not necessary as no valley-seeking minimisation approach is being used. To begin the procedure of optimisation, a weighted sum-of-squared residual (WSSR) is defined which is commonly employed in model updating and parameter estimation to determine the total discrepancy between the observed and predicted outputs. The WSSR is subsequently minimised to reduce the distance between the observed and predicted outputs, leading to the determination of optimal values for $\theta^{(k)}$, often denoted as θ^* . The model outputs comprise, in the present case, natural frequencies and modes. Therefore, the residual term can be decomposed into a residual term associated with natural frequencies $\mathbf{r}_f^{(k)}$ and a residual term associated with the natural modes $\mathbf{r}_\psi^{(k)}$. Using a concatenation of $\mathbf{r}_f^{(k)}$ and $\mathbf{r}_\psi^{(k)}$. Hence, the total residual can be defined and used to compute the WSSR as:

$$\mathcal{E}^{(k)} = \mathbf{r}^{(k)\top} \mathbf{W}^{(k)} \mathbf{r}^{(k)} = \begin{bmatrix} \mathbf{r}_f^{(k)\top} & \mathbf{r}_\psi^{(k)\top} \end{bmatrix} \begin{bmatrix} \mathbf{W}_f^{(k)} & \mathbf{0}^{(k)} \\ \mathbf{0}^{(k)} & \mathbf{W}_\psi^{(k)} \end{bmatrix} \begin{bmatrix} \mathbf{r}_f^{(k)} \\ \mathbf{r}_\psi^{(k)} \end{bmatrix}, \quad (4)$$

where $\mathbf{W}^{(k)}$ is a symmetric positive semi-definite matrix reflecting the uncertainty in the residual terms concerning the tuning parameters θ , and contains the residual weighting of the natural frequencies and their conjugate modes, i.e., $\mathbf{W}_f^{(k)}$ and $\mathbf{W}_\psi^{(k)}$. In the present work, a simple choice of \mathbf{W} is considered using the Tikhonov regularisation $\mathbf{W} = \mathbf{I}$, [19,44]. Other choices of \mathbf{W} suitable for gradient-based optimisation can comprise the inverse of the observed and predicted parameter covariance matrices, as elaborated in [45–48].

The matrix multiplication in (4) results in two WSSR terms as follows:

$$\mathcal{E}_f^{(k)} = \mathbf{r}_f^{(k)\top} \mathbf{W}_f^{(k)} \mathbf{r}_f^{(k)}, \quad (5a)$$

$$\mathcal{E}_\psi^{(k)} = \mathbf{r}_\psi^{(k)\top} \mathbf{W}_\psi^{(k)} \mathbf{r}_\psi^{(k)}, \quad (5b)$$

where $\mathcal{E}_f^{(k)}$ and $\mathcal{E}_\psi^{(k)}$ refer to the WSSR terms associated with the natural frequencies and natural modes, respectively.

The residual term associated with the natural frequencies can be formulated using a relative difference between the observed outputs $\bar{\mathbf{z}}$ and the predicted outputs $\mathbf{z}^{(k)}(\theta)$,

$$\mathbf{r}_f^{(k)} = \left(\mathbf{z}_f^{(k)}(\theta) \cdot \mathbf{I} \right)^{-1} \left(|\bar{\mathbf{z}}_f - \mathbf{z}_f^{(k)}(\theta)| \right), \quad (6)$$

where the dot product denotes element-by-element operation. The observed and predicted undamped natural frequencies are respectively defined as:

$$\tilde{\mathbf{z}}_f = [\tilde{f}_1, \tilde{f}_2, \dots, \tilde{f}_{N_j}]^T \quad (7a)$$

$$\mathbf{z}_f^{(k)}(\theta) = [f_1^{(k)}(\theta), f_2^{(k)}(\theta), \dots, f_{N_j}^{(k)}(\theta)]^T \quad (7b)$$

The components in (7) are rearranged, if necessary, using mode pairing, as described in [49]. The natural frequencies of the vibrating substructure are assumed to be decoupled, resulting in a diagonalised form of \mathbf{W}_f . Hence, the $\mathcal{E}_f^{(k)}$ in (5a) can be simplified to

$$\mathcal{E}_f^{(k)} = \mathbf{r}_f^{(k)T} \mathbf{W}_f^{(k)} \mathbf{r}_f^{(k)} = \sum_{j=1}^{N_j} W_{f,jj}^{(k)} \left(|\tilde{f}_j - f_j^{(k)}(\theta)| / f_j^{(k)}(\theta) \right)^2. \quad (8)$$

The residual term associated with the natural modes can be defined as the discrepancy between the observed and predicted modes,

$$\mathbf{r}_\psi^{(k)} = \tilde{\mathbf{z}}_\psi - \mathbf{z}_\psi^{(k)}(\theta), \quad (9)$$

where the observed and predicted mode matrices (sorted according to the pairing results) are respectively defined as:

$$\tilde{\mathbf{z}}_\psi = [\tilde{\psi}_1, \tilde{\psi}_2, \dots, \tilde{\psi}_{N_j}], \quad (10a)$$

$$\mathbf{z}_\psi^{(k)}(\theta) = [\lambda_1^{(k)}(\theta) \psi_1^{(k)}(\theta), \lambda_2^{(k)}(\theta) \psi_2^{(k)}(\theta), \dots, \lambda_{N_j}^{(k)}(\theta) \psi_{N_j}^{(k)}(\theta)]. \quad (10b)$$

In the expression above, the observed mode matrix $\tilde{\mathbf{z}}_\psi$ contains the j th unit-normalised modes, determined as $\tilde{\psi}_j = \tilde{\psi}_j / \sqrt{\tilde{\psi}_j^T \tilde{\psi}_j}$. In the same manner, the predicted mode matrix $\mathbf{z}_\psi^{(k)}(\theta)$ contains the j th unit-normalised mode vector $\psi_j^{(k)}(\theta)$ using the modal scale factor $\lambda_j^{(k)}(\theta) = \tilde{\psi}_j^T \psi_j^{(k)}(\theta)$. The modal scaling factor reflects the difference between $\tilde{\psi}_j$ and $\psi_j^{(k)}(\theta)$ considering a least-square approach, [44,49].

The decoupled characteristics of the natural frequencies and their conjugate modes result in a diagonalised $\mathbf{W}_\psi^{(k)}$, thus, the $\mathcal{E}_\psi^{(k)}$ in (5b) can be simplified to

$$\mathcal{E}_\psi^{(k)} = \mathbf{r}_\psi^{(k)T} \mathbf{W}_\psi^{(k)} \mathbf{r}_\psi^{(k)} = \sum_{j=1}^{N_j} W_{\psi,jj}^{(k)} \mathbf{r}_{\psi,j}^{(k)T} \mathbf{r}_{\psi,j}^{(k)} = \sum_{j=1}^{N_j} W_{\psi,jj}^{(k)} \left\| \tilde{\psi}_j - \lambda_j \psi_j^{(k)}(\theta) \right\|_2^2, \quad (11)$$

where the residual term associated with j th mode-pair is defined as $\mathbf{r}_{\psi,j}^{(k)} = \tilde{\psi}_j^{(k)} - \lambda_j^{(k)} \psi_j^{(k)}(\theta)$ and $\| \cdot \|_2$ denotes the L^2 norm. The crossMAC between the observed and predicted modes can be defined as:

$$\text{MAC}^{(k)}(\tilde{\psi}_i, \psi_j^{(k)}(\theta)) = \frac{|\tilde{\psi}_i^H \psi_j^{(k)}(\theta)|^2}{(\tilde{\psi}_i^H \tilde{\psi}_i) (\psi_j^{(k)H}(\theta) \psi_j^{(k)}(\theta))}, \quad (12)$$

where the superscript H denotes the Hermitian transpose, [49]. Substituting (12) into (11) simplifies the expression of $\mathcal{E}_\psi^{(k)}$ in (11) to

$$\mathcal{E}_\psi^{(k)} = \mathbf{r}_\psi^{(k)T} \mathbf{W}_\psi^{(k)} \mathbf{r}_\psi^{(k)} = \sum_{i,j=1}^{N_j} W_{\psi,ij}^{(k)} \left[1 - \text{diag} \left(\text{MAC}^{(k)}(\tilde{\psi}_i, \psi_j^{(k)}(\theta)) \right) \right]. \quad (13)$$

Combining expressions (8) and (13) yields a simplified expression for WSSR in (4) as:

$$\mathcal{E}^{(k)} = \sum_{j=1}^{N_j} W_{f,jj}^{(k)} \left(|\tilde{f}_j - f_j^{(k)}(\theta)| / f_j^{(k)}(\theta) \right)^2 + \sum_{i,j=1}^{N_j} W_{\psi,ij}^{(k)} \left[1 - \text{diag} \left(\text{MAC}^{(k)}(\tilde{\psi}_i, \psi_j^{(k)}(\theta)) \right) \right]. \quad (14)$$

The WSSR contains all model outputs to be correlated, which subsequently will be used in the formulation of the objective function.

2.2. Model parameterisation

The parametrisation is a crucial aspect of model updating within an FE framework. This is because the numerical model involves a multitude of parameters that encompass geometrical definitions, material properties, and external conditions. Effective parameterisation is essential for the success of the overall model updating process. The parametrisation must adhere to the following criteria, as outlined in [50,51]:

1. Mitigate ill-posedness by restricting the number of tuning parameters,
2. Ensure that the parameters capture model uncertainty, and

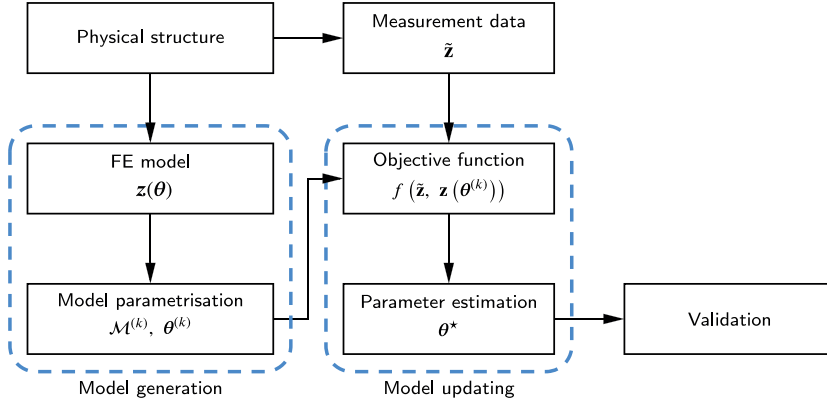


Fig. 1. Flowchart illustrating the sequential steps in the generation, updating, and validation of FE models in structural dynamics. The symbols $\tilde{\mathbf{z}}$, $\mathbf{z}(\theta)$, $\mathcal{M}^{(k)}$, $\theta^{(k)}$, and θ^* represent, respectively, the observed results, predicted results, FE model at iteration k , tuning parameters at iteration k , and the optimal tuning parameters.

3. Confirm that the FE model outputs exhibit sensitivity to the chosen parameters.

Since each FE e in the discretised model has its properties, updating $\theta^{(k)}$, which can contain many parameters varying in magnitude, can result in ill-conditioning of the objective function. Therefore each element system matrix, i.e., \mathbf{M}_e and \mathbf{K}_e , shall be modified at each iteration before summation into the global system matrices as:

$$\mathbf{M}^{(k)}(\theta) = \sum_{e=1}^{n_{el}} \mathbf{M}_e^{(k)}(1 - \delta_e^m) = \mathbf{M}_0 - \sum_{e=1}^{n_{el}} \mathbf{M}_e^{(k)} \delta_e^m, \quad (15a)$$

$$\mathbf{K}^{(k)}(\theta) = \sum_{e=1}^{n_{el}} \mathbf{K}_e^{(k)}(1 - \delta_e^k) = \mathbf{K}_0 - \sum_{e=1}^{n_{el}} \mathbf{K}_e^{(k)} \delta_e^k, \quad (15b)$$

where the system matrices $\mathbf{M}_0^{(k)}$ and $\mathbf{K}_0^{(k)}$ are respectively the global mass and stiffness matrices computed using the initial guess of the parameters θ_0 . The update of the mass and stiffness parameters is denoted δ_e^m and δ_e^k associated with FE e , respectively. In this work, the updating process focuses exclusively on the orthotropic stiffness parameters E_x , $G_{xy} = G_{xz}$, and G_{yz} . Consequently, for each FE, the associated modification parameters are $\delta_e^{k,1}$ (about E_x), $\delta_e^{k,2}$ (related to $G_{xy} = G_{xz}$) and $\delta_e^{k,3}$ (linked to G_{yz}). Therefore, the overall count of the modification parameters is $d = 3 \times n_{el}$, where n_{el} denotes the total number of FEs.

In some cases, the substructure system matrices contain a large number of equations, which can be computationally intensive. To overcome computational barriers, the system matrices in (15) can be truncated using, for example, Modal Truncation (MT) [52], or Component Mode Synthesis (CMS) approaches [53–55].

2.3. Objective function

With the expression (14), the following objective function can be formulated as a nested minimisation problem to update the FE model. The objective is to minimise the discrepancy between the observed and predicted outcomes and the model tuning parameters θ^* ,

$$\theta^* = \underset{\theta}{\operatorname{argmin}} \left\{ \sum_{j=1}^{N_j} W_{f,jj}^{(k)} \left(|\tilde{f}_j - f_j^{(k)}(\theta)| / f_j^{(k)}(\theta) \right)^2 + \sum_{i,j=1}^{N_j} W_{\psi,jj}^{(k)} \left[1 - \operatorname{diag} \left(\operatorname{MAC}^{(k)} \left(\tilde{\psi}_i, \psi_j^{(k)}(\theta) \right) \right) \right] \right\}. \quad (16)$$

In this formulation, the optimisation task involves simultaneously minimising two nested objectives: the first related to the frequencies $f_j^{(k)}(\theta)$, and the second related to the vibration modes $\psi_j^{(k)}(\theta)$. The minimisation mechanism seeks to identify the optimal tuning parameters of θ by simultaneously minimising both nested objectives, which results in a Single-objective optimisation (SOO) problem, [56,57]. Given the unknown upper and lower limits of the model parameters θ , the problem inherently takes the form of an unconstrained minimisation problem.

2.4. Parameter identification and model validation

To identify the optimal tuning parameters discussed in Section 2.2, the gradient-free simplex method by Nelder and Mead [40] can be used to minimise the objective function in (16). Widely recognised for its robustness and efficacy, especially in handling

Algorithm 1 Model updating, parameter identification and validation procedure.

```

1: Initialise:  $\mathbf{M}_0, \mathbf{K}_0, \tilde{\mathbf{z}}_f, \tilde{\mathbf{z}}_\psi, \mathbf{W}_f^{(0)}, \mathbf{W}_\psi^{(0)}, \theta_0$ 
2: while  $\|\theta^{(k)} - \theta^{(k-1)}\| < 1 \times 10^{-2}$  do
3:   Compute predicted outputs  $\mathbf{z}_f^{(k)}(\theta), \mathbf{z}_\psi^{(k)}(\theta)$ , in Eqs. (2), (7b), and (10b)
4:   Compute nested objectives  $\mathcal{E}_f^{(k)}$  and  $\mathcal{E}_\psi^{(k)}$ , in Eqs. (8) and (13)
5:   Compute the objective function  $\mathcal{E}^{(k)}$ , in Eq. (14)
6:   Minimise the objective function  $\underset{\theta}{\operatorname{argmin}}\{\mathcal{E}^{(k)}\}$  and determine  $\theta^{(k)}$ , in Eq. (16)
7:   if  $\|\theta^{(k)} - \theta^{(k-1)}\| < 1 \times 10^{-2}$  then
8:      $\theta^* = \theta^{(k)}$ 
9:     break
10:  else
11:    Update  $\theta^{(k-1)}$  with  $\theta^{(k)}$ 
12:    Update  $\mathbf{M}^{(k)}(\theta)$  and  $\mathbf{K}^{(k)}(\theta)$ , in Eqs. (15a) and (15b)
13:  end if
14: end while
15: Output: Optimal tuning parameters  $\theta^*$ 
16: Validation: Validate the model using  $\theta^*$ , in Eqs. (17) and (18)

```

objective functions with noise or discontinuities while avoiding local minima, this method proves advantageous in the quest for global optima amid challenges posed by multiple local minima. The simplex method is well documented in the literature and, while implementation details are not provided here, the readers are referred to [40,58] for comprehensive information. For a detailed understanding of the parameter identification process, the reader can refer to the step-by-step procedure outlined in Algorithm 1.

Once the optimal parameters θ^* are identified, a validation against observed data can be performed to ensure the correctness of the predicted optimal parameters. To achieve this, the expression in (14) can be used to assess the relative difference between the predicted and observed natural frequencies, as well as the correlation MAC values between the predicted and observed modes. The relative frequency difference between the natural frequencies can be quantified using the following.

$$\text{Relative frequency difference} = \frac{|\tilde{f}_j - f_j(\theta^*)|}{f_j(\theta^*)}, \quad j = 1, 2, \dots, N_j, \quad (17)$$

where \tilde{f}_j and $f_j(\theta^*)$ denote respectively natural frequency components of the observed and predicted outcomes, and N_j is the total number of natural frequencies to be compared. The predicted natural frequencies are evaluated using the optimal set of model parameters, namely $\theta_j^* \in \{1, 2, \dots, p\}$, in which p denotes the total number of tuning parameters.

The natural modes can be compared using a MAC to determine their associated correlation,

$$\text{MAC}(\tilde{\psi}_i, \psi_j(\theta^*)) = \frac{|\tilde{\psi}_i^H \psi_j(\theta^*)|^2}{(\tilde{\psi}_i^H \tilde{\psi}_i)(\psi_j^H(\theta^*) \psi_j(\theta^*))}, \quad i, j = 1, 2, \dots, N_j, \quad (18)$$

where $\tilde{\psi}_i$ and $\psi_j(\theta^*)$ denote the observed and predicted modes, respectively, and N_j is the total number of modes to be compared. It is noted that the predicted modes are evaluated using the optimal set of model parameters, namely $\theta_j^* \in \{1, 2, \dots, p\}$. The diagonal terms of (18) represent the degree of correlation between corresponding predicted and observed modes, whilst the off-diagonal terms represent the correlation between non-corresponding modes.

The procedure for model updating from the physical structure to a validated FE model is illustrated in the flowchart presented in Fig. 1.

3. Model updating of Cross-laminated Timber

The process of FE model updating for CLT substructures involves a series of essential steps. These include: (i) collecting observed data through EMA, (ii) creating FE models, (iii) formulating an objective function, and (iv) minimising the objective function to identify the key tuning parameters. The effectiveness of model updating heavily relies on the quality of observed data, emphasising the importance of having a sufficient number of data points, especially related to natural modes and their resonances. With a well-defined objective function and high-quality observed data, the model updating can use the simplex minimisation algorithm to identify the tuning parameters.

In subsequent sections, we will apply the framework introduced in Section 2 to multiple CLT substructures, aiming to identify critical stiffness parameters such as the axial Young's modulus (E_x), shear modulus (G_{xz}) and rolling shear modulus (G_{yz}). The vibration characteristics of the substructures were determined through EMA, providing data points related to vibration modes and resonances. These vibration data points, along with the FE representation of the substructures, were used to formulate an SOO. Subsequently, the SOO was minimised to determine the aforementioned tuning parameters. Additional details about the model-updating procedure are available in the step-by-step Algorithm 1.

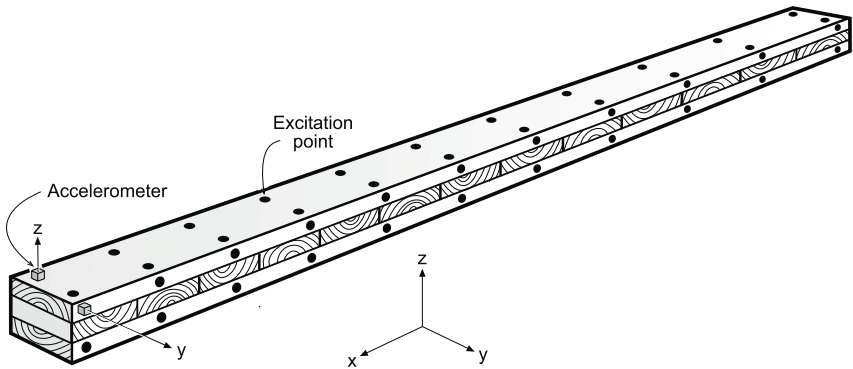


Fig. 2. Experimental setup of a CLT beam with dimensions Length \times Breadth \times Height giving 2 m \times 0.12 m \times 0.12 m. The excitation points ($2 \times 11 \times 2$) are uniformly distributed across the beam. The coordinate system is associated with global structure and consistent with the top and bottom layers. For the mid-layer, the coordinate system must be oriented by an angle of 90° about z-axis.

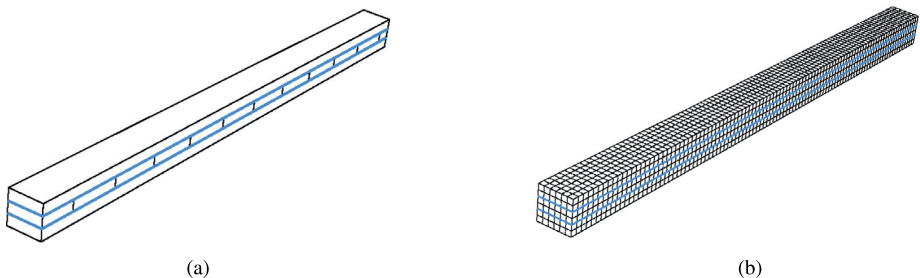


Fig. 3. (a) Solid model of the beam shown in Fig. 2, depicting individual intermediate boards individually modelled. (b) Discretised model of the CLT beam from Fig. 2, represented using brick FEs. The blue line indicates the coupling interface between the top-mid-bottom layers. These models pertain to the CLT beams in Section 3.1. (For interpretation of the references to colour in this figure legend, the reader is referred to the web version of this article.)

Table 1
Orthotropic material properties of lumber boards of strength class C35 from [59,60]. The subscripts x, y, and z are respectively consistent with the orthotropic orientations of wood.

E_x [MPa]	E_y [MPa]	E_z [MPa]	G_{xy} [MPa]	G_{xz} [MPa]	G_{yz} [MPa]	ν_{xy} [-]	ν_{xz} [-]	ν_{yz} [-]
13,000	262	430	810	810	57	0.48	0.42	0.28

3.1. Cross-laminated Timber beams

In the first model updating example, observed data points from EMA were used to update FE models of 24 nominally identical CLT beam substructures. These beams consist of two outer layers of Norway spruce and a central layer of Scots pine, as illustrated in Fig. 2. The density of the beams were determined by weighing them and calculating their weight-to-volume ratio. The beams were suspended using low-stiffness bungee cords, simulating free-free conditions to eliminate uncertainties resulting from frequency-dependent and contact stiffness associated with boundary conditions. Throughout the measurement campaign, the beams were excited both transversely (against the z-axis) and laterally (against the y-axis), Fig. 2. Consequently, vibration modes were obtained in both directions. The measurement campaign resulted in a total of six bending modes in each transverse and lateral direction, along with six torsional modes. All of these modes were considered and included in the subsequent model updating procedure.

The CLT beams were modelled using three solid layers within an FE framework, with each intermediate lamella individually modelled. Distinct material orientations were assigned to each layer, and tie coupling between the top, intermediate, and bottom layers was implemented, while no coupling between individual lamellae was considered. The model was discretised using standard solid brick elements with quadratic interpolation and reduced integration, as depicted in Fig. 3, [61]. In alignment with the measurements, Dirichlet boundary conditions were not applied to the model, and rigid-body modes were excluded from the updating procedure. Initially, each layer in the FE model was assigned the measured density along with the material properties from Table 1. The material properties in Table 1 were determined for the beams in a preliminary study in [59], as follows: the measured density (presented in Table 2), the E_x and $G_{xz} = G_{xy}$ were extracted from SS-EN 338:2016 [60] corresponding to the mean density value

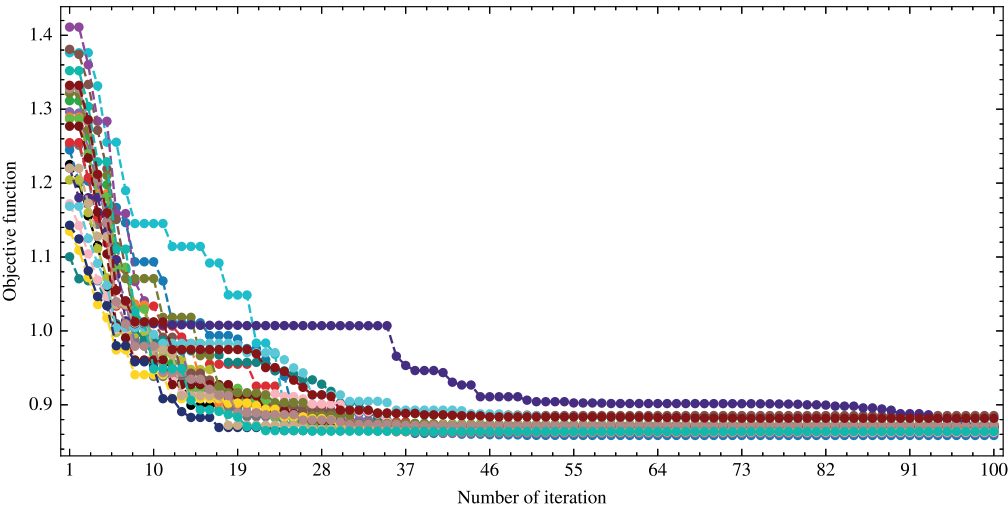


Fig. 4. Convergence behaviour of the objective function associated with 24 CLT beams in Section 3.1.

Table 2
Identified dynamic stiffness parameters of CLT beams using model updating strategy. The data is associated with the CLT beams in Section 3.1.

ρ [kg/m ³]	E_x [MPa]	$G_{xy} = G_{xz}$ [MPa]	G_{yz} [MPa]	ρ [kg/m ³]	E_x [MPa]	$G_{xy} = G_{xz}$ [MPa]	G_{yz} [MPa]
440	11,071	704	198	458	11,086	693	187
478	12,480	818	181	486	11,463	815	202
424	10,206	677	214	507	13,277	871	171
476	12,267	824	198	489	11,552	824	207
464	12,257	798	182	493	12,231	750	158
509	13,201	907	192	448	10,254	725	188
483	11,996	842	232	458	11,170	727	170
448	12,463	788	167	461	11,541	712	172
483	11,479	766	214	461	11,996	769	180
462	11,761	781	204	507	13,212	884	180
487	11,005	892	202	479	12,256	843	211
445	10,522	720	147	516	12,941	862	182

of the beams, and the rest of the material properties (E_y , E_z , G_{yz} , ν_{xy} , ν_{xz} , ν_{yz}) were determined using previous studies. In [59], a sensitivity study was conducted, revealing that parameters such as material density, E_x , $G_{xz} = G_{xy}$, and G_{yz} significantly influence the FE model. In the present case, the density is known. Therefore, E_x , $G_{xz} = G_{xy}$, and G_{yz} were updated until their optimal values were identified.

The minimisation mechanism successively minimised the objective function until the distance between the current and previous iteration steps was reached 10^{-2} , Fig. 4. In agreement with the minimisation of the objective function, the tuning parameters were optimised to reach a similar level of precision, Fig. 5. In particular, the minimisation of the objective function approaches a stability level after roughly 50 iterations Fig. 4, indicating that the tuning parameters have been roughly estimated at iteration number 50. This is except for the outlier plotted in dark purple in Figs. 4, 5, and 6. However, the algorithm explores the objective domain further for accuracy and precision purposes. This is particularly observable in the convergence behaviour of the objective function in Fig. 6. The optimal tuning parameters determined through the model updating procedure are presented in Table 2.

The optimal tuning parameters in Table 2 showcase variability, and therefore it is important to quantify the influence of the variability on the model updating procedure. Hence, a cross-validation investigation has been conducted to quantify the discrepancy between the updated FE model and the observed data. The FE model together with the observed density ρ and determined optimal tuning parameters E_x , $G_{xy} = G_{xz}$, G_{yz} Table 3, together with the un-updated parameters E_y , E_z , ν_{xy} , ν_{xz} , ν_{yz} in Table 1 has been executed and their associated natural frequencies and vibration modes have been validated against their corresponding observed data from EMA using Eqs. (17) and (18). The cross-validation results indicate excellent MAC values (> 0.9) associated with the modes 1–11 and 12–17, with the exception of lower MAC values (> 0.6) for modes 12 and 18. The predicted natural frequencies also indicate an excellent correlation with the observed natural frequencies, as evident indicated by the relative frequency difference values in Fig. 7. In addition, the mean values of all predicted natural frequencies in comparison to the mean values of all observed natural frequencies convey an excellent correlation, Fig. 7.

Since the determined optimal tuning parameters in Table 2 showcase variability, it is important to determine optimal tuning parameters using the mean values of the observed data. In this regard, the mean value of the natural frequencies and vibration

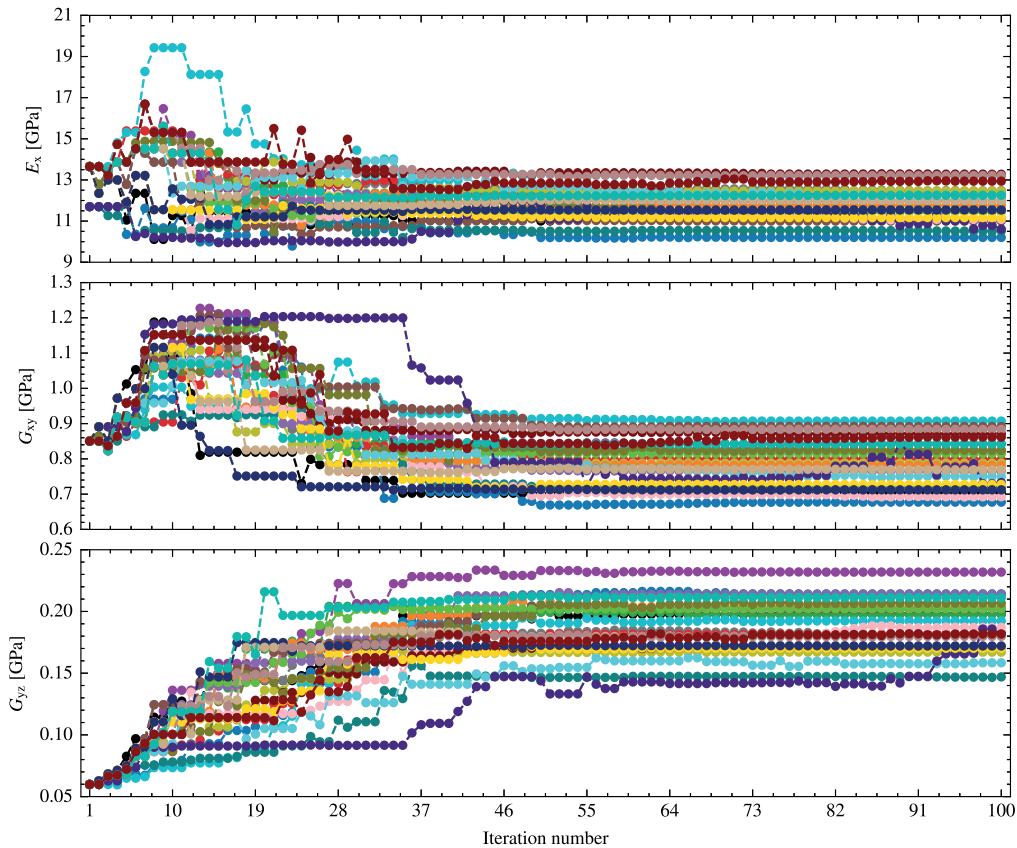


Fig. 5. Convergence behaviour of the tuning parameters Young's modulus E_x , Shear modulus $G_{xy} = G_{xz}$, and rolling shear modulus G_{yz} associated with 24 CLT beams in Section 3.1.

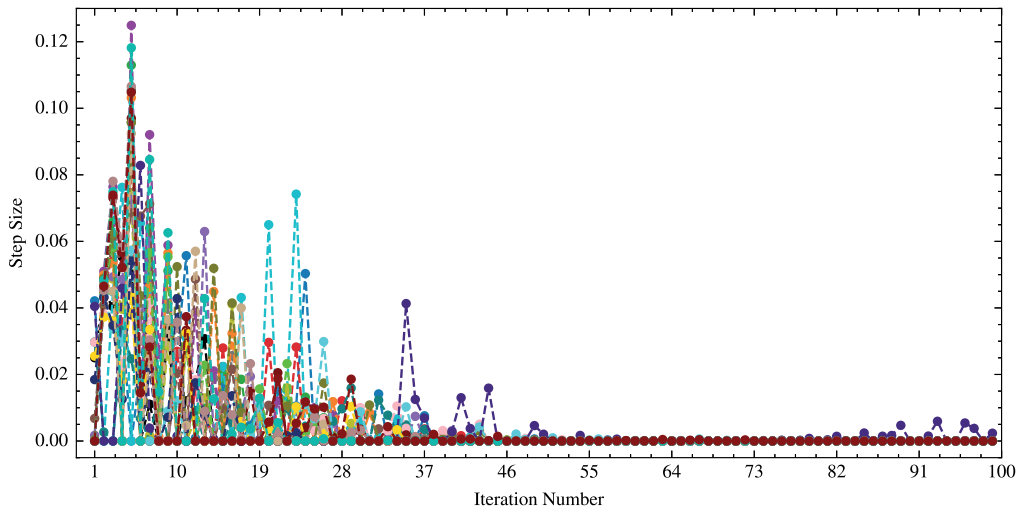


Fig. 6. Convergence behaviour of the simplex optimisation algorithm, depicting step size variations over iterations for 24 CLT beams in Section 3.1.

Table 3
Comparison of optimal tuning parameters obtained from FE model updating using averaged observed data and averaged optimal tuning parameters after updating all beams, Table 2. Data pertains to CLT beams in Section 3.1.

	E_x [MPa]	$G_{xy} = G_{xz}$ [MPa]	G_{yz} [MPa]
Optimal tuning parameters using mean observed data	11,835	775	194
Mean optimal tuning parameters using all observed data (in Table 2)	11,835	792	189
Percentage difference	0%	2.1%	2.6%

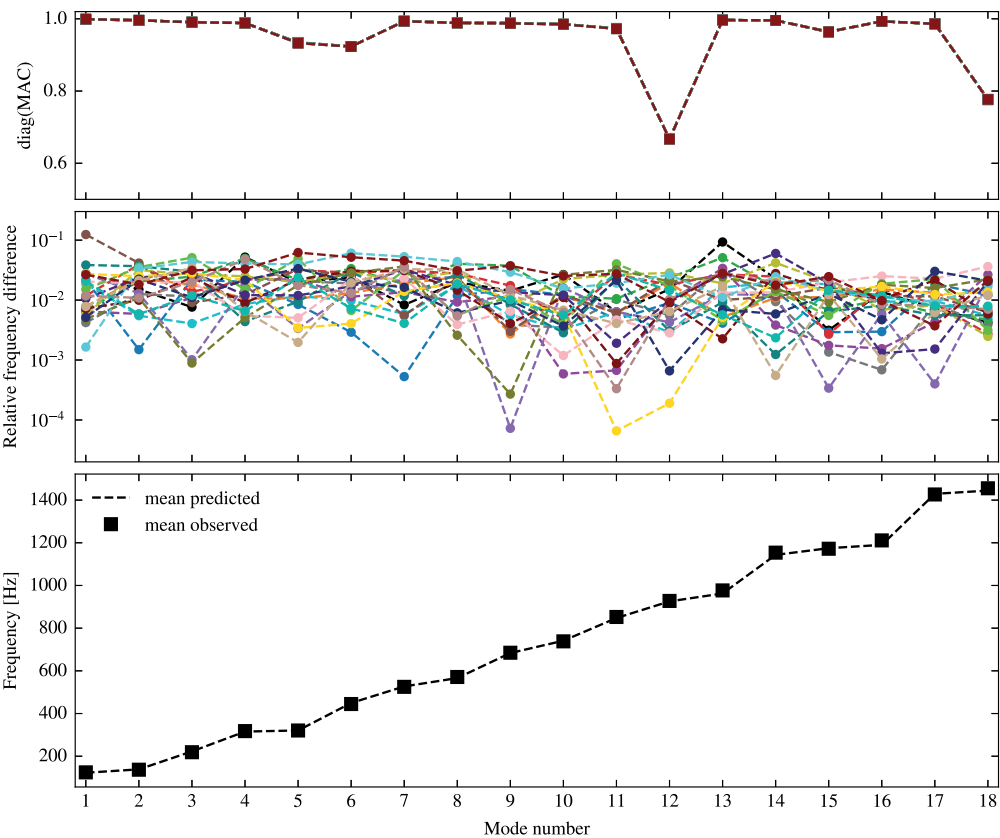


Fig. 7. Cross-validation of observed and predicted natural frequencies (using optimal parameters in Table 2), their associated relative difference, and vibration modes. The data is associated with the CLT beams in Section 3.1.

modes with the lowest modal complexity is used to update an FE model of the beams. The FE model was assigned the mean density value of the beams and the material properties in Table 1 as initial parameters. An objective function was formulated and subsequently minimised to determine the optimal tuning parameters. These optimal tuning parameters determined using the mean observed data are subsequently compared to the mean optimal tuning parameters from Table 2. The comparison in Table 3 indicates that updating all the beams and averaging their corresponding optimal tuning parameters do not differ significantly from the optimal tuning parameters determined by updating the FE model using averaged observed data. This is an important indication that leads to significant computational efficiency.

3.2. Cross-laminated Timber cutouts

In the second example of the model updating process, EMA data is employed to update FE models of 10 CLT cutout substructures. These CLT cutouts comprise 5 juxtaposed layers of Norway spruce arranged with thicknesses of 30 mm, 20 mm, 20 mm, 20 mm, and

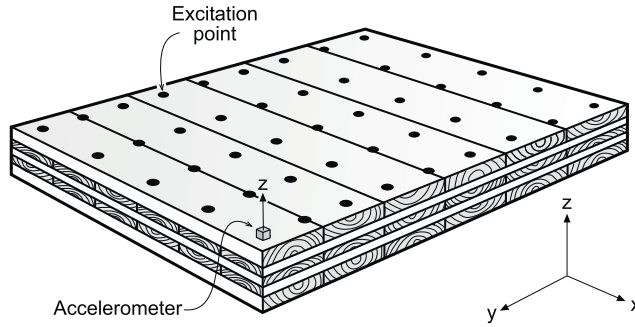


Fig. 8. Experimental setup of a CLT cutout with dimensions length (in the x -direction) of 1.0 [m], breadth (in the y -direction) of 1.5 [m] and height (in the z -direction) of 0.12 [m]. The thickness of the covering layers is 30 [mm] each, while the three intermediate layers have a thickness of 20 [mm] each. The excitation points (9×5) are uniformly distributed across the xy surface.

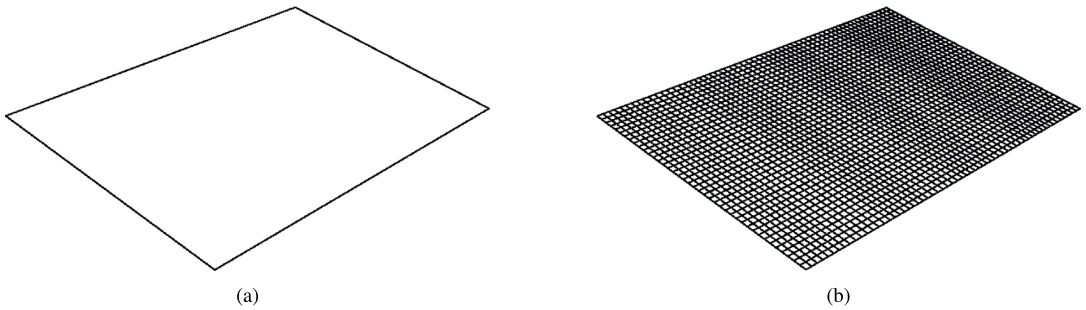


Fig. 9. (a) Two-dimensional representation of the cutout depicted in Fig. 8. (b) Discretised model of the CLT cutout from Fig. 8, employing laminated doubly-curved composite shell FEs. These models pertain to the CLT cutouts in Section 3.2.

30 mm, respectively, as illustrated in Fig. 8. The cutouts were cut from a CLT slab. The density, calculated as the volume-to-weight ratio, was determined by weighing and measuring the geometric dimensions of the cutouts. The measurement grid was designed based on preliminary simulations to ensure an adequate number of data points, with each point excited transversely (against the z axis), Fig. 8. To mitigate uncertainties arising from boundary conditions, the cutouts were suspended using low-stiffness bungee cords. In total, five vibration modes and their associated resonances have been obtained for all the CLT cutouts.

The CLT cutouts were modelled using a two-dimensional plate approach, which was further discretised within an FE framework. The FE model employed laminated doubly curved composite shell elements, ensuring that each nodal point had six degrees of freedom (three translations and three rotations), as illustrated in Fig. 9. The elements employed quadratic interpolation with reduced integration [61,62]. In accordance with the measurements, the model was not subjected to Dirichlet boundary conditions, and rigid-body modes were excluded from the updating procedure.

The initial mechanical properties of the FEs were selected as follows: the measured density ρ , the stiffness constants E_x , $G_{xy} = G_{xz}$ corresponding to the mean measured density value according to SS-EN 338:2016 [60], the rolling shear modulus G_{yz} , and the rest of the material constants (E_y , E_z , ν_{xy} , ν_{xz} , ν_{yz}) were selected using the strategy reported in [59], Table 1. In other words, the initial FE model of each CLT cutout was assigned the orthotropic properties reported in Table 1 together with its associated measured density in Table 4. For each FE model, an objective function was formulated according to (16), which was subsequently minimised with respect to the tuning parameters E_x , $G_{xy} = G_{xz}$, G_{yz} . The simplex optimisation algorithm successfully minimises the objective function to find the optimal tuning parameters shown in Fig. 10. The minimisation procedure reaches a stable level after 30 iterations. However, as the convergence criterion was set to 10^{-2} , the simplex algorithm iterates until equilibrium is reached, Figs. 10, 11, and 12. Although minimisation of the objective function reaches stability after 30 iterations (Fig. 10), the tuning parameters, in particular the rolling shear modulus G_{yz} , reach stability after 60 iterations. This behaviour has been observed in the optimisation of the rolling shear modulus G_{yz} of the beams in Section 3.1. In agreement with the minimisation procedure of the objective function, the simplex algorithm takes larger steps towards minima at the beginning of the minimisation procedure. These steps will become smaller after iteration 30, as the algorithm seeks a finer solution and oscillates around the optima, Fig. 12. This behaviour is consistent with the minimisation of the objective associated with the beams in [59].

The optimal tuning parameters determined at the last iteration step display variability, as is expected due to the variability in the observed data, Table 4. Therefore, a cross-validation of the predicted results against the observed results has been conducted.

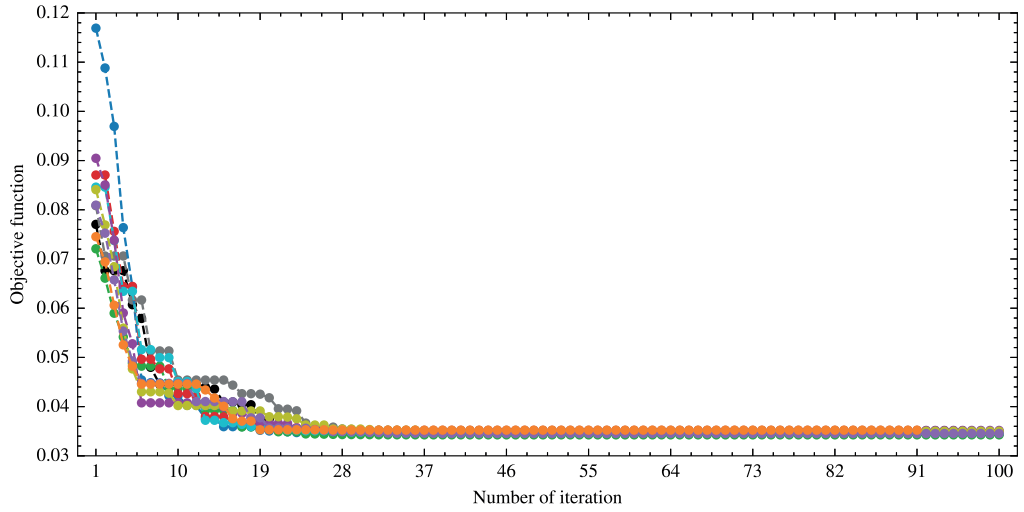


Fig. 10. Convergence behaviour of the objective function associated with 10 CLT cutouts in Section 3.2.

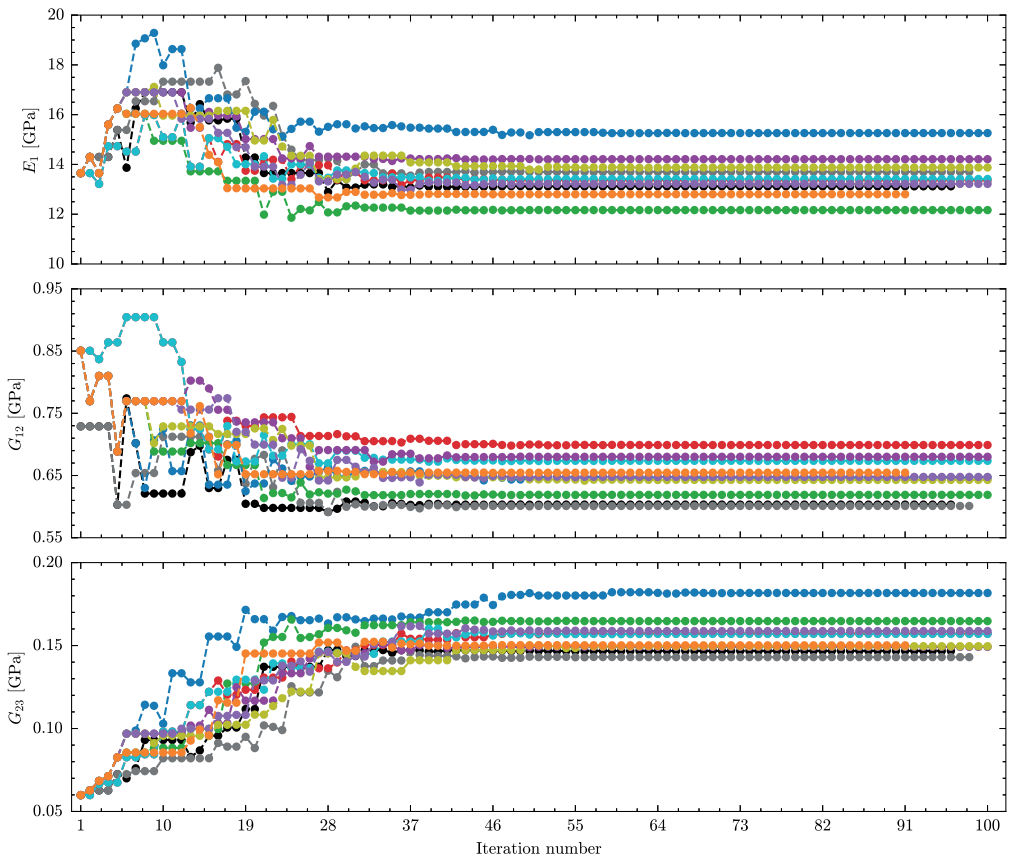


Fig. 11. Convergence behaviour of the tuning parameters Young's modulus E_x , Shear modulus $G_{xy} = G_{xz}$, and rolling shear modulus G_{yz} associated with 10 CLT cutouts in Section 3.2.

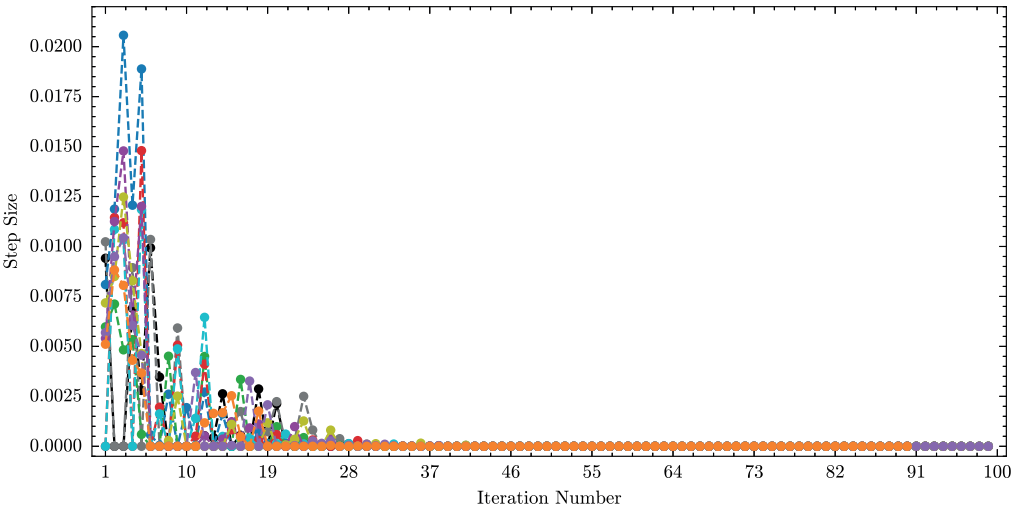


Fig. 12. Convergence behaviour of the simplex optimisation algorithm, depicting step size variations over iterations for 10 CLT cutouts in Section 3.2.

Table 4
Identified dynamic stiffness parameters of CLT cutouts using model updating strategy. The data is associated with the CLT cutouts in Section 3.2.

ρ [kg/m ³]	E_x [MPa]	$G_{xy} = G_{xz}$ [MPa]	G_{yz} [MPa]	ρ [kg/m ³]	E_x [MPa]	$G_{xy} = G_{xz}$ [MPa]	G_{yz} [MPa]
483	13,121	603	147	471	13,415	674	157
478	13,701	601	143	476	14,211	680	149
501	15,260	647	182	472	13,878	643	150
478	12,165	619	165	487	13,217	648	159
471	13,363	699	157	478	12,803	655	150

Table 5
Comparison of optimal tuning parameters obtained from FE model updating using averaged observed data and averaged optimal tuning parameters after updating all cutouts, Table 4. Data pertain to CLT cutouts in Section 3.2.

	E_x [MPa]	$G_{xy} = G_{xz}$ [MPa]	G_{yz} [MPa]
Optimal tuning parameters using mean observed data	13,500	647	155
Mean optimal tuning parameters using all observed data (in Table 4)	13,513	647	156
Percentage difference	1%	0%	0.6%

In this regard, the FE models were fed with the measured density ρ and optimal tuning parameters concerning E_x , $G_{xy} = G_{xz}$, G_{yz} in Table 4, and E_y , E_z , ν_{xy} , ν_{xz} , ν_{yz} in Table 1. Subsequently, the predicted and observed results in terms of the MAC values and relative frequency difference have been evaluated. The evaluation presented in Fig. 13 indicates an excellent correlation between the predicted and observed modes with MAC values > 98. In the same manner, the relative difference between the predicted and observed natural frequencies demonstrates an excellent match. To gain further insight into the correlation of the predicted and observed natural frequencies, the mean values of the observed and predicted natural frequencies are compared and show excellent correlation, Fig. 13.

Given the variability observed in the optimal tuning parameters outlined in Table 4, it is imperative to quantify this variability. To address this, an objective function was formulated with inputs such as the observed mean density value of the cutouts, elastic parameters from Table 1, and mean values of the natural frequencies, and modes characterised by the lowest modal complexity values. Subsequently, the objective function underwent a minimisation process to determine the optimal tuning parameters aligned with the mean observed data obtained from EMA.

The tuning parameters obtained through minimising the objective function, which used the mean observed data, closely align with the mean values of the tuning parameters obtained when updating all cutouts individually. Analysis of the results reveals no significant differences between the optimal tuning parameters derived from minimising the objective function with mean observed data (Table 4) and the mean values obtained by updating all cut-outs, Table 5. Consequently, it is computationally more efficient to minimise the objective function configured with the mean observed data, rather than updating each cutout separately if the variability of the tuning parameters is not of interest. This agrees with the behaviour of the updating procedure of the beams in Section 3.1.

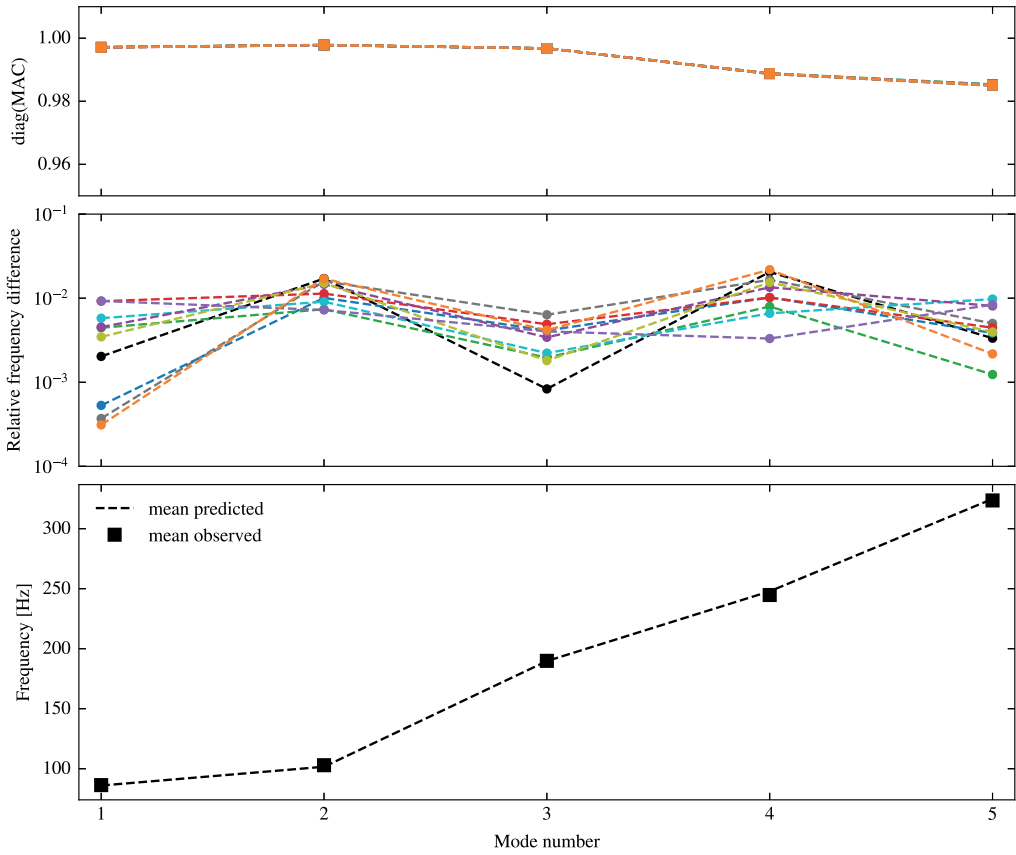


Fig. 13. Cross-validation of the observed and predicted vibration modes, natural frequencies and their associated frequency difference in comparison to their corresponding observed counterparts. The predicted outcomes are obtained using the optimal parameters in Table 4. The data is associated with the CLT cutouts in Section 3.2.

4. Conclusions

In this work, a comprehensive computational framework has been established for the model updating of Cross-Laminated Timber (CLT) substructures, focusing on both beams and cutouts from slabs. By taking into account the observed data from Experimental Modal Analysis (EMA) and employing a Finite Element Method (FEM) framework, an appropriate objective function was derived. This objective function encapsulated the key sensitive parameters associated with the CLT substructures, namely the longitudinal Young's modulus E_x , the interior shear moduli $G_{xy} = G_{xz}$, and the cross-sectional rolling shear modulus G_{yz} . The formulated objective function was subsequently optimised to minimise the disparity between observed and predicted results, specifically targeting natural frequencies and vibration modes. To achieve this optimisation, a computational simplex approach was employed, allowing efficient fine-tuning of the tuning parameters within the defined computational framework. As a result, optimal tuning parameters, together with their associated variability, were obtained satisfactorily.

During the optimisation procedure, it was observed that the simplex method tends to oscillate around the optima and requires several additional steps to reach convergence. This behaviour can be managed by setting a fixed number of iterations. However, detailed information regarding the convergence behaviour of the specific case study is essential to effectively control this process.

The mechanical properties of CLT were identified through Tables 2 and 4, revealing distinct characteristics between beams and cutouts. The beams, composed of three layers, Norway spruce, Scots pine, and Norway spruce, exhibit improved internal and rolling shear capacity (Section 3.1) when Norway spruce is combined with Scots pine. However, this combination results in a lower longitudinal Young's modulus compared to using only Norway spruce. In contrast, cutouts, composed solely of five layers of Norway spruce, achieve a higher longitudinal Young's modulus but demonstrate lower internal and rolling shear moduli compared to the mixed Norway spruce and Scots pine configuration in beams (Section 3.2).

The updating procedure further highlighted that employing the mean value of natural frequencies and a selected set of clear modes (preferably with low modal complexity) results in nearly identical tuning parameters as updating all substructures and averaging their respective optimal tuning parameters. Consequently, when focusing on the values of the mean tuning parameters, updating all substructures may not be necessary. Instead, updating one substructure using the mean natural frequencies and a clear mode set suffices to determine the mean values of the desired tuning parameters.

The identified tuning parameters indicate differences compared to those suggested by SS-EN 338:2016 [60]. Therefore, it is important to reassess the mechanical properties of CLT and account for their associated variability in structural analysis. This re-evaluation is essential to ensure accurate performance predictions and safe utilisation of CLT in various structural applications. Furthermore, SS-EN 338:2016 [60] does not specify a rolling shear modulus G_{yz} . Hence, there is a need to update the standard to include the precise mechanical properties of the softwoods commonly used in CLT production.

The optimal tuning parameters, quantified variability, and robust model updating framework established in this article emerge as valuable tools for engineers engaged in the design of timber structures and researchers in the field of vibroacoustic. The demonstrated efficacy of the proposed framework in the identification of sensitive tuning parameters of CLT substructures underscores its practical significance.

Potential extensions of this work include adapting the updating procedure to both time and frequency domains. Additionally, evaluating the effectiveness of this procedure in detecting damage in reinforced concrete structures and assessing the coupling stiffness between reinforcement and concrete would be valuable. Another area of interest is applying this model updating approach to identify the degradation of mechanical properties in structures over time, particularly those exposed to radiation, such as nuclear reactors, spacecraft components, radiation shielding materials, and high-energy particle accelerators. Further research could also explore applying the procedure to update models of coupled vibroacoustic and thermoelastic vibrations.

CRedit authorship contribution statement

Benjamin Bondsman: Writing – review & editing, Writing – original draft, Visualization, Validation, Software, Resources, Methodology, Investigation, Formal analysis, Data curation, Conceptualization. **Andrew Peplow:** Writing – review & editing, Validation, Conceptualization.

Declaration of competing interest

The authors declare that they have no known competing financial interests or personal relationships that could have appeared to influence the work reported in this paper.

Data availability

Data will be made available on request.

Acknowledgement

The first author thanks the forest owners association Södra for providing access to the testing materials. The production of this article received no financial support.

References

- [1] Klaus-Jürgen Bathe, *Finite Element Procedures*, Klaus-Jürgen Bathe, 2006.
- [2] John E. Mottershead, Michael Link, Michael I. Friswell, The sensitivity method in finite element model updating: A tutorial, *Mech. Syst. Signal Process.* 25 (7) (2011) 2275–2296.
- [3] Yves Govers, Marc Böswald, Ulrich Füllekrug, Dennis Göge, Michael Link, Analysis of sources and quantification of uncertainty in experimental modal data, in: *Proceedings of the International Seminar on Modal Analysis*, 2006, pp. 4161–4173.
- [4] Sifeng Bi, Michael Beer, Scott Cogan, John Mottershead, Stochastic model updating with uncertainty quantification: an overview and tutorial, *Mech. Syst. Signal Process.* 204 (2023) 110784.
- [5] Michael Friswell, John E. Mottershead, *Finite Element Model Updating in Structural Dynamics*, vol. 38, Springer Science & Business Media, 1995.
- [6] John E. Mottershead, M.I. Friswell, Model updating in structural dynamics: a survey, *J. Sound Vib.* 167 (2) (1993) 347–375.
- [7] Babak Moaveni, Iman Behmanesh, Effects of changing ambient temperature on finite element model updating of the Dowling Hall Footbridge, *Eng. Struct.* 43 (2012) 58–68.
- [8] Kaipeng Sun, Yonghui Zhao, Haiyan Hu, Identification of temperature-dependent thermal-structural properties via finite element model updating and selection, *Mech. Syst. Signal Process.* 52 (2015) 147–161.
- [9] José Humberto S Almeida Jr., Tales V Lisboa, Axel Spickenheuer, Luc St-Pierre, A sequential finite element model updating routine to identify creep parameters for filament wound composite cylinders in aggressive environments, *Comput. Struct.* 276 (2023) 106939.
- [10] Xuefei Guan, Ratneshwar Jha, Yongming Liu, Model selection, updating, and averaging for probabilistic fatigue damage prognosis, *Struct. Saf.* 33 (3) (2011) 242–249.
- [11] Boris A. Zárate, Juan M. Caicedo, Jianguo Yu, Paul Ziehl, Bayesian model updating and prognosis of fatigue crack growth, *Eng. Struct.* 45 (2012) 53–61.
- [12] Ruoxue Zhang, Sankaran Mahadevan, Model uncertainty and Bayesian updating in reliability-based inspection, *Struct. Saf.* 22 (2) (2000) 145–160.
- [13] Menahem Baruch, Itzhack Y. Bar Itzhack, Optimal weighted orthogonalization of measured modes, *AIAA J.* 16 (4) (1978) 346–351.
- [14] Menahem Baruch, Optimization procedure to correct stiffness and flexibility matrices using vibration tests, *AIAA J.* 16 (11) (1978) 1208–1210.
- [15] Alex Berman, Mass matrix correction using an incomplete set of measured modes, *AIAA J.* 17 (10) (1979) 1147–1148.

- [16] J.-C. Chen, C.-P. Kuo, J. Garba, Direct structural parameter identification by modal test results, in: 24th Structures, Structural Dynamics and Materials Conference, 1983, p. 812.
- [17] A. Berman, E.J. Nagy, Improvement of a large analytical model using test data, *AIAA J.* 21 (8) (1983) 1168–1173.
- [18] B. Titurus, M.I. Friswell, Regularization in model updating, *Internat. J. Numer. Methods Engrg.* 75 (4) (2008) 440–478.
- [19] Andrei Nikolaevich Tikhonov, Viak Arsenin, *Solutions of Ill-Posed Problems*, V. H. Winston & Sons, 1977.
- [20] Iman Behmanesh, Babak Moaveni, Geert Lombaert, Costas Papadimitriou, Hierarchical Bayesian model updating for structural identification, *Mech. Syst. Signal Process.* 64 (2015) 360–376.
- [21] Dag Pasquale Pasca, Angelo Aloisio, Massimo Fragiaco, Roberto Tomasi, Dynamic characterization of timber floor subassemblies: Sensitivity analysis and modeling issues, *J. Struct. Eng.* 147 (12) (2021) 05021008.
- [22] Angelo Aloisio, Dag Pasca, Roberto Tomasi, Massimo Fragiaco, Dynamic identification and model updating of an eight-storey CLT building, *Eng. Struct.* 213 (2020) 110593.
- [23] Mladen Gibanica, Thomas J.S. Abrahamsson, Magnus Olsson, Model updating of multiple nominally identical car components, *Exp. Tech.* 44 (2020) 391–407.
- [24] Pierre Landel, Andreas Linderholt, Reduced and test-data correlated FE-models of a large timber truss with dowel-type connections aimed for dynamic analyses at serviceability level, *Eng. Struct.* 260 (2022) 114208.
- [25] Svein Kleiven, Warren N. Hardy, Correlation of an FE Model of the Human Head with Local Brain Motion-Consequences for Injury Prediction, Technical Report, SAE Technical Paper, 2002.
- [26] Heung Fai Lam, Lambros S. Katafygiotis, Neil Colin Mickleborough, Application of a statistical model updating approach on phase I of the IASC-ASCE structural health monitoring benchmark study, *J. Eng. Mech.* 130 (1) (2004) 34–48.
- [27] Vahid Yaghoubi, Majid K. Vakilezadeh, Anders T. Johansson, Thomas Abrahamsson, Stochastic finite element model updating by bootstrapping, in: *Model Validation and Uncertainty Quantification, Volume 3: Proceedings of the 34th IMAC, a Conference and Exposition on Structural Dynamics 2016*, Springer, 2016, pp. 117–130.
- [28] Faisal Shabbir, Piotr Omenzetter, Particle swarm optimization with sequential niche technique for dynamic finite element model updating, *Comput.-Aided Civ. Infrastruct. Eng.* 30 (5) (2015) 359–375.
- [29] Seung-Seop Jin, Hyung-Jo Jung, Sequential surrogate modeling for efficient finite element model updating, *Comput. Struct.* 168 (2016) 30–45.
- [30] Andreas Linderholt, Thomas Abrahamsson, Optimising the informativeness of test data used for computational model updating, *Mech. Syst. Signal Process.* 19 (4) (2005) 736–750.
- [31] B. Caesar, Update and identification of dynamic mathematical models, in: *International Modal Analysis Conference*, 4 Th, Los Angeles, CA, 1986, pp. 394–401.
- [32] Bernd Caesar, Updating system matrices, in: *International Modal Analysis Conference*, 5 Th, London, England, 1987, pp. 453–459.
- [33] Alvar M. Kabe, Stiffness matrix adjustment using mode data, *AIAA J.* 23 (9) (1985) 1431–1436.
- [34] J. Sidhu, D.J. Ewins, Correlation of finite element and modal test studies of a practical structure, in: *Proceedings of the 2nd International Modal Analysis Conference*, Vol. 2, Union College Schenectady, NY, 1984, pp. 756–762.
- [35] Shankar Sehgal, Harmesh Kumar, Structural dynamic model updating techniques: A state of the art review, *Arch. Comput. Methods Eng.* 23 (2016) 515–533.
- [36] Reinhard Brandner, Georg Flatscher, Andreas Ringhofer, Gerhard Schickhofer, Alexandra Thiel, Cross laminated timber (CLT): overview and development, *Eur. J. Wood Wood Prod.* 74 (2016) 331–351.
- [37] Blaž Kurent, Boštjan Brank, Wai Kei Ao, Model updating of seven-storey cross-laminated timber building designed on frequency-response-functions-based modal testing, *Struct. Infrastruct. Eng.* 19 (2) (2023) 178–196.
- [38] Blaž Kurent, Noemi Friedman, Wai Kei Ao, Boštjan Brank, Bayesian updating of tall timber building model using modal data, *Eng. Struct.* 266 (2022) 114570.
- [39] Michael Kawrza, Thomas Furtmüller, Christoph Adam, Experimental and numerical modal analysis of a cross laminated timber floor system in different construction states, *Constr. Build. Mater.* 344 (2022) 128032.
- [40] John A. Nelder, Roger Mead, A simplex method for function minimization, *Comput. J.* 7 (4) (1965) 308–313.
- [41] A. Maia, E. Ferreira, M.C. Oliveira, L.F. Menezes, A. Andrade-Campos, 3 - numerical optimization strategies for springback compensation in sheet metal forming, in: J. Paulo Davim (Ed.), *Computational Methods and Production Engineering*, in: Woodhead Publishing Reviews: Mechanical Engineering Series, Woodhead Publishing, 2017, pp. 51–82.
- [42] Yoshihiko Ozaki, Masaki Yano, Masaki Onishi, Effective hyperparameter optimization using nelder-mead method in deep learning, *IPSN Trans. Comput. Vis. Appl.* 9 (2017) 1–12.
- [43] Andrew R. Conn, Katya Scheinberg, Luis N. Vicente, *Introduction to Derivative-Free Optimization*, SIAM, 2009.
- [44] Daniel T. Bartilson, Jinwoo Jang, Andrew W. Smyth, Finite element model updating using objective-consistent sensitivity-based parameter clustering and Bayesian regularization, *Mech. Syst. Signal Process.* 114 (2019) 328–345.
- [45] Jon D. Collins, Gary C. Hart, T.K. Hasselman, Bruce Kennedy, Statistical identification of structures, *AIAA J.* 12 (2) (1974) 185–190.
- [46] M.I. Friswell, The adjustment of structural parameters using a minimum variance estimator, *Mech. Syst. Signal Process.* 3 (2) (1989) 143–155.
- [47] Tilo Strutz, *Data Fitting and Uncertainty: A Practical Introduction to Weighted Least Squares and Beyond*, vol. 1, Springer, 2011.
- [48] Michael Link, Updating of analytical models-procedures and experience, in: *Proceedings of the Conference on Modern Practice in Stress and Vibration Analysis*, Sheffield, Academic Press, 1993, pp. 35–52.
- [49] R.J. Allemang, A correlation coefficient for modal vector analysis, in: *proc. of the 1st IMAC*, 1982, pp. 110–116.
- [50] James M.W. Brownjohn, Alessandro De Stefano, You-Lin Xu, Helmut Wenzel, A. Emin Aktan, Vibration-based monitoring of civil infrastructure: challenges and successes, *J. Civ. Struct. Health Monit.* 1 (2011) 79–95.
- [51] Daniel T. Bartilson, Jinwoo Jang, Andrew W. Smyth, Sensitivity-based singular value decomposition parametrization and optimal regularization in finite element model updating, *Struct. Control Health Monit.* 27 (6) (2020) e2539.
- [52] Roy R. Craig Jr., Andrew J. Kurdila, *Fundamentals of Structural Dynamics*, John Wiley & Sons, 2006.
- [53] Roy Craig Jr., Coupling of substructures for dynamic analyses-an overview, in: *41st Structures, Structural Dynamics, and Materials Conference and Exhibit*, 2000, p. 1573.
- [54] Daniel J. Rixen, A dual Craig-Bampton method for dynamic substructuring, *J. Comput. Appl. Math.* 168 (1–2) (2004) 383–391.
- [55] Benjamin Bondsman, Chang-uk Ahn, Jin-Gyun Kim, Interface reduction technique for enhanced craig-bampton method, *Mech. Syst. Signal Process.* 208 (2024) 111074.
- [56] Mohd Z. Zakaria, Hishamuddin Jamaluddin, Robiah Ahmad, Sayed M.R. Loghmanian, Comparison between multi-objective and single-objective optimization for the modeling of dynamic systems, *Proc. Inst. Mech. Eng. I* 226 (7) (2012) 994–1005.
- [57] Suzana Ereiz, Ivan Duvnjak, Javier Fernando Jiménez-Alonso, Review of finite element model updating methods for structural applications, *Structures* 41 (2022) 684–723.
- [58] Fuchang Gao, Lixing Han, Implementing the Nelder-Mead simplex algorithm with adaptive parameters, *Comput. Optim. Appl.* 51 (1) (2012) 259–277.

- [59] Benjamin Bondsman, Ola Flodén, Henrik Danielsson, Peter Persson, Erik Serrano, Modal analysis of CLT beams: Measurements and predictive simulations, in: Alphose Zingoni (Ed.), *Current Perspectives and New Directions in Mechanics, Modelling and Design of Structural Systems*, CRC Press/Balkema, 2022, pp. 56–62, 8th International Conference on Structural Engineering, Mechanics and Computation, SEMC 2022 ; Conference date: 05-09-2022 Through 07-09-2022.
- [60] SIS, *Structural Timber – Strength Classes, Standard SS-EN 338:2016*, Swedish Institute for Standards, Stockholm, Sweden, 2016.
- [61] Michael Smith, *ABAQUS/Standard User's Manual, Version 6.9*, Dassault Systèmes Simulia Corp, United States, 2009.
- [62] Francesco Tornabene, Michele Baccocchi, Nicholas Fantuzzi, Erasmo Viola, *Laminated Composite Doubly-Curved Shell Structures: Differential Geometry Higher-Order Structural Theories*, Società Editrice Esculapio, 2016.

Paper III

B. Bondsman

Uncertainty quantification of mechanical properties and modal characteristics in Cross-laminated Timber

To be published

Uncertainty quantification of mechanical properties and modal characteristics in Cross-laminated Timber

Benjamin Bondsman^{a,*}

^aLund University, John Ericssons väg 1, SE-223 63, Lund, Kingdom of Sweden

ARTICLE INFO

Keywords:

Uncertainty quantification
Cross-laminated Timber
Mechanical properties
Natural frequencies
Modal parameters

ABSTRACT


Uncertainty in the mechanical properties and modal characteristics of Cross-Laminated Timber (CLT) significantly affects its predictive design and analysis. Although previous studies have focused on determining sensitive mechanical properties of CLT using model updating, the uncertainty quantification of these properties and their influence on natural frequencies and modes remain underexplored. In this study, the mechanical properties of beam-like CLT substructures, determined through model updating with Experimental Modal Analysis (EMA) as a reference, are used to generate probabilistic and stochastic mechanical properties. These properties include wood density, longitudinal Young's modulus, interior shear moduli, and cross-sectional rolling shear modulus. Gaussian processes (GP), Latin Hypercube Sampling (LHS), and Monte Carlo (MC) sampling techniques are applied to propagate these distributions into a Finite Element (FE) model to evaluate their effects on natural frequencies and vibration modes. The variability in input properties is used to determine how uncertainty in these properties affects the output natural frequencies and modes. The results are presented in terms of normal distributions and relative differences in natural frequencies across modes and propagation techniques. A local sensitivity analysis is performed to assess the impact of individual mechanical properties on the natural frequencies and mode shapes across different types of modes, and linear regression is used to explore the relationships between wood density and other properties. Furthermore, the article comprises algebraic derivations and an implementation algorithm to facilitate application.

1. Introduction

Numerical analysis and Finite Element (FE) modelling have become integral parts of predictive modelling in various engineering fields, ranging from civil, aerospace, and structural engineering to automotive design and product lifecycle analysis. FE modelling and simulation permit the prediction of structural responses under various loading scenarios, leading to improvements in design accuracy and safety, performance efficiency, product optimisation, and cost savings. Although the engineering industry relies on extensive simulations, experimental measurements often reveal discrepancies between the simulated and measured results. Hence, the concept of model updating was developed to tune the simulated results toward their measured counterparts using experimental data as reference, [1, 2, 3, 4, 5]. In particular, non-destructive testing, such as Experimental Modal Analysis (EMA), has been widely used as a reference in model updating. The updated model only brings the simulated results as close as possible to their measured counterparts whilst identifying the sensitive tuning parameters of the model. However, model updating often cannot eliminate all uncertainties due to modelling errors, noisy measurements, and truncated updating using only a few vibration modes. A more comprehensive description of modelling errors can be found in the literature [6, 7, 8]. Once the model is updated and validated against the corresponding experimental data, Uncertainty Quantification (UQ) is necessary to quantify the degree of uncertainty or variability in simulated and measured quantities. The uncertainties are subsequently propagated back into the numerical model to identify the relationship between the input and output uncertainty.

The concept of UQ is particularly important in the analysis of structures with inherent variability in their mechanical characteristics. Specifically, wood, as a natural material, exhibits variability in its mechanical properties due to growing conditions, leading to different patterns of fibre orientation [9, 10]. Other contributing factors include natural defects, such as knots, checks, splits, and distortion caused by variations in moisture content, [11, 12, 13]. Wood is also characterised by a high strength-to-mass ratio [14] and is therefore vulnerable to vibration at low frequencies. When wooden boards are juxtaposed in a crosswise pattern to form Cross-Laminated Timber (CLT), a robust structural

*Corresponding author

 benjamin.bondsman@construction.lth.se (B. Bondsman)
ORCID(s): 0000-0003-4235-5099 (B. Bondsman)

material is formed with diverse variability in its mechanical properties [15]. Despite the variability in its mechanical characteristics, CLT has become a conventional structural material and structural system component in sustainable and environmentally friendly constructions. Examples of CLT applications are commonly seen in multi-storey wooden buildings, where they are used as load-bearing slabs and shear walls. Hence, quantification of the variability in the mechanical properties of CLT is of particular importance as the world continues to embrace sustainable building practices in response to global warming and climate change [16, 17]. Consequently, probabilistic models of the mechanical properties of wood are accordingly widely adopted with a particular emphasis on the longitudinal Young's modulus and the internal shear moduli [18, 19, 20, 21]. Research by Yin et al. [22] has identified that the density of CLT and its associated longitudinal dynamic Young's modulus can be represented using the normal distribution. Recently, Ge et al. [23] presented results from the propagation of uncertainties in the mechanical properties of a wooden floor system made of a combination of orientated standard board and glued laminated timber beam joists. The natural frequencies of the floor were found to exhibit significant randomness due to the variability in mechanical properties. While substantial progress has been made in understanding the probabilistic nature of the mechanical properties of wood—such as the longitudinal Young's modulus and in-plane shear moduli—research into the influence of the rolling-shear modulus on the dynamic properties of wood, particularly CLT, remains limited. The rolling-shear modulus, which resists deformation perpendicular to the grain, has been extensively studied in the context of static testing. For example, an evaluation of CLT made from Japanese cedar [24] demonstrated that rolling shear strength depends on lamina width and annual ring patterns. A comprehensive static assessment of rolling shear in CLT is also presented in [25]. More recently, dynamic model updating of CLT conducted by the author [26] identified the rolling-shear modulus as a mechanically sensitive parameter influencing natural frequencies and mode shapes. Despite these contributions, comprehensive quantification of uncertainty in the dynamic properties of CLT remains incomplete. In particular, data sampled from multiple nominally identical CLT structures is essential to understanding how uncertainty in mechanical properties propagates to variability in modal parameters. Therefore, quantifying uncertainty in the dynamic mechanical properties of CLT—and the resulting natural frequencies and mode shapes—is imperative for improving predictive analyses of the dynamic behaviour of CLT.

In response to this gap in the literature, the present study aims to quantify how uncertainty in the input mechanical parameters of CLT propagates to uncertainty in modal parameters, specifically natural frequencies and mode shapes. To achieve this, mechanical properties known to influence modal behaviour are evaluated in this study. These properties were derived through model updating of 24 nominally identical CLT beam-like substructures, as described in [26], using experimental EMA results from [27] as a reference. The study then generates both probabilistic and stochastic mechanical property datasets, which are subsequently propagated through an FE model to examine how uncertainty in mechanical parameters translates into variability in modal parameters. The mechanical properties evaluated comprise material density, longitudinal Young's modulus, in-plane shear moduli, and the rolling-shear modulus. Probabilistic property distributions were generated using Gaussian Processes (GPs), while random samples were drawn using Latin Hypercube Sampling (LHS) and Monte Carlo (MC) methods. In addition, the individual minimum and maximum effects of these mechanical properties on the natural frequencies were evaluated through one-parameter variation. Furthermore, relationships between material density and the longitudinal Young's modulus, in-plane shear moduli, and rolling-shear modulus were established using linear regression.

The remaining sections of this article are organised as follows: Section 2 covers the methodology, including a brief discussion on previous EMA, model updating of CLT and their associated results and the methodologies used here for analysis and evaluations. Section 3 presents the results obtained from this research and their associated trends. Finally, Section 4 contains the conclusions drawn from this research and recommendations.

2. Methodology

This section provides a brief overview of previous research on EMA, model updating, and identification of the mechanical properties of the CLT structures studied here. It includes further FE modelling and formulation of a residual function to facilitate the evaluation of input-output uncertainties. The input parameters comprise the mechanical properties of CLT described using GP, LHS, and MC sampling, whereas the output parameters comprise natural frequencies and vibration modes. In addition, evaluation metrics are presented and references to the relevant literature are provided where deemed necessary.

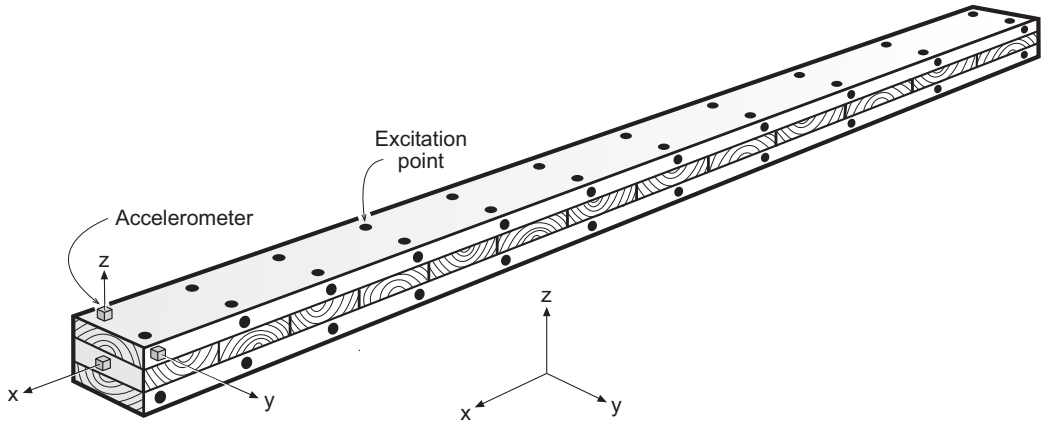


Figure 1: Illustration of the experimental setup of a three-layer CLT beam substructure with dimensions length (l) \times width (w) \times height (h) of 2 m \times 0.12 m \times 0.12 m. Each layer has a thickness of 40 mm. The outer layers are made of Norway Spruce, whereas the middle layer is made of Scots Pine. The substructure is discretised with 22 measurement points in the xy and xz planes, respectively. A single point in the yz plane was also measured but excluded in the model updating [26] and also herein. The coordinate system is consistent with the outer layers, and for the middle layer, the coordinate system is oriented about the z -axis at an angle of 90° .

Table 1

Coefficient of variation (CoV) of resonance frequencies for each mode, across 24 CLT beams.

Mode number	Out-of-plane bending (%)	Torsional (%)	In-plane bending (%)	Axial (%)
1	4.0	4.2	4.1	3.5
2	3.8	3.5	3.7	
3	3.2	3.7	2.6	
4	2.5	3.2	2.0	
5	2.4	3.5	1.9	
6	2.5	3.0	1.9	

2.1. Experimental Modal Analysis

The results of the EMA, as presented in [27], provide a comprehensive insight into the variability in the modal parameters of the CLT substructures used in this article. A total of 24 nominally identical CLT substructures were tested using 22 transverse (against the z axis), 22 lateral (against the y axis), and one axial (along the x axis) excitation points, as shown in Fig. 1. The beams were excited across a frequency range of 0-2 kHz using a modal hammer, and the corresponding acceleration for each point was measured using a piezoelectric accelerometer in each direction. The beams were tested under free-free conditions, suspended by bungee cords. After sampling and frequency domain transformations, the modal properties—comprising six out-of-plane bending modes, six torsional modes, six in-plane bending modes, and one axial mode—were determined, along with their natural frequencies and modal damping. The Coefficient of Variation (CoV) for the natural frequencies of each mode, expressed as a percentage, is computed as the ratio of the standard deviation to the mean for each frequency and is provided in Tab. 1.

The key results from the EMA highlight the variability in the modal properties of the CLT beams, even though they are geometrically nominally identical and made of the same wood species. This variability suggests that the dynamic properties of CLT are influenced by inherent material heterogeneity, which introduces uncertainty into the modelling of CLT structures. Consequently, accounting for this uncertainty in FE modelling is essential to ensure the robustness of the predictive models. Furthermore, the bending and torsional modes, along with their corresponding natural frequencies observed in EMA, provide critical benchmarks for the model updating procedure and the identification of the sensitive mechanical properties of CLT used in this study. Further discussion on model updating is provided in Section 2.2.

Table 2

Identified dynamic stiffness parameters of CLT beams following the model updating process. The initial values for the updated parameters were set as: $E_1 = 13,000$ MPa, $G_{12} = G_{13} = 810$ MPa, and $G_{23} = 57$ MPa. The parameters that were not updated, including the identified density, were fixed at the following values: $E_2 = 262$ MPa, $E_3 = 430$ MPa, $\nu_{12} = 0.48$, $\nu_{13} = 0.42$, and $\nu_{23} = 0.28$. Further information on the updating procedure can be found in [26].

ρ (kg/m ³)	E_1 (MPa)	$G_{12} = G_{13}$ (MPa)	G_{23} (MPa)	ρ (kg/m ³)	E_1 (MPa)	$G_{12} = G_{13}$ (MPa)	G_{23} (MPa)
440	11071	704	198	458	11086	693	187
478	12480	818	181	486	11463	815	202
424	10206	677	214	507	13277	871	171
476	12267	824	198	489	11552	824	207
464	12257	798	182	493	12231	750	158
509	13201	907	192	448	10254	725	188
483	11996	842	232	458	11170	727	170
448	12463	788	167	461	11541	712	172
483	11479	766	214	461	11996	769	180
462	11761	781	204	507	13212	884	180
487	11005	892	202	479	12256	843	211
445	10522	720	147	516	12941	862	182

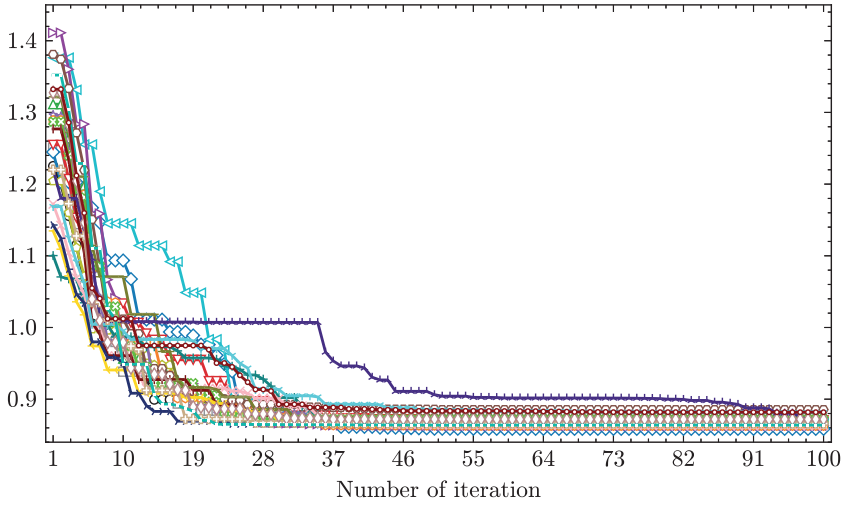


Figure 2: Convergence behaviour and progressive reduction of the residual in (4) through iterative adjustment of the sensitive material parameters (E_1 , $G_{12} = G_{13}$, G_{23}). Full methodological details are provided in [26].

2.2. Finite Element modelling

The tested substructures were modelled as solid bodies and discretised using brick FEs with quadratic interpolation, as implemented in Abaqus [28]. The layers were coupled transversally (along the z-axis) using a node-to-node tie coupling, assuming perfect bonding between them. No coupling was considered between the individual boards along the x-axis (see Fig. 1), indicating the absence of adhesive bonding between them. The discretisation was refined to an element size of 0.02 m, ensuring convergence across all relevant natural frequencies of interest. The corresponding homogeneous equations of motion were derived as:

$$\mathbf{M}^{(k)}(\theta) \ddot{\mathbf{a}}(t) + \mathbf{K}^{(k)}(\theta) \mathbf{a}(t) = \mathbf{0}, \quad (1)$$

where the mass and stiffness matrices, i.e., $\mathbf{M}^{(k)}(\theta)$ and $\mathbf{K}^{(k)}(\theta)$, contain the substructure's lumped mass and corresponding nodal stiffness in the physical domain at iteration k for a set of model parameters $\theta \in \{\theta_1, \theta_2, \dots, p\}$.

The nodal acceleration and displacement fields are collected in $\ddot{\mathbf{a}}(t)$ and $\mathbf{a}(t)$, respectively. As the system is undamped and homogenous, its corresponding natural frequencies and vibration modes can be computed iteratively using Lanczos solver [29] from an eigenvalue problem,

$$\left[\mathbf{K}^{(k)}(\boldsymbol{\theta}) - \omega_j^{(k)^2}(\boldsymbol{\theta}) \mathbf{M}^{(k)}(\boldsymbol{\theta}) \right] \boldsymbol{\psi}_j^{(k)}(\boldsymbol{\theta}) = \mathbf{0}, \quad j = 1, 2, \dots, N_j, \quad (2)$$

where $\omega_j^{(k)^2}(\boldsymbol{\theta})$ and $\boldsymbol{\psi}_j^{(k)}(\boldsymbol{\theta})$ denote respectively the system's j th eigenvalue and eigenmode for k th subset of model parameters. The equation is solved for N_j modes of interest. The corresponding natural frequency of the eigenvalue in Hz can be determined using the following relation $f_j^{(k)}(\boldsymbol{\theta}) = \sqrt{\omega_j^{(k)^2}(\boldsymbol{\theta})}/2\pi$. The eigenmodes are all mass normalised so that $\boldsymbol{\Psi}(\boldsymbol{\theta})^T \mathbf{M}(\boldsymbol{\theta}) \boldsymbol{\Psi}(\boldsymbol{\theta}) = \mathbf{I}$ and $\boldsymbol{\Psi}(\boldsymbol{\theta})^T \mathbf{K}(\boldsymbol{\theta}) \boldsymbol{\Psi}(\boldsymbol{\theta}) = \boldsymbol{\Lambda}(\boldsymbol{\theta})$, where \mathbf{I} is an identity matrix and $\boldsymbol{\Lambda}(\boldsymbol{\theta}) = \text{diag}(\omega_1^{(k)^2}, \omega_2^{(k)^2}, \dots, \omega_{N_j}^{(k)^2})$. Systems without Dirichlet conditions can exhibit rigid body modes for which $\omega_j \approx 0$, otherwise $\omega_j > 0$. The equation above represents a computational model $\mathcal{M}(\boldsymbol{\theta})$, which for a certain model input $\boldsymbol{\theta}$ produces natural frequencies and modes.

Natural frequencies and vibration modes determined through EMA were used together with their corresponding FE counterparts to identify the sensitive mechanical properties of these substructures, including E_1 , $G_{12} = G_{13}$, G_{23} [26]. The primary reason for updating only the sensitive mechanical properties is their influence on the objective function, which allows them to be tuned towards their optimal values. In contrast, updating insensitive parameters leads to an ill-conditioned problem, where the objective function cannot be effectively minimised or optimised. Furthermore, the mechanical properties are assumed to be constant throughout the entire structure, which means that no random fields were considered in the material. This assumption simplifies the analysis, though it may limit the representation of spatial variability in material properties. In addition, it was assumed that the uncertainties arising from the distribution of geometrical dimensions (e.g., thickness of layers) and orientation angles were negligible.

The density ρ of the substructures was determined by dividing their respective weight by their volume, whereas the other insensitive orthotropic parameters (E_2 , E_3 , ν_{12} , ν_{13} , ν_{23}) were fixed to (262 MPa, 430 MPa, 0.48, 0.42, 0.28), respectively. Consequently, the following unconstrained problem was formulated,

$$(\mathbb{P}) \begin{cases} \underset{\boldsymbol{\theta} \in \mathbb{R}^3}{\text{argmin}} & \mathcal{R}(\boldsymbol{\theta}), \\ \text{where} & \boldsymbol{\theta} \in \{E_1, G_{12} = G_{13}, G_{23}\}, \end{cases} \quad (3)$$

with the residual function $\mathcal{R}(\boldsymbol{\theta})$ defined as:

$$\mathcal{R}(\boldsymbol{\theta}) = \sum_{j=1}^n \left(|\tilde{f}_j - f_j^{(k)}(\boldsymbol{\theta})| / f_j^{(k)}(\boldsymbol{\theta}) \right)^2 + \sum_{i,j=1}^n \left[1 - \left(\text{MAC}^{(k)} \left(\tilde{\boldsymbol{\psi}}_i, \boldsymbol{\psi}_j^{(k)}(\boldsymbol{\theta}) \right) \right) \right], \quad (4)$$

where MAC is a quantitative tool for comparing two vibration modes, as further discussed in Section 2.4. The j th observed and predicted natural frequencies together with their corresponding modes are denoted \tilde{f}_j , $f_j^{(k)}$, $\tilde{\boldsymbol{\psi}}_j$, $\boldsymbol{\psi}_j^{(k)}$, respectively. It is noted that a tilde refers to observed quantities (obtained from EMA) which are neither dependent on the inputs of the model $\boldsymbol{\theta}$ nor the state of the model denoted k . The optimisation problem formulated in (3) was solved iteratively using the Nelder–Mead simplex algorithm [30, 31], in order to minimise the discrepancy between the FE model predictions and the modal parameters identified from EMA. The convergence behaviour of the objective function over successive iterations is presented in Fig. 2. As a result of the updating procedure, the sensitive mechanical properties of the CLT beams were estimated, and the corresponding values are reported in Tab. 2. These sensitive mechanical properties of CLT substructures, determined using the above approach in [26], will henceforth be referred to as the observed mechanical properties.

2.3. Probabilistic modelling and sampling

The inherent variability and randomness observed in the mechanical properties of CLT suggest that the 24 available data subsets may be insufficient to fully capture the underlying uncertainty. Consequently, stochastic modelling techniques become essential for accurately characterising these properties. An effective approach is to use Gaussian processes (GPs) to obtain a full posterior distribution over the mechanical property values. In GP regression, a kernel

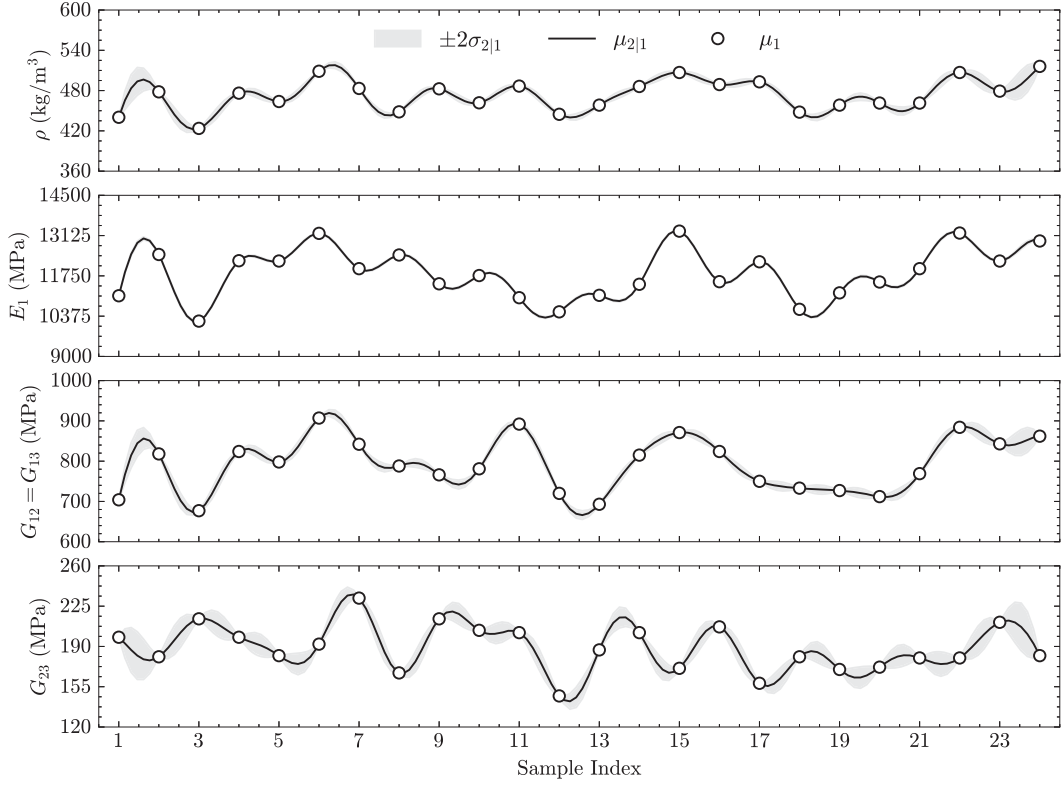


Figure 3: Illustration of the application of Gaussian Processes (GPs) to generate 150 additional samples of the mechanical properties of CLT, based on the 24 observed data points. The observed data points (density ρ , E_1 , $G_{12} = G_{13}$, and G_{23}) were obtained through model updating, as detailed in [26]. The observed data is denoted as μ_1 , whereas the generated data is represented by $\mu_{2|1}$, with its associated confidence interval denoted by $\pm 2\sigma_{2|1}$.

(covariance) function is used to encode assumptions about the smoothness and structure of the underlying function. The observed data (denoted by \mathbf{x}_1) and the new (predicted) data points (denoted by \mathbf{x}_2) are assumed to be jointly Gaussian. Thus, their combined multivariate distribution can be written as

$$\begin{Bmatrix} \mathbf{x}_1 \\ \mathbf{x}_2 \end{Bmatrix} \sim \mathcal{N} \left(\begin{Bmatrix} \boldsymbol{\mu}_1 \\ \boldsymbol{\mu}_2 \end{Bmatrix}, \begin{bmatrix} \boldsymbol{\Sigma}_{11} & \boldsymbol{\Sigma}_{12} \\ \boldsymbol{\Sigma}_{21} & \boldsymbol{\Sigma}_{22} \end{bmatrix} \right), \quad (5)$$

where the notations $\boldsymbol{\mu}$ and $\boldsymbol{\Sigma}$ represent the mean vector and covariance matrix, respectively. The conditional probability of predicting new random variables, given the observed data from (5), can be expressed as:

$$p(\boldsymbol{\mu}_2 | \boldsymbol{\mu}_1, \mathbf{x}_1, \mathbf{x}_2) \sim \mathcal{N}(\boldsymbol{\mu}_{2|1}, \boldsymbol{\Sigma}_{2|1}), \quad (6)$$

where the conditional quantities are derived as

$$\boldsymbol{\mu}_{2|1} = \boldsymbol{\Sigma}_{21} \boldsymbol{\Sigma}_{11}^{-1} \mathbf{x}_1, \quad (7a)$$

$$\boldsymbol{\Sigma}_{2|1} = \boldsymbol{\Sigma}_{22} - \boldsymbol{\Sigma}_{21} \boldsymbol{\Sigma}_{11}^{-1} \boldsymbol{\Sigma}_{12}. \quad (7b)$$

and the covariance matrices are computed using the Radial Basis Function (RBF) kernel defined as

$$k(\mathbf{x}_1, \mathbf{x}_2) = \exp \left(-\frac{1}{2l^2} \|\mathbf{x}_1 - \mathbf{x}_2\|^2 \right), \quad (8)$$

Table 3

Summary of mechanical properties using various methods: FE Model Updating (Observed), Gaussian Processes (GP), Latin Hypercube Sampling (LHS), and Monte Carlo (MC) sampling.

Parameter	Method	Min	Mean	Max	Variance	Std. Dev.	CoV (%)	95% Confidence Interval
ρ (kg/m ³)	weight/volume	423	473	516	549	23	4.95	[463, 483]
	GP	422	473	517	470	21	4.58	[470, 477]
	LHS	424	469	515	710	26	5.67	[465, 474]
	MC	424	470	515	686	26	5.57	[465, 474]
E_1 (MPa)	Observed	10206	11835	13277	717574	847	7.16	[11477, 12192]
	GP	10207	11851	13289	670931	819	6.91	[11719, 11983]
	LHS	10210	11741	13263	786387	886	7.55	[11598, 11884]
	MC	10272	11841	13269	748629	865	7.31	[11701, 11980]
$G_{12} = G_{13}$ (MPa)	Observed	677	791	907	4349	65	8.33	[763, 819]
	GP	666	793	919	4063	63	8.03	[783, 803]
	LHS	677	791	905	4400	66	8.39	[781, 802]
	MC	677	790	904	4907	70	8.86	[779, 801]
G_{23} (MPa)	Observed	147	188	232	383	19	10.38	[180, 197]
	GP	142	188	235	372	19	10.21	[185, 192]
	LHS	147	189	231	601	24	12.93	[185, 193]
	MC	147	186	231	558	23	12.65	[183, 190]

where the length scale l determines the smoothness of the distribution and is obtained through hyper-parameter optimisation. The term $\|x_1 - x_2\|$ represents the Euclidean distance between two data points [32, 33, 34]. The mechanical properties of CLT determined through model updating in Tab. 2 were used as input data for the GP, which subsequently generated 150 samples, as illustrated in Fig. 3. The number of samples was determined by monitoring the stability of the conditional standard deviation to ensure adequate coverage of the predictive uncertainty.

To validate the Gaussian Process (GP) model, which facilitates a smooth interpolation between the observed data points, both Latin Hypercube Sampling (LHS) [35, 36, 37] and Monte Carlo (MC) sampling [38, 39] were used to generate stochastic random variables that represent the variability in the mechanical properties of the beams. The LHS and MC sampling techniques were applied using the minimum and maximum bounds of the observed mechanical properties in Tab. 3.

The LHS technique ensures an even distribution of samples across the input space by stratifying the space into intervals, providing an efficient coverage of the parameter space. In contrast, the MC sampling method relies on random sampling according to the probability distributions of the input variables, offering a more exhaustive exploration of the input space at the cost of increased computational effort.

To ensure a robust comparison with the GP model, 150 samples were generated using both LHS and MC techniques for each mechanical property. Subsequently, these samples were used in the FE model in (2) to determine the corresponding natural frequencies and vibration modes. A summary of the mechanical properties used in the analysis, along with their respective generated counterparts, is presented in Table 3.

2.4. Uncertainty quantification

To quantify the uncertainty relationship between inputs and outputs, the sampled parameters are propagated into the FE model in (1), which was further used to solve the eigenvalue problem in (2) to determine the natural frequencies and modes of the system for each set of input data. Similarly to EMA measurements, a distinction is made between the out-of-plane, torsional, and in-plane bending modes. To distinguish between these modes and identify their respective natural frequencies, the numerical modes from (2) were compared with the observed ones using the Modal Assurance Criterion (MAC):

$$\text{MAC}^{(k)}(\hat{\psi}_i, \psi_j^{(k)}(\theta)) = \frac{|\hat{\psi}_i^H \psi_j^{(k)}(\theta)|^2}{(\hat{\psi}_i^H \hat{\psi}_i) (\psi_j^{(k)}(\theta)^H \psi_j^{(k)}(\theta))}, \quad (9)$$

where $\hat{\psi}_i$ is an observed mode vector whereas $\psi_j^{(k)}(\theta)$ is the corresponding predicted counterpart at iteration k . The MAC returns a value between zero and unity, where zero denotes orthogonality, and unity denotes perfect correlation.

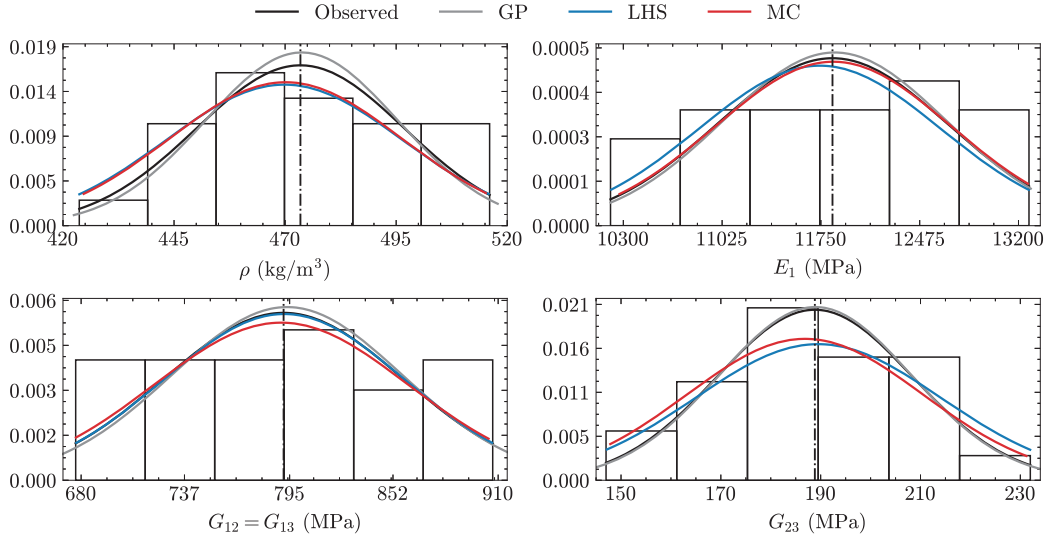


Figure 4: Estimated probability density distributions of the observed mechanical properties of CLT substructures, comparing the distributions of various sampling methods: Gaussian Process (GP), Latin Hypercube Sampling (LHS), and Monte Carlo (MC) sampling. The Gaussian distributions follow the expression in (12).

Once the mode is identified, its associated natural frequency is stored to ensure a distinction between the bending and torsional modes. The axial mode was excluded from this procedure as it contains only one value and could therefore not be identified using the MAC approach in (9). To assess the uncertainty span within the mechanical properties and their associated natural frequencies, a relative difference to their mean values was employed using

$$\text{relative difference} = \frac{\mathbf{x} - \mu(\mathbf{x})}{\mu(\mathbf{x})}, \quad (10)$$

where $\mu(\mathbf{x})$ is a mean value operator. Furthermore, a univariate normal distribution was used to evaluate the distribution of the mechanical properties and their corresponding natural frequencies following

$$\mathbf{x} \sim \mathcal{N}(\mu(\mathbf{x}), \sigma^2), \quad (11)$$

where $\mu(\mathbf{x})$ is the mean and σ^2 is the variance. The Probability Density Function (PDF) of a normalised Gaussian function is given by

$$p(\mathbf{x}|\mu(\mathbf{x}), \sigma) = \frac{1}{\sqrt{2\pi\sigma^2}} \exp\left(-\frac{(\mathbf{x} - \mu(\mathbf{x}))^2}{2\sigma^2}\right), \quad (12)$$

which represents a univariate normal distribution for the random variables in \mathbf{x} . The PDF distributions of the mechanical properties are illustrated in Fig. 4. To further evaluate the distribution of the probabilities in (12), a sum of their probabilities is computed using the Cumulative distribution function (CDF) using

$$F(\mathbf{x}) = \sum \frac{1}{\sqrt{2\pi\sigma^2}} \exp\left(-\frac{(\mathbf{x} - \mu(\mathbf{x}))^2}{2\sigma^2}\right). \quad (13)$$

A brief summary of the procedural framework for uncertainty quantification proposed in this study is presented in Algorithm 1. The procedure begins with model updating and the inverse identification of the mechanical properties. This is followed by probabilistic and stochastic sampling based on the identified parameters. Subsequently, the framework outlines the uncertainty quantification through FE propagation and concludes with a sensitivity analysis to assess the influence of input variability on the output natural frequencies and modes.

Algorithm 1 Uncertainty and quantification of CLT framework.

```

1: Initialise  $\mathbf{M}(\theta), \mathbf{K}(\theta)$ 
2: Formulate the minimisation problem ( $\mathbb{P}$ ), in (3)
3: Minimise  $\mathcal{R}(\theta)$  and identify  $\theta \in \{\theta_1, \theta_1, \dots, \theta_{N_j}\}$ , in (4)
4: Model  $\theta$  probabilistically, in (5) – (8)
5: Model  $\theta$  stochastically using LHS and MC sampling
6: for all  $\theta$  do ▷ Evaluate uncertainty
7:   Solve  $\mathcal{M}(\theta)$ , in (2)
8:   Identify mode types using MAC, in (9)
9:   Compute relative difference, in (10)
10: end for
11: for all  $\theta^\pm$  and  $\theta^\mu$  do ▷ Evaluate sensitivity
12:   Solve  $\mathbf{y}^\pm = \mathcal{M}(\theta^\pm)$ , in (2)
13:   Solve  $\mathbf{y}^\mu = \mathcal{M}(\theta^\mu)$ , in (2)
14:   Identify mode types using MAC, in (9)
15:   Compute  $S_{j,\omega}^\pm(\theta)$ , in (16)
16:   Compute  $S_{j,\psi}^\pm(\theta)$ , in (17)
17: end for

```

2.5. Local sensitivity analysis

The influence of individual mechanical properties on the natural frequencies can be quantified using a one-parameter variation approach. The minimum, mean, and maximum values of the mechanical properties, as listed in Tab. 3, were used as input to the model $\mathcal{M}(\theta)$ in (2). The corresponding natural frequencies were determined using (2):

$$\mathbf{y}^\pm(\theta) = \mathcal{M}(\theta^\pm), \quad (14a)$$

$$\mathbf{y}^\mu(\theta) = \mathcal{M}(\theta^\mu), \quad (14b)$$

where $\theta^\mu \in \{\theta_1^\mu, \theta_2^\mu, \dots, \theta_{N_j}^\mu\}$ represents the mean values of the model parameters, and $\theta^\pm \in \{\theta_1^-, \theta_2^-, \dots, \theta_{N_j}^-; \theta_1^+, \theta_2^+, \dots, \theta_{N_j}^+\}$ represents the minimum and maximum values of the parameters, as shown in Tab. 3. The corresponding outputs in (14) are:

$$\mathbf{y}^\pm(\theta) = \{\omega_1^-, \omega_2^-, \dots, \omega_{N_j}^-, \psi_1^-, \psi_2^-, \dots, \psi_{N_j}^-; \omega_1^+, \omega_2^+, \dots, \omega_{N_j}^+, \psi_1^+, \psi_2^+, \dots, \psi_{N_j}^+\}, \quad (15a)$$

$$\mathbf{y}^\mu(\theta) = \{\omega_1^\mu, \omega_2^\mu, \dots, \omega_{N_j}^\mu, \psi_1^\mu, \psi_2^\mu, \dots, \psi_{N_j}^\mu\}. \quad (15b)$$

The sensitivity of the model outputs to variations in the input parameters was examined by setting one parameter at a time to its maximum or minimum value, while keeping all other parameters fixed at their mean values. The natural frequencies and modes for each set of parameters were then determined. The sensitivity of the natural frequencies was computed as:

$$S_{j,\omega}^\pm(\theta) = \frac{\mathbf{y}_{j,\omega}^\pm(\theta) - \mathbf{y}_{j,\omega}^\mu(\theta)}{\mathbf{y}_{j,\omega}^\mu(\theta)}, \quad (16)$$

while the sensitivity of the mode shapes was determined using the MAC in (9) as:

$$S_{j,\psi}^\pm(\theta) = \frac{\text{MAC}(\psi_j^\pm(\theta), \psi_j^\mu(\theta)) - \text{MAC}(\psi_j^\mu(\theta), \psi_j^\mu(\theta))}{\text{MAC}(\psi_j^\mu(\theta), \psi_j^\mu(\theta))}, \quad (17)$$

Here, $\psi^\mu(\theta)$, $\psi^-(\theta)$, and $\psi^+(\theta)$ denote the modes determined using the mean value, the lower and upper values of the mechanical properties in Tab. 3, respectively. Sensitivity analysis in (16) and (17) was evaluated for all j , including six out-of-plane bending, torsional, and in-plane bending modes; however, only the minimum and maximum values of $S_{j,\omega}^\pm(\theta)$ and $S_{j,\psi}^\pm(\theta)$ were used to evaluate the uncertainty of the output.

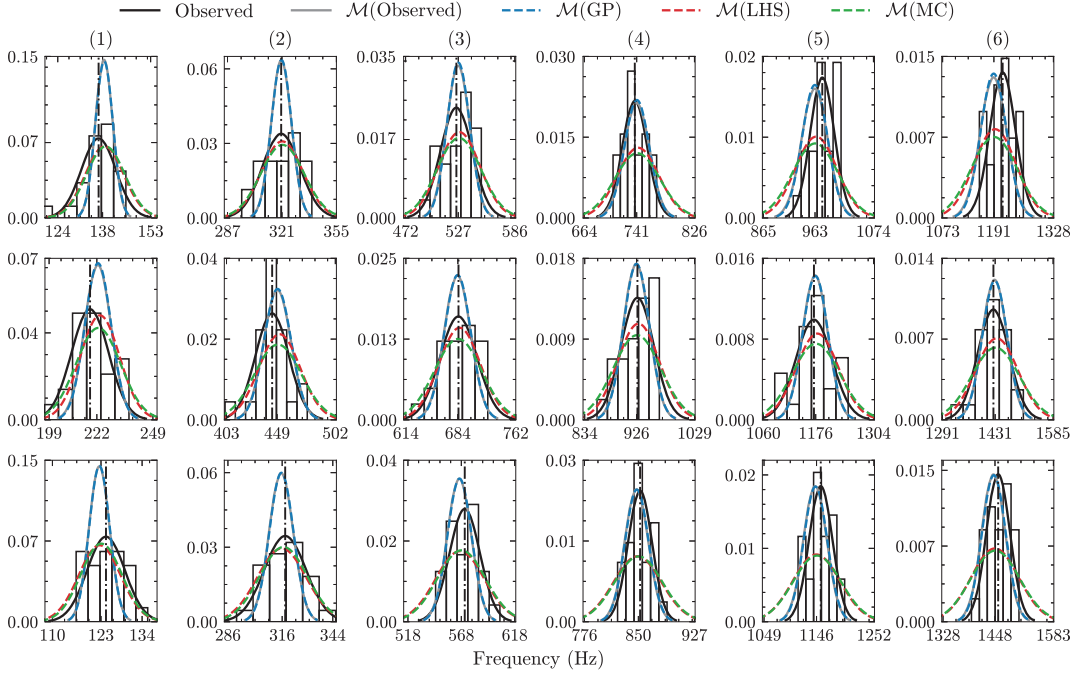


Figure 5: From top to bottom: probability density distribution of six out-of-plane bending (top subplots), torsional (middle subplots), and in-plane bending (bottom subplots) natural frequencies following the Gaussian distribution in (12).

3. Results and analysis

This section presents the results of the uncertainty quantification, including the distributions of the natural frequencies and their corresponding cumulative distributions across different vibration modes. The relative differences of the natural frequencies with respect to their mean values are evaluated for both the EMA results and the different propagation techniques (GP, LHS, and MC sampling). Furthermore, results from a local sensitivity analysis are presented, in which the influence of individual mechanical properties on the natural frequencies and mode shapes is assessed by examining their minimum and maximum impacts. Finally, the relationship between material density and the longitudinal Young's modulus, interior shear moduli, and rolling shear modulus is investigated using linear regression.

3.1. Effect of uncertainty on the natural frequencies and modes

As depicted in Fig. 5, the Gaussian distributions of the output natural frequencies reveal distinct characteristics associated with each category from which the mechanical properties originate. The Gaussian distribution of the natural frequencies associated with observed and GP mechanical properties results in a nearly similar distribution, which is narrower than their experimental counterparts. In contrast, with increased stochastic variation in mechanical properties, particularly those originating from stochastic LHS and MC sampling, the probability distribution becomes broader. In the same way, the cumulative distribution curves of the natural frequencies associated with observed and GP parameters are steeper compared to those associated with stochastic parameters, Fig. 6. The cumulative distribution curves further indicate that with an increased stochastic nature of the mechanical properties, particularly those stemming from LHS and MC sampling, the cumulative distribution curves become broader.

In contrast to natural frequencies, their associated modes are not significantly influenced by uncertainty in mechanical properties. The vibration modes associated with the natural frequencies in Fig. 7 show an excellent correlation with their corresponding observed modes of EMA with $MAC_{jj} > 0.98$ for $j \in \{1, 2, \dots, 6\}$. With an exception for the lower correlation associated with the sixth torsional and in-plane bending modes with $MAC_{66} \approx 0.67$

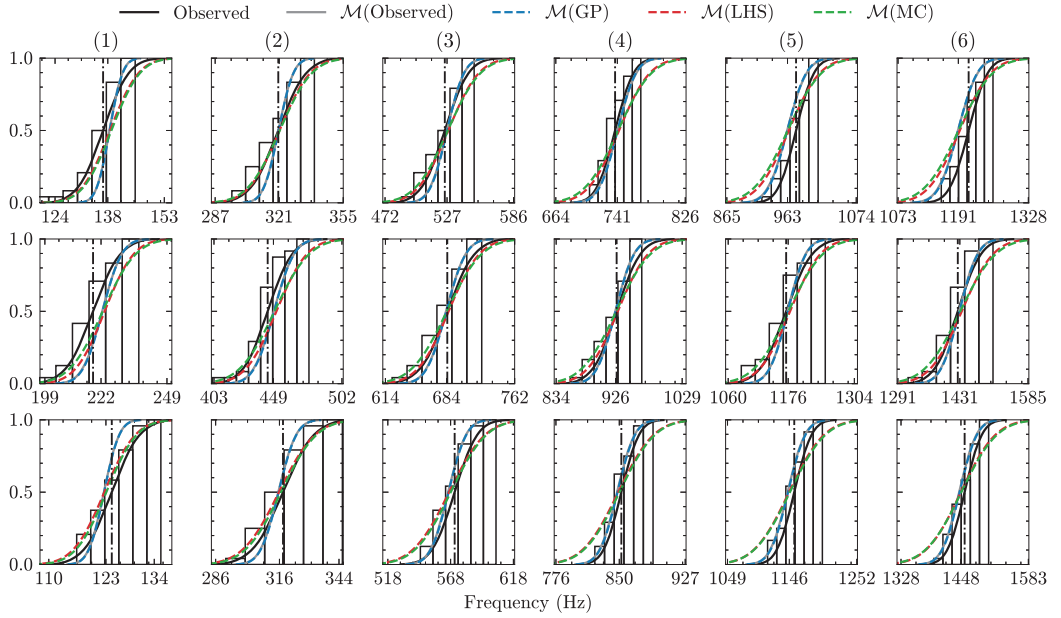


Figure 6: From top to bottom: cumulative distribution of six out-of-plane bending (top subplots), torsional (middle subplots), and in-plane bending (bottom subplots) natural frequencies following the expression in (13).

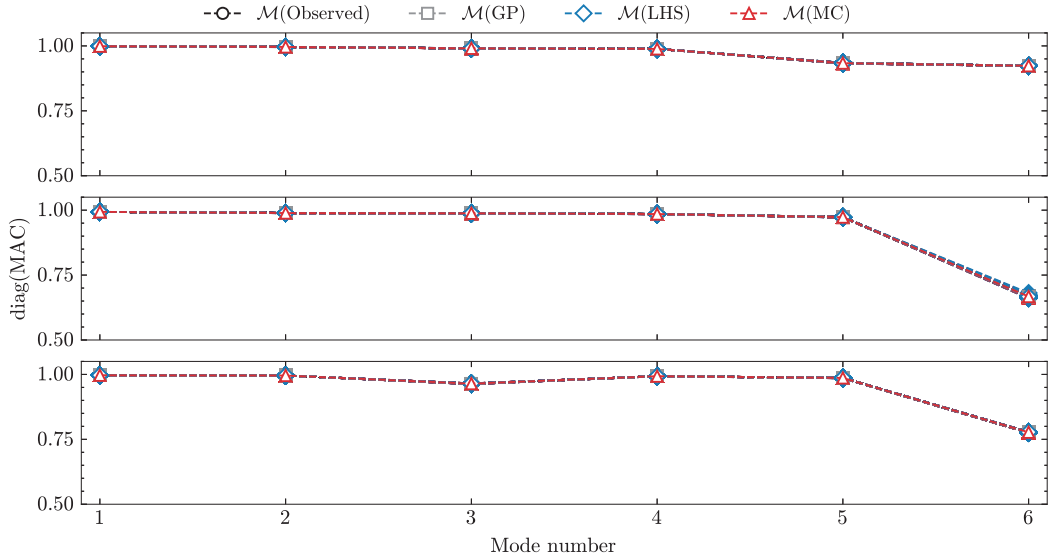


Figure 7: From top to bottom: Cross MAC between six out-of-plane bending (top subplot), torsional (middle subplot), and in-plane bending (bottom subplot) modes and their corresponding modes from EMA using (9).

and $MAC_{66} \approx 0.77$, respectively. The insensitivity of the modes to variability in the mechanical properties has been previously exploited for variability prediction in FE models of laminated structures [40, 41].

The probability and cumulative distribution of the natural frequencies in Figs. 5 and 6 require further evaluation of the uncertainty in the natural frequencies with respect to their mean values. In this evaluation, the MACs were not included as Fig. 7 indicates a minor influence of uncertainty in the mechanical properties on the vibration modes.

To quantify the uncertainty in the outputs, a relative difference between the natural frequencies and their corresponding mean values was calculated, Fig. 8. The experimental data indicate that an uncertainty between 5-10% is expected. In contrast, the FE evaluation indicates a marginally lower variability than the observed ones. With an increase in the number of probabilistic data, using GP variability in the uncertainty becomes somewhat more stable. However, outliers appear in the torsional natural frequencies. Consequently, the uncertainty in the out-of-plane bending

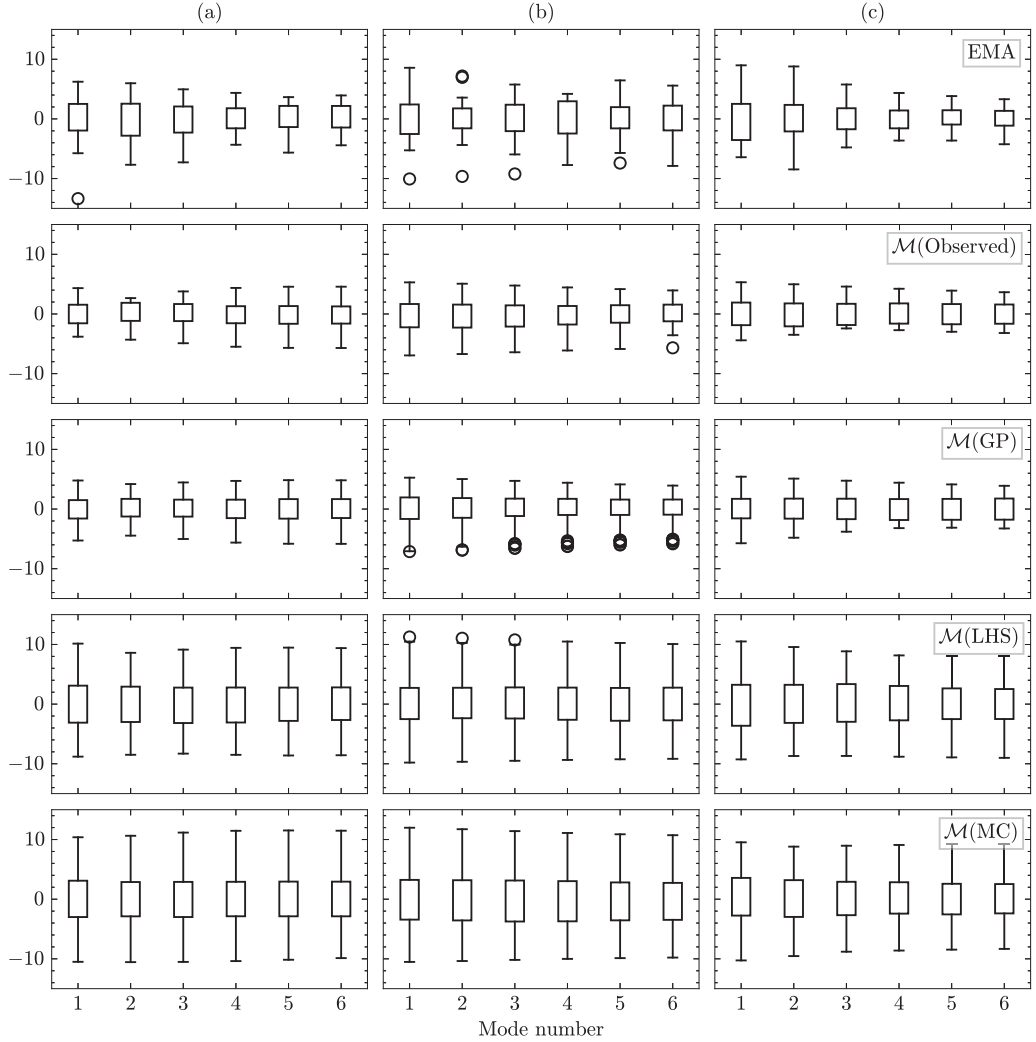


Figure 8: Minimum and maximum percentage variability in natural frequencies relative to their mean values, as defined in (10). Columns (a), (b), and (c) correspond to out-of-plane bending, torsional, and in-plane bending modes, respectively. The subplot rows represent data obtained from Experimental Modal Analysis (EMA) and different propagation methods: observed data $\mathcal{M}(\text{Observed})$, Gaussian Process $\mathcal{M}(\text{GP})$, Latin Hypercube Sampling $\mathcal{M}(\text{LHS})$, and Monte Carlo sampling $\mathcal{M}(\text{MC})$. Representative visualisations of these mode shapes are provided in the Appendix of [27].

(row 3 in subplot (a) in Fig. 8) and in-plane bending (row 3 in subplot (c) in Fig. 8) natural frequencies fall under 5%. On the other hand, the uncertainties in the torsional modes (row 3 in subplot (b) of Fig. 8) are less than 8%. When mechanical properties vary stochastically, the uncertainty in natural frequencies increases to 12%, as seen for natural frequencies associated with LHS and MC samplings (rows 4 and 5 of (a), (b) and (c) in Fig. 8). The natural frequencies associated with the in-plane bending modes exhibit an uncertainty below 10% in contrast to the out-of-plane bending and torsional modes. Overall, the results indicate that an increase in the number of data points stabilises the uncertainty distribution in the vibration natural frequencies.

3.2. Local sensitivity analysis

To assess the sensitivity of individual mechanical properties on the natural frequencies and modes across different propagation techniques, the minimum, maximum, and mean values of each parameter from Tab.3 were propagated into the FE model. Their corresponding outputs were then evaluated using (16) and (17), as shown in Figs.9 and 10. The results reveal distinct variations in the natural frequencies associated with different types of modes.

The density ρ influences the natural frequencies of all modes. An uncertainty of $\pm 10\%$ in the density ρ (Fig. 9(d)) results in a minimum or maximum uncertainty of up to $\pm 6\%$ in the natural frequencies. In contrast, the variation in density ρ did not influence the modes as seen in the evaluation in Fig. 10.

The longitudinal Young's modulus, E_1 , has the greatest influence on the bending modes and only a minor effect on the torsional modes. An uncertainty of $\pm 14\%$ in E_1 (Fig. 9(d)) results in an uncertainty up to $\pm 7\%$ in the bending-mode frequencies, see as shown in Figs. 9(a) and (c). However, E_1 did not significantly affect the sensitivity of the modes to its variation, Fig. 10.

The interior shear moduli, $G_{12} = G_{13}$ (Fig. 9(d)), exert the greatest influence on the torsional and in-plane bending natural frequencies, while their effect on the out-of-plane bending frequencies is comparatively smaller, see as shown in Figs. 9(a) – (c). An uncertainty of approximately 14.5% in $G_{12} = G_{13}$ leads to up to $\pm 5\%$ uncertainty in the torsional and in-plane bending frequencies, and around $\pm 2\%$ in the out-of-plane bending frequencies. In contrast to the natural frequencies, the vibration modes themselves are not significantly affected by variations in these shear moduli, Fig. 10.

Finally, the rolling shear modulus, G_{23} , is the parameter with the highest variability—up to 23% (Fig. 9(d)) and primarily influences the out-of-plane bending and torsional natural frequencies, as shown in Figs. 9(a) and (b). However, the variability in G_{23} has almost no influence on the corresponding vibration modes. An uncertainty of almost $\pm 23\%$ in G_{23} results in up to $\pm 6\%$ uncertainty in the out-of-plane bending and torsional natural frequencies, Figs., Fig. 9 and , Fig. 10.

The results further indicate that probabilistic or stochastic variation in the parameters did not influence the sensitivity analysis results due to the use of lower, mean, and upper limits of the parameters since their distributions are nearly similar, Fig. 4. Furthermore, the results in Fig. 10 indicate that the use of different sampling techniques to generate the input mechanical properties did not influence the sensitivity of the modes, as a similar degree of sensitivity was obtained for the parameters sampled by GP, LHS and MC.

3.3. Relation between the mechanical properties

Despite the variability in the mechanical properties of wood, a relationship can be established between density ρ , longitudinal Young's modulus E_1 , and interior shear moduli $G_{12} = G_{13}$. In this analysis, only the observed mechanical properties and their corresponding probabilistic ones generated using GP are included, whereas the stochastic data points generated using LHS and MC sampling were excluded due to their stochastic nature. A linear regression using $y(\rho) = a_0 + a_2\rho$ was used to assess the degree of correlation between ρ and E_1 , ρ and $G_{12} = G_{13}$, and ρ and G_{23} . The ρ was used as an input parameter due to the ease of identifying the density of the wood using, for example, the weight/volume ratio.

Consequently, a regression model with $R^2 = 0.58$ was achieved for the $\rho - E_1$ relation and a stronger linearity between $\rho - (G_{12} = G_{13})$ corresponding to $R^2 = 0.70$. However, no linear relationship between $\rho - G_{23}$ was established, indicating a nearly independency of G_{23} on ρ , Fig. 11. Furthermore, the use of GP data did not improve the linearity relations $\rho - E_1$ and $\rho - (G_{12} = G_{13})$, but marginally reduced them. The established relations for density as input values, as shown in Fig. 11, can be found in the following expressions

$$E_1(\rho) = 27.46\rho - 1166.43, \quad R^2 = 0.58, \quad \text{Observed}, \quad (18a)$$

$$E_1(\rho) = 28.11\rho - 1465.69, \quad R^2 = 0.55, \quad \text{GP}, \quad (18b)$$

$$[G_{12} = G_{13}](\rho) = 2.35\rho - 319.33, \quad R^2 = 0.70, \quad \text{Observed}, \quad (18c)$$

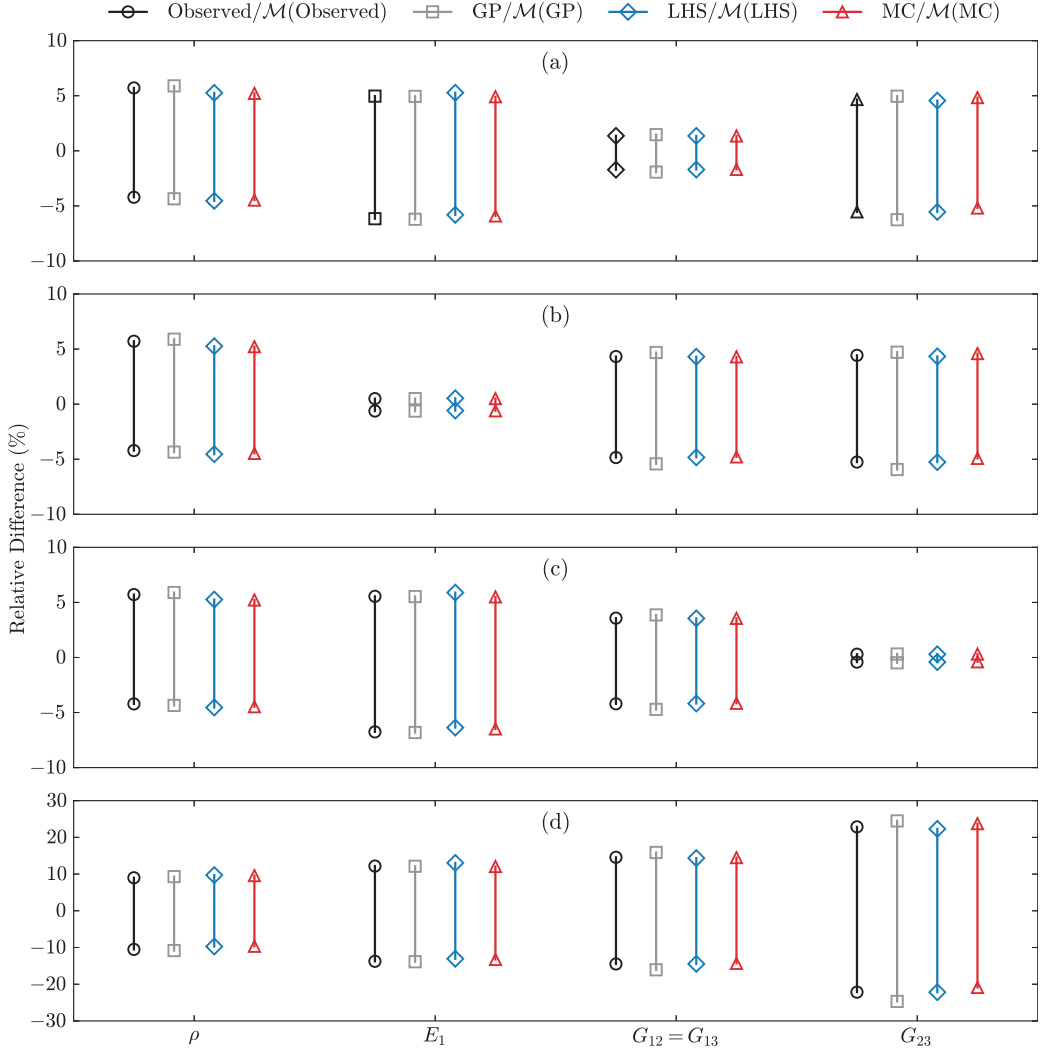


Figure 9: Relative deviations in natural frequencies for (a) out-of-plane bending, (b) torsional, and (c) in-plane bending modes, due to variability in individual mechanical properties. The deviations are normalised with respect to the frequencies obtained using mean mechanical properties, as defined in (16). Panel (d) shows the relative differences in the mechanical properties (ρ , E_1 , $G_{12} = G_{13}$, G_{23}), normalised with respect to their corresponding means. The bars represent the range (minimum to maximum) of deviations for each uncertainty propagation method: Observed, Gaussian Process (GP), Latin Hypercube Sampling (LHS), and Monte Carlo (MC).

$$[G_{12} = G_{13}](\rho) = 2.42\rho - 354.49, \quad R^2 = 0.68, \quad \text{GP}, \quad (18d)$$

$$G_{23}(\rho) = 0.05\rho + 166.57, \quad R^2 = 0.00, \quad \text{Observed}, \quad (18e)$$

$$G_{23}(\rho) = 0.12\rho + 129.78, \quad R^2 = 0.02, \quad \text{GP}. \quad (18f)$$

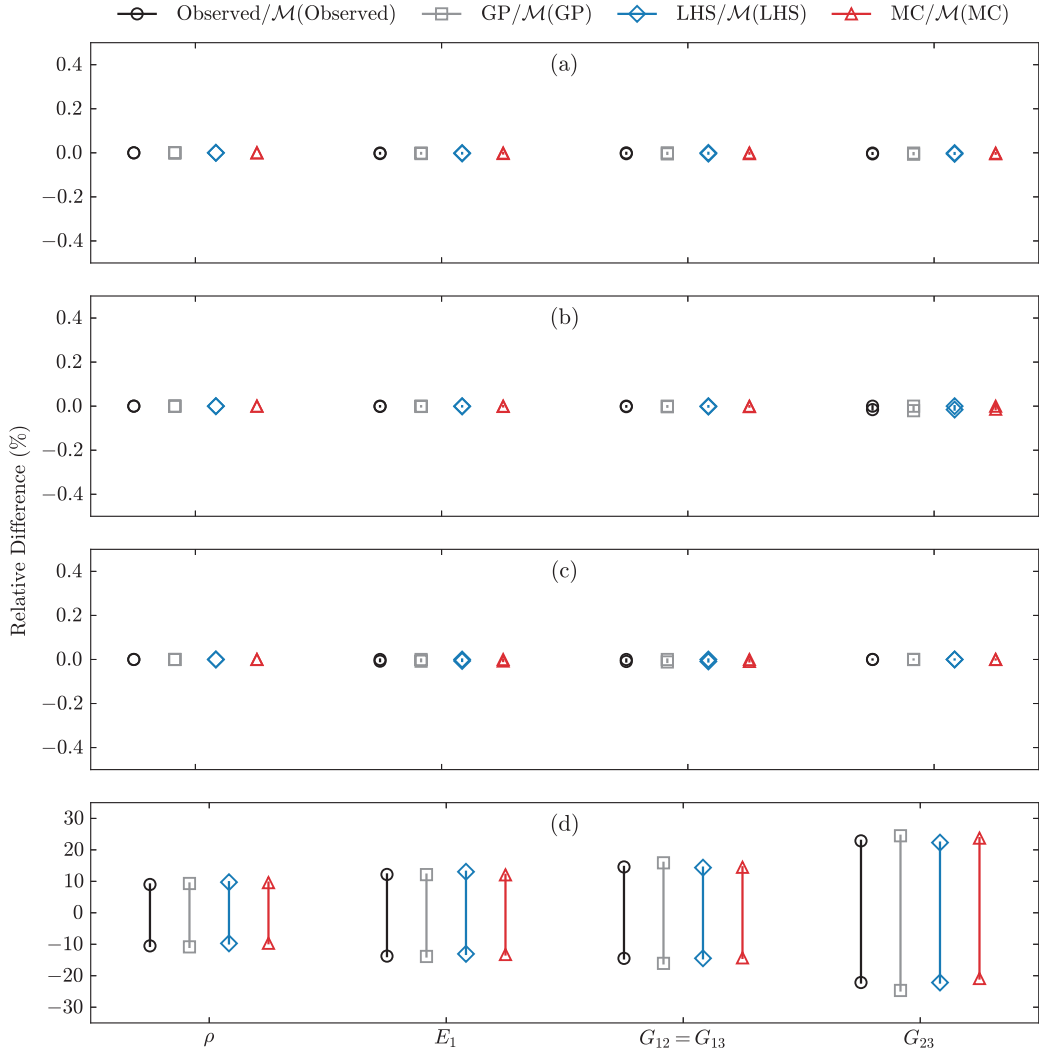


Figure 10: Relative deviations in MAC values for (a) out-of-plane bending, (b) torsional, and (c) in-plane bending modes, due to variability in mechanical properties. The MAC deviations are normalised with respect to the values obtained from the mean mechanical properties, as defined in (17). Panel (d) shows the relative differences in the mechanical properties (ρ , E_1 , $G_{12} = G_{13}$, G_{23}), normalised with respect to their corresponding means. The bars represent the range (minimum to maximum) of deviations for each uncertainty propagation method: Observed, Gaussian Process (GP), Latin Hypercube Sampling (LHS), and Monte Carlo (MC).

4. Conclusion

In this article, an uncertainty quantification investigation was performed on the influence of uncertainty in the sensitive mechanical properties of CLTs on their associated natural frequencies and modes. The probabilistic Gaussian process and stochastic LHS and MC sampling were used to describe the probabilistic and randomness in the mechanical properties of CLT. Using probabilistic and stochastic variation in the mechanical properties resulted in the following:

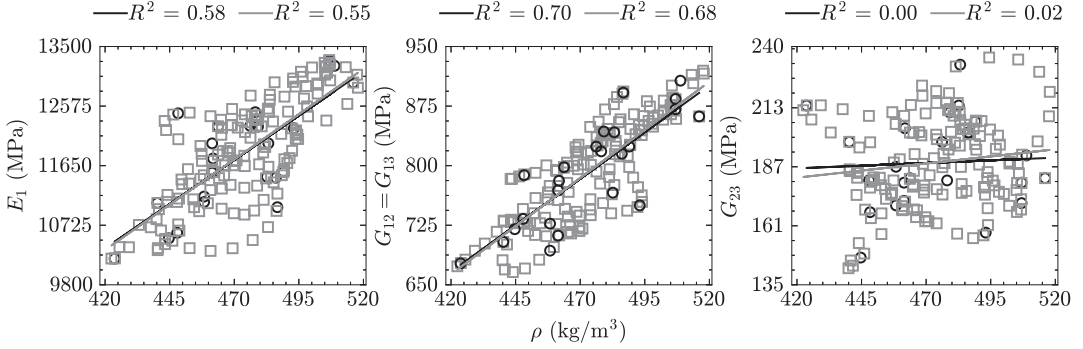


Figure 11: Correlation between density ρ , longitudinal Young's modulus E_1 , interior shear moduli $G_{12} = G_{13}$, and rolling shear modulus G_{23} . The black circles encompass observed data points, whereas the grey squares are their corresponding probabilistic data generated using Gaussian Process (GP).

- The observed mechanical properties from model updating and their associated predicted ones using Gaussian Processes (GPS) result in a narrower Gaussian distribution of the natural frequencies and a steeper cumulative distribution.
- The stochastic distribution of the mechanical properties resulted in a broader probability distribution of the natural frequencies, and their corresponding cumulative distribution became broader.
- The probabilistic and stochastic nature of the mechanical properties did not result in sensitivity in the modes.

The analysis of the sensitivity of each mechanical property (namely ρ , E_1 , $G_{12} = G_{13}$, and G_{23}) on the natural frequencies and modes indicated:

- The density ρ influences all natural frequencies. With an uncertainty in ρ corresponding to $\pm 10\%$, an uncertainty in the natural frequencies corresponding to $\pm 6\%$ is expected.
- The variability of $\pm 14\%$ for E_1 resulted in the variability up to $\pm 7\%$ for natural frequencies.
- The interior shear moduli, $G_{12} = G_{13}$, primarily influence the torsional and in-plane bending natural frequencies. A minor influence on the out-of-plane bending natural frequencies is also observed. With an uncertainty of approximately $\pm 14.5\%$ in $G_{12} = G_{13}$, a corresponding uncertainty of up to $\pm 5\%$ is expected in the associated torsional and in-plane bending natural frequencies, whereas only $\pm 1.7\%$ uncertainty is expected in the out-of-plane bending frequencies.
- The rolling shear modulus G_{23} shows the highest variability, up to 23%, and results in an uncertainty of 6% in the out-of-plane bending and torsional natural frequencies.

In addition, variability in the mechanical properties did not result in variability in the mode shapes. The correlation between mechanical properties also shows a relationship between density ρ and the longitudinal Young's modulus E_1 and interior shear moduli $G_{12} = G_{13}$. However, no linear relationship was observed between density ρ and rolling shear modulus G_{23} , which shows the highest uncertainty. Hence, further investigation into the rolling shear modulus is necessary for a comprehensive understanding of its variability.

Future research can analyse a larger observed data set to refine the probabilistic model established in this study, enhancing its accuracy and reliability. In addition, further research on the influence of environmental factors such as humidity, temperature, and natural defects on the mechanical properties of CLT is essential. Implementing real-time monitoring techniques, such as operational modal analysis coupled with inverse dynamics, will allow for continuous tracking of the mechanical properties of CLT. This approach will provide a deeper understanding of the uncertainties and variations in the mechanical properties over time. Long-term studies are recommended to observe changes in

mechanical properties and natural frequencies throughout the lifespan of CLT structures. This will provide valuable information on the durability and performance of CLT over time. Following these recommendations, the uncertainty in the mechanical properties of CLT can be significantly reduced, leading to more reliable and robust structural applications.

Data Availability

Data will be made available on request.

Acknowledgements

The production of this article received no financial support.

References

- [1] Menahem Baruch and Itzhack Y. Bar Itzhack. Optimal weighted orthogonalization of measured modes. *AIAA journal*, 16(4):346–351, 1978.
- [2] Menahem Baruch. Optimization procedure to correct stiffness and flexibility matrices using vibration tests. *AIAA journal*, 16(11):1208–1210, 1978.
- [3] Alex Berman. Mass matrix correction using an incomplete set of measured modes. *AIAA journal*, 17(10):1147–1148, 1979.
- [4] J-C Chen, C-P Kuo, and J Garba. Direct structural parameter identification by modal test results. In *24th Structures, Structural Dynamics and Materials Conference*, page 812, 1983.
- [5] A Berman and EJ Nagy. Improvement of a large analytical model using test data. *AIAA journal*, 21(8):1168–1173, 1983.
- [6] John E Mottershead, Michael Link, and Michael I Friswell. The sensitivity method in finite element model updating: A tutorial. *Mechanical systems and signal processing*, 25(7):2275–2296, 2011.
- [7] Michael Friswell and JE Mottershead. *Finite element model updating in structural dynamics*. Kluwer Academic Publishers, 1995.
- [8] John E Mottershead and MI Friswell. Model updating in structural dynamics: a survey. *Journal of sound and vibration*, 167(2):347–375, 1993.
- [9] Forest Products Laboratory (US). *Wood handbook: wood as an engineering material*. The Laboratory, 1987.
- [10] David W Green, Jerrold E Winandy, and David E Kretschmann. Mechanical properties of wood. *Wood handbook: wood as an engineering material*. Madison, WI: USDA Forest Service, Forest Products Laboratory, 1999. General technical report FPL; GTR-113: Pages 4.1-4.45, 113, 1999.
- [11] Vanessa Baño, Francisco Arriaga, and Manuel Guaita. Determination of the influence of size and position of knots on load capacity and stress distribution in timber beams of pinus sylvestris using finite element model. *Biosystems engineering*, 114(3):214–222, 2013.
- [12] Elke Mergny, Raquel Mateo, Miguel Esteban, Thierry Descamps, and Pierre Latteur. Influence of cracks on the stiffness of timber structural elements. In *Proceedings of the World conference on timber engineering*, Vienna, Austria, 2016.
- [13] Charles C Gerhards. Effect of moisture content and temperature on the mechanical properties of wood: an analysis of immediate effects. *Wood and Fiber Science*, pages 4–36, 1982.
- [14] Hans Joachim Blaß and Carmen Sandhaas. *Timber engineering-principles for design*. KIT scientific publishing, 2017.
- [15] R. Brandner, G. Flatscher, A. Ringhofer, G. Schickhofer, and A. Thiel. Cross laminated timber (clt): Overview and development. *European Journal of Wood and Wood Products*, 74(3):331–351, May 2016.
- [16] Zhencheng Xing, Jigan Wang, and Jie Zhang. Expansion of environmental impact assessment for eco-efficiency evaluation of china's economic sectors: An economic input-output based frontier approach. *Science of the Total Environment*, 635:284–293, 2018.
- [17] Arnold Tukker and Bart Jansen. Environmental impacts of products: A detailed review of studies. *Journal of Industrial Ecology*, 10(3):159–182, 2006.
- [18] David V Rosowsky. Evolution of probabilistic analysis of timber structures from second-moment reliability methods to fragility analysis. *Structural safety*, 41:57–63, 2013.
- [19] Jochen Köhler, John Dalsgaard Sørensen, and Michael Havbro Faber. Probabilistic modeling of timber structures. *Structural safety*, 29(4):255–267, 2007.
- [20] Reinhard Brandner and Gerhard Schickhofer. Probabilistic models for the modulus of elasticity and shear in serial and parallel acting timber elements. *Wood science and technology*, 49:121–146, 2015.
- [21] Diego A García, Marta B Rosales, and Rubens Sampaio. Dynamic behaviour of a timber footbridge with uncertain material properties under a single deterministic walking load. *Structural safety*, 77:10–17, 2019.
- [22] Tianxiao Yin, Lei He, Qianzhi Huang, Yingchun Gong, Zhiqiang Wang, and Meng Gong. Effect of lamination grade on bending and shear properties of clt made from fast-growing chinese fir. *Industrial Crops and Products*, 207:117741, 2024.
- [23] Qian Ge, Haoqi Wang, Jun Chen, and Bo Wen. Investigation on the propagation of uncertainties of a timber floor under human excitation. *Structural Safety*, 111:102519, 2024.
- [24] Seichiro Ukyo, Kenta Shindo, and Atsushi Miyatake. Evaluation of rolling shear modulus and strength of japanese cedar cross-laminated timber (clt) laminae. *Journal of Wood Science*, 65(1):31, 2019.
- [25] Shaheda T. Akter. *Experimental characterization and numerical modeling of compression perpendicular to the grain in wood and cross-laminated timber*. PhD thesis, Linnéuniversitetet, Fakulteten för teknik (FTK), Institutionen för byggt teknik (BY), Växjö, May 2022. Doctoral thesis, comprehensive summary.

- [26] Benjamin Bondsman and Andrew Peplow. Inverse parameter identification and model updating for cross-laminated timber substructures. *Journal of Building Engineering*, 95, June 2024.
- [27] Benjamin Bondsman and Andrew Peplow. Experimental modal analysis and variability assessment in cross-laminated timber. *Mechanical Systems and Signal Processing*, 2025.
- [28] Michael Smith. *ABAQUS/Standard User's Manual, Version 6.9*. Dassault Systèmes Simulia Corp, United States, 2009.
- [29] Cornelius Lanczos. An iteration method for the solution of the eigenvalue problem of linear differential and integral operators. *Journal of Research of the National Bureau of Standards*, 1950.
- [30] John A Nelder and Roger Mead. A simplex method for function minimization. *The computer journal*, 7(4):308–313, 1965.
- [31] Fuchang Gao and Lixing Han. Implementing the nelder-mead simplex algorithm with adaptive parameters. *Computational Optimization and Applications*, 51(1):259–277, 2012.
- [32] David Duvenaud. The kernel cookbook: Advice on covariance functions. URL <https://www.cs.toronto.edu/duvenaud/cookbook>, 2014.
- [33] Christopher KI Williams and Carl Edward Rasmussen. *Gaussian processes for machine learning*, volume 2. MIT press Cambridge, MA, 2006.
- [34] F. Pedregosa, G. Varoquaux, A. Gramfort, V. Michel, B. Thirion, O. Grisel, M. Blondel, P. Prettenhofer, R. Weiss, V. Dubourg, J. Vanderplas, A. Passos, D. Cournapeau, M. Brucher, M. Perrot, and E. Duchesnay. Scikit-learn: Machine learning in Python. *Journal of Machine Learning Research*, 12:2825–2830, 2011.
- [35] Michael D McKay, Richard J Beckman, and William J Conover. A comparison of three methods for selecting values of input variables in the analysis of output from a computer code. *Technometrics*, 42(1):55–61, 2000.
- [36] Jon C Helton and Freddie Joe Davis. Latin hypercube sampling and the propagation of uncertainty in analyses of complex systems. *Reliability Engineering & System Safety*, 81(1):23–69, 2003.
- [37] Rickard Sjögren and Daniel Svensson. pydoe2: An experimental design package for python, 2018.
- [38] Christiane Lemieux. *Monte carlo and quasi-monte carlo sampling*, volume 20. Springer, 2009.
- [39] Charles R. Harris, K. Jarrod Millman, Stéfan J. van der Walt, Ralf Gommers, Pauli Virtanen, David Cournapeau, Eric Wieser, Julian Taylor, Sebastian Berg, Nathaniel J. Smith, Robert Kern, Matti Picus, Stephan Hoyer, Marten H. van Kerkwijk, Matthew Brett, Allan Haldane, Jaime Fernández del Río, Mark Wiebe, Pearu Peterson, Pierre Gérard-Marchant, Kevin Sheppard, Tyler Reddy, Warren Weckesser, Hameer Abbasi, Christoph Gohlke, and Travis E. Oliphant. Array programming with NumPy. *Nature*, 585(7825):357–362, September 2020.
- [40] Étienne Arnoult, Pascal Lardeur, and Luigi Martini. The modal stability procedure for dynamic and linear finite element analysis with variability. *Finite elements in analysis and design*, 47(1):30–45, 2011.
- [41] Q Yin, P Lardeur, and Frédéric Druésne. Performances assessment of the modal stability procedure for the probabilistic free vibration analysis of laminated composite structures. *Composite structures*, 203:474–485, 2018.

Paper IV

B. Bondsman and C-u. Ahn, & J-g. Kim
Interface reduction technique for Enhanced Craig-Bampton method
Mechanical Systems and Signal Processing, Vol. 208, 111074, 29.12.2023



Contents lists available at ScienceDirect

Mechanical Systems and Signal Processing

journal homepage: www.elsevier.com/locate/ymssp

Interface reduction technique for Enhanced Craig-Bampton method

Benjamin Bondsman^{a,*}, Chang-uk Ahn^b, Jin-Gyun Kim^b^a Department of Construction Sciences, Lund University, John Ericssons väg 1, Lund, Box 118, Kingdom of Sweden^b Department of Mechanical Engineering (Integrated Engineering), Kyung Hee University, Deogyong-daero, Giheung-gu, Yongin-si Jagathy, 1732, Gyeonggi-do 17104, Republic of Korea

ARTICLE INFO

Communicated by J.E. Mottershead

Keywords:

Reduced-order modelling
 Component mode synthesis
 Dynamic substructuring
 Enhanced Craig-Bampton
 Interface reduction

ABSTRACT

Substructure coupling and model order reduction using Component Mode Synthesis (CMS) have, over recent years, gained considerable attention in the vibroacoustic analysis of complex structures. In the CMS methodology, the interior dynamics of each subcomponent in a substructured system are represented by a truncated set of normal modes within the lower frequency range, while all physical degrees of freedom (DOFs) at the interface are retained. In cases where there are many interconnected subcomponents within a system, in particular when these components are finely discretised in the Finite Element (FE) domain, the reduced system matrices may still involve a significant number of equations. This, in turn, leads to a considerable computational workload. To address this issue, further reduction of the system matrices concerning the interface DOFs by using a set of truncated interface modes can be considered. However, the accuracy of the reduced matrices depends on the representation of the truncated dynamics in the reduction process. In this work, two interface reduction techniques are presented to truncate the interface dynamics of the Enhanced Craig-Bampton (ECB) equations of motion. The first technique is a classical interface reduction approach that assumes decoupled internal and interface dynamics. The second approach is an extension of the first one by incorporating an additional coupling term that accounts for interactions between the truncated internal and interface dynamics. The performance of each interface reduction technique is evaluated by applying them to three practical engineering examples. In these instances, resonance frequencies, associated errors, transfer functions, and normal modes are compared to those obtained using both the classical CB method and the full model.

1. Introduction

Substructure coupling for dynamic analysis or Component Mode Synthesis (CMS) has, since the introduction of the Craig-Bampton (CB) method [1], gained great popularity within the field of Structural Dynamics. The CMS method is an extension of static condensation by Hurty [2,3] and Guyan-Irons [4,5], which in difference compensates for the neglected inertia terms by inclusion of a set of generalised coordinates. The objective of CMS comprises the fragmentation of a complex structure into several distinct regions or substructures, reducing the representation system matrices with contribution from component normal modes and assembling a reduced-order system with interface constraint (or attachment) modes for the entire system, Fig. 1. The constraint modes are defined as static deformation due to the application of a unit displacement at one interface degree-of-freedom (DOF), whilst restraining the remaining DOFs. Attachment modes are defined as displacement vectors due to the application of a unit force at one DOF, and hence are simply just columns of the associated flexibility matrix, [6]. Component normal modes are eigenvectors

* Corresponding author.

E-mail address: Benjamin.bondsman@Construction.lth.se (B. Bondsman).<https://doi.org/10.1016/j.ymssp.2023.111074>

Received 6 September 2023; Received in revised form 17 December 2023; Accepted 22 December 2023

Available online 28 December 2023

0888-3270/© 2023 The Author(s). Published by Elsevier Ltd. This is an open access article under the CC BY license (<http://creativecommons.org/licenses/by/4.0/>).

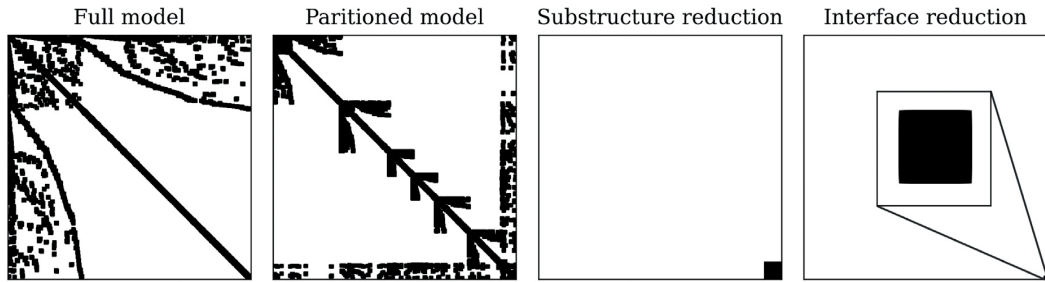


Fig. 1. Illustration of reduction process from the full model to interface reduction in the CMS domain. The black dots denote numbers associated with DOFs in the system matrix. The presented data is associated with the stiffened steel plate example in Section 4.1.

computed through eigenvalue analysis and may be classified as fixed-interface, free-interface, hybrid-interface and loaded interface normal modes, [7]. The number of component normal modes (dominant modes) are often selected within the lower frequency range or chosen based on mode selection methods, for example, [8–10]. Further review of substructure coupling and CMS methods can be found in [1,7,11,12].

The Craig-Bampton method employs a truncated set of fixed-interface normal modes together with a set of constraint modes to reduce the substructure system matrices. The fixed-interface modes are computed through an eigenvalue analysis for the substructure system matrices with restrained interface boundary DOFs. In the 1970s, another class of the CMS method was introduced to employ free-interface modes, in particular MacNeal's Method [13], Rubin's Method [14], Hintz's method [15] and Craig-Chang Method [16], and others [17–20]. Substructures with truncated internal dynamics are assembled into a coupled global system using displacement compatibility at their interfaces, referred to as primal assembly, [11,21]. Considering force compatibility at the substructure interfaces, Rixen [21] introduced a Dual Assembly approach allowing for small discontinuities in displacement across the interfaces. Park and Park also proposed a robust free interface CMS method known as flexibility-based CMS (F-CMS) with localised Lagrange multipliers to ensure mathematical independence between substructures [22]. The present study focuses on the primal assembly approach first introduced by Craig Jr. and Bampton [1]. This approach considers the coupling of the substructures at their interfaces through the use of constraint modes, thereby allowing for the description of the motion at the coupling interfaces through these constraint modes.

The adoption of reduced substructural models instead of full models in computational mechanics results in improved computational efficiency, simplified modelling, and increased flexibility. Hence, in addition to its use in structural mechanics to study mechanical response of structures, the CMS method has been recently extended to address computational efficiency in fluid–structure interaction, thermo-mechanical vibration, vibro-acoustic analyses and simulation of protein dynamics, as reported in [23–26]. Accordingly, reduction methods, particularly the CB method, have been integrated into commercial FE software, [27,28].

The accuracy of CMS methods, including the CB method, is often contingent upon the number of component normal modes included in the compensation for neglected inertia. To address this limitation, Kim and Lee [19] developed the Enhanced Craig-Bampton (ECB) method, which incorporates both dominant and residual modes truncated in the original CB method. This results in a significant improvement in the accuracy of the CB method with a minimal additional computational cost. Accurate reduced models are crucial for structural design, system identification, and model calibration based on experimental data.

The reduction process within the CMS framework involves truncation of the internal dynamics of each subcomponent within a substructured system using a set of dominant modes, whilst preserving the physical DOFs at the interfaces between the substructures. This procedure is particularly useful in the analysis of structural assemblies consisting of a limited number of interconnected substructures or with a limited number of interaction nodes between the substructures. Nonetheless, for extremely large and complex structures with multiple substructures and a substantial number of interaction nodes, the CMS domain may be dominated by the interface DOFs. As a result, the reduced-order system matrices may still contain a significant number of DOFs, leading to computational costs. In 1977, Craig and Chang introduced the interface reduction technique to further reduce the number of DOFs by applying Guyan, Ritz, and modal reduction techniques, as documented in [29]. The modal reduction technique underwent further development by Castanier et al. [30], who applied a secondary eigenvalue analysis on the system-level interface partition of the assembled system matrices. This led to the identification of eigenvectors known as system-level Characteristic Constraint (CC) modes. Using a truncated set of CC modes allows for further reduction of the equations of motion and results in a significant decrease in the size of the assembled system matrices.

The work by Castanier et al. [30] inspired subsequent studies in the field of interface reduction technique. For example, Rixen proposed an interface reduction technique for the Dual Craig-Bampton method utilising free interface modes [21]. Holzwarth et al. [31] proposed the utilisation of Legendre Polynomials as basis functions to represent the interface deformation patterns as an approach to reducing the interface DOFs. The performance of this method was then compared to that of the CC mode approach. Ahn et al. [32] presented a refinement technique of the interface reduction technique by Castanier et al. [30] by incorporating the influence of residual flexibility into the CC modes. Additionally, interface reduction of the F-CMS method was proposed by using mathematical basis reconstruction of the interface DOFs, [17,33]. Hong et al. [34] proposed a technique for conducting eigenvalue

analysis on the CB interface DOFs at the substructure level before assembly using exact interface compatibility, and reducing the interface DOFs by employing augmented modes. Given the popularity of the CB method, most of the existing interface reduction techniques are associated with it. Further information on these techniques can be found in a review by Krattiger et al. [35].

The interface reduction technique using CC modes results in reduced-order system matrices, the accuracy of which depends on the number of interface constraint modes retained. However, the reduction process may result in system matrices of lower accuracy compared to the original system matrices due to approximations introduced during the reduction procedure. To mitigate this issue, the interface reduction technique based on CC modes can be combined with the ECB method, instead of CB. The ECB method has been shown to produce system matrices of greater accuracy compared to the original CB method, [19,36–38]. The approach to the interface reduction proposed by Castanier et al. [30] encompass a classical modal truncation based on the assumption of decoupled internal and interface DOFs. This approach is valid, considering the decoupled stiffness characteristics of the CB system matrices. However, as evidenced further in the paper, this assumption is not entirely correct and the internal and interface DOFs are not fully decoupled when the ECB method is employed. This may result in system matrices with reduced accuracy. Incorporating the coupling between internal and interface dynamics can improve the accuracy of the interface reduction technique and produce system matrices with greater accuracy compared to the classical approach proposed by Castanier et al. [30].

In this study, two interface reduction techniques are coupled with the ECB method. The first option, as proposed by Castanier et al. [30], is considered. The second option builds upon the first approach and includes a coupling term to address the transmission of vibrational energy between the internal and interface dynamics. The efficacy of each of these interface reduction techniques has been evaluated through three practical engineering examples, and the results demonstrate an improvement in the accuracy of the system matrices. Furthermore, the results are compared with the classical CB method, both with and without the interface reduction proposed by Castanier et al. [30]. Further mathematical derivations and a step-by-step implementation algorithm are also provided to facilitate the practical application of this work.

The structure of the rest of this paper is outlined as follows: Section 2 provides a comprehensive overview of substructure coupling and reduction of internal dynamics of substructures. Section 3 outlines the derivation of interface reduction techniques in conjunction with CB and ECB. The performance of each proposed interface reduction technique is evaluated through 3 examples in Section 4, and conclusions are drawn in Section 5.

2. Substructure coupling and model order reduction

This section provides a brief introduction to substructure reduction and coupling, comprising substructure partitioning, internal dynamics truncation, and subsequent coupling. The reduction methods used to truncate substructure internal dynamics include the Craig-Bampton (CB) and Enhanced Craig-Bampton methods. In the CMS domain, substructures are assembled block-diagonally and share interfaces, Fig. 1. With the aim of achieving a partitioned global system, the substructures are decomposed into internal and interface regions before the coupling procedure.

The equations of motion for a discretised substructure, in the absence of damping, can be formulated as:

$$\mathbf{M}^{(s)}\ddot{\mathbf{u}}^{(s)} + \mathbf{K}^{(s)}\mathbf{u}^{(s)} = \mathbf{f}^{(s)}, \quad s = 1, 2, \dots, N_s, \quad (1)$$

where $\mathbf{M}^{(s)}$, $\mathbf{K}^{(s)} \in \mathbb{R}^{N^{(s)} \times N^{(s)}}$ are mass and stiffness matrices and $\mathbf{u}^{(s)}$, $\mathbf{f}^{(s)} \in \mathbb{R}^{N^{(s)} \times 1}$ are nodal displacement and force vectors for substructure s , respectively. An upper double-dot denotes second-order time-derivative d^2/dt^2 and N_s denotes the total number of substructures. To simplify subsequent substructure coupling, the substructure's internal and boundary regions are decomposed to

$$\mathbf{M}^{(s)} = \begin{bmatrix} \mathbf{M}_{ii}^{(s)} & \mathbf{M}_{ib}^{(s)} \\ \mathbf{M}_{bi}^{(s)} & \mathbf{M}_{bb}^{(s)} \end{bmatrix}, \quad \mathbf{K}^{(s)} = \begin{bmatrix} \mathbf{K}_{ii}^{(s)} & \mathbf{K}_{ib}^{(s)} \\ \mathbf{K}_{bi}^{(s)} & \mathbf{K}_{bb}^{(s)} \end{bmatrix}, \quad \mathbf{u}^{(s)} = \begin{Bmatrix} \mathbf{u}_i^{(s)} \\ \mathbf{u}_b^{(s)} \end{Bmatrix}, \quad \mathbf{f}^{(s)} = \begin{Bmatrix} \mathbf{f}_i^{(s)} \\ \mathbf{f}_b^{(s)} \end{Bmatrix}, \quad (2)$$

where the substructure system matrices $\mathbf{M}^{(s)}$ and $\mathbf{K}^{(s)}$ are symmetric positive semi-definite. Hence, the system matrix blocks $\mathbf{M}_{ib}^{(s)} = \mathbf{M}_{bi}^{(s)T}$ and $\mathbf{K}_{ib}^{(s)} = \mathbf{K}_{bi}^{(s)T}$. The subscripts i and b denote internal and boundary (interface) regions, respectively. The total number of substructure internal and boundary DOFs are defined as $N_i^{(s)}$ and $N_b^{(s)}$, respectively. Thus, the total number of substructure DOFs is $N^{(s)} = N_i^{(s)} + N_b^{(s)}$.

The system matrices and force vector associated with N_s substructures to be coupled can be assembled in a block-diagonal format as follows:

$$\check{\mathbf{M}} \stackrel{\Delta}{=} \text{diag}(\mathbf{M}^{(1)}, \dots, \mathbf{M}^{(N_s)}) = \begin{bmatrix} \mathbf{M}^{(1)} & & \\ & \ddots & \\ & & \mathbf{M}^{(N_s)} \end{bmatrix}, \quad \check{\mathbf{K}} \stackrel{\Delta}{=} \text{diag}(\mathbf{K}^{(1)}, \dots, \mathbf{K}^{(N_s)}), \quad \check{\mathbf{f}} \stackrel{\Delta}{=} \begin{Bmatrix} \mathbf{f}^{(1)} \\ \vdots \\ \mathbf{f}^{(N_s)} \end{Bmatrix}. \quad (3)$$

In the CMS field, substructures in a coupled system share their boundary DOFs at their interfaces. To ensure compatibility between the coupled substructure DOFs, the Boolean matrix \mathbf{L} is used to impose interface coupling between the substructures, as described in [11]. This establishes a relationship between the substructure displacement vector $\mathbf{u}^{(s)}$ and the global displacement vector \mathbf{u}_g as follows:

$$\mathbf{u}^{(s)} = \mathbf{L}^{(s)}\mathbf{u}_g, \quad \mathbf{u}_g = \begin{Bmatrix} \mathbf{u}_i \\ \mathbf{u}_b \end{Bmatrix}, \quad (4)$$

where $\mathbf{L}^{(s)}$ is a substructure primal assembly Boolean operator. This relationship ensures the recovery of the substructure displacement vector from the global displacement vector. Considering a primal assembly approach, the substructures in Eq. (3) can be coupled as follows:

$$\mathbf{M}_g \stackrel{\Delta}{=} \mathbf{L}^\top \tilde{\mathbf{M}} \mathbf{L} = \begin{bmatrix} \mathbf{M}_{ii} & \mathbf{M}_{ib} \\ \mathbf{M}_{bi} & \mathbf{M}_{bb} \end{bmatrix}, \quad (5a)$$

$$\mathbf{K}_g \stackrel{\Delta}{=} \mathbf{L}^\top \tilde{\mathbf{K}} \mathbf{L} = \begin{bmatrix} \mathbf{K}_{ii} & \mathbf{K}_{ib} \\ \mathbf{K}_{bi} & \mathbf{k}_{bb} \end{bmatrix}, \quad (5b)$$

$$\mathbf{F}_g \stackrel{\Delta}{=} \mathbf{L}^\top \tilde{\mathbf{f}} = \begin{Bmatrix} \mathbf{f}_i \\ \mathbf{f}_b \end{Bmatrix}, \quad (5c)$$

where the size of the global mass matrix \mathbf{M}_g , stiffness matrix \mathbf{K}_g and force vector \mathbf{F}_g is $N \times N$, $N \times N$, and $N \times 1$, respectively. The total number of DOFs is denoted $N = N_i + N_b$, where N_i represents the total number of internal DOFs, and N_b represents the total number of interface DOFs in the global system. The total number of internal DOFs is defined as $N_i = \sum_{s=1}^{N_s} N_i^{(s)}$. Because the substructures share interfaces within the global system, the total number of global interface DOFs is less than the sum of all individual substructure interface DOFs, i.e., $N_b < \sum_{k=1}^{N_s} N_b^{(s)}$.

The dimensions of \mathbf{L} , $\mathbf{u}^{(s)}$, and \mathbf{u}_g are $N_b \times N$, $N^{(s)} \times 1$, and $N \times 1$, respectively. The global force vector \mathbf{F}_g contains a zero partition for \mathbf{f}_i since all loaded DOFs are considered as interface DOFs and included in the \mathbf{f}_b partition. Information on constructing the Boolean matrix \mathbf{L} can be found in [11]. It is important to note that these equations represent the coupling equations, originally proposed by Craig Jr. and Bampton [1], and referred to as primal assembly by Rixen [39]. The next section will provide a brief review of the CB and ECB methods for reducing the substructure internal DOFs before the assembly procedure outlined in Eq. (5).

2.1. Reduction of internal DOFs

The internal DOFs of each substructure can be reduced by utilising a set of component fixed-interface normal modes before the assembly and coupling procedure outlined in Eqs. (3) and (5). The normal modes are obtained by restraining all interface DOFs and conducting an eigenvalue analysis for the internal DOFs as:

$$\left(\mathbf{K}_{ii}^{(s)} - \omega_{i,j}^{(s)2} \mathbf{M}_{ii}^{(s)} \right) \boldsymbol{\phi}_{i,j}^{(s)} = \mathbf{0}, \quad j = 1, 2, \dots, N_{i,d}^{(s)}, \quad (6)$$

where the system matrices $\mathbf{M}_{ii}^{(s)}$ and $\mathbf{K}_{ii}^{(s)}$ are respectively internal partitions of the substructure mass and stiffness matrices outlined in Eq. (2), whilst $\omega_{i,j}^{(s)2}$ and $\boldsymbol{\phi}_{i,j}^{(s)}$ are associated j th eigensolution. The number of substructure dominant modes retained is defined as $N_{i,d}^{(s)}$. The dominant modes are often selected within the lower frequency range, or according to mode selection techniques, [9,10].

Considering a fixed-interface truncation approach, the substructure displacement vector can be approximated to

$$\mathbf{u}^{(s)} \approx \tilde{\mathbf{T}}_{\text{CB}}^{(s)} \hat{\mathbf{u}}^{(s)} = \tilde{\mathbf{T}}_{\text{CB}}^{(s)} \begin{Bmatrix} \mathbf{q}_{i,d}^{(s)} \\ \mathbf{u}_b^{(s)} \end{Bmatrix}, \quad (7a)$$

$$\tilde{\mathbf{T}}_{\text{CB}}^{(s)} = \begin{bmatrix} \boldsymbol{\Phi}_{i,d}^{(s)} & \boldsymbol{\Psi}_{ib}^{(s)} \\ \mathbf{0} & \mathbf{I}_{bb}^{(s)} \end{bmatrix}, \quad \boldsymbol{\Phi}^{(s)} = \begin{bmatrix} \boldsymbol{\phi}_{i,1}^{(s)} & \boldsymbol{\phi}_{i,2}^{(s)} & \dots & \boldsymbol{\phi}_{i,d}^{(s)} \\ \mathbf{0} & \mathbf{0} & \dots & \mathbf{0} \end{bmatrix}, \quad \boldsymbol{\Psi}^{(s)} = \begin{bmatrix} \boldsymbol{\Psi}_{ib}^{(s)} \\ \mathbf{I}_{bb}^{(s)} \end{bmatrix}, \quad \boldsymbol{\Psi}_{ib}^{(s)} = -\mathbf{K}_{ii}^{(s)-1} \mathbf{K}_{ib}^{(s)}, \quad (7b)$$

where the substructure displacement vector $\mathbf{u}^{(s)}$ is approximated to $\hat{\mathbf{u}}^{(s)}$, by making use of the substructure transformation matrix $\tilde{\mathbf{T}}_{\text{CB}}^{(s)}$, where an over-bar denotes approximated quantities. The fixed-interface mode matrix $\boldsymbol{\Phi}^{(s)}$ contains $N_{i,d}$ columns of the dominant modes obtained in Eq. (6). The constraint mode matrix $\boldsymbol{\Psi}^{(s)}$ contains static mode shapes of the internal DOFs due to unit displacement of the interface boundary DOFs $\boldsymbol{\Psi}_{ib}^{(s)}$ and an identity matrix $\mathbf{I}_{bb}^{(s)}$. Thus, the motion of the interface is entirely described by the constraint modes, [30]. The $\boldsymbol{\Phi}^{(s)}$ together with $\boldsymbol{\Psi}^{(s)}$ are referred to as a complete set of fixed-interface normal mode and constraint mode and have the dimensions $N \times N_{i,d}$ and $N \times N_b$, respectively. Truncating the substructure internal DOFs using Eq. (7) in Eq. (1) and pre-multiplying by $\tilde{\mathbf{T}}_{\text{CB}}^{(s)\top}$, the reduced substructure equations of motion can be expressed as:

$$\tilde{\mathbf{T}}_{\text{CB}}^{(s)\top} \mathbf{M}^{(s)} \tilde{\mathbf{T}}_{\text{CB}}^{(s)} \begin{Bmatrix} \hat{\mathbf{q}}_{i,d}^{(s)} \\ \hat{\mathbf{u}}_b^{(s)} \end{Bmatrix} + \tilde{\mathbf{T}}_{\text{CB}}^{(s)\top} \mathbf{K}^{(s)} \tilde{\mathbf{T}}_{\text{CB}}^{(s)} \begin{Bmatrix} \mathbf{q}_{i,d}^{(s)} \\ \mathbf{u}_b^{(s)} \end{Bmatrix} = \tilde{\mathbf{T}}_{\text{CB}}^{(s)\top} \begin{Bmatrix} \mathbf{f}_i^{(s)} \\ \mathbf{f}_b^{(s)} \end{Bmatrix}, \quad (8)$$

with

$$\hat{\mathbf{M}}^{(s)} = \tilde{\mathbf{T}}_{\text{CB}}^{(s)\top} \mathbf{M}^{(s)} \tilde{\mathbf{T}}_{\text{CB}}^{(s)} = \begin{bmatrix} \hat{\mathbf{M}}_{ii}^{(s)} & \hat{\mathbf{M}}_{ib}^{(s)} \\ \hat{\mathbf{M}}_{bi}^{(s)} & \hat{\mathbf{M}}_{bb}^{(s)} \end{bmatrix}, \quad (9a)$$

$$\hat{\mathbf{K}}^{(s)} = \tilde{\mathbf{T}}_{\text{CB}}^{(s)\top} \mathbf{K}^{(s)} \tilde{\mathbf{T}}_{\text{CB}}^{(s)} = \begin{bmatrix} \hat{\mathbf{K}}_{ii}^{(s)} & \mathbf{0}_{ib}^{(s)} \\ \mathbf{0}_{bi}^{(s)} & \hat{\mathbf{K}}_{bb}^{(s)} \end{bmatrix}, \quad (9b)$$

$$\hat{\mathbf{F}}^{(s)} = \tilde{\mathbf{T}}_{\text{CB}}^{(s)\top} \begin{Bmatrix} \mathbf{f}_i^{(s)} \\ \mathbf{f}_b^{(s)} \end{Bmatrix} = \begin{Bmatrix} \hat{\mathbf{f}}_i^{(s)} \\ \hat{\mathbf{f}}_b^{(s)} \end{Bmatrix}, \quad (9c)$$

where $\hat{\mathbf{M}}^{(s)}$ and $\hat{\mathbf{K}}^{(s)}$ are substructure system matrices representing mass and stiffness, with internal dynamics truncated using a set of dominant modes $N_{i,d}$, and $\hat{\mathbf{F}}$ is the corresponding force vector. Referred to as the Craig-Bampton method in the literature [1], this approach is characterised by coupled mass and decoupled stiffness between internal and interface regions, as evident in Eq. (9). Considering a primal coupling approach introduced in Eqs. (3) and (5), the reduced global equations of motion in Eq. (9) can be derived as:

$$\hat{\mathbf{M}}_{\mathbf{g}} \ddot{\mathbf{u}}_{\mathbf{g}} + \hat{\mathbf{K}}_{\mathbf{g}} \dot{\mathbf{u}}_{\mathbf{g}} = \hat{\mathbf{F}}_{\mathbf{g}}, \quad (10)$$

where $\hat{\mathbf{M}}_{\mathbf{g}}$ and $\hat{\mathbf{K}}_{\mathbf{g}}$ are respectively global mass and stiffness matrices with truncated internal dynamics using CB method, and $\hat{\mathbf{F}}_{\mathbf{g}}$ is the corresponding global force vector. The size of the system matrices and force vector are respectively $\hat{N} \times \hat{N}$ and $\hat{N} \times 1$, with $\hat{N} = N_{i,d} + N_b$.

In the original CB method, the residual substructural modes are truncated without any consideration. To acquire an improved accuracy of the reduced matrices, Kim and Lee [19] proposed an ECB method where the residual substructural modes are in addition to the dominant structural modes included in the transformation matrix. Considering the ECB approach in [19], the substructure displacement vector can be approximated as:

$$\mathbf{u}^{(s)} \approx \bar{\mathbf{T}}_{\text{ECB}}^{(s)} \bar{\mathbf{u}}^{(s)} = \bar{\mathbf{T}}_{\text{ECB}}^{(s)} \begin{Bmatrix} \mathbf{q}_{i,d}^{(s)} \\ \mathbf{u}_b^{(s)} \end{Bmatrix}, \quad \bar{\mathbf{T}}_{\text{ECB}} = \bar{\mathbf{T}}_{\text{CB}}^{(s)} + \bar{\mathbf{T}}_{\text{R}}^{(s)}, \quad (11a)$$

$$\bar{\mathbf{T}}_{\text{R}}^{(s)} = \begin{bmatrix} \mathbf{0} & \mathbf{F}_{\text{rs}}^{(s)} \left[-\mathbf{M}_{ii}^{(s)} \mathbf{K}_{ii}^{(s)-1} \mathbf{K}_{ib}^{(s)} + \mathbf{M}_{ib}^{(s)} \right] \\ \mathbf{0} & \mathbf{0} \end{bmatrix} \bar{\mathbf{M}}_{\text{CB}}^{(s)-1} \bar{\mathbf{K}}_{\text{CB}}^{(s)}, \quad (11b)$$

$$\mathbf{F}_{\text{rs}}^{(s)} = \mathbf{K}_{ii}^{(s)} - \Phi_{i,d}^{(s)} \Lambda_{i,d}^{(s)-1} \Phi_{i,d}^{(s)\top}, \quad \Lambda_{i,d}^{(s)} = \Phi_{i,d}^{(s)\top} \mathbf{K}_{ii}^{(s)} \Phi_{i,d}^{(s)}. \quad (11c)$$

The equation above indicates that the CB transformation matrix $\bar{\mathbf{T}}_{\text{CB}}^{(s)}$ has been supplemented with another transformation matrix, namely $\bar{\mathbf{T}}_{\text{R}}^{(s)}$ which contains residual modal effect $\mathbf{F}_{\text{rs}}^{(s)}$. With the ECB transformation matrix derived in Eq. (11), the substructure equations of motion in Eq. (1) can be approximated as follows:

$$\bar{\mathbf{T}}_{\text{ECB}}^{(s)\top} \mathbf{M}^{(s)} \bar{\mathbf{T}}_{\text{ECB}}^{(s)} \begin{Bmatrix} \mathbf{q}_{i,d}^{(s)} \\ \mathbf{u}_b^{(s)} \end{Bmatrix} + \bar{\mathbf{T}}_{\text{ECB}}^{(s)\top} \mathbf{K}^{(s)} \bar{\mathbf{T}}_{\text{ECB}}^{(s)} \begin{Bmatrix} \mathbf{q}_{i,d}^{(s)} \\ \mathbf{u}_b^{(s)} \end{Bmatrix} = \bar{\mathbf{T}}_{\text{ECB}}^{(s)\top} \begin{Bmatrix} \mathbf{f}_i^{(s)} \\ \mathbf{f}_b^{(s)} \end{Bmatrix}, \quad (12)$$

with

$$\bar{\mathbf{M}}^{(s)} = \bar{\mathbf{T}}_{\text{ECB}}^{(s)\top} \mathbf{M}^{(s)} \bar{\mathbf{T}}_{\text{ECB}}^{(s)} = \begin{bmatrix} \bar{\mathbf{M}}_{ii}^{(s)} & \bar{\mathbf{M}}_{ib}^{(s)} \\ \bar{\mathbf{M}}_{bi}^{(s)} & \bar{\mathbf{M}}_{bb}^{(s)} \end{bmatrix}, \quad (13a)$$

$$\bar{\mathbf{K}}^{(s)} = \bar{\mathbf{T}}_{\text{ECB}}^{(s)\top} \mathbf{K}^{(s)} \bar{\mathbf{T}}_{\text{ECB}}^{(s)} = \begin{bmatrix} \bar{\mathbf{K}}_{ii}^{(s)} & \bar{\mathbf{K}}_{ib}^{(s)} \\ \bar{\mathbf{K}}_{bi}^{(s)} & \bar{\mathbf{K}}_{bb}^{(s)} \end{bmatrix}, \quad (13b)$$

$$\bar{\mathbf{f}}^{(s)} = \bar{\mathbf{T}}_{\text{ECB}}^{(s)\top} \begin{Bmatrix} \mathbf{f}_i^{(s)} \\ \mathbf{f}_b^{(s)} \end{Bmatrix} = \begin{Bmatrix} \bar{\mathbf{f}}_i^{(s)} \\ \bar{\mathbf{f}}_b^{(s)} \end{Bmatrix}, \quad (13c)$$

where $\bar{\mathbf{M}}^{(s)}$ and $\bar{\mathbf{K}}^{(s)}$ are system matrices for which the internal DOFs are truncated using a fixed-interface based ECB method. In Eq. (13), it is evident that the off-diagonal terms of $\bar{\mathbf{K}}^{(s)}$ are non-zero. This is in contrast to the classical CB method, which features decoupled internal and interface dynamics, as demonstrated in Eq. (9). As a result, the ECB method exhibits stiffness coupling between internal and boundary regions. For further insight into CMS methods, the reader is referred to [7,11]. With the primal coupling approach in Eqs. (3) and (5) the reduced system in Eq. (13) can be assembled to derive the reduced equations of motion as follows:

$$\bar{\mathbf{M}}_{\mathbf{g}} \ddot{\mathbf{u}}_{\mathbf{g}} + \bar{\mathbf{K}}_{\mathbf{g}} \dot{\mathbf{u}}_{\mathbf{g}} = \bar{\mathbf{F}}_{\mathbf{g}} \quad (14)$$

where $\bar{\mathbf{M}}_{\mathbf{g}}$, $\bar{\mathbf{K}}_{\mathbf{g}}$ and $\bar{\mathbf{F}}_{\mathbf{g}}$ are respectively global mass, stiffness matrices, and force vector, with truncated internal dynamics using ECB method. The substructures are coupled at their boundaries with constraint modes. The number of dominant internal modes retained and included in the reduction for substructure s was defined as $N_{i,d}^{(s)}$ in Eq. (6). Hence, the total number of retained modes associated with all substructures must become $N_{i,d} = \sum_{k=1}^{N_s} N_{i,d}^{(s)}$. The number of DOFs in the reduced system becomes $\bar{N} = N_{i,d} + N_b$, which is fewer than the total DOFs before reduction, denoted as N . Note that the total internal DOFs were originally N_i and the total number of the internal DOFs after reduction has become $N_{i,d} \ll N_i$.

The equations presented above may still comprise a significant number of DOFs, depending on the extent of coupling between the substructures at their interfaces. As such, in the following section, techniques for reducing the size of the interface region will be described.

3. Reduction of interface DOFs

In the previous section, the internal dynamics of each substructure were truncated using a set of fixed-interface normal modes and subsequently coupled at their interfaces using constraint modes. In other words, the substructure internal DOFs were reduced whilst the physical interface DOFs were retained. Since the motion on the substructural interface is described by the constraint modes, the number of DOFs associated with the constraint modes may result in a further computational cost. In particular, for a sufficiently fine FE discretisation with many substructural components, the size of the CMS model may be dominated by the constraint mode DOFs. Therefore, a reduced interface approach can be considered to reduce computational burden and achieve a reduced set of system matrices. In this section, two interface reduction techniques will be introduced to truncate the interface dynamics of system matrices with truncated internal dynamics. The first option, introduced in Section 3.1, is based on the classical approach proposed by Castanier et al. [30] to truncate interface dynamics of the CB method. This approach is referred to as IR1 in subsequent derivations. The second option is a refinement of Castanier et al.'s [30] approach, which accounts for the coupled stiffness terms between internal and interface DOFs. This refinement is particularly important because, in contrast to the CB method, the ECB method comprises coupled internal and interface stiffness. This refined approach is denoted as IR2 in the following derivations in Section 3.2.

To reduce the interface DOFs, a similar approach as for the internal DOFs reduction can be considered, namely truncating the interface dynamics with a set of fixed-internal modes obtained from computing an eigenvalue analysis for the interface DOFs as:

$$(\mathbf{K}_{bb} - \omega_{b,j}^2 \mathbf{M}_{bb}) \boldsymbol{\phi}_{b,j} = \mathbf{0}, \quad j = 1, 2, \dots, N_{b,d}, \quad (15)$$

where $\omega_{b,j}^2$ and $\boldsymbol{\phi}_{b,j}$ are j th eigenvalue and eigenvector associated with the interface DOFs, respectively. The interface mode $\boldsymbol{\phi}_{b,j}$ is often referred to as system-level Characteristic Constraint (CC) mode. The number of dominant modes associated with the interface boundary is labelled as $N_{b,d}$, which is less than the total number of boundary modes N_b , i.e. $N_{b,d} \ll N_b$. In this study, the number of dominant interface modes, denoted as $N_{b,d}$, is selected based on mode convergence, as shown in Figs. 9, 4, and 17. The entry system matrices in Eq. (15) are the interface partitions of the assembled (global) system matrices defined in Eq. (10) for CB and Eq. (14) for ECB, respectively.

3.1. Interface reduction technique

Selecting a number of dominant interface modes, the structural displacement vector of the boundary DOFs can be approximated as:

$$\mathbf{u}_b \approx \boldsymbol{\Phi}_{b,d} \mathbf{q}_{b,d}, \quad (16)$$

where the modal matrix $\boldsymbol{\Phi}_{b,d}$ contains dominant interface eigenvectors and has the dimension $N_b \times N_{b,d}$, where $N_{b,d} \ll N_b$, and $\mathbf{q}_{b,d}$ is the eigenvector's associated generalised coordinates. Truncating the boundary DOFs using a set of dominant modes, the displacement vector of the coupled systems in Eqs. (10) and (14) can be further reduced as follows:

$$\hat{\mathbf{u}}_g \approx \bar{\mathbf{T}}_{\text{IR1}} \begin{Bmatrix} \mathbf{q}_{i,d} \\ \mathbf{q}_{b,d} \end{Bmatrix}, \quad \bar{\mathbf{u}}_g \approx \bar{\mathbf{T}}_{\text{IR1}} \begin{Bmatrix} \mathbf{q}_{i,d} \\ \mathbf{q}_{b,d} \end{Bmatrix}, \quad \bar{\mathbf{T}}_{\text{IR1}} = \begin{bmatrix} \mathbf{I}_{i,d} & \mathbf{0} \\ \mathbf{0} & \boldsymbol{\Phi}_{b,d} \end{bmatrix}, \quad (17)$$

where $\hat{\mathbf{u}}_g$ and $\bar{\mathbf{u}}_g$ are displacement vectors associated with the equations of motion, for which the internal dynamics are truncated using CB and ECB methods, respectively. The interface transformation matrix $\bar{\mathbf{T}}_{\text{IR1}}$ was originally proposed by [30] for use in the interface reduction of the original Craig-Bampton method. The displacement vector, after truncation of the interface DOFs, now contains generalised internal and interface coordinates. As evident in Eq. (17), $\bar{\mathbf{T}}_{\text{IR1}}$ implies decoupled internal and interface dynamics, as indicated by the zeros in the off-diagonal terms. This approach aligns with the decoupled stiffness characteristics of CB, as demonstrated in Eq. (9). However, the coupled stiffness characteristics of ECB in Eq. (13) make this approach unsuitable for ECB, as shown further through the application examples in Section 4. Considering the $\bar{\mathbf{T}}_{\text{IR1}}$ to truncate interface dynamics of the global system matrices for which internal dynamics is truncated using the CB method in Eq. (9), the equations of motion in Eq. (10) can be further reduced to

$$\bar{\mathbf{T}}_{\text{IR1}}^T \bar{\mathbf{M}}_g \bar{\mathbf{T}}_{\text{IR1}} \begin{Bmatrix} \dot{\mathbf{q}}_{i,d} \\ \dot{\mathbf{q}}_{b,d} \end{Bmatrix} + \bar{\mathbf{T}}_{\text{IR1}}^T \bar{\mathbf{K}}_g \bar{\mathbf{T}}_{\text{IR1}} \begin{Bmatrix} \mathbf{q}_{i,d} \\ \mathbf{q}_{b,d} \end{Bmatrix} = \bar{\mathbf{T}}_{\text{IR1}}^T \begin{Bmatrix} \hat{\mathbf{f}}_i \\ \hat{\mathbf{f}}_b \end{Bmatrix}, \quad (18)$$

with

$$\bar{\mathbf{M}} = \bar{\mathbf{T}}_{\text{IR1}}^T \hat{\mathbf{M}}_g \bar{\mathbf{T}}_{\text{IR1}} = \begin{bmatrix} \bar{\mathbf{M}}_{ii} & \bar{\mathbf{M}}_{ib} \\ \bar{\mathbf{M}}_{bi} & \bar{\mathbf{M}}_{bb} \end{bmatrix}, \quad (19a)$$

$$\bar{\mathbf{K}} = \bar{\mathbf{T}}_{\text{IR1}}^T \hat{\mathbf{K}}_g \bar{\mathbf{T}}_{\text{IR1}} = \begin{bmatrix} \bar{\mathbf{K}}_{ii} & \bar{\mathbf{K}}_{ib} \\ \bar{\mathbf{K}}_{bi} & \bar{\mathbf{K}}_{bb} \end{bmatrix}, \quad (19b)$$

$$\bar{\mathbf{F}} = \bar{\mathbf{T}}_{\text{IR1}}^T \begin{Bmatrix} \hat{\mathbf{f}}_i \\ \hat{\mathbf{f}}_b \end{Bmatrix} = \begin{Bmatrix} \check{\mathbf{f}}_i \\ \check{\mathbf{f}}_b \end{Bmatrix}. \quad (19c)$$

The component terms of the system matrices in Eq. (19) are computed using the components of the system matrices in Eq. (10), as:

$$\tilde{\mathbf{M}}_{ii} = \hat{\mathbf{M}}_{ii}, \quad \tilde{\mathbf{M}}_{ib} = \hat{\mathbf{M}}_{ii} \Phi_{b,d}, \quad \tilde{\mathbf{M}}_{bi} = \tilde{\mathbf{M}}_{ib}^T, \quad \tilde{\mathbf{M}}_{bb} = \Phi_{b,d}^T \hat{\mathbf{M}}_{bb} \Phi_{b,d}, \quad (20a)$$

$$\tilde{\mathbf{K}}_{ii} = \hat{\mathbf{K}}_{ii}, \quad \tilde{\mathbf{K}}_{ib} = \hat{\mathbf{K}}_{ii} \Phi_{b,d}, \quad \tilde{\mathbf{K}}_{bi} = \tilde{\mathbf{K}}_{ib}^T, \quad \tilde{\mathbf{K}}_{bb} = \Phi_{b,d}^T \hat{\mathbf{K}}_{bb} \Phi_{b,d}, \quad (20b)$$

$$\tilde{\mathbf{f}}_i = \hat{\mathbf{f}}_i, \quad \tilde{\mathbf{f}}_b = \Phi_{b,d}^T \hat{\mathbf{f}}_b, \quad (20c)$$

where it is noted that the interface partition of the CB system matrices, i.e. $\hat{\mathbf{M}}_{bb}$ and $\hat{\mathbf{K}}_{bb}$ are reduced using classical modal truncation. However, the truncated internal partition of the CB system matrices, i.e. $\hat{\mathbf{M}}_{ii}$ and $\hat{\mathbf{K}}_{ii}$ are just retained. Accordingly, the equations of motion in Eq. (10) can be further reduced to

$$\tilde{\mathbf{M}} \ddot{\mathbf{u}} + \tilde{\mathbf{K}} \mathbf{u} = \tilde{\mathbf{F}}, \quad (21)$$

where the system matrices $\tilde{\mathbf{M}}$, $\tilde{\mathbf{K}}$ and force vector $\tilde{\mathbf{F}}$ are those for which the internal and boundary DOFs are reduced using the CB method and interface reduction matrix $\tilde{\mathbf{T}}_{IR1}$, respectively. Hence the size of the mentioned system matrices and the force vector are respectively $\tilde{N} \times \tilde{N}$ and $\tilde{N} \times 1$, where $\tilde{N} = N_{i,d} + N_{b,d}$, which is smaller than \hat{N} , \tilde{N} and N . This combination of CB and IR1 is denoted CB-IR1 in the application examples in Section 4.

Considering $\tilde{\mathbf{T}}_{IR1}$ to truncate interface dynamics of the global system matrices for which the internal dynamics are truncated using the ECB method, the system matrices in Eq. (14) can be further reduced to

$$\tilde{\mathbf{T}}_{IR1}^T \tilde{\mathbf{M}}_g \tilde{\mathbf{T}}_{IR1} \begin{Bmatrix} \hat{\mathbf{q}}_{i,d} \\ \hat{\mathbf{q}}_{b,d} \end{Bmatrix} + \tilde{\mathbf{T}}_{IR1}^T \tilde{\mathbf{K}}_g \tilde{\mathbf{T}}_{IR1} \begin{Bmatrix} \mathbf{q}_{i,d} \\ \mathbf{q}_{b,d} \end{Bmatrix} = \tilde{\mathbf{T}}_{IR1}^T \begin{Bmatrix} \hat{\mathbf{f}}_i \\ \hat{\mathbf{f}}_b \end{Bmatrix}, \quad (22)$$

with

$$\tilde{\mathbf{M}} = \tilde{\mathbf{T}}_{IR1}^T \tilde{\mathbf{M}}_g \tilde{\mathbf{T}}_{IR1} = \begin{bmatrix} \tilde{\mathbf{M}}_{ii} & \tilde{\mathbf{M}}_{ib} \\ \tilde{\mathbf{M}}_{bi} & \tilde{\mathbf{M}}_{bb} \end{bmatrix}, \quad (23a)$$

$$\tilde{\mathbf{K}} = \tilde{\mathbf{T}}_{IR1}^T \tilde{\mathbf{K}}_g \tilde{\mathbf{T}}_{IR1} = \begin{bmatrix} \tilde{\mathbf{K}}_{ii} & \tilde{\mathbf{K}}_{ib} \\ \tilde{\mathbf{K}}_{bi} & \tilde{\mathbf{K}}_{bb} \end{bmatrix}, \quad (23b)$$

$$\tilde{\mathbf{F}} = \tilde{\mathbf{T}}_{IR1}^T \begin{Bmatrix} \hat{\mathbf{f}}_i \\ \hat{\mathbf{f}}_b \end{Bmatrix} = \begin{Bmatrix} \tilde{\mathbf{f}}_i \\ \tilde{\mathbf{f}}_b \end{Bmatrix}, \quad (23c)$$

where the elements of the system matrices $\tilde{\mathbf{M}}$ and $\tilde{\mathbf{K}}$, and the force vector $\tilde{\mathbf{F}}$ are defined as:

$$\tilde{\mathbf{M}}_{ii} = \hat{\mathbf{M}}_{ii}, \quad \tilde{\mathbf{M}}_{ib} = \hat{\mathbf{M}}_{ii} \Phi_{b,d}, \quad \tilde{\mathbf{M}}_{bi} = \tilde{\mathbf{M}}_{ib}^T, \quad \tilde{\mathbf{M}}_{bb} = \Phi_{b,d}^T \hat{\mathbf{M}}_{bb} \Phi_{b,d}, \quad (24a)$$

$$\tilde{\mathbf{K}}_{ii} = \hat{\mathbf{K}}_{ii}, \quad \tilde{\mathbf{K}}_{ib} = \hat{\mathbf{K}}_{ii} \Phi_{b,d}, \quad \tilde{\mathbf{K}}_{bi} = \tilde{\mathbf{K}}_{ib}^T, \quad \tilde{\mathbf{K}}_{bb} = \Phi_{b,d}^T \hat{\mathbf{K}}_{bb} \Phi_{b,d}. \quad (24b)$$

$$\tilde{\mathbf{f}}_i = \hat{\mathbf{f}}_i, \quad \tilde{\mathbf{f}}_b = \Phi_{b,d}^T \hat{\mathbf{f}}_b. \quad (24c)$$

The equation above indicates that the interface portions of the system matrices, i.e., $\hat{\mathbf{M}}_{bb}$ and $\hat{\mathbf{K}}_{bb}$, and the force vector $\hat{\mathbf{f}}_b$, are truncated using classical modal truncation. However, this approach does not account for the stiffness coupling present in the ECB method, as shown in Eq. (13). With the system matrices and force vector in Eq. (23), the equations of motion in Eq. (14) can be reduced to

$$\tilde{\mathbf{M}} \ddot{\mathbf{u}} + \tilde{\mathbf{K}} \mathbf{u} = \tilde{\mathbf{F}}, \quad (25)$$

where the sizes of the system matrices $\tilde{\mathbf{M}}$ and $\tilde{\mathbf{K}}$, and the force vector $\tilde{\mathbf{F}}$ are $\tilde{N} \times \tilde{N}$ and $\tilde{N} \times 1$, respectively, where $\tilde{N} = N_{i,d} + N_{b,d}$. This size is smaller than that of \hat{N} , \tilde{N} , and N . The approach using a combination of ECB and IR1 is denoted as ECB-IR1 in the application examples in Section 4.

3.2. Refined interface reduction technique

Referring back to Eq. (13), it is evident that the off-diagonal terms of ECB, which indicates the interaction between the truncated internal and boundary DOFs, are not entirely decoupled. These off-diagonal terms serve as a forcing function, resulting in the excitation of the internal dynamics by the motion at the interface. Consequently, to project the truncated internal dynamics onto the interface, the consideration of an additional constraint mode matrix is necessary to facilitate the transfer of the vibration energy. In this section, the interface reduction matrix presented in the previous section denoted as $\tilde{\mathbf{T}}_{IR1}$, will be modified to enhance its accuracy. This modification is intended for cases where internal dynamics are truncated using the ECB method in Eq. (14).

Considering an additional coupling term, the interface boundary displacement vector in Eq. (16) can be approximated as:

$$\mathbf{u}_b \approx \Xi \mathbf{q}_{i,d} + \Phi_{b,d} \mathbf{q}_{b,d}, \quad (26)$$

where Ξ is a constraint mode matrix which projects the internal DOFs onto the interface DOFs, $\Phi_{b,d}$ is a mode matrix containing dominant interface modes, obtained in Eq. (15) with a column size of $N_{b,d}$, and $\mathbf{q}_{b,d}$ is its associated generalised coordinates. The shape of the constraint coupling term Ξ is similar to a static condensation of the interface DOFs. This consideration is valid for low-frequency vibrations considering the interface DOFs respond quasi-statically to the truncated internal DOFs.

The global displacement vector in Eq. (14) can be further reduced to

$$\tilde{\mathbf{u}}_g \approx \tilde{\mathbf{T}}_{\text{IR}2} \begin{Bmatrix} \mathbf{q}_{i,d} \\ \mathbf{q}_{b,d} \end{Bmatrix}, \quad \tilde{\mathbf{u}}_g = \begin{Bmatrix} \mathbf{q}_{i,d} \\ \mathbf{q}_{b,d} \end{Bmatrix}, \quad \tilde{\mathbf{T}}_{\text{IR}2} = \begin{bmatrix} \mathbf{I}_{i,d} & \mathbf{0} \\ \Xi & \Phi_{b,d} \end{bmatrix}, \quad \Xi = -\tilde{\mathbf{K}}_{bb}^{-1} \tilde{\mathbf{K}}_{bi}, \quad (27)$$

where Ξ is computed using components of $\tilde{\mathbf{K}}_g$ Eq. (14), for which the internal DOFs are reduced using the ECB method and has the dimension of $\tilde{N}_b \times \tilde{N}_{i,d}$. It is noted that the transformation matrix $\tilde{\mathbf{T}}_{\text{IR}2}$ in Eq. (27) is similar to the $\mathbf{T}_{\text{IR}1}$ in Eq. (17), however, with an additional coupling term Ξ .

Considering the refined interface reduction technique which takes the coupling between the truncated internal and interface DOFs into account, i.e. $\tilde{\mathbf{T}}_{\text{IR}2}$, the equations of motion in Eq. (14) can be further reduced to

$$\tilde{\mathbf{T}}_{\text{IR}2}^T \tilde{\mathbf{M}}_g \tilde{\mathbf{T}}_{\text{IR}2} \begin{Bmatrix} \dot{\mathbf{q}}_{i,d} \\ \dot{\mathbf{q}}_{b,d} \end{Bmatrix} + \tilde{\mathbf{T}}_{\text{IR}2}^T \tilde{\mathbf{K}}_g \tilde{\mathbf{T}}_{\text{IR}2} \begin{Bmatrix} \mathbf{q}_{i,d} \\ \mathbf{q}_{b,d} \end{Bmatrix} = \tilde{\mathbf{T}}_{\text{IR}2}^T \begin{Bmatrix} \tilde{\mathbf{f}}_i \\ \tilde{\mathbf{f}}_b \end{Bmatrix}, \quad (28)$$

where

$$\tilde{\mathbf{M}} = \tilde{\mathbf{T}}_{\text{IR}2}^T \tilde{\mathbf{M}}_g \tilde{\mathbf{T}}_{\text{IR}2} = \begin{bmatrix} \tilde{\mathbf{M}}_{ii} & \tilde{\mathbf{M}}_{ib} \\ \tilde{\mathbf{M}}_{bi} & \tilde{\mathbf{M}}_{bb} \end{bmatrix}, \quad (29a)$$

$$\tilde{\mathbf{K}} = \tilde{\mathbf{T}}_{\text{IR}2}^T \tilde{\mathbf{K}}_g \tilde{\mathbf{T}}_{\text{IR}2} = \begin{bmatrix} \tilde{\mathbf{K}}_{ii} & \tilde{\mathbf{K}}_{ib} \\ \tilde{\mathbf{K}}_{bi} & \tilde{\mathbf{K}}_{bb} \end{bmatrix}, \quad (29b)$$

$$\tilde{\mathbf{F}} = \tilde{\mathbf{T}}_{\text{IR}2}^T \begin{Bmatrix} \tilde{\mathbf{f}}_i \\ \tilde{\mathbf{f}}_b \end{Bmatrix} = \begin{Bmatrix} \tilde{\mathbf{f}}_i \\ \tilde{\mathbf{f}}_b \end{Bmatrix}, \quad (29c)$$

with

$$\tilde{\mathbf{M}}_{ii} = \tilde{\mathbf{M}}_{ii} + \Xi^T \tilde{\mathbf{M}}_{bi} + \tilde{\mathbf{M}}_{bi} \Xi + \Xi^T \tilde{\mathbf{M}}_{bb} \Xi, \quad (30a)$$

$$\tilde{\mathbf{M}}_{ib} = \tilde{\mathbf{M}}_{ib} \Phi_{b,d} + \Xi^T \tilde{\mathbf{M}}_{bb} \Phi_{b,d}, \quad \tilde{\mathbf{M}}_{bi} = \tilde{\mathbf{M}}_{ib}^T, \quad (30b)$$

$$\tilde{\mathbf{M}}_{bb} = \Phi_{b,d}^T \tilde{\mathbf{M}}_{bb} \Phi_{b,d}, \quad (30c)$$

$$\tilde{\mathbf{K}}_{ii} = \tilde{\mathbf{K}}_{ii} + \Xi^T \tilde{\mathbf{K}}_{bi} + \tilde{\mathbf{K}}_{bi} \Xi + \Xi^T \tilde{\mathbf{K}}_{bb} \Xi, \quad (30d)$$

$$\tilde{\mathbf{K}}_{ib} = \tilde{\mathbf{K}}_{ib} \Phi_{b,d} + \Xi^T \tilde{\mathbf{K}}_{bb} \Phi_{b,d}, \quad \tilde{\mathbf{K}}_{bi} = \tilde{\mathbf{K}}_{ib}^T, \quad (30e)$$

$$\tilde{\mathbf{K}}_{bb} = \Phi_{b,d}^T \tilde{\mathbf{K}}_{bb} \Phi_{b,d}, \quad (30f)$$

$$\tilde{\mathbf{f}}_i = \tilde{\mathbf{f}}_i, \quad \tilde{\mathbf{f}}_b = \Xi^T \tilde{\mathbf{f}}_i + \Phi_{b,d}^T \tilde{\mathbf{f}}_b, \quad (30g)$$

where the system matrices $\tilde{\mathbf{M}}$ and $\tilde{\mathbf{K}}$ and force vector $\tilde{\mathbf{F}}$ are those for which the internal and boundary DOFs are reduced using ECB method and the refined interface reduction transformation matrix $\tilde{\mathbf{T}}_{\text{IR}2}$, respectively. The components of the reduced system matrices in Eq. (30) clearly show that the truncated internal and coupling terms, i.e. $\tilde{\mathbf{M}}_{ii}$ and $\tilde{\mathbf{M}}_{ib} = \tilde{\mathbf{M}}_{bi}^T$, have been enhanced by additional terms accounting for the coupling between the truncated internal and interface DOFs, cf. Eqs. (20) and (24). Accordingly, the equations of motion in Eq. (14) can be further reduced to

$$\tilde{\mathbf{M}} \ddot{\tilde{\mathbf{u}}} + \tilde{\mathbf{K}} \tilde{\mathbf{u}} = \tilde{\mathbf{f}}, \quad (31)$$

where the size of the system matrices $\tilde{\mathbf{M}}$ and $\tilde{\mathbf{K}}$ is $\tilde{N} \times \tilde{N}$ and the size of the force vector $\tilde{\mathbf{f}}$ is $\tilde{N} \times 1$ with $\tilde{N} = N_{i,d} + N_{b,d}$, which is smaller than both \tilde{N} and N , Table 1. The approach using a combination of ECB and IR2 is denoted ECB-IR2 in the application examples in Section 4.

With the aim of providing a concise summary of each interface reduction technique and its key attributes, a brief comparison is provided in Table 1. Additionally, to assist the implementation of the interface reduction techniques, a supplementary step-by-step procedure is provided in Algorithm 1.

Table 1

Comparison between CB with interface reduction (CB-IR1), ECB with interface reduction (ECB-IR1), and ECB with refined interface reduction (ECB-IR2). The checkmark denotes valid operations.

	CB-IR1	ECB-IR1	ECB-IR2
Transformation matrix	$\bar{\mathbf{T}}_{IR1}^T \bar{\mathbf{T}}_{CB}$	$\bar{\mathbf{T}}_{IR1}^T \bar{\mathbf{T}}_{ECB}$	$\bar{\mathbf{T}}_{IR2}^T \bar{\mathbf{T}}_{ECB}$
Reduced mass matrix	$\bar{\mathbf{T}}_{IR1}^T \bar{\mathbf{T}}_{CB}^T \mathbf{M} \bar{\mathbf{T}}_{CB} \bar{\mathbf{T}}_{IR1}$	$\bar{\mathbf{T}}_{IR1}^T \bar{\mathbf{T}}_{ECB}^T \mathbf{M} \bar{\mathbf{T}}_{ECB} \bar{\mathbf{T}}_{IR1}$	$\bar{\mathbf{T}}_{IR2}^T \bar{\mathbf{T}}_{ECB}^T \mathbf{M} \bar{\mathbf{T}}_{ECB} \bar{\mathbf{T}}_{IR2}$
Reduced stiffness matrix	$\bar{\mathbf{T}}_{IR1}^T \bar{\mathbf{T}}_{CB}^T \mathbf{K} \bar{\mathbf{T}}_{CB} \bar{\mathbf{T}}_{IR1}$	$\bar{\mathbf{T}}_{IR1}^T \bar{\mathbf{T}}_{ECB}^T \mathbf{K} \bar{\mathbf{T}}_{ECB} \bar{\mathbf{T}}_{IR1}$	$\bar{\mathbf{T}}_{IR2}^T \bar{\mathbf{T}}_{ECB}^T \mathbf{K} \bar{\mathbf{T}}_{ECB} \bar{\mathbf{T}}_{IR2}$
Size of the reduced matrices	$\bar{N} = N_{i,d} + N_{b,d}$	$\bar{N} = N_{i,d} + N_{b,d}$	$\bar{N} = N_{i,d} + N_{b,d}$
Reduced internal dynamics	✓	✓	✓
Reduced interface dynamics	✓	✓	✓

Algorithm 1 Implementation of interface reduction using CB-IR1, ECB-IR1, and ECB-IR2.

Input: Full model substructure system matrices ($\mathbf{M}^{(s)}, \mathbf{K}^{(s)}, \mathbf{f}^{(s)}$)

Output: Reduced system matrices ($(\tilde{\mathbf{M}}, \tilde{\mathbf{K}}, \tilde{\mathbf{f}})$, $(\bar{\mathbf{M}}, \bar{\mathbf{K}}, \bar{\mathbf{f}})$, $(\tilde{\mathbf{M}}, \tilde{\mathbf{K}}, \tilde{\mathbf{f}})$)

procedure

1. Solve the internal eigenvalue problem for substructure $s = 1, 2, \dots, N_s$

$$(\mathbf{K}_{ii}^{(s)} - \omega_{i,j}^2 \mathbf{M}_{ii}^{(s)}) \boldsymbol{\phi}_{i,j}^{(s)} = \mathbf{0}, \quad j = 1, 2, \dots, N_{i,d}^{(s)}, \quad \text{in Eq. (6)}$$

2. Compute the CB reduction matrix $\bar{\mathbf{T}}_{CB}^{(s)}$, in Eq. (7)

3. Compute the ECB reduction matrix $\bar{\mathbf{T}}_{ECB}^{(s)}$, in Eq. (11)

4. Truncate the interior dynamics of each substructure and compute

$$\hat{\mathbf{M}}_g, \hat{\mathbf{K}}_g, \hat{\mathbf{f}}_g \text{ and } \bar{\mathbf{M}}_g, \bar{\mathbf{K}}_g, \bar{\mathbf{f}}_g, \quad \text{in Eqs. (10) and (14)}$$

5. Solve the system-level interface eigenvalue problem and obtain CC modes:

$$(\mathbf{K}_{bb} - \omega_{b,j}^2 \mathbf{M}_{bb}) \boldsymbol{\phi}_{b,j} = \mathbf{0}, \quad j = 1, 2, \dots, N_{b,d}, \quad \text{in Eq. (15)}$$

6. Compute the interface reduction transformation $\bar{\mathbf{T}}_{IR1}$ in Eq. (17)

7. Compute the refined interface reduction transformation matrix $\bar{\mathbf{T}}_{IR2}$ in Eq. (27)

8. Truncate system-level interface dynamics and compute:

- CB-IR1 system matrices and force vector: $\tilde{\mathbf{M}}, \tilde{\mathbf{K}}, \tilde{\mathbf{f}}$
- ECB-IR1 system matrices and force vector: $\bar{\mathbf{M}}, \bar{\mathbf{K}}, \bar{\mathbf{f}}$
- ECB-IR2 system matrices and force vector: $\tilde{\mathbf{M}}, \tilde{\mathbf{K}}, \tilde{\mathbf{f}}$

end procedure

4. Application examples

In this section, the interface reduction techniques discussed in the previous section are applied to reduce the interface DOFs in three examples. To assess each model's performance, the results are compared with those from the full model, CB model, and ECB model. The accuracy of each model is then evaluated by considering the relative frequency error as:

$$\text{Relative frequency error} = \frac{|\bar{f}_i - f_i|}{f_i}, \quad (32)$$

where f_i represents the resonance frequency of component i for comparison. An over-bar, as previously explained, indicates an approximate quantity. Therefore, \bar{f}_i and f_i respectively correspond to the frequency components of the reduced and full models.

The accuracy of the models is further evaluated in the frequency domain by considering their harmonic response due to the application of a harmonic unit load. The equations of motion in the frequency domain in the absence of damping can be expressed as:

$$\mathbf{Z}(\omega) \mathbf{u}(\omega) = \mathbf{F}(\omega), \quad \mathbf{Z}(\omega) = -\omega^2 \mathbf{M} + \mathbf{K}, \quad (33)$$

where $\mathbf{Z}(\omega)$ represents a block-diagonal matrix containing the dynamic stiffness of the coupled substructures. The system matrices \mathbf{M} and \mathbf{K} are mass and stiffness matrices, respectively. The response vector is denoted by $\mathbf{u}(\omega)$ and the force amplitude vector is defined as $\mathbf{F}(\omega)$. The response is a function of the driving angular frequency ω in [rad/s]. Hence, the dynamic stiffness matrix $\mathbf{Z}(\omega)$ as well as the force vector $\mathbf{F}(\omega)$ are also functions of the driving frequency ω . The transfer function representing normalised displacement response under unit loading is often referred to as Admittance. For additional insight into the admittance response, the representation plots are supplemented with the phase shift angle of the admittance at each discrete frequency step.

To evaluate the accuracy of the vibration modes associated with the reduced models in comparison with the full model, the statistical indicator Modal Assurance Criterion (MAC) can be employed, [40,41]. The advantages of employing MAC stem from the fact that it is a quantitative tool for comparing the degree of consistency between two modes, whilst being sensitive to large

Table 2
Number of internal and interface modes computed for the stiffened plate example in Section 4.1.

Method	Number of internal modes retained						Number of interface modes retained	Total number of DOFs
	$N_{i,d}^{(1)}$	$N_{i,d}^{(2)}$	$N_{i,d}^{(3)}$	$N_{i,d}^{(4)}$	$N_{i,d}^{(5)}$	$N_{i,d}^{(6)}$		
Full model	4542	3252	1584	1584	2214	2214	972	$N = 16362$
CB	20	10	5	5	10	10	972	$\tilde{N} = 1032$
ECB	20	10	5	5	10	10	972	$\tilde{N} = 1032$
CB-IR1	20	10	5	5	10	10	196	$\tilde{N} = 256$
ECB-IR1	20	10	5	5	10	10	196	$\tilde{N} = 256$
ECB-IR2	20	10	5	5	10	10	196	$\tilde{N} = 256$

differences and relatively insensitive to small differences between two modes. Another advantage is that MAC produces a real quantity despite the degree of complexity of the modes. Considering MAC as a correlation constant we can find:

$$\text{MAC}_{rs} = \frac{|\phi_r^H \phi_s|^2}{(\phi_r^H \phi_r)(\phi_s^H \phi_s)}, \quad (34)$$

where ϕ_r and ϕ_s are two mode vectors to be compared and a superscript H denotes the Hermitian transpose, [42]. The MAC yields a normalised correlation coefficient between two modes with a value between zero and unity, where unity denotes excellent correlation and zero denotes absolute orthogonality.

4.1. Stiffened steel plate

In the first example, a stiffened plate inspired by [43] made of steel is considered. Such plates are on a larger scale commonly employed in bridge structures to withstand lateral torsional buckling as a consequence of significant compression perpendicular to its axial direction. The dimension of the plate is as follows, Length L is 4.8 [m], width B is 3.2 [m] and thickness t is 0.03 [m]. The plate is stiffened in the axial and transversal directions with two and four stiffeners, respectively. The stiffeners in the axial direction have a centre-to-centre distance of 1.2 [m], whilst the transversal stiffeners have a centre-to-centre distance of 1 [m]. The stiffeners have a height H of 0.5 [m]. To the plate, material properties of steel are assigned, with Young's modulus E as 210 [GPa], density ρ as 7850 [kg/m³] and Poisson's ratio of 0.3. The domain is discretised using shell FEs with 6 DOFs per nodal point and linear approximation as well as reduced integration. The element size of 0.1 [m] is chosen in each direction resulting in 2656 elements with 2727 nodes and a total number of DOFs of 16362. The system matrices are subsequently derived and partitioned to 6 substructures coupled at the interface Γ denoted by a blue line in Fig. 2. Information regarding the number of modes employed in the truncation of internal and interface dynamics of each region can be found in Table 2. Throughout the analyses, no Dirichlet boundary condition has been imposed on the plate and no rigid-body modes and resonances have been included in the results presented herein.

The evaluation results indicate that the interface reduction technique IR2 in conjunction with ECB, i.e. ECB-IR2, performs better than the classical interface reduction technique using CB-IR1 and ECB-IR1, in terms of accuracy in the prediction of the resonance frequencies, Fig. 3. The convergence plot in Fig. 4 shows that CB-IR1 converges faster than ECB-IR1 and ECB-IR2. This suggests that adding more interface modes in CB-IR1 does not enhance the results, while the opposite is true for ECB-IR1 and ECB-IR2. Thus, users might prefer to select the convergence criteria in ECB-IR2, cf. Table 2 and Fig. 4. Evaluation of the transfer functions indicates improvement in accuracy when ECB-IR2 is employed compared to CB-IR1 and ECB-IR1, Fig. 5. Notably, the ECB-IR2 with only 256 DOFs produces normal modes with an accuracy similar to the ECB with 1032 DOFs in comparison with the full model with 16362 DOFs, Fig. 6.

4.2. Composite cross-laminated timber plate

Cross-laminated timber (CLT) plates have gained great popularity as a sustainable alternative to conventional construction materials, such as steel and concrete, since the commercial launch of engineered wood products (EWPs). However, in contrast to the mentioned conventional construction materials, wooden structural elements possess a low mass density, making them extra sensitive to vibration at lower frequencies. The structure of CLT consists of an odd number of wooden boards arranged in layers, with each layer oriented at a 90-degree angle to the adjacent ones. For additional information regarding CLT and its production and development, the reader is referred to the state-of-the-art review by Brandner [44] and the overview in [45]. Wood as a material possesses a high degree of orthotropy in three main directions: longitudinal (parallel to wood fibres), denoted as L ; tangential (tangent with the concentric growth rings), denoted as T ; and radial (perpendicular to the concentric growth rings), denoted as R .

In this example, a CLT plate with a total length of 7 [m] and a width of 2.4 [m] is considered, Fig. 7. The plate consists of 7 cross-wisely bonded layers with a material orientation of 90° about the z -axis between one layer and the adjacent ones. The plate is discretised using doubly-curved composite shell elements with 7 layups, [47]. The thickness of each layup is 40| 20| 40| 40| 20| 40 millimetres, respectively. For the bottom and top layers, the material direction of the fibres is spanning along the x -axis, whilst for the second layer from the bottom the fibres are oriented by an angle of 90° about the z -axis and so forth. Such plates are commonly used as structural elements in multi-storey timber buildings. To the plate, orthotropic material properties of softwood of strength

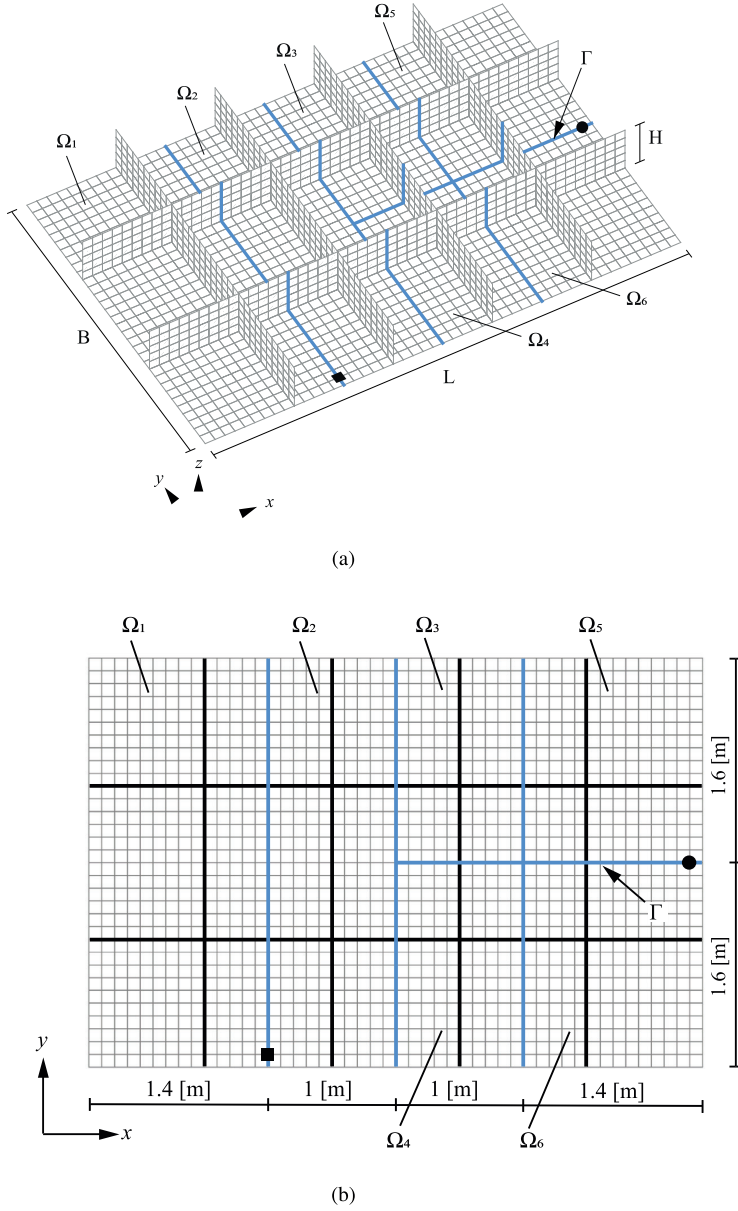


Fig. 2. Discretised geometry of a stiffened plate with $L = 4.8$ [m], $B = 3.2$ [m], $H = 0.5$ [m] in (a) 3D and (b) 2D, as discussed in Section 4.1. Black lines in (b) denote the stiffeners and $\Omega_i \in \{1, 2, \dots, 6\}$ denote substructure regions. The blue line Γ denotes the interface, a black circle denotes the unit excitation point and a black square denotes the evaluation point of the transfer functions in the frequency domain.

class C35 in [46] have been assigned, Table 3. Throughout the analyses, no Dirichlet boundary condition has been imposed on the plate and the rigid-body resonances and modes have not been considered in the results presented herein. Further information regarding the number of modes retained for each substructure can be found in Table 4.

The evaluations indicate improvement in the accuracy prediction of the resonance frequencies associated with the ECB-IR2 compared with CB-IR1 in comparison to the full model, Fig. 8. The interface mode convergence indicates that CB-IR1 and ECB-IR2

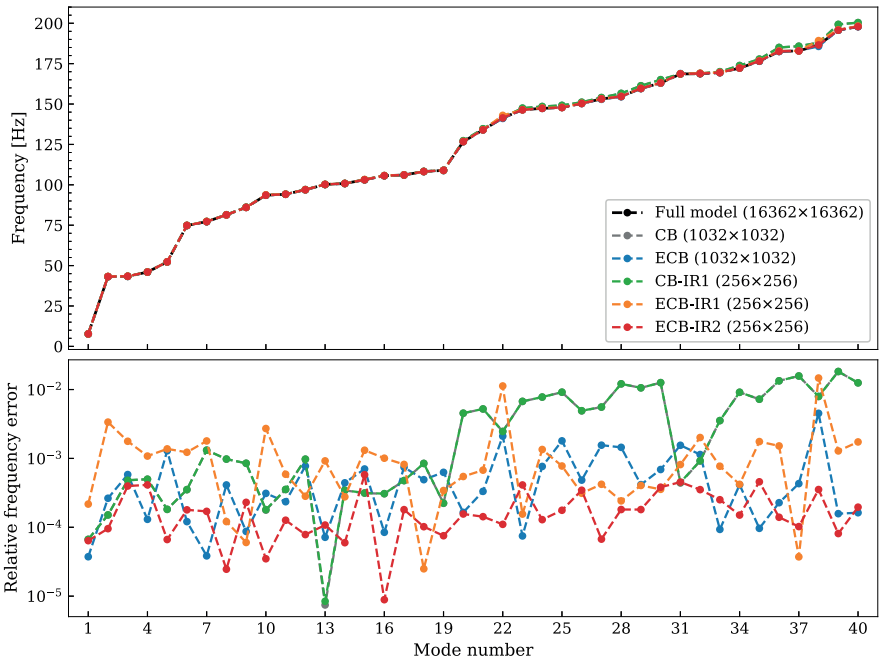


Fig. 3. Resonance frequencies and their associated relative error of the stiffened plate example in Section 4.1. The numbers in the legend indicate the size of the system matrices.

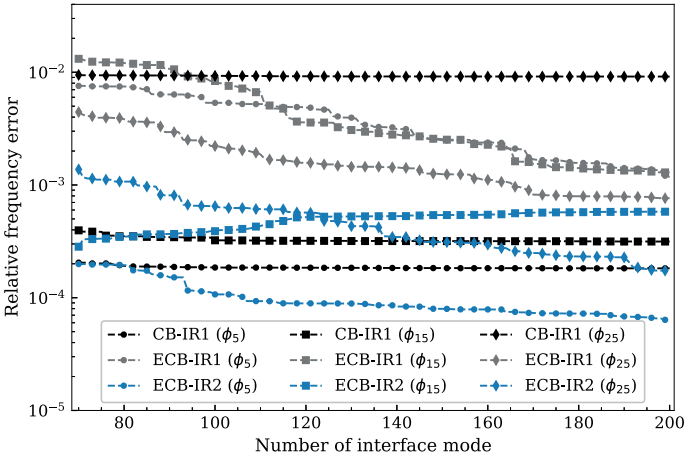


Fig. 4. Interface mode convergence of the stiffened plate example in Section 4.1, with respect to modes number 5, 15, and 25.

Table 3
Orthotropic material properties of CLT of strength class C35 from Ref. [46]. The subscripts L , T , and R respectively denote orthotropic orientations of wood in longitudinal, tangential and radial directions.

E_L [MPa]	E_T [MPa]	E_R [MPa]	G_{LT} [MPa]	G_{LR} [MPa]	G_{RT} [MPa]	ν_{LT} [-]	ν_{LR} [-]	ν_{RT} [-]	ρ [kg/m ³]
13 000	262	430	810	810	57	0.48	0.42	0.28	470

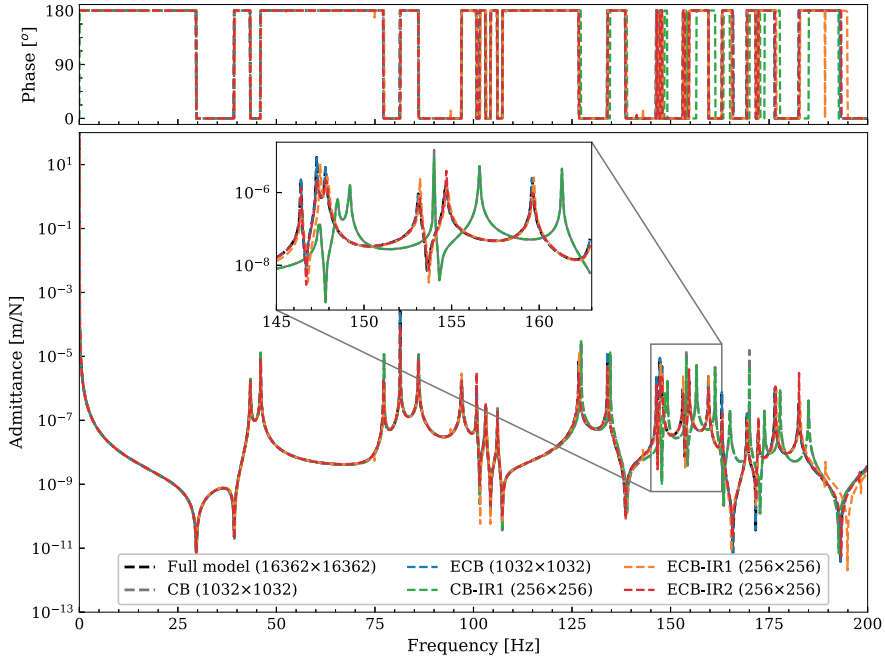


Fig. 5. Bode plot of the transfer functions and their associated phase shift angle of the stiffened plate example in Section 4.1, to unit loading. The numbers in the legend indicate the size of the system matrices.

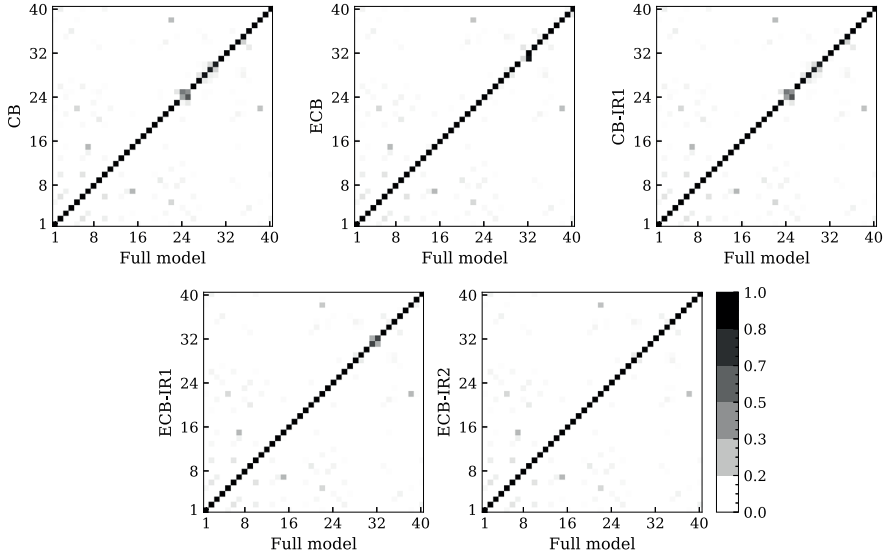


Fig. 6. Modal Assurance Criterion comparing 40 flexible modes of the stiffened plate example in Section 4.1.

converge faster than the ECB-IR1, Fig. 9. This explains that an increase in the number of interface modes in CB-IR1 does not improve its accuracy, while the opposite is true for ECB-IR1 and ECB-IR2. Evaluation of the transfer functions indicates further improvement in predicting the resonance peaks in Fig. 10. The MAC evaluation also indicates that ECB-IR2 produces normal modes with only 110 DOFs with an accuracy nearly as for the ECB with 281 DOFs in comparison to the full model with 2808 DOFs, Fig. 11. To gain

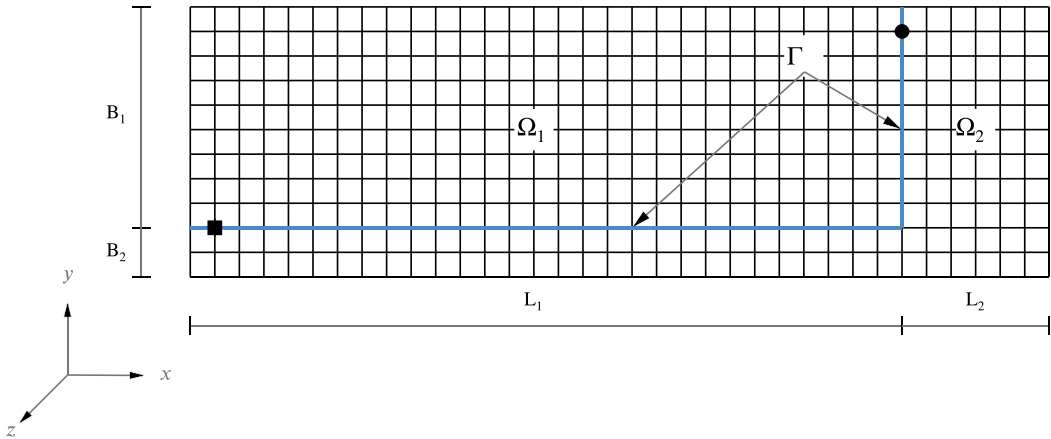


Fig. 7. Discretised Composite Cross-Laminated Timber (CLT) plate geometry (Section 4.2): Substructures Ω_1 and Ω_2 are interface-coupled at Γ . A black circle represents unit loading in the out-of-plane direction (z-axis), while a black square indicates the corresponding transfer function. Geometrical dimensions: $L_1 = 5.8$ [m], $L_2 = 1.2$ [m], $B_1 = 2$ [m], and $B_2 = 0.4$ [m].

Table 4				
Number of internal and interface modes computed for the composite CLT plate example in Section 4.2.				
Method	Number of internal modes retained		Number of interface modes retained	Total number of DOFs
	$N_{i,d}^{(1)}$	$N_{i,d}^{(2)}$		
Full model	1740	828	240	$N = 2808$
CB	25	16	240	$\tilde{N} = 281$
ECB	25	16	240	$\tilde{N} = 281$
CB-IR1	25	16	69	$\tilde{N} = 110$
ECB-IR1	25	16	69	$\tilde{N} = 110$
ECB-IR2	25	16	69	$\tilde{N} = 110$

further insight into the modes predicted by each model in this study, 3D visualisations of modes 13 and 26 are shown in Figs. 12 and 13.

4.3. Multi-storey CLT building

In the last example a multi-storey CLT building comprising 4 CLT plates, a CLT core and 18 Glued-Laminated Timber (GLT) beams, is fragmented into 4 substructures. Each substructure is connected at the interface Γ , indicated by a blue line in Figs. 14 and 15. The plane dimension (length \times breadth) of the building is 20×16 [m²] and each storey is connected with another at a height of 3.4 [m], giving the building a total height of 13.6 [m]. The core has the dimension (length \times breadth) of 12×8 [m²], placed at the centre of the building. The beams have a cross sectional area of 215×405 [mm²] with a centre-to-centre distance of 4 [m]. The core and the plates are assumed to be of 5-ply CLT elements with layup thicknesses 40| 40| 40| 40| 40 millimetres and strength class of C35, for which the orthotropic elastic properties are presented in Table 3. For the plates, the top and bottom layers of the CLT plates span along the global $x -$ axis, whilst for the core, the top and bottom layers of the CLT span along the global $z -$ axis. Elastic properties of GL30c with Young's modulus of 13000 [MPa], density of 500 [kg/m³] and Poisson's ratio 0.42 have been assigned to the beams.

The CLT core and plates are discretised using doubly curved composite shell elements with reduced integration and hourglass control, as described in [47]. The global element size is set to 0.5 [m] in each direction, using linear interpolation. Additionally, a convergence analysis of the discretisation has been performed. The beams are modelled according to the Bernoulli-Euler beam theory (without shear deformation) with the same element size as the plates and the core. Full interaction between the upper and lower floors as well as the beams and the floors is considered. The geometry of the building analysed herein is inspired by the study in [48]. Throughout the analyses presented herein, pinned (fixed translational DOFs) Dirichlet boundary conditions were applied to the bottom of the multi-storey building, i.e., the bottom of the beams and the core. The rigid-body resonances and their associated modes have not been considered in the results presented herein. The number of modes computed for each model can be found in Table 5.

The evaluation results align with the previously presented examples, demonstrating that ECB-IR2 provides resonance frequencies with enhanced accuracy compared to CB-IR1 and ECB-IR1. This improvement is particularly evident in the prediction of the lower

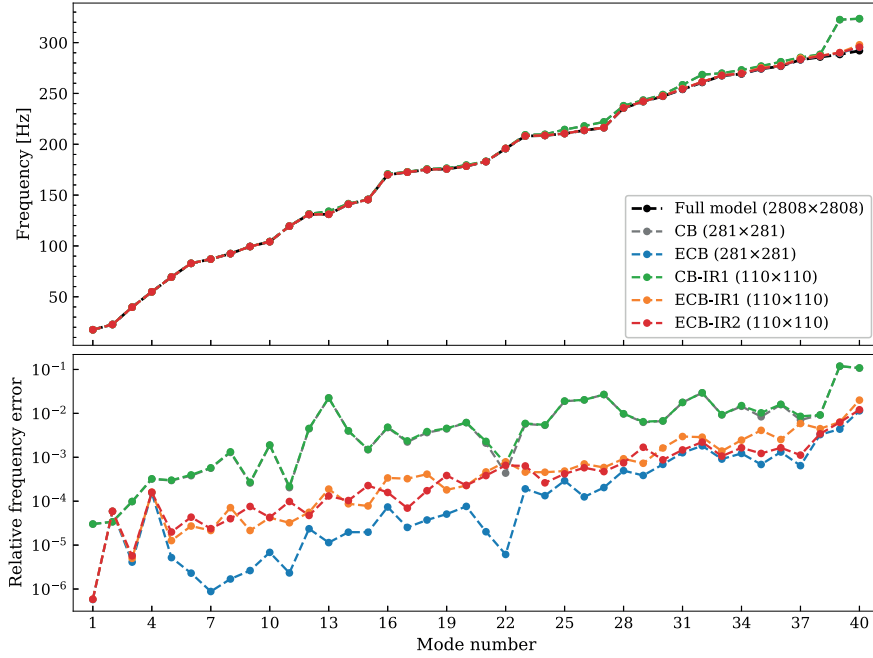


Fig. 8. Resonance frequencies and their associated relative error of the composite CLT plate example in Section 4.2. The numbers in the legend indicate the size of the system matrices.

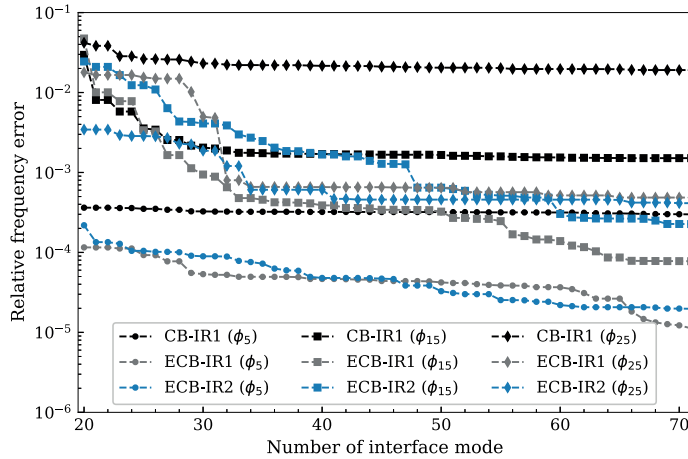


Fig. 9. Interface mode convergence of the composite CLT plate example in Section 4.2, with respect to modes number 5, 15, and 25.

frequency elastic resonances, as shown in Fig. 16. The interface mode convergence analysis in Fig. 17 indicates that increasing the number of modes further can enhance the accuracy of ECB-IR1 and ECB-IR2. Therefore, users may choose a convergence criteria that meets their requirements. In the prediction of the transfer functions, an obvious improvement can be observed in the frequency range of 9–11 [Hz], in particular the double peaks, Fig. 18. Thus the transfer functions predicted by ECB-IR2 are of greater accuracy compared to CB-IR1 and ECB-IR1, in comparison to the full model. Furthermore, the MAC evaluations indicate that the ECB-IR2 with

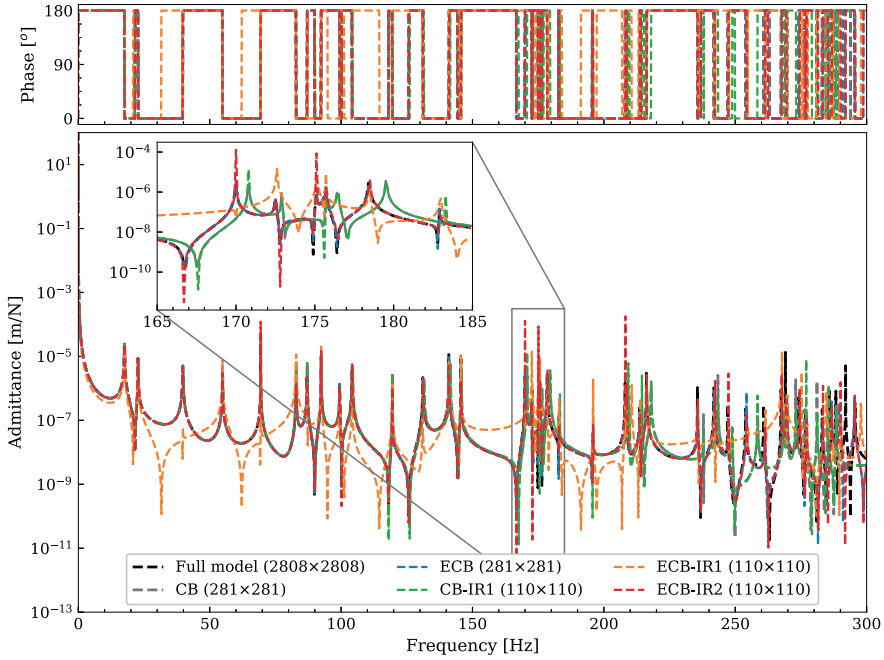


Fig. 10. Bode plot of the transfer functions and their associated phase shift angle of the composite CLT plate example in Section 4.2, to unit loading. The numbers in the legend indicate the size of the system matrices.

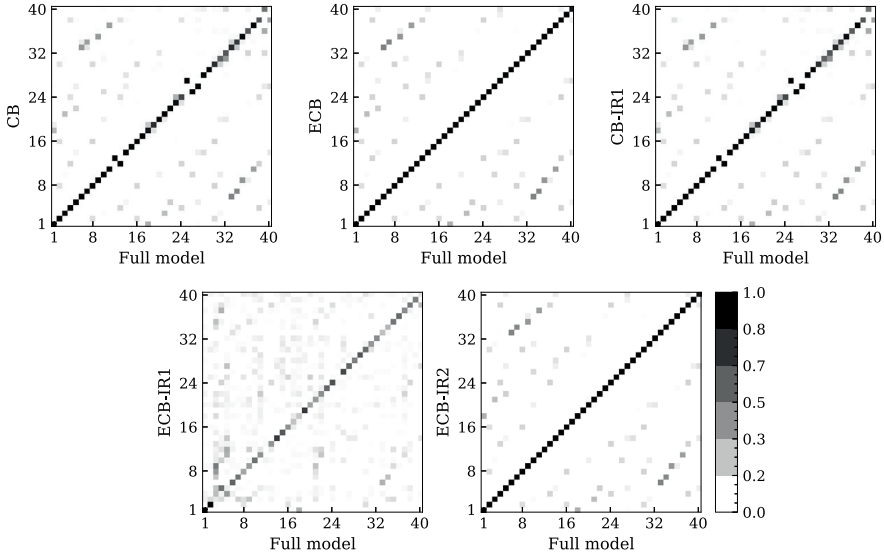


Fig. 11. Modal Assurance Criterion comparing 40 flexible modes of the composite CLT plate example in Section 4.2.

only 342 DOFs produces vibration modes nearly as accurate as the ECB method with 1559 DOFs in comparison with the full model with 38892 DOFs, Fig. 19. Consistent with previous results, ECB-IR1 does not achieve the same level of accuracy in normal modes as CB-IR1 or ECB-IR2. This discrepancy can be attributed to the influence of internal and interface stiffness coupling characteristics of the ECB method, Fig. 19.

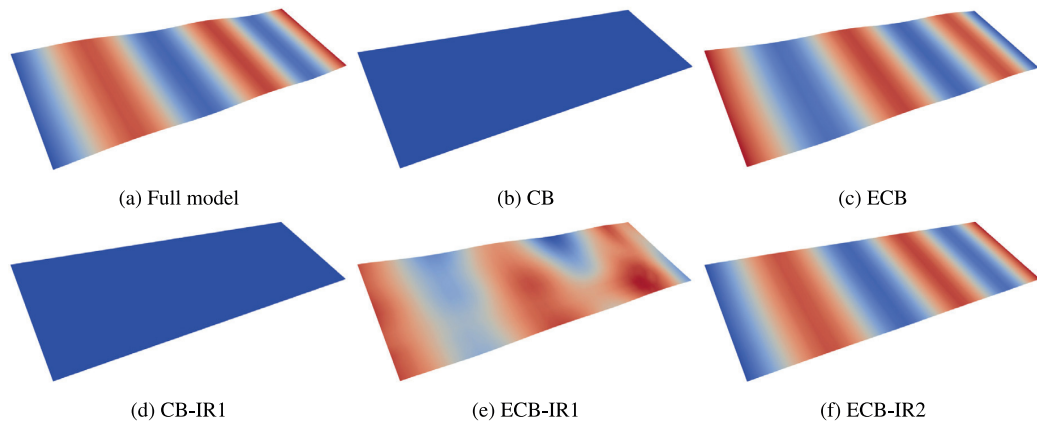


Fig. 12. 3D visualisation of 13th flexible mode of the CLT plate discussed in Section 4.2.

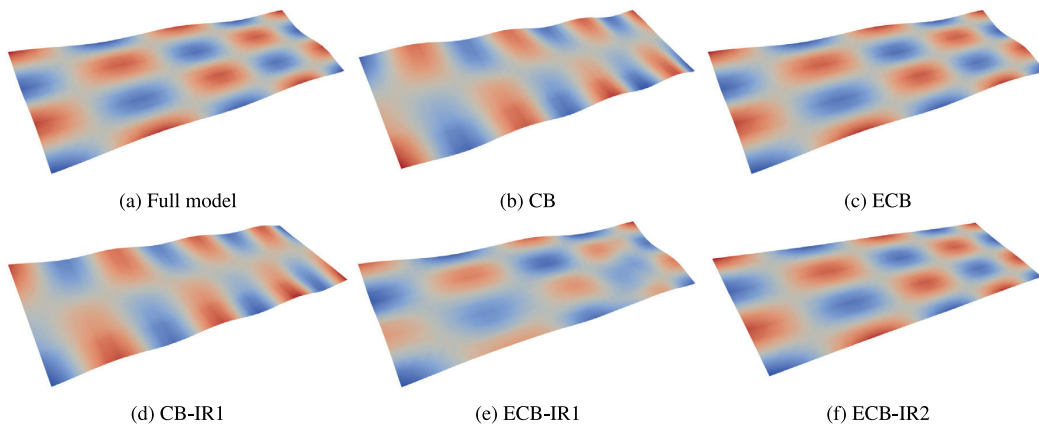


Fig. 13. 3D visualisation of 26th flexible mode of the CLT plate discussed in Section 4.2.

Table 5
Number of internal and interface modes computed for the multi-storey building example in Section 4.3.

Method	Number of internal modes retained				Number of interface modes retained	Total number of DOFs
	$N_{i,d}^{(1)}$	$N_{i,d}^{(2)}$	$N_{i,d}^{(3)}$	$N_{i,d}^{(4)}$		
Full model	7818	13 974	10 896	4740	1464	$N = 38892$
CB	15	20	35	25	1464	$\tilde{N} = 1559$
ECB	15	20	35	25	1464	$\tilde{N} = 1559$
CB-IR1	15	20	35	25	247	$\tilde{N} = 342$
ECB-IR1	15	20	35	25	247	$\tilde{N} = 342$
ECB-IR2	15	20	35	25	247	$\tilde{N} = 342$

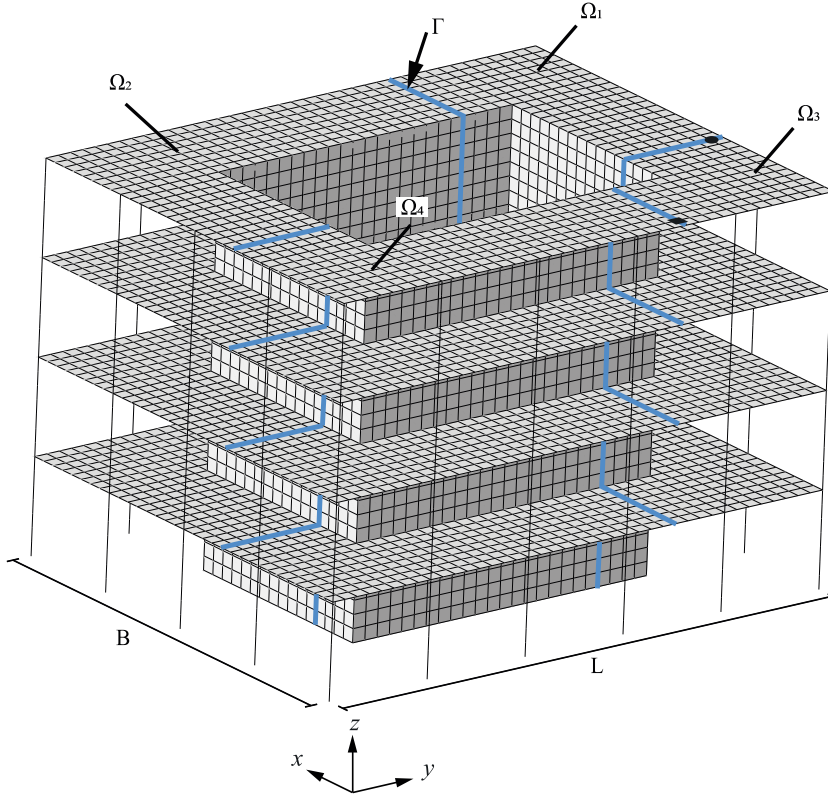


Fig. 14. Discretised geometry of a multi-storey timber building with GLT supporting beams and 5-ply CLT core and plates in Section 4.3. Geometrical dimensions length (L) \times breadth (B) \times height (H) are $20 \times 16 \times 13.6$ [m³]. The notation $\Omega_i \in \{1, 2, \dots, 4\}$ denotes substructure regions, whilst a blue line denotes the coupling interface Γ . A black circle denotes unit loading, and a black square denotes the corresponding transfer function.

5. Conclusions

In this study, two interface reduction techniques based on Characteristic Constraint (CC) modes in conjunction with Craig-Bampton (CB) and Enhanced Craig-Bampton (ECB) methods were presented. Among these techniques, ECB-IR2, which considers coupling between truncated internal and interface DOFs, outperforms the classical method proposed by Castanier et al. [30] when ECB is employed. The coupling term is particularly important due to the stiffness coupling characteristics of the ECB method. This approach provides an improved representation of vibration energy transmission between the truncated internal and interface dynamics. This improves accuracy in predicting resonance frequencies, transfer functions, and normal modes. The ECB-IR2 is a valuable choice when the accuracy of reduced system matrices is of great importance.

The application examples suggest that models with reduced interface dynamics achieve accuracy levels comparable to their CB and ECB counterparts (without interface reduction), from which they are derived. Notably, the inclusion of a large number of CC modes did not enhance the accuracy of the CB-IR1 method, contrasting with the ECB-IR1 and ECB-IR2, where additional CC modes improved accuracy. Therefore, it is evident that additional CC modes enhance the accuracy of the ECB method with interface reduction, especially in the case of ECB-IR2. Furthermore, CB-IR1 demonstrated better convergence properties, while ECB-IR2 exhibited better accuracy with the same number of CC modes.

Potential future avenues of study may include extending the present research to interface reduction of free-interface CMS models, such as Rubin's approach in [14] and the Dual Craig-Bampton method by Rixen [39]. Additionally, exploring the performance of ECB-IR2 in coupled vibroacoustic problems, multi-physics scenarios, and systems involving heat, mass transfer, and damping could be of interest.

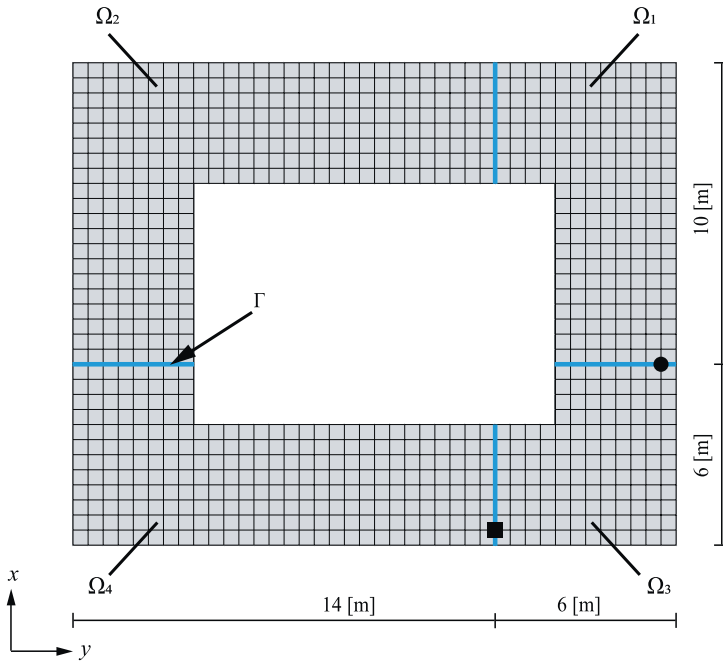


Fig. 15. Discretised plate geometry of a 5-ply CLT plate with length (L) \times breadth (B) of 20×16 [m²], in Section 4.3. The inner core has dimensions length \times breadth of 12×4 [m²]. An Ω denotes a substructural region, whilst a blue line denotes coupling interface Γ . The black circle and rectangle denote respectively excitation node and evaluation node in the frequency domain.

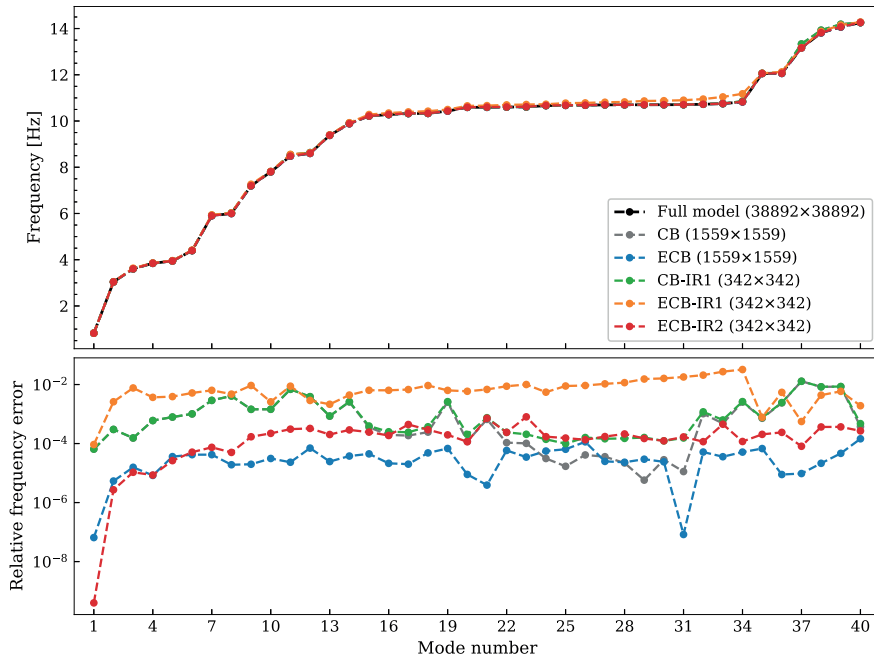


Fig. 16. Resonance frequencies and their associated relative error of the multi-storey CLT building example in Section 4.3. The numbers in the legend indicate the size of the system matrices.

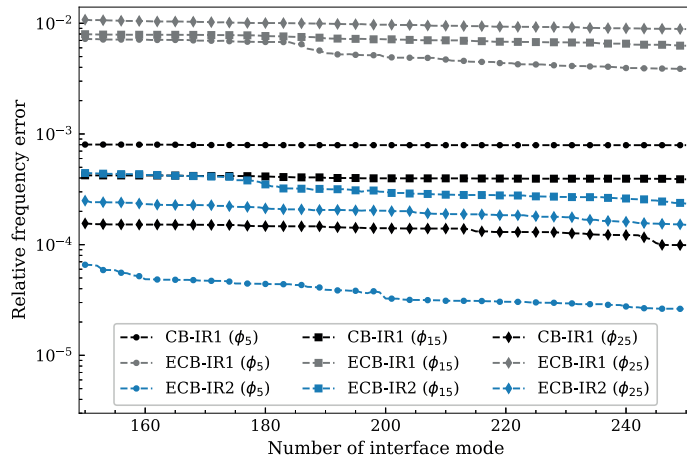


Fig. 17. Interface mode convergence of the multi-storey CLT building example in Section 4.3, concerning modes number 5, 15, and 25.

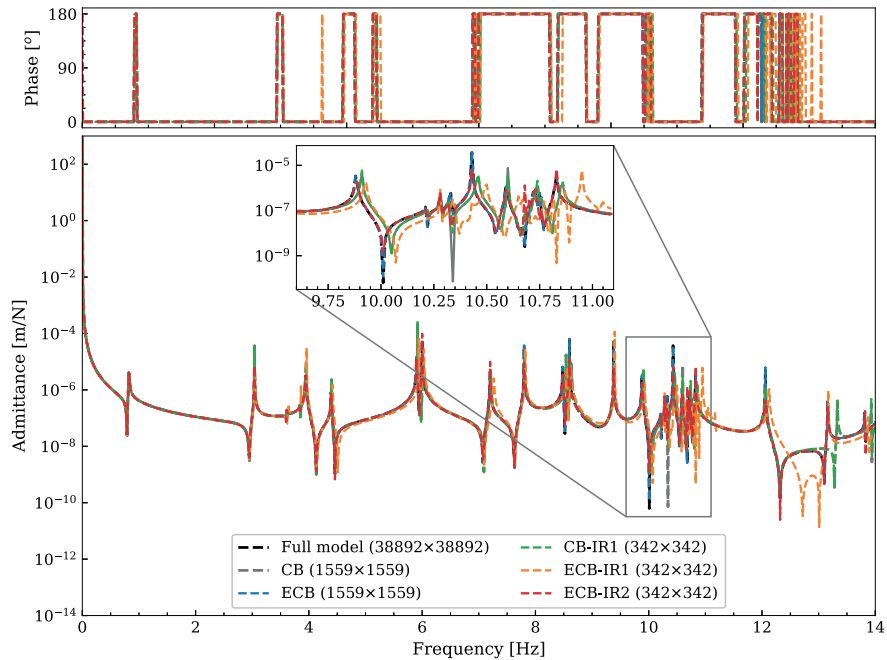


Fig. 18. Bode plot of the transfer functions and their associated phase shift angle of the multi-storey CLT building example in Section 4.3, to unit loading. The numbers in the legend indicate the size of the system matrices.

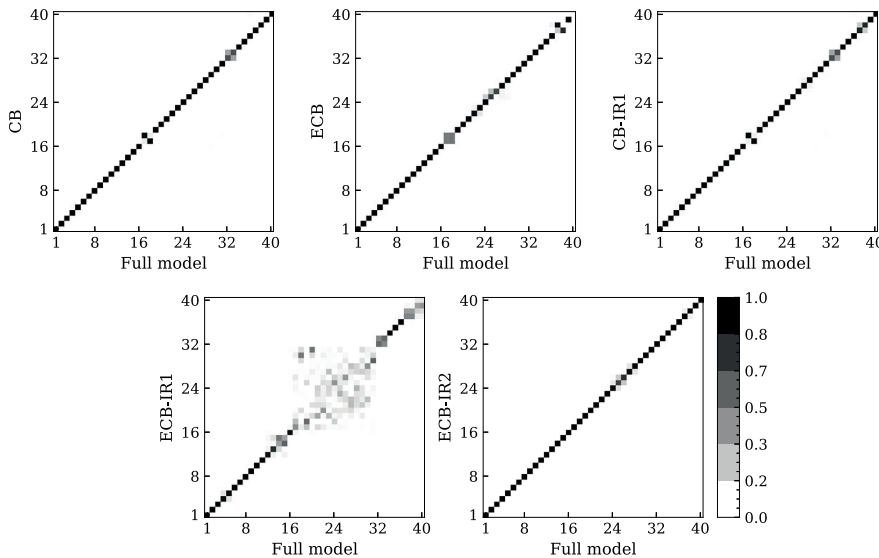


Fig. 19. Modal Assurance Criterion comparing 40 flexible modes of the multi-storey CLT building example in Section 4.3.

CRediT authorship contribution statement

Benjamin Bondsman: Conceptualization, Data curation, Formal analysis, Investigation, Methodology, Resources, Software, Validation, Visualization, Writing – original draft, Writing – review & editing. **Chang-uk Ahn:** Conceptualization, Formal analysis, Methodology, Validation. **Jin-Gyun Kim:** Conceptualization, Funding acquisition, Supervision, Validation, Writing – review & editing.

Declaration of competing interest

The authors declare that they have no known competing financial interests or personal relationships that could have appeared to influence the work reported in this paper.

Data availability

Data will be made available on request.

Acknowledgements

This research was funded by the National Research Foundation of Korea, South Korea (NRF-2021R1A2C4087079).

References

- [1] R.R. Craig Jr., M.C. Bampton, Coupling of substructures for dynamic analyses., *AIAA J.* 6 (7) (1968) 1313–1319.
- [2] W.C. Hurty, Dynamic analysis of structural systems using component modes, *AIAA J.* 3 (4) (1965) 678–685.
- [3] W.C. Hurty, Vibrations of structural systems by component mode synthesis, *J. Eng. Mech. Div.* 86 (4) (1960) 51–69.
- [4] R.J. Guyan, Reduction of stiffness and mass matrices, *AIAA J.* 3 (2) (1965) 380.
- [5] B. Irons, Structural eigenvalue problems-elimination of unwanted variables, *AIAA J.* 3 (5) (1965) 961–962.
- [6] R. Bamford, A modal combination program for dynamic analysis of structures, *NASA TM* 33 (1967) 290.
- [7] R.R. Craig Jr., A.J. Kurdila, *Fundamentals of Structural Dynamics*, John Wiley & Sons, 2006.
- [8] J.T. Spanos, W.S. Tsuha, Selection of component modes for flexible multibody simulation, *J. Guid. Control Dyn.* 14 (2) (1991) 278–286.
- [9] S.M. Kim, J.-G. Kim, S.-W. Chae, K. Park, Evaluating mode selection methods for component mode synthesis, *AIAA J.* 54 (9) (2016) 2852–2863.
- [10] S.M. Kim, J.-G. Kim, K. Park, S.-W. Chae, A component mode selection method based on a consistent perturbation expansion of interface displacement, *Comput. Methods Appl. Mech. Engrg.* 330 (2018) 578–597.
- [11] D. de Klerk, D.J. Rixen, S. Voormeeren, General framework for dynamic substructuring: history, review and classification of techniques, *AIAA J.* 46 (5) (2008) 1169–1181.
- [12] L. Meirovitch, *Computational Methods in Structural Dynamics*, Vol. 5, Springer Science & Business Media, 1980.
- [13] R.H. MacNeal, A hybrid method of component mode synthesis, *Comput. Struct.* 1 (4) (1971) 581–601.

- [14] S. Rubin, Improved component-mode representation for structural dynamic analysis, *AIAA J.* 13 (8) (1975) 995–1006.
- [15] R.M. Hintz, Analytical methods in component modal synthesis, *AIAA J.* 13 (8) (1975) 1007–1016.
- [16] R. Craig Jr., On the use of attachment modes in substructure coupling for dynamic analysis, in: 18th Structural Dynamics and Materials Conference, 1977, p. 405.
- [17] D. Markovic, K. Park, A. Ibrahimbegovic, Reduction of substructural interface degrees of freedom in flexibility-based component mode synthesis, *Internat. J. Numer. Methods Engrg.* 70 (2) (2007) 163–180.
- [18] J.-G. Kim, Y.-J. Park, G.H. Lee, D.-N. Kim, A general model reduction with primal assembly in structural dynamics, *Comput. Methods Appl. Mech. Engrg.* 324 (2017) 1–28.
- [19] J.-G. Kim, P.-S. Lee, An enhanced craig–bampton method, *Internat. J. Numer. Methods Engrg.* 103 (2) (2015) 79–93.
- [20] M.-S. Go, J.H. Lim, J.-G. Kim, K.-r. Hwang, A family of craig–bampton methods considering residual mode compensation, *Appl. Math. Comput.* 369 (2020) 124822.
- [21] D.J. Rixen, Interface reduction in the dual craig–bampton method based on dual interface modes, in: *Linking Models and Experiments*, Vol. 2, Springer, 2011, pp. 311–328.
- [22] K. Park, Y.H. Park, Partitioned component mode synthesis via a flexibility approach, *AIAA J.* 42 (6) (2004) 1236–1245.
- [23] J.-G. Ahn, J.-C. Lee, J.-G. Kim, H.-I. Yang, Multiphysics model reduction of thermomechanical vibration in a state-space formulation, *Eng. Comput.* (2022) 1–29.
- [24] K.-H. Lee, R.W. Hagos, S. Chang, J.-G. Kim, Multiphysics mode synthesis of fluid–structure interaction with free surface, *Eng. Comput.* (2022) 1–16.
- [25] J. Herrmann, M. Maess, L. Gaul, Substructuring including interface reduction for the efficient vibro-acoustic simulation of fluid-filled piping systems, *Mech. Syst. Signal Process.* 24 (1) (2010) 153–163.
- [26] J. Kim, J.-G. Kim, G. Yun, D.-N. Kim, Applying the enhanced craig–bampton method to equilibrium protein dynamics, in: *Proceedings of the 2015 World Congress on Advances in Structural Engineering & Mechanics, ASEM2015*, 2015.
- [27] Simulia, ABAQUS/Standard User's Manual, Version 6.14, Dassault Systèmes Simulia Corp, United States, 2014.
- [28] M. Nastran, Release Guide, MSC Software Corporation, 2004.
- [29] R.R. Craig Jr., C.-J. Chang, Substructure Coupling for Dynamic Analysis and Testing, Technical Report, NASA, 1977.
- [30] M.P. Castanier, Y.-C. Tan, C. Pierre, Characteristic constraint modes for component mode synthesis, *AIAA J.* 39 (6) (2001) 1182–1187.
- [31] P. Holzwarth, P. Eberhard, Interface reduction for CMS methods and alternative model order reduction, *IFAC-PapersOnLine* 48 (1) (2015) 254–259.
- [32] C. uk Ahn, S.M. Kim, D.I. Park, J.-G. Kim, Refining characteristic constraint modes of component mode synthesis with residual modal flexibility, *Mech. Syst. Signal Process.* 178 (2022) 109265.
- [33] J.-G. Kim, D. Markovic, High-fidelity flexibility-based component mode synthesis method with interface degrees of freedom reduction, *AIAA J.* 54 (2016) 1–13.
- [34] S.-K. Hong, B.I. Epureanu, M.P. Castanier, Next-generation parametric reduced-order models, *Mech. Syst. Signal Process.* 37 (1–2) (2013) 403–421.
- [35] D. Krattiger, L. Wu, M. Zacharczuk, M. Buck, R.J. Kuether, M.S. Allen, P. Tiso, M.R. Brake, Interface reduction for hurty/craig–bampton substructured models: Review and improvements, *Mech. Syst. Signal Process.* 114 (2019) 579–603.
- [36] J.-G. Kim, S.-H. Boo, P.-S. Lee, Performance of the enhanced craig–bampton method, *Struct. Eng. Mech.* (ASEM2015) (2015).
- [37] J.-G. Kim, J. Seo, J.H. Lim, Novel modal methods for transient analysis with a reduced order model based on enhanced craig–bampton formulation, *Appl. Math. Comput.* 344–345 (2019) 30–45.
- [38] J.H. Lim, D.-S. Hwang, K.-W. Kim, G.H. Lee, J.-G. Kim, A coupled dynamic loads analysis of satellites with an enhanced Craig–Bampton approach, *Aerosp. Sci. Technol.* 69 (2017) 114–122.
- [39] D.J. Rixen, A dual Craig–Bampton method for dynamic substructuring, *J. Comput. Appl. Math.* 168 (1) (2004) 383–391, *Selected Papers from the Second International Conference on Advanced Computational Methods in Engineering (ACOMEN 2002)*.
- [40] R.J. Allemang, A correlation coefficient for modal vector analysis, in: *Proc. 1st Int. Modal Analysis Conference*, 1982, pp. 110–116.
- [41] M. Pastor, M. Binda, T. Harčarik, Modal assurance criterion, *Procedia Eng.* 48 (2012) 543–548, *Modelling of Mechanical and Mechatronics Systems*.
- [42] A. Brandt, *Noise and Vibration Analysis: Signal Analysis and Experimental Procedures*, John Wiley & Sons, 2011.
- [43] J.-G. Kim, On the finite element model reduction methods in structural dynamics (Ph.D. thesis), Ph.D. thesis, 2014.
- [44] R. Brandner, Production and technology of cross laminated timber (CLT): A state-of-the-art report, in: *Focus Solid Timber Solutions–European Conference on Cross Laminated Timber, CLT*, University of Bath, 2013, pp. 3–36, *Focus Solid Timber Solutions–European Conference on Cross Laminated Timber (CLT), CLT* ; Conference date: 21-05-2013 Through 22-05-2013.
- [45] R. Brandner, G. Flatscher, A. Ringhofer, G. Schickhofer, A. Thiel, Cross laminated timber (CLT): overview and development, *Eur. J. Wood Wood Prod.* 74 (2015) 331–351.
- [46] B. Bondsman, O. Flodén, H. Danielsson, P. Persson, E. Serrano, Modal analysis of CLT beams: Measurements and predictive simulations, in: A. Zingoni (Ed.), *Current Perspectives and New Directions in Mechanics, Modelling and Design of Structural Systems*, CRC Press/Balkema, 2022, pp. 56–62.
- [47] F. Tornabene, M. Baccocchi, N. Fantuzzi, E. Viola, Laminated Composite Doubly-Curved Shell Structures: Differential Geometry Higher-Order Structural Theories, Società Editrice Esculapio, 2016.
- [48] M. Johansson, A. Linderholt, K. Jarnerö, P. Landel, Tall timber buildings: a preliminary study of wind-induced vibrations of a 22-storey building, in: *World Conference on Timber Engineering (WCTE 2016)*, August 22–25, 2016, Vienna, Austria, Vienna University of Technology, 2016.

